

Diss. ETH No. 25056

EIDGENÖSSISCHE TECHNISCHE HOCHSCHULE ZÜRICH

2018

**PRODUCTION, CHARACTERIZATION, AND  
MONITORING OF SURFACE MUON BEAMS FOR  
CHARGED LEPTON FLAVOR VIOLATION  
EXPERIMENTS**

A THESIS SUBMITTED TO ATTAIN THE DEGREE OF  
DOCTOR OF SCIENCES OF ETH ZÜRICH

(Dr. sc. ETH ZÜRICH)

PRESENTED BY

ZACHARY DONOVAN HODGE

© 2018 Zachary Donovan Hodge

M.Sc. Northern Illinois University

BORN ON MAY 26, 1988

CITIZEN OF  
THE UNITED STATES OF AMERICA

Dissertation accepted on the recommendation of:

Prof. Dr. Klaus Kirch, Director

Prof. Dr. Christoph Grab

## ABSTRACT

The next-generation of charged lepton flavor violation experiments are currently in preparation and will begin taking data in the coming years. Due to the nature of these extremely rare decays, the new experiments also come with the desire for the highest muon beam rates achievable. The Mu3e Phase I experiment aims for a sensitivity level  $\mathcal{O}(10^{-15})$  on the decay  $\mu^+ \rightarrow e^+e^-e^+$ . The MEG II experiment will search for the  $\mu^+ \rightarrow e^+\gamma$  decay with an expected sensitivity of  $6 \cdot 10^{-14}$ . Both experiments will therefore require muon beam rates  $\mathcal{O}(10^8) \mu^+/s$  to reach their sensitivity goals. The Paul Scherrer Institut (PSI) in Switzerland currently provides the highest intensity muon beams in the world, in excess of  $10^8 \mu^+/s$  and will host both MEG II and Mu3e.

An optimization of the current muon production target at PSI has been undertaken in order to fully characterize the production of muons from charged pions, and to aide the design of a new High Intensity Muon Beam (HiMB) for the next-generation charged lepton flavor violation experiments. A new pion production cross section model has been developed as a foundation for these studies, using a parameterization of the available data from meson production facilities around the world. This has further led to the development of a new muon production target design, with optimized geometry and material. A rotated-slab target leads to potential surface muon yield increases of between 30% to 60% for the different orientated PSI secondary beam lines. This corresponds to the equivalent of raising the current proton beam intensity from 2.2 mA to between 2.9-3.5 mA, while preserving the proton beam intensity characteristics downstream on the spallation neutron target.

The muon and positron rates generated in simulation using the new pion production model have been used to optimize beamline elements, and have been compared with measurements along the beamline. A method has also been developed to differentiate the beam positrons from Michel positrons in beam measurements. The method has been used to estimate the absolute beam positron rates reaching the Mu3e experiment along with steps to minimize or eliminate the positron rate completely. Furthermore, the impact, of this beam correlated background on the sensitivity of the experiment has been assessed and found to be negligible for the Mu3e Phase I experiment.

A beam monitoring system has been developed for use in the MEG II and Mu3e experiments using ultra-thin CsI(Tl) luminophore foils and a high performance camera system. The beam monitor has been tested in air and within the vacuum beam pipe along the muon beamline, measuring beam profiles, normalized rates, and the transverse phase space. This new beam monitor provides fast, in situ, non-invasive measurements of high-intensity beams at the intensity frontier, and has been validated by more conventional, destructive methods.

## ZUSAMMENFASSUNG

Die nächste Generation von Experimenten auf der Suche nach Leptonenzahlverletzung im geladenen Sektor befindet sich zur Zeit im Aufbau und wird mit der Datennahme in den nächsten Jahren beginnen. Auf Grund der Natur dieser extrem seltenen Zerfälle benötigen diese neue Experimente die intensivsten, verfügbaren Myonenstrahlen. Die Phase I des Mu3e Experiments zielt auf eine Sensitivität von  $\mathcal{O}(10^{-15})$  auf den Zerfall  $\mu^+ \rightarrow e^+e^-e^+$ . Das MEG II Experiment wird nach dem Zerfall  $\mu^+ \rightarrow e^+\gamma$  mit einer Sensitivität von  $6 \cdot 10^{-14}$  suchen. Beide Experimente benötigen daher Myonenraten von  $\mathcal{O}(10^8) \mu^+/s$ , um ihre Sensitivitätsziele zu erreichen. Das Paul Scherrer Institut (PSI) stellt zur Zeit die intensivsten Myonenstrahlen der Welt zur Verfügung – über  $10^8 \mu^+/s$  – und daher werden sowohl MEG II wie auch Mu3e hier durchgeführt werden.

Im Rahmen dieser Doktorarbeit wurde eine Optimierung der bestehenden Myonenproduktionstargets durchgeführt, um die Produktion der Myonen von geladenen Pionen komplett zu charakterisieren und die Entwicklung eines neuen, hochintensiven Myonenstrahls (HiMB) für die nächste Generation von Experimenten zur geladenen Leptonenzahlverletzung zu unterstützen. Als Grundlage für diese Studien wurde ein neues Modell der Wirkungsquerschnitte zur Pionproduktion entwickelt, das sich auf eine Parametrisierung existierender Messdaten von Mesonenfabriken aus der ganzen Welt abstützt. Dies hat weiter zu einer neuen Bauform des Myonenproduktionstargets geführt mit optimierter Geometrie und Material. Die Geometrie einer leicht gegenüber dem Strahl abgedrehten Scheibe führt zu potenziellen Erhöhungen der Oberflächenmyonenraten von 30 bis 60% für die verschiedenen orientierten Sekundärstrahllinien des PSI. Das entspricht einer äquivalenten Erhöhung des jetzigen Protonenstrahlstroms von 2.2 mA auf 2.9-3.5 mA mit der gleichzeitigen Einhaltung der Protonenstrahlcharakteristik für die darauffolgende Neutronenspallationsquelle.

Die Myonen- und Positronenraten, die mit dem neuen Pionenproduktionsmodell simuliert wurden, wurden verwendet, um Elemente der Strahllinien zu optimieren und wurden direkt mit Messungen an verschiedenen Stellen der Strahllinie verglichen. Ebenfalls wurde eine neue Methode entwickelt, um in den Strahlmessungen zwischen Strahl- und Michel-Positronen zu unterscheiden. Dadurch konnte die absolute Positronenrate, die entlang des Strahls bis zum Mu3e Experiment gelangen, abgeschätzt werden und verschiedene Möglichkeiten zu deren Unterdrückung oder Elimination aufgezeigt werden. Zusätzlich wurde der Einfluss dieses mit dem Strahl korrelierten Untergrunds auf die Sensitivität des Mu3e Experiments abgeschätzt und als vernachlässigbar für die Phase I taxiert.

Ein Strahlmonitorierungssystem wurde für den Gebrauch in den MEG II und Mu3e Experimenten entwickelt basierend auf ultradünnen CsI(Tl) Luminophor-Folien und einer Hochleistungskamera. Dieses Strahlmonitorierungssystem wurde in Luft und in Vakuum an verschiedenen Orten der Strahllinie getestet und das Strahlprofil, die normalisierte Strahlenintensität und der transversale Phasenraum bestimmt. Dieses neue Strahlmonito-

rierungssystem bietet eine schnelle in-situ und nicht-invasive Charakterisierung von Hochintensitätsstrahlen, die mit konventionelleren, destruktiven Methoden validiert wurde.

---

## Acknowledgements

---

I would first like to express my deep gratitude to my advisor Prof. Dr. Klaus Kirch for his continuous support and advice. I would like to thank muon group leader Dr. Stefan Ritt for allowing me the opportunity to join PSI and contribute to the MEG II and Mu3e experiments. I would also like to thank Prof. Dr. Christoph Grab for agreeing to be a member of my committee and for all his corrections and suggestions.

I would like to thank my supervisors Peter-Raymond Kettle and Dr. Andreas Knecht for all of their guidance and for teaching me everything they know about experimental physics. I am grateful for all their dedication, support, and encouragement throughout this long journey.

I would like to express my sincere gratitude to my colleagues in the MEG and Mu3e collaborations, and for all the fruitful discussions at collaboration meetings. I would like to thank Dr. Felix Berg, for sharing all his immense knowledge on beam physics and for the many discussions we had over coffee. I would like to thank Dr. Giada Rutar for all our enlightening discussions over physics and life in general.

I would like to thank Dr. Angela Papa for all her help on the beamline and for sharing her detector expertise. My grateful thanks are also extended to Dr. Malte Hildebrandt for his help with the material density measurements, and his always enlightening discussions. I would like to extend my thanks to the Florian Barchetti for all his assistance in mechanical design and whose workshop was always open for help. I would also like to thank all the members of the PSI Hallendienst for their assistance in setting up all the magnets and other beamline elements, as well as many other contributions that made all these measurements possible. I would like to express my gratitude to Anita van Loon, and all her administrative assistance over the years.

Finally, I wish to thank my mother Michelle and brother Travis for their endless support and encouragement throughout these years.

---

## Dedication

---

for my father, Larry Wayne Hodge.

---

## Table of Contents

---

	Page
List of Tables . . . . .	vii
List of Figures . . . . .	ix
Chapter	
1 Introduction . . . . .	1
2 Charged Lepton Flavor Violation. . . . .	4
2.1 The Standard Model . . . . .	4
2.2 Flavor Violation in the Quark Sector. . . . .	5
2.3 Flavor Violation in the Lepton Sector . . . . .	5
2.3.1 Neutrino Oscillations . . . . .	6
2.3.2 Muon Flavor Violating Processes . . . . .	6
2.4 Current Status of CLFV Worldwide . . . . .	11
3 PSI and the MEG II and Mu3e Experiments . . . . .	13
3.1 The PSI High Intensity Proton Accelerator. . . . .	13
3.2 The $\pi$ E5 Beamline . . . . .	17
3.3 The $\mu$ E4 Beamline . . . . .	18
3.4 The $\pi$ E1 Beamline . . . . .	19
3.5 The MEG II Experiment. . . . .	20
3.5.1 Signal and Background for $\mu \rightarrow e\gamma$ . . . . .	20
3.5.2 The MEG II Detector . . . . .	23
3.6 The Mu3e Experiment . . . . .	27
3.6.1 Signal and Background for $\mu \rightarrow eee$ . . . . .	28
3.6.2 The Mu3e Detector . . . . .	30

Chapter	Page	
4	Characterization and Optimization of Surface Muon Production . . . . .	33
4.1	Pion Production in the Target . . . . .	33
4.1.1	Parameterized Pion Production Cross Sections . . . . .	34
4.1.2	Pion Decay and Muon Production Overview . . . . .	38
4.2	Surface Muon Production . . . . .	41
4.2.1	Muon Production Kinematics . . . . .	41
4.2.2	Selection Depth . . . . .	44
4.2.3	Surface Muon Distribution . . . . .	44
4.3	Geometry Optimization . . . . .	45
4.3.1	Standard Target E . . . . .	45
4.3.2	Radial Grooved Target . . . . .	52
4.3.3	Trapezoidal Target . . . . .	56
4.3.4	Forked Target . . . . .	59
4.3.5	Rotated Slab Target . . . . .	62
4.4	Target Geometry Effects on the Proton Beam . . . . .	68
4.5	Alternate Materials . . . . .	70
4.6	Summary . . . . .	73
5	Beam-Correlated Backgrounds in the Mu3e Experiment . . . . .	74
5.1	Background Production from the Muon Beam in Mu3e . . . . .	74
5.1.1	Bhabha Production in Mu3e . . . . .	76
5.2	The $\pi E5$ Channel . . . . .	78
5.2.1	The Compact Muon Beamline . . . . .	80
5.3	Simulation of $\pi E5$ Channel . . . . .	82
5.3.1	Muon and Positron Production at Target E . . . . .	82
5.3.2	Transport in the $\pi E5$ Channel . . . . .	84
5.3.3	Estimated Background Rates from Simulation . . . . .	84
5.3.4	Modified Wien Filter . . . . .	89

Chapter	Page
5.4 Beam Measurements at the $\pi$ E5 Beamline . . . . .	93
5.4.1 The Pill Scintillator Scanner System . . . . .	94
5.4.2 Beam Measurements and Data Analysis . . . . .	97
5.4.3 Fundamental Momentum Characteristics of the Beam. . . . .	97
5.4.4 Beam-Correlated Background Measurements. . . . .	100
5.4.5 Measurement at the Collimator System . . . . .	105
5.4.6 Measurement at the Injection to the Mu3e Solenoid . . . . .	116
5.5 Impact on the Mu3e Sensitivity . . . . .	123
5.6 Summary . . . . .	127
6 Development of a Ultra-Thin CsI(Tl) Luminophore Foil Muon Beam Mon- itor . . . . .	128
6.1 Scintillation Mechanism of CsI(Tl) . . . . .	129
6.2 The CsI(Tl) Foil Muon Beam Monitor. . . . .	132
6.2.1 The Ultra-Thin CsI(Tl) Foils . . . . .	132
6.2.2 The CCD Camera Systems . . . . .	135
6.2.3 The Detector Setups. . . . .	137
6.2.4 Beam Image Analysis . . . . .	140
6.2.5 CsI(Tl) Layer Uniformity . . . . .	146
6.3 Muon Beam Measurements with Thin CsI(Tl) Foils . . . . .	149
6.3.1 Beam Profiles . . . . .	149
6.3.2 Spatial Resolution . . . . .	155
6.3.3 Beam Intensity Regulation via Beam Slits . . . . .	158
6.3.4 Range Curve . . . . .	160
6.3.5 Phase Space . . . . .	170
6.4 Summary . . . . .	174
7 Summary . . . . .	176
Appendices . . . . .	178
A Pion Cross Section Parameterization . . . . .	179

Chapter	Page
B Image Analysis . . . . .	184
B.1 Perspective Transformation . . . . .	184
B.2 Pixel Error Estimate . . . . .	185
C Beam Phase Space . . . . .	187
References . . . . .	190

---

## List of Tables

---

Table	Page
2.1 The Standard Model fermions. . . . .	4
2.2 The lower limits on the branching ratios of muon charged lepton flavor violating processes. . . . .	11
4.1 The solid angle acceptance of secondary beamlines used in this simulation . . . . .	46
4.2 The expected enhancement of surface muons due to increased surface volume compared to the equivalent gain by increasing the proton beam current from the present 2.2 mA. . . . .	52
4.3 The simulated muon rate enhancement from a radially grooved target in the $\mu$ E4 and $\pi$ E5 beamlines. . . . .	54
4.4 Simulated muon rate enhancement from a trapezoidal target in the $\mu$ E4 and $\pi$ E5 beamlines. . . . .	57
4.5 Simulated muon rate enhancement from a forked target in the $\mu$ E4 and $\pi$ E5 beamlines. . . . .	60
4.6 Simulated muon rate enhancement in the $\mu$ E4, $\pi$ E5, and $\pi$ E1 beamlines from a slab target with increasing rotation angle and a fixed 150 mm length . . . . .	63
4.7 Simulated muon rate enhancement in the $\mu$ E4, $\pi$ E5, and $\pi$ E1 beamlines from a slab target at a fixed $10^\circ$ rotation angle and increasing overall length . . . . .	63
4.8 The proton beam power downstream of the target for each target geometry. . . . .	69
4.9 Material properties for Carbon, $B_4C$ , and $Be_2C$ relevant to the use as a meson production target. . . . .	71
5.1 Positions and beamline elements included for the several stages of optimization of the $\pi$ E5 channel. . . . .	84
5.2 Beam particle rates from simulation optimized for muon rate transmission to Mu3e Injection without $e^+$ stopper in TII. . . . .	86

Table	Page
5.3 Beam particle rates from simulation optimized for muon rate transmission to Mu3e Injection with $e^+$ stopper in TII. . . . .	86
5.4 Muon and Positron rates at the Mu3e Injection point with a standard, symmetric potential, and an enhanced symmetric potential SEP41. . . .	92
5.5 Beam particle rates measured in $\pi E5$ channel optimized for muon rate transmission to Mu3e Injection without $e^+$ stopper in TII. . . . .	120
5.6 Beam particle rates measured in $\pi E5$ channel optimized for muon rate transmission to Mu3e Injection with $e^+$ stopper in TII. . . . .	120
6.1 Technical specifications of the IDS and ORCA camera system. . . . .	136
6.2 The mean signal and background count and variance within the region of interest for both the IDS and ORCA cameras. . . . .	142
6.3 Material thickness for range curve measurement using the Pill Scanner System. . . . .	166
6.4 Material thickness for Bragg curve measurements using the luminophore foil and ORCA camera system. . . . .	166
6.5 The muon momentum and range in MYLAR in simulation and measurements using the pill scanner and luminophore detector systems. 169	
6.6 The muon beam transverse phase space Twiss parameters, measured with the pill scanner in air and luminophore system in vacuum. . . . .	172

---

## List of Figures

---

Figure	Page
2.1 Standard Model processes for charged lepton flavor violation. . . . .	9
2.2 Beyond Standard Model processes for charged lepton flavor violation. .	9
2.3 Limits on the Wilson coefficients contributing to muon lepton flavor violation from current and future experiments. . . . .	10
2.4 Limits on muon CLFV processes over time. . . . .	12
3.1 The 590 MeV Ring Cyclotron. . . . .	14
3.2 The layout of the PSI accelerator complex. . . . .	15
3.3 A schematic view of the proton beam channel, Target E station, and secondary beamlines. . . . .	16
3.4 The layout of the $\pi$ E5 channel relative to Target E. . . . .	17
3.5 The layout of the $\mu$ E4 channel relative to Target E. . . . .	18
3.6 The layout of the $\pi$ E1 channel relative to Target E. . . . .	19
3.7 Schematics of the signal and background processes in the MEG II experiment. . . . .	21
3.8 The sensitivity of the MEG II experiment to the $\mu \rightarrow e\gamma$ decay over the expected running time. . . . .	22
3.9 A schematic drawing of the MEG II detector. . . . .	23
3.10 The sub-detectors of the MEG II experiment. . . . .	26
3.11 The single event sensitivity (SES) and corresponding 90% and 95% confidence level (CL) upper limits on the branching ratio versus time for the Mu3e Phase-I experiment. . . . .	27
3.12 Schematics of the signal and background processes in the Mu3e experiment. . . . .	29
3.13 The branching ratio of $\mu^+ \rightarrow e^+ \bar{\nu}_\mu \nu_e e^+ e^-$ as a function of the missing energy carried away by the neutrinos. . . . .	29
3.14 A rendering of the Mu3e detector. . . . .	30

Figure	Page
3.15 The target and sub-detectors of the Mu3e experiment. . . . .	32
4.1 Differential cross section comparison of the various hadronic models available in GEANT4 for pion production on carbon at at $22.5^\circ$ with a proton energy of 585 MeV.. . . .	36
4.2 Differential cross section comparison of the GEANT4 standard BERT hadronic model, Data, and parameterized cross section model (HiMB) for pion production. . . . .	37
4.3 A drawing of pion and muon production inside or outside the target volume. . . . .	39
4.4 The transverse and longitudinal pion stop distribution for the Target E geometry using G4Beamline and the HiMB pion production model. . .	40
4.5 The helicity states of the neutrino ( $\nu_l$ ) and lepton ( $l^+$ ) emitted in charged pion decay. . . . .	42
4.6 The momentum spectrum of all positive muons within the geometric acceptance of a nearby beamline. . . . .	43
4.7 The initial energy spectrum of those pions that subsequently stop in a layer near the target surface. . . . .	47
4.8 The initial x-positions of surface muons that are within the geometric and momentum acceptances of a nearby beamline. . . . .	48
4.9 A picture of the actual Target E. . . . .	48
4.10 A schematic drawing of the target position relative to surrounding beamlines with sizes proportional to their geometric acceptance. . . . .	49
4.11 The initial x-y positions of muons from the standard target geometry that reach the geometric acceptance of the $\mu$ E4 and $\pi$ E5 beamlines. . .	49
4.12 The initial x-z positions of muons from the standard target geometry that reach the geometric acceptance of the $\mu$ E4 and $\pi$ E5 beamlines . .	50
4.13 The initial y-z positions of muons from the standard target geometry that reach the geometric acceptance of the $\mu$ E4 and $\pi$ E5 beamlines . .	50
4.14 The horizontal phase space of surface muons from the standard target geometry at the geometric acceptance of the $\mu$ E4 or $\pi$ E5 beamlines. . .	51
4.15 The vertical phase space of surface muons from the standard target geometry at the geometric acceptance of the $\mu$ E4 or $\pi$ E5 beamlines. . .	51
4.16 A visual comparison of the surface volume for a flat target (left) and a grooved target (right). . . . .	52

Figure	Page
4.17 A model of the target section with grooves along the outside surface. . . . .	53
4.18 The initial x-y position of muons detected in the $\mu$ E4 and $\pi$ E5 beam- lines for a 2 mm radius grooved target. . . . .	54
4.19 The initial x-z position of muons detected in the $\mu$ E4 and $\pi$ E5 beam- lines for a 2 mm radius grooved target. . . . .	54
4.20 The initial y-z position of muons detected in the $\mu$ E4 and $\pi$ E5 beam- lines for a 2 mm radius grooved target. . . . .	55
4.21 A model of the trapezoidal target with a narrow upstream width and nominal 6 mm downstream width. . . . .	56
4.22 The initial x-y position of muons detected in the $\mu$ E4 and $\pi$ E5 beam- lines for a 2 mm upstream width trapezoidal target. . . . .	57
4.23 The initial x-z position of muons detected in the $\mu$ E4 and $\pi$ E5 beam- lines for a 2 mm upstream width trapezoidal target. . . . .	57
4.24 The initial y-z position of muons detected in the $\mu$ E4 and $\pi$ E5 beam- lines for a 2 mm upstream width trapezoidal target. . . . .	58
4.25 A model of the fork target with 2 mm widths for all three target sections such that the total target width is the nominal 6 mm. . . . .	59
4.26 The initial x-y position of muons detected in the $\mu$ E4 and $\pi$ E5 beam- lines from a forked target with a 2 mm central target section. . . . .	60
4.27 The initial x-z position of muons detected in the $\mu$ E4 and $\pi$ E5 beam- lines from a forked target with a 2 mm central target section. . . . .	60
4.28 The initial y-z position of muons detected in the $\mu$ E4 and $\pi$ E5 beam- lines from a forked target with a 2 mm central target section. . . . .	61
4.29 A model of the rotated slab target. . . . .	62
4.30 The initial x-y position of muons detected in the $\mu$ E4 and $\pi$ E5 beam- lines from a slab target with a $10^\circ$ rotation. . . . .	64
4.31 The initial x-z position of muons detected in the $\mu$ E4 and $\pi$ E5 beam- lines from a slab target with a $10^\circ$ rotation. . . . .	64
4.32 The initial y-z position of muons detected in the $\mu$ E4 and $\pi$ E5 beam- lines from a slab target with a $10^\circ$ rotation. . . . .	65
4.33 The dependance of simulated muon rate enhancements for a rotated slab target with respect to the target rotation angle and target length. . . . .	66
4.34 Comparison of the longitudinal and horizontal pion stop distributions for all target geometries considered. . . . .	67

Figure	Page
4.35 The total proton momentum downstream of the target station for the target geometries studied. . . . .	69
4.36 The pion yield and normalized surface muon yield for a proton energy of 585 MeV relative to carbon as a function of atomic number $Z$ . . . . .	72
5.1 The Feynman diagrams for s- and t-channel contributions to Bhabha scattering. . . . .	75
5.2 <b>Process A</b> - The combination of a Michel positron with a Bhabha pair from an additional Michel positron. . . . .	77
5.3 <b>Process B</b> - The combination of a Michel positron with a Bhabha pair coming from an incident beam positron. . . . .	77
5.4 <b>Process C</b> - The combination of two beam positrons, where one undergoes Bhabha scattering. . . . .	78
5.5 <b>Process D</b> - The combination of a beam positron with a Michel positron that undergoes Bhabha scattering. . . . .	78
5.6 The $\pi$ E5 beamline, MEG beamline elements, and Mu3e extension in the MEG configuration. . . . .	79
5.7 The $\pi$ E5 beamline, MEG beamline elements, and Mu3e extension in the CMBL configuration.. . . .	81
5.8 The momentum spectrum of positively charged particles produced in Target E, 150 mm downstream in the direction of the $\pi$ E5 channel. . .	83
5.9 The momentum spectrum of negatively charged particles produced in Target E, 150 mm downstream in the direction of the $\pi$ E5 channel. . .	83
5.10 Muon beam transmission and profile through the $\pi$ E5 channel and CMBL. . . . .	87
5.11 Positron beam transmission through $\pi$ E5 channel and CMBL. . . . .	88
5.12 Schematic of the working principle of a Wien Filter velocity separator.	89
5.13 The magnetic field along the z-axis at $y = 0$ in SEP41 calculated using OPERA. . . . .	90
5.14 The electric field along the z-axis at $x = 0$ in SEP41 calculated using OPERA. . . . .	91
5.15 The electric field along the z axis at $x = 0$ in SEP41 for a symmetric potential, calculated using OPERA. . . . .	92
5.16 Panoramic view of the $\pi$ E5 front area, in CMBL configuration. . . . .	93
5.17 Detector characteristics for the beam scanner detector system. . . . .	94

Figure	Page
5.18 Beam Scanner System and mini-PMT.. . . . .	95
5.19 Basic electronics schematic for the Pill Scintillator Scanner System. . .	96
5.20 Momentum Spectrum in the $\pi$ E5 channel near the surface muon kinematic edge. . . . .	99
5.21 Beam scan software output . . . . .	100
5.22 The lead collimator positron-stopper. . . . .	101
5.23 The measured raster scans using polyethylene to stop muons and extract the underlying beam positron contamination. . . . .	103
5.24 The rasters for Michel and beam positrons, generated by filling bins of <b>A</b> based on the classifier $\alpha$ . . . . .	104
5.25 The final calculated raster for beam positrons, after subtracting the fit of the Michel positron background. . . . .	104
5.26 QSM final focus optics measured at the collimator system showing the horizontal and vertical beam profile measured with the pill scanner system and using the high threshold discriminator. . . . .	106
5.27 Raster scan of the beam at the collimator position using QSM optics. .	107
5.28 The scan of the SEP41 magnet current from 60 A to 0 A. . . . .	108
5.29 The high and low threshold raster scans using reduced separation power of SEP41. . . . .	109
5.30 The measured raster scans at the collimator focus, using reduced separation power of SEP41, using polyethylene. . . . .	110
5.31 The rasters for Michel and beam positrons at the collimator focus, using reduced separation power of SEP41. . . . .	111
5.32 The final calculated raster for beam positrons using reduced separation power of SEP41, with the polyethylene sheet. . . . .	111
5.33 The measured raster scans at the collimator focus, without the positron-stopper, using polyethylene. . . . .	112
5.34 The rasters for Michel and beam positrons at the collimator focus, without the positron-stopper. . . . .	113
5.35 The final calculated raster for beam positrons with the polyethylene sheet at the collimator focus. . . . .	113
5.36 The measured raster scans at the collimator focus, with the positron-stopper, using polyethylene. . . . .	114

Figure	Page
5.37 The rasters for Michel and beam positrons at the collimator focus, with the positron-stopper. . . . .	115
5.38 The final calculated raster for beam positrons with the polyethylene sheet at the collimator focus with the lead collimator positron-stopper in TII. . . . .	115
5.39 Raster scan of the beam at the Mu3e solenoid injection position without the positron-stopper installed in TII. . . . .	116
5.40 The measured raster scans at the Mu3e solenoid injection focus, without the positron-stopper. . . . .	117
5.41 The rasters for Michel and beam positrons at the Mu3e solenoid injection focus, without the positron-stopper. . . . .	118
5.42 The final calculated raster for beam positrons with the polyethylene sheet at the Mu3e solenoid injection point, after subtracting the fit of the Michel positron background. . . . .	118
5.43 Raster scan of the beam at the Mu3e solenoid injection position with the positron-stopper installed in TII. . . . .	119
5.44 The measured raster scans at the Mu3e solenoid injection focus, with the positron-stopper, using polyethylene. . . . .	121
5.45 The rasters for Michel and beam positrons at the Mu3e solenoid injection focus, without the positron-stopper. . . . .	122
5.46 The final calculated raster for beam positrons with the polyethylene sheet at the Mu3e solenoid injection point with the positron-stopper in TII, after subtracting the fit of the Michel positron background. . . . .	122
5.47 The momentum spectrum of positrons and electrons that participate in Bhabha scattering as a result of beam positrons and are subsequently seen by the inner tracking layer. . . . .	125
5.48 Momentum spectra for high momentum positrons in the inner tracking layer. . . . .	126
6.1 The band structure for an impurity activated crystal. . . . .	130
6.2 The light yield output from a CsI(Tl) crystal with increasing thallium dopant concentrations. . . . .	131
6.3 The granular structure of a 4.1 $\mu\text{m}$ CsI(Tl) deposited on a glass substrate. . . . .	133
6.4 One of the CsI(Tl) luminophore foils used in the muon beam test with a CsI(Tl) layer thickness of 5.2 $\mu\text{m}$ on a 3 $\mu\text{m}$ MYLAR substrate. . . . .	134

Figure	Page
6.5 The spectral response for the IDS and ORCA camera sensor from 400 to 1000 nm. . . . .	135
6.6 Raw images of the muon beam captured from the IDS and ORCA cameras under the same conditions. . . . .	136
6.7 The overhead view of the luminophore setup inside the light-tight box.	137
6.8 Plan-view of the luminophore vacuum setup at the MEG collimator position.. . . .	138
6.9 Image of the luminophore vacuum setup at the MEG collimator position. . . . .	139
6.10 Image of the calibration grid using the UV LED installed inside the beampipe. This image was captured with the IDS camera system. . . .	139
6.11 The signal and background images captured with the IDS camera system in the light-tight box. . . . .	143
6.12 The signal and background images captured with the ORCA camera system in the light-tight box. . . . .	144
6.13 The signal-to-noise characteristics $S\sigma_N R$ for both cameras relative to the muon beam intensity. . . . .	145
6.14 The original and corrected images of the luminophore foil in vacuum, under UV LED illumination. . . . .	147
6.15 The pixel intensity spatial distribution in the region of interest on the CsI(Tl) foil under UV LED illumination. . . . .	147
6.16 The histogram of pixel intensity in the region of interest on the CsI(Tl) foil under UV LED illumination, and a gaussian fit which indicates the spread in individual pixel intensities. . . . .	148
6.17 The contour plot showing the spatial distribution of regionally averaged pixel intensities within $5 \times 5 \text{ mm}^2$ grid blocks. . . . .	148
6.18 Comparison of the four foils using the beam profile projection. . . . .	150
6.19 The beam profiles in X and Y measured with the pill scintillator in (a) and (b) and the luminophore foil in (c) and (d). . . . .	151
6.20 Projection of the horizontal and vertical beam profiles measured with the luminophore system in vacuum. . . . .	153
6.21 A pseudo-3D light intensity plot of both the muon beam (small peak) and positron beam spots (large peak) imaged with the luminophore system with reduced separation power of SEP41. . . . .	154
6.22 Muon radiography using soldering wire and the luminophore system. .	155

Figure	Page
6.23 Beam profile with an aluminum grating placed on the upstream side of the luminophore foil, stopping muons from hitting the foil. . . . .	156
6.24 Spatial resolution test showing the beam profile projections with an aluminum grating placed directly on the upstream side of the luminophore foil. . . . .	157
6.25 The muon rate as a function of the beam line slit opening, measured using the pill scintillator and luminophore foil. . . . .	159
6.26 The muon beam width as a function of the beam line slit opening, measured using the luminophore foil. . . . .	159
6.27 A schematic diagram of a range curve with increasing degrader thickness. . . . .	161
6.28 A simplified schematic diagram of the materials between the muon beam in vacuum and the pill detector system. . . . .	162
6.29 A schematic diagram of a Bragg curve with increasing degrader thickness. . . . .	163
6.30 A simplified schematic diagram of the materials between the muon beam in vacuum and the CsI(Tl) foil used in the luminophore system. . . . .	163
6.31 The mean range of monochromatic muons in MYLAR as a function of their initial momentum simulated in G4Beamline. . . . .	164
6.32 The total energy deposited in the CsI(Tl) layer relative to the initial muon momentum and the total thickness of MYLAR degrader material. . . . .	165
6.33 Range curve measurements using pill scanner and luminophore simulation for the full degrader thickness range. . . . .	167
6.34 Bragg curve measurements using the luminophore foil in the light-tight box and corresponding simulation for the full degrader thickness range. . . . .	168
6.35 Transverse muon beam width measurements using the pill scanner downstream in air and adjusting the QSK43 focusing strength. . . . .	171
6.36 Muon beam transverse phase space ellipses using the pill scanner downstream in air. . . . .	172
6.37 Transverse muon beam width measurements using the luminophore foil in vacuum and adjusting the QSK43 focusing strength. . . . .	172
6.38 Muon beam transverse phase space ellipses using the luminophore foil in vacuum. . . . .	173
C.1 The two dimensional phase space ellipse. . . . .	189

## Introduction

---

The following thesis is set in the context of developing a fundamental understanding of surface muon beams for next generation charged lepton flavor violation experiments at the Paul Scherrer Institut. Surface muons are ideally suited for Intensity Frontier experiments due to their high rates at relatively low energies, reducing the material needed to stop the muon and search for rare decays. The Mu3e Phase I experiment will search for the rare three body decay  $\mu^+ \rightarrow e^+e^-e^+$  at a sensitivity level  $\mathcal{O}(10^{-15})$ . The MEG II experiment will search for the  $\mu^+ \rightarrow e^+\gamma$  decay with an expected sensitivity of  $6 \cdot 10^{-14}$ . To achieve these sensitivity goals, and search for these extremely rare decays, both experiments require the highest intensity muon beams at  $\mathcal{O}(10^8) \mu^+/s$ , only available at PSI. Characterization of surface muons from production, transport, and delivery to the experiment has been carried out, as well as the development of a novel in situ beam monitor to maintain continuous beam operation throughout the experiment run periods.

- A brief overview of charged lepton violation and the current status of experimental searches is described in Chapter 2.
- An introduction to the Paul Scherrer Institut accelerator complex, production targets, and secondary beamlines, as well as an overview of the MEG II and Mu3e experiments at PSI, the physics signal and backgrounds, and the detector systems is described in Chapter 3.
- An extensive optimization of the current muon production target, Target E, at PSI to fully characterize and improve the production of muons for use in charged lepton flavor violation experiments is described in Chapter 4. A new pion production cross section model using a parameterization of the available data has been developed to aid the design of a new High Intensity Muon Beam (HiMB), necessary to meet the requirements for Mu3e Phase-II. Further details for the parameterization are described in Appendix A. Significant effort has been spent on optimization of the geometry of the production target to deliver maximum surface muon rates, with the constraint to simultaneously preserve the proton intensity characteristics for downstream use in the spallation neutron target SINQ. Simulations of a rotated slab geometry have shown enhancements to the surface

muon rates in the surrounding beamlines of between 30-60%, which is equivalent to raising the proton current from 2.2 mA to between 2.9-3.5 mA, and as a result of target material investigations further improvements of 10-15% from using low- $Z$  carbides is expected.

- The use of the new parameterized pion production model to generate muons and positrons from protons on target and to optimize beamline elements in the  $\pi E5$  channel, together with measurements of the muon and beam-correlated positron rate along the beamline, have allowed an extensive comparison of Bhabha pair production from such beam-correlated positron backgrounds in the context of the dominant accidental background in the experiment, that of Bhabha pair production from Michel positrons, and is described in Chapter 5. From this, the expected background contributions and the sensitivity impact on the Mu3e Phase-I experiment are described in Chapter 5. A method has been developed to differentiate the beam positrons from Michel positrons in beam measurements, and has also been used to estimate the absolute beam positron rates reaching the Mu3e experiment. An unexpected beam positron background was measured and a solution in simulation using a lead collimator and then physically implemented inside the quadrupole triplet vacuum chamber significantly reduced the positron rate, but further simulations implementing an increased 395 kV symmetric potential to the the current asymmetric electric field SEP41 Wien filter lead to the elimination of all beam positrons at the Mu3e solenoid injection point. While the implementation of such a higher performance Wien filter is underway, the expected residual beam positron contribution, using the lead collimator is twelve orders of magnitude below the dominant background Bhabha-scattering process and will have no impact on the sensitivity of the Mu3e Phase-I experiment.
- The development of a new beam monitoring system for use in the MEG II and Mu3e experiments using ultra-thin CsI(Tl) luminophore foils and a high performance CCD camera system is described in Chapter 6. The system has been tested along the muon beamline and is installed as a permanent in-situ, non-destructive beam monitor within the vacuum beam pipe, capable of measuring beam profiles, normalized rates, and the transverse phase space. Comparison of the beam profiles using the pill scintillator scanner to transverse projections of the luminophore foil shows excellent agreement and differences in the transverse emittances between the pill scanner measurements in air and the luminophore measurements in vacuum offer insights into higher order effects, such as momentum dispersion, on the beam. The image transformation procedure needed to reproduce the correct beam size and shape is described in Appendix B and the phase space calculation formalism is described in Appendix C. A range-curve and momentum study using both a conventional PMT and scintillator scanner sys-

tem and the luminophore system show that range-curve simulations and scanner data, show reasonable agreement but disagree somewhat with the measured and simulated luminophore Bragg peak based on energy deposition. Nevertheless, the derived beam momentum from both, the pill range-curve measurements and the luminophore Bragg-curve measurements differ by only 2%, for two different methods, one counting sampled stopped particles and the other measuring the through-going relative light-yield from the whole beam.

- Finally, the Appendices A to C give further insight into the various detailed aspects encountered during the implementation of simulation software and the analysis of image data produced by the new beam monitoring system.

---

## Charged Lepton Flavor Violation

---

### 2.1 The Standard Model

The Standard Model (SM) describes the interactions of fundamental fermion fields with the gauge fields associated with the strong, weak, and electromagnetic interactions. The fermions carry spin-1/2 and are grouped in three generations or flavors, each with progressively larger mass and are listed in Table 2.1. The four gauge bosons carry spin-1 and are

- gluon ( $g$ ) which mediates the strong interaction
- $W^\pm$  and  $Z^0$  which mediate the weak interaction
- photon ( $\gamma$ ) which mediates the electromagnetic interaction

The scalar Higgs boson is the excitation of the Higgs field, responsible for the generation of the  $W^\pm$  and  $Z^0$  masses through electroweak symmetry breaking.

Each fermion generation contains two quarks which couple to strong, weak, and electromagnetic interactions, and two leptons which couple only to weak and electromagnetic interactions. The quarks and leptons of the second and third generations are identical to those of the first generation except for mass.

	$1^{st}$	$2^{nd}$	$3^{rd}$	Electric Charge
Quarks	$u (\bar{u})$	$c (\bar{c})$	$t (\bar{t})$	+2/3 (-2/3)
	$d (\bar{d})$	$s (\bar{s})$	$b (\bar{b})$	-1/3 (+1/3)
Leptons	$e^- (e^+)$	$\mu^- (\mu^+)$	$\tau^- (\tau^+)$	-1(+1)
	$\nu_e (\bar{\nu}_e)$	$\nu_\mu (\bar{\nu}_\mu)$	$\nu_\tau (\bar{\nu}_\tau)$	0

Table 2.1: The Standard Model fermions.

The SM Lagrangian is given by the following

$$\mathcal{L}_{SM} = \mathcal{L}_{Gauge} + \mathcal{L}_{Higgs} + \mathcal{L}_{Yukawa} \quad (2.1)$$

Only the Yukawa interaction of these fermion fields with the Higgs field distinguishes the flavor of the fermions and leads to the mixing among different generations.

## 2.2 Flavor Violation in the Quark Sector

In the SM the Yukawa interaction of quarks with the Higgs field ( $\phi$ ) is given by

$$-\mathcal{L}_{Yukawa}^{SM} = Y_d^{ij} \bar{Q}_L^i \phi D_R^j + Y_u^{ij} \bar{Q}_L^i \tilde{\phi} U_R^j \quad (2.2)$$

where  $Y_q^{ij}$  are the Yukawa coupling matrices,  $Q_L^i$  are left-handed quark doublets, and  $D_R^j$  and  $U_R^j$  are right-handed down- and up-type quark singlets, respectively. The transformation from the flavor basis to the mass basis is given by the following

$$U_L^u Y^u U_R^{u\dagger} = \text{diag}(y_u, y_c, y_t) \quad (2.3)$$

where  $y_q = m_q/v$  and  $m_q$  are the quark masses and the vacuum expectation value of the Higgs field  $\langle \phi \rangle = v$ . The product of the diagonalizing matrices of the up- and down-type quark mass matrices is the Cabibbo-Kobayashi-Maskawa (CKM) mixing matrix and relates the quark flavor eigenstates ( $d', s', b'$ ) and the quark mass eigenstates ( $d, s, b$ ). In the standard parametrization the CKM matrix, in terms of three rotational angles ( $\theta_{ij}$ ) and a complex phase ( $\delta$ ), is given by the following

$$\begin{aligned} V &= U_L^u U_L^{d\dagger} = \begin{pmatrix} V_{ud} & V_{us} & V_{ub} \\ V_{cd} & V_{cs} & V_{cb} \\ V_{td} & V_{ts} & V_{tb} \end{pmatrix} \\ &= \begin{pmatrix} c_{12}c_{13} & s_{12}c_{13} & s_{13}e^{-i\delta} \\ -s_{12}c_{23} - c_{12}s_{23}s_{13}e^{i\delta} & c_{12}c_{23} - s_{12}s_{23}s_{13}e^{i\delta} & s_{23}c_{13} \\ s_{12}s_{23} - c_{12}c_{23}s_{13}e^{i\delta} & -s_{23}c_{12} - s_{12}c_{23}s_{13}e^{i\delta} & c_{23}c_{13} \end{pmatrix} \end{aligned} \quad (2.4)$$

where  $s_{ij} = \sin(\theta_{ij})$  and  $c_{ij} = \cos(\theta_{ij})$ . The charged-current couplings to the left-handed quark fields are proportional to the elements of  $V$  and since  $V$  is not diagonal, the  $W^\pm$  gauge bosons couple to the quark mass eigenstates of different generations [1, 2].

## 2.3 Flavor Violation in the Lepton Sector

In the Standard Model, lepton flavor conservation is accidental, and relies on assuming vanishingly small neutrino masses. However, the observations made by SuperKamiokande [3] and Sudbury Neutrino Observatory [4] experiments on atmospheric and solar neutrinos provide clear evidence of neutrino oscillations and therefore neutrino masses, and additional data from independent neutrino sources further support this, such as the KamLAND [5], Double Chooz [6], and Daya Bay [7] reactor neu-

trino experiments. Similar initial confirmation was also given by the accelerator-based experiments such as K2K [8, 9] and MINOS [10].

### 2.3.1 Neutrino Oscillations

The phenomenon of neutrino mixing and oscillation arises from the result of neutrinos having mass and implies that neutrinos are produced as a superposition of mass-eigenstates, and thus a neutrino with a defined flavor  $\nu_\alpha$  has some probability to be measured as a neutrino  $\nu_\beta$  of a different flavor. The probability  $P(\nu_\alpha \rightarrow \nu_\beta)$  for this oscillation depends on the neutrino energy  $E$ , the propagation distance  $L$ , two independent neutrino mass-squared differences,  $\Delta m_{ij}^2 = m_i^2 - m_j^2$ , and the elements of the Pontecorvo-Maki-Nakagawa-Sakata (PMNS) leptonic mixing matrix,  $U$  [11], and is given by the following expression

$$P(\nu_\alpha \rightarrow \nu_\beta) = \sum_{i,j} U_{\alpha i}^* U_{\beta i} U_{\alpha j} U_{\beta j}^* e^{-i(\Delta m_{ij}^2 L/2E)} \quad (2.5)$$

The PMNS matrix was introduced by Maki, Nakagawa, and Sakata [12] to explain neutrino oscillations predicted by Pontecorvo [13] by relating neutrino flavor eigenstates ( $\nu_e, \nu_\mu, \nu_\tau$ ) to neutrino mass eigenstates ( $\nu_1, \nu_2, \nu_3$ ) (similar to the CKM matrix in the quark sector) and is given by

$$\begin{pmatrix} \nu_e \\ \nu_\mu \\ \nu_\tau \end{pmatrix} = \begin{pmatrix} U_{e1} & U_{e2} & U_{e3} \\ U_{\mu1} & U_{\mu2} & U_{\mu3} \\ U_{\tau1} & U_{\tau2} & U_{\tau3} \end{pmatrix} \begin{pmatrix} \nu_1 \\ \nu_2 \\ \nu_3 \end{pmatrix} \quad (2.6)$$

There are then six SM parameters that can be measured currently in neutrino oscillation experiments [14]. The two mass-related observables are  $\Delta m_{21}^2$ ,  $|\Delta m_{31}^2|$ , the three mixing angle observables are  $\theta_{12}$ ,  $\theta_{23}$ , and  $\theta_{13}$ , and the CP violating phase  $\delta_{CP}$ . The neutrino mass ordering is necessary to relate mixing elements to experimental observables and is given by  $m_2^2 > m_1^2$  and  $\Delta m_{21}^2 < |\Delta m_{31}^2|$ . For a normal mass hierarchy,  $\Delta m_{31}^2$  is positive and with  $m_3^2 > m_2^2$ , and for an inverted hierarchy  $\Delta m_{31}^2$  is negative with  $m_3^2 < m_1^2$  [15].

### 2.3.2 Muon Flavor Violating Processes

The discovery of neutrino oscillations establishes charged lepton flavor violation (CLFV) at some level, but CLFV has yet to be observed experimentally. There can be three possibilities for sources of lepton flavor violation,

- SM including massive neutrinos, where the only source of CLFV is from the operators responsible for neutrino masses.
- Neutrino masses via the seesaw mechanism, which introduce heavy, right-handed Majorana neutrinos at the GUT scale, with interactions violating total lepton number [16, 17].
- New physics models at the TeV scale, containing new sources of CLFV [17, 18]

The muon is considered one of the most sensitive probes for studying CLFV due to its copious production rate and relatively long lifetime, and the CLFV processes involving muons include [19, 20]

- $\mu^+ \rightarrow e^+\gamma$  the decay of a muon to a positron and photon.
- $\mu^+ \rightarrow e^+e^-e^+$  the decay of a muon to two positrons and an electron.
- $\mu^- + N \rightarrow e^- + N$  the conversion of a muon to an electron in the field of a nucleus.
- $\mu^- + (A, Z) \rightarrow e^+ + (A, Z - 2)$  the conversion of a muon to a positron, involving two nucleons.
- $\mu^+e^- \rightarrow \mu^-e^+$  muonium to anti-muonium conversion.
- $\mu^-e^- \rightarrow e^-e^-$  muonic atom conversion.

where the complementarity of these “golden” channels for muons can offer significant insight into the mechanisms for CLFV [21]. The Feynman diagrams for CLFV in the SM via neutrino mixing for  $\mu^+ \rightarrow e^+\gamma$  and  $\mu^+ \rightarrow e^+e^-e^+$  are shown in Figure 2.1.

The standard model branching ratio for  $\mu^+ \rightarrow e^+\gamma$ , assuming only massive neutrinos, is given by

$$BR(\mu^+ \rightarrow e^+\gamma) = \frac{3\alpha}{32\pi} \left| \sum_i U_{\mu i}^* U_{e i} \frac{m_{\nu_i}^2}{m_W^2} \right|^2 \sim 10^{-52} \quad (2.7)$$

where  $U_{li}$  are the leptonic mixing matrix elements. This is well below the sensitivity reach of any existing or foreseeable future experiment, and therefore any observed CLFV is a clear indication of New Physics [15, 19]. Examples of possible supersymmetric CLFV processes for  $\mu^+ \rightarrow e^+\gamma$  and  $\mu^+ \rightarrow e^+e^-e^+$  are shown in Figure 2.2.

Using the effective field theory approach, the SM can be considered an approximation to a complete theory, valid up to some yet unknown energy scale  $\Lambda$ . From the method of [22, 23], the Lagrangian therefore can be built from an expansion in  $1/\Lambda$  that includes all operators constructed from SM fields and is given by the following,

$$\mathcal{L} = \mathcal{L}_{\text{SM}} + \frac{1}{\Lambda} \sum_k C_k^{(5)} Q_k^{(5)} + \frac{1}{\Lambda^2} \sum_k C_k^{(6)} Q_k^{(6)} + \mathcal{O}\left(\frac{1}{\Lambda^3}\right). \quad (2.8)$$

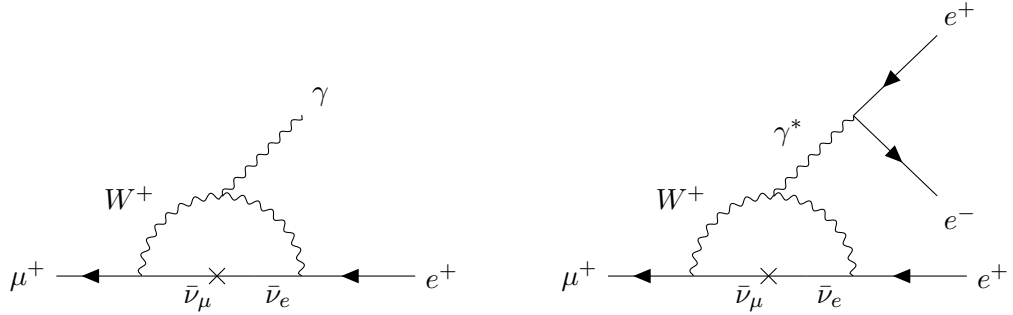
where the Wilson coefficients  $C_k^d$  are the couplings and  $Q_k^d$  the operators. The Dim-5 operator provides the neutrino mass term and flavor violation in the neutrino sector, but due to the constraints on the neutrino masses, has negligible contribution to charged lepton flavor violation. The Dim-6 operators are therefore of most interest when investigating charged lepton flavor violation. The branching ratio for the  $\mu^+ \rightarrow e^+ \gamma$  decay is given by

$$BR(\mu^+ \rightarrow e^+ \gamma) = \frac{48 \pi^2 (|C_{TL}|^2 + |C_{TR}|^2)}{G_F^2 m_\mu^2 \Lambda^4} \quad (2.9)$$

and the branching ratio for  $\mu^+ \rightarrow e^+ e^- e^+$

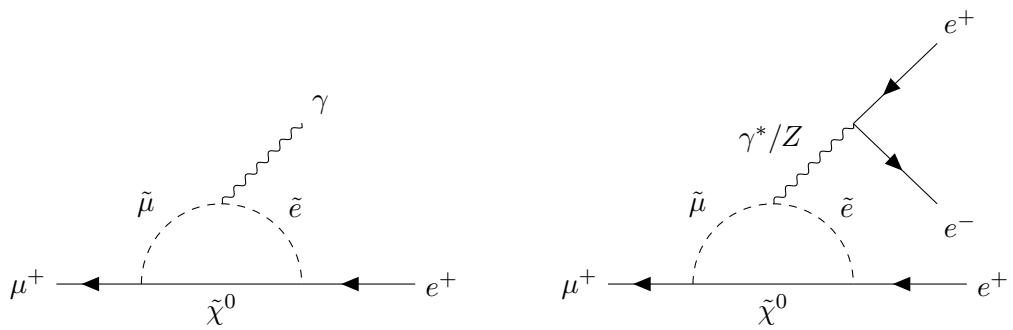
$$\begin{aligned} BR(\mu^+ \rightarrow e^+ e^- e^+) = & \left( 40e^2 v^2 (|C_{e\gamma}^{12}|^2 + |C_{e\gamma}^{21}|^2) \left( 8 \ln \left[ \frac{m_1}{m_2} \right] - 11 \right) \right. \\ & + \frac{2m_\mu^4}{m_Z^2} \left( (5 - 20s_W^2 + 36s_W^4) |C_{eZ}^{12}|^2 \right. \\ & \quad \left. + 4(1 - 4s_W^2 + 9s_W^4) |C_{eZ}^{21}|^2 \right) \\ & + \frac{15m_e^2 m_\mu^2 v^2 (|C_{e\varphi}^{12}|^2 + |C_{e\varphi}^{21}|^2)}{8m_H^4} \\ & + 10m_\mu^2 (1 - 4s_W^2 + 12s_W^4) |C_{\varphi e}^{12}|^2 \\ & + 20m_\mu^2 (1 - 4s_W^2 + 6s_W^4) \left( |C_{\varphi l(1)}^{12}|^2 + |C_{\varphi l(3)}^{12}|^2 \right) + \\ & + 10m_\mu^2 (|C_{le}^{1112}|^2 + |C_{le}^{1211}|^2) \\ & \left. + 80m_\mu^2 (|C_{ee}^{1112}|^2 + |C_{ll}^{1112}|^2) \right) \frac{1}{80 G_F^2 m_\mu^2 \Lambda^4} \quad (2.10) \end{aligned}$$

The limits on two of the Wilson coefficients resulting from the branching ratio limits set by previous experiments and the expected limits based on the sensitivity of upcoming experiments are shown in Figure 2.3.



(a) The Standard Model process for  $\mu^+ \rightarrow e^+ \gamma$ , via neutrino mixing. (b) The Standard Model process for  $\mu^+ \rightarrow e^+ e^- e^+$ , via neutrino mixing.

Figure 2.1: Standard Model processes for charged lepton flavor violation.



(a) The beyond Standard Model process for  $\mu^+ \rightarrow e^+ \gamma$ , via a neutralino ( $\tilde{\chi}^0$ ) and slepton mixing ( $\tilde{e}$  and  $\tilde{\mu}$ ) (b) The beyond Standard Model process for  $\mu^+ \rightarrow e^+ e^- e^+$ , via a neutralino ( $\tilde{\chi}^0$ ) and slepton mixing ( $\tilde{e}$  and  $\tilde{\mu}$ )

Figure 2.2: Beyond Standard Model processes for charged lepton flavor violation.

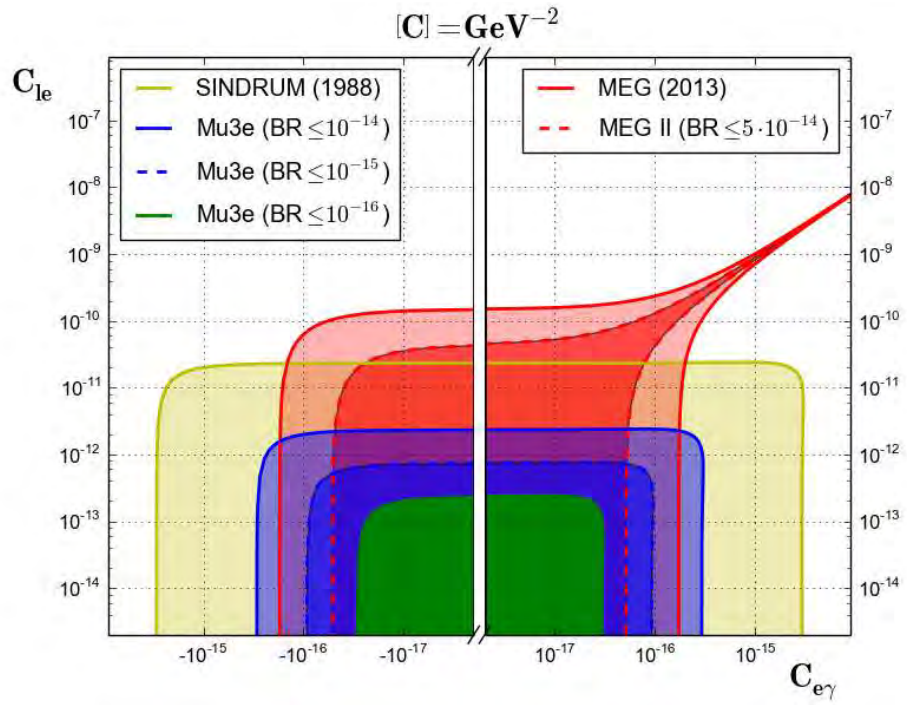


Figure 2.3: Limits on the Wilson coefficients contributing to muon lepton flavor violation from current and future experiments [24].

## 2.4 Current Status of CLFV Worldwide

The MEG experiment at PSI set the most recent limit in 2016 on the  $\mu^+ \rightarrow e^+\gamma$  decay, with  $BR(\mu^+ \rightarrow e^+\gamma) < 4.2 \cdot 10^{-13}$  @ 90% CL [25]. This establishes the most stringent limit on any charged lepton flavor violating decay. The current limits on the golden muon CLFV channels are listed in Table 2.2 and the progression of several muon CLFV limits over time is shown in Figure 2.4. The MEG collaboration plans an upgraded experiment, MEG II, improving the sensitivity by an order of magnitude to  $6 \cdot 10^{-14}$  [26]. Within the next few years several more experiments will come online searching additional channels for CLFV. The Mu3e experiment at PSI will search for  $\mu^+ \rightarrow e^+e^-e^+$  with sensitivity  $\mathcal{O}(10^{-15})$  [27]. Mu2e at Fermilab and COMET at J-PARC will search for  $\mu^- + N \rightarrow e^- + N$  with single-event sensitivities of  $\mathcal{O}(10^{-17})$  [28, 29]. Many beyond the SM (BSM) theoretical models predict rates for muon lepton flavor violating processes within reach of the proposed experiments [17, 19].

Process	Current Limit @ 90% CL	Experiment	Year	Reference
$\mu^+ \rightarrow e^+\gamma$	$<4.2 \cdot 10^{-13}$	MEG	2016	[25]
$\mu^+ \rightarrow e^+e^-e^+$	$<1.0 \cdot 10^{-12}$	SINDRUM	1988	[30]
$\mu^- + Ti \rightarrow e^- + Ti$	$<4.3 \cdot 10^{-12}$	SINDRUM II	1993	[31]
$\mu^- + Pb \rightarrow e^- + Pb$	$<4.6 \cdot 10^{-11}$	SINDRUM II	1996	[32]
$\mu^- + Au \rightarrow e^- + Au$	$<7.0 \cdot 10^{-13}$	SINDRUM II	2006	[33]
$\mu^+e^- \rightarrow \mu^-e^+$	$<8.3 \cdot 10^{-11}$	Willmann <i>et al.</i>	1999	[34]

Table 2.2: The lower limits on the branching ratios of muon charged lepton flavor violating processes.

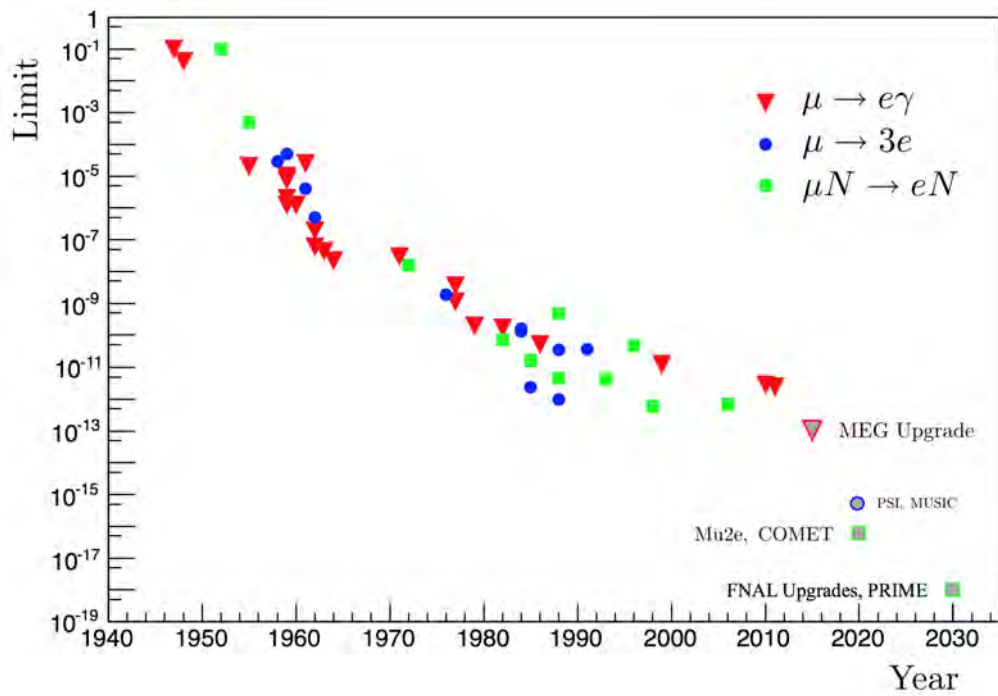


Figure 2.4: Limits on muon CLFV processes over time [35].

---

## PSI and the MEG II and Mu3e Experiments

---

The Paul Scherrer Institut in Switzerland will host two next-generation charged lepton flavor violation experiments, MEG II and Mu3e. Due to the nature of these extremely rare decays, both experiments come with the requirement of the highest achievable muon beam rates at  $\mathcal{O}(10^8) \mu^+/s$ , only available at PSI.

### 3.1 The PSI High Intensity Proton Accelerator

The PSI High Intensity Proton Accelerator (HIPA) chain consists of a Cockcroft-Walton pre-accelerator, delivering 870 keV protons to a set of two in-house designed, isochronous cyclotrons which further accelerate to the maximum 590 MeV [36]. The Injector II cyclotron accelerates the protons to 72 MeV, thereafter the protons are transferred to the Ring cyclotron where they are accelerated, in four copper resonator cavities operated in continuous wave (CW) mode at a frequency of 50.6 MHz, giving the known periodic 19.75 ns beam microstructure and their final energy of 590 MeV. An image of the Ring Cyclotron is shown in Figure 3.1. The proton beam with maximum 2.4 mA current and 1.4 MW beam power, is directed through two rotating graphite target stations to produce pions and muons by nuclear interactions with carbon [37]. After the two graphite targets, the remaining beam, with 1 MW, is then used to produce neutrons in a spallation target (SINQ) consisting of lead filled Zircaloy tubes surrounded by a heavy water (D<sub>2</sub>O) moderator tank. The layout of the PSI accelerator complex is shown in Figure 3.2. A schematic view of the proton beam channel with the two pion and muon production target stations and surrounding secondary beamlines is shown in Figure 3.3a, and a close-in schematic view of the Target E station with the secondary beamlines extraction directions is shown in Figure 3.3b. As the muon yield versus extraction channel orientation is studied later, in the context of optimizing a muon production target in comparison to Target E, the three extraction channels  $\pi E1$ ,  $\mu E4$ , and  $\pi E5$  corresponding to forwards ( $8^\circ$ ), sideways ( $90^\circ$ ) and backwards ( $165^\circ$ ) extraction are explicitly presented.

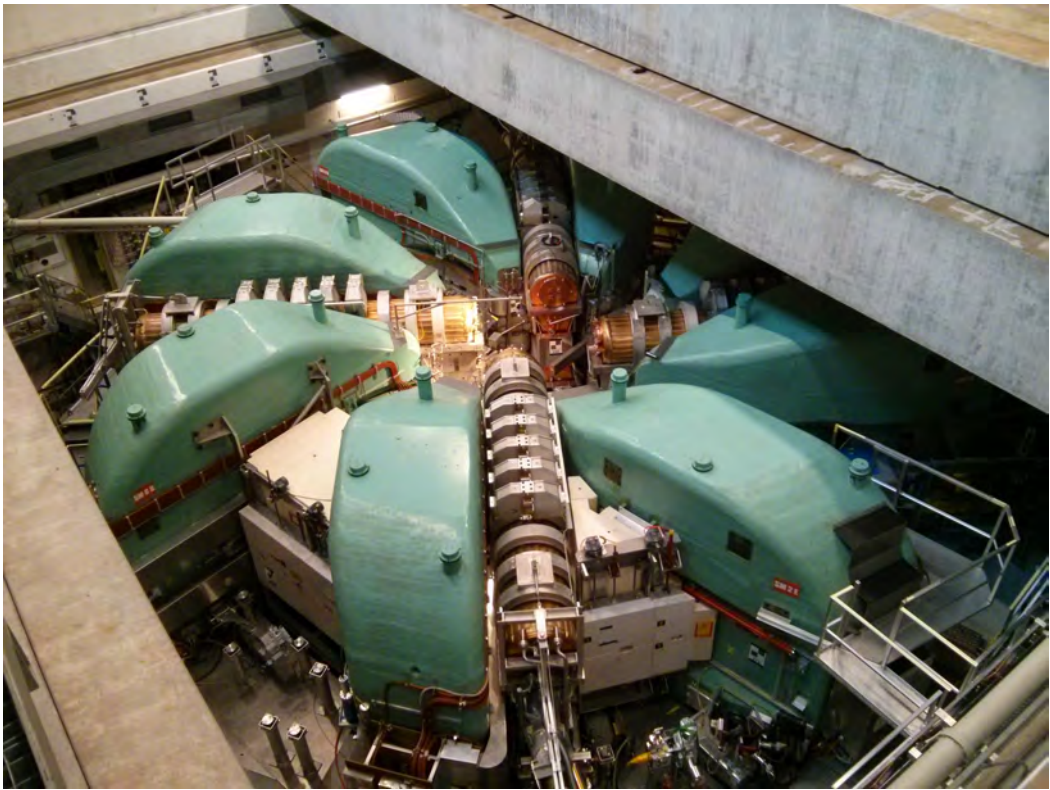


Figure 3.1: The 590 MeV Ring Cyclotron.

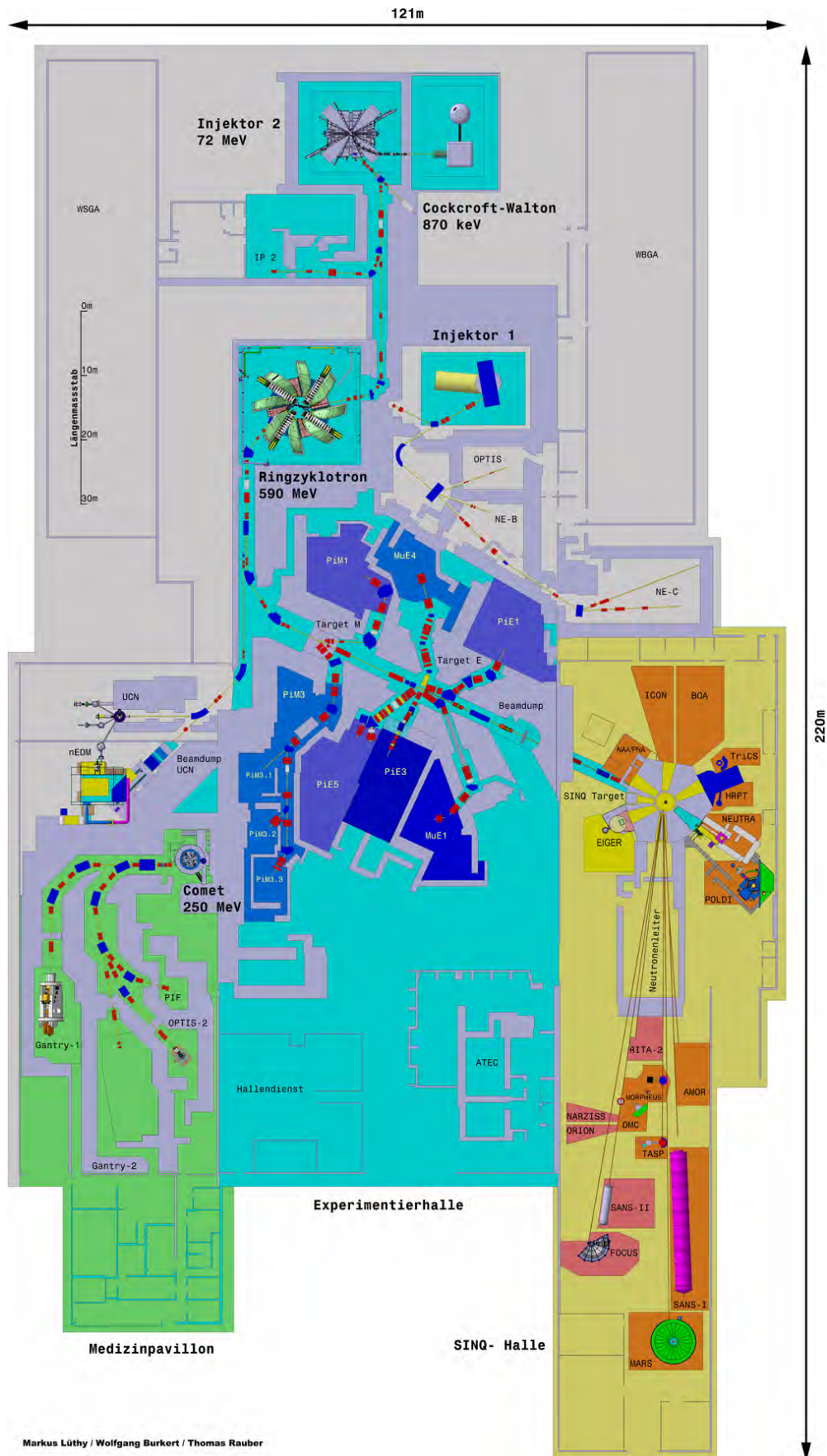
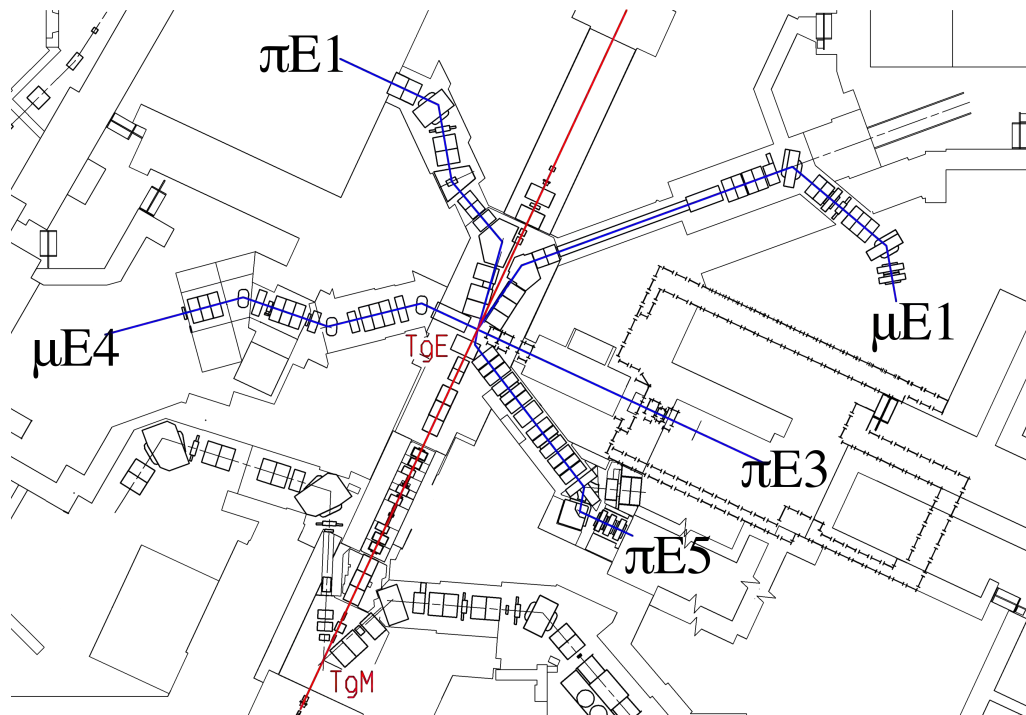
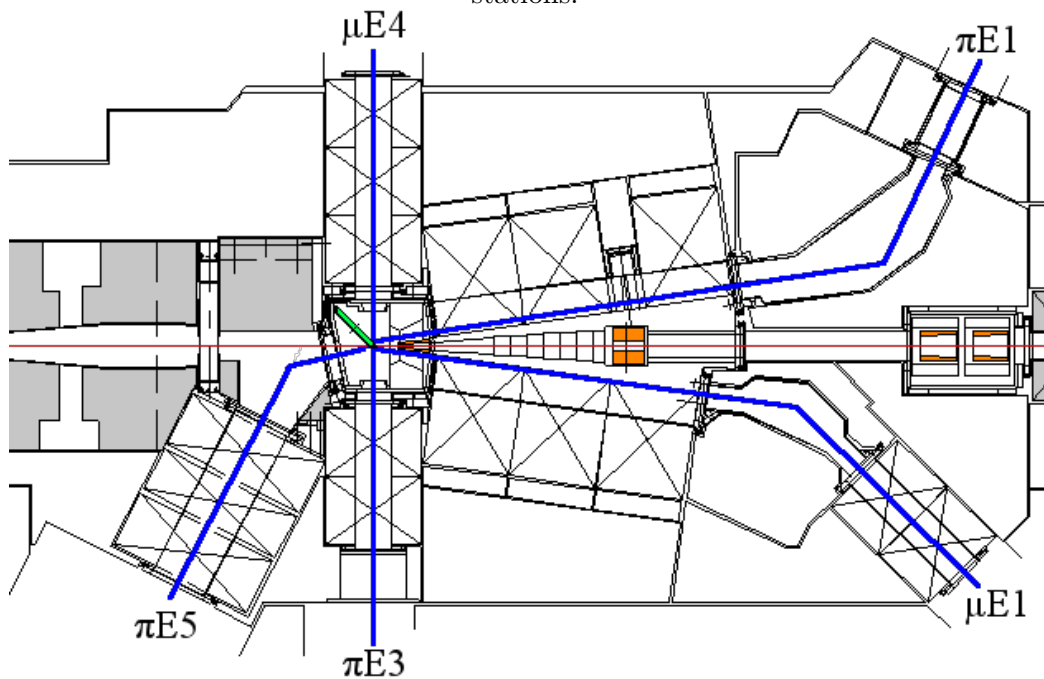


Figure 3.2: The layout of the PSI accelerator complex [38]



(a) .

A schematic view of the proton beam channel with the two graphite target stations.



(b) A close-in schematic view of the Target E station with the secondary beamlines extraction directions. Target E is shown in green at the center.

Figure 3.3: A schematic view of the proton beam channel, Target E station, and secondary beamlines. The proton beam is shown in red and the secondary muon and pion beamlines are shown in blue.

### 3.2 The $\pi$ E5 Beamline

The  $\pi$ E5 channel is a high-intensity low-energy muon and pion beamline, with a maximum momentum of 120 MeV/c, that views the second graphite target (Target E) at  $165^\circ$  with respect to the proton beam axis. A figure of the  $\pi$ E5 beamline relative to Target E is shown in Figure 3.4. The  $\pi$ E5 channel is used exclusively for particle physics experiments, and has been the home to previous CLFV searches such as SINDRUM II and the original MEG experiment. Upgrades to the proton accelerators and intense optimizations of the beamline elements have resulted in a maximum muon beam rate at the end of the beamline exceeding  $10^8 \mu^+/s$ , and is therefore the only viable possibility for the next-generation CLFV experiments such as MEG II and Mu3e.

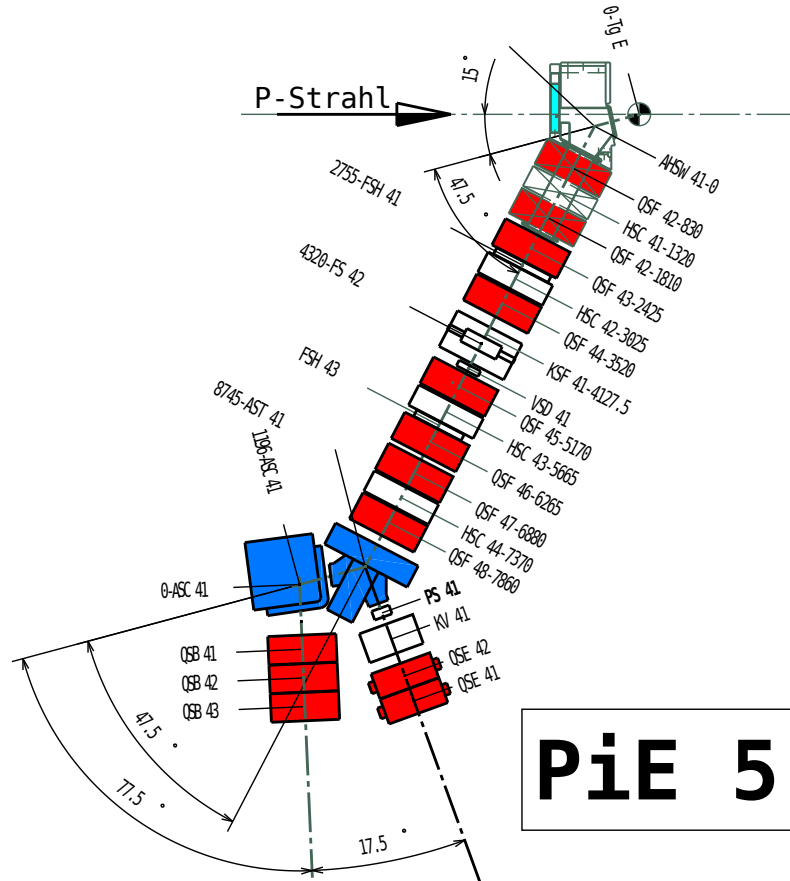


Figure 3.4: The layout of the  $\pi$ E5 channel relative to Target E.  $\pi$ E5 extracts from Target E in the backward direction,  $165^\circ$  with respect to the proton beam axis.

### 3.3 The $\mu$ E4 Beamline

The  $\mu$ E4 channel is a low energy muon beamline that views Target E at  $90^\circ$  with respect to the proton beam axis. The  $\mu$ E4 beamline is used exclusively for materials science and muon spin rotation spectroscopy ( $\mu$ SR) for condensed-matter studies [39]. The beamline was constructed using two sequential 500 mm large aperture solenoids (WSX61,WSX62) that extracts surface muons from the side face of Target E. The muons are then transported through a conventional dipole and quadrupole channel to a moderation volume, where the surface-muon beam is slowed down to energies on the order of 20 eV. This extreme moderation has efficiencies between  $10^{-5}$ - $10^{-4}$ , and therefore requires a very high initial muon intensity. Due to this large solid angle acceptance the  $\mu$ E4 beamline has a maximum muon rate of  $4.2 \cdot 10^8 \mu^+ / s$  [40]. A figure of the  $\mu$ E4 beamline relative to Target E is shown in Figure 3.5.

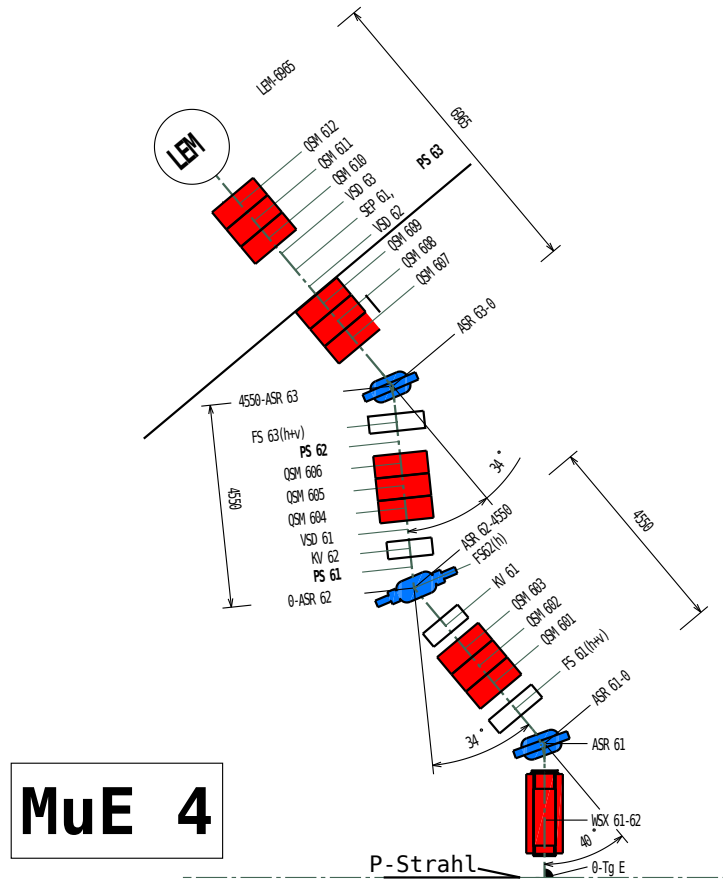


Figure 3.5: The layout of the  $\mu$ E4 channel relative to Target E.  $\mu$ E4 extracts from Target E in the sideways direction,  $90^\circ$  with respect to the proton beam axis.



### 3.5 The MEG II Experiment

The MEG II experiment is an upgrade of the original MEG experiment that ran from 2009-2013, and will continue the search for the  $\mu^+ \rightarrow e^+\gamma$  decay with an order of magnitude improved sensitivity [41]. The current best limit on this decay was set by the MEG experiment in 2016 at  $4.2 \cdot 10^{-13}$  @ 90% CL [25]. Each detector system has undergone an extensive upgrade to improve resolutions and efficiencies by approximately a factor two to meet the needs of the factor two increase in the beam stopping intensity, leading to an expected branching ratio sensitivity of  $6 \cdot 10^{-14}$  within three years of running. The sensitivity over the expected running time for the MEG II experiment is shown in Figure 3.8. MEG II will run at the same  $\pi E5$  beamline, and is currently in the engineering run phase with expected performance data-taking to begin in late 2018.

#### 3.5.1 Signal and Background for $\mu \rightarrow e\gamma$

The signal event kinematics of the  $\mu^+ \rightarrow e^+\gamma$  decay at rest is a positron and a photon in back-to-back coincidence, with both energies equal to half the muon mass ( $m_\mu/2 = 52.83 \text{ MeV}/c^2$ ). There are two categories of backgrounds, irreducible and accidental. The irreducible background comes from radiative muon decay (RMD)  $\mu^+ \rightarrow e^+\nu_e\bar{\nu}_\mu\gamma$  where the  $e^+$  and  $\gamma$  are emitted back-to-back and the neutrinos carry away only a small amount of energy, mimicking a signal event. The accidental backgrounds come from combinations with other physics processes that can mimic the signal event structure, such as the coincidence of an  $e^+$  from normal muon Michel decay, accompanied by a high energy photon originating from RMD, bremsstrahlung, or positron annihilation-in-flight (AIF). Schematic diagrams for the signal and background processes in the MEG II experiment are shown in Figure 3.7.

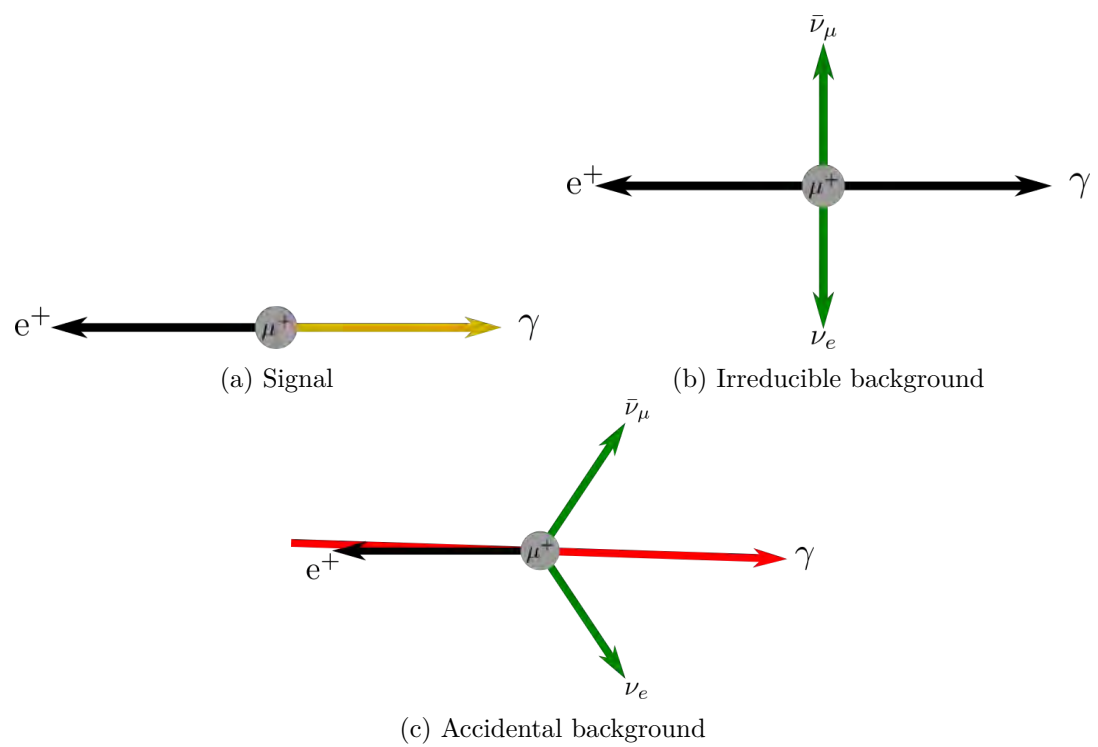


Figure 3.7: Schematics of the signal and background processes in the MEG II experiment.

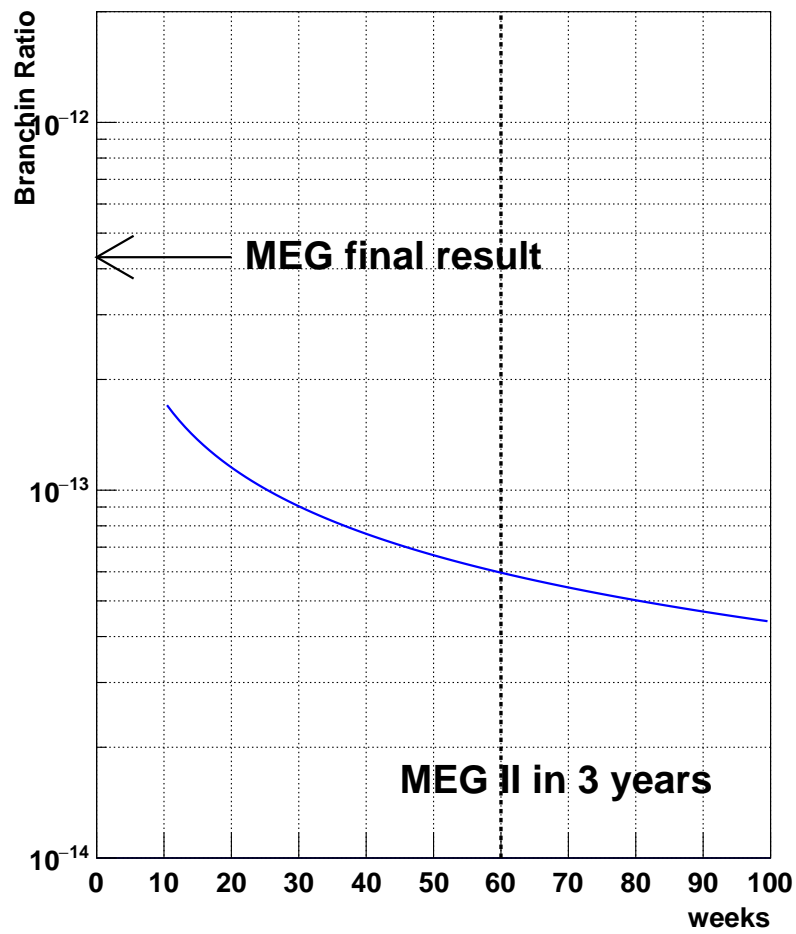


Figure 3.8: The sensitivity of the MEG II experiment to the  $\mu \rightarrow e\gamma$  decay over the expected running time.

### 3.5.2 The MEG II Detector

The MEG II detector consists of three primary detection systems (measuring the positron energy and timing and the photon energy) and one auxiliary detector (dedicated to observing RMD) and is described in detail in [26]. A schematic drawing of the MEG II experiment including each detector system is shown in Figure 3.9. The muon beam with a stopping rate of  $7 \cdot 10^7 \mu^+/s$  is brought to rest on a planar 150  $\mu\text{m}$  thick plastic scintillation target oriented at  $15^\circ$  relative to the muon beam axis, where the muon then decays.

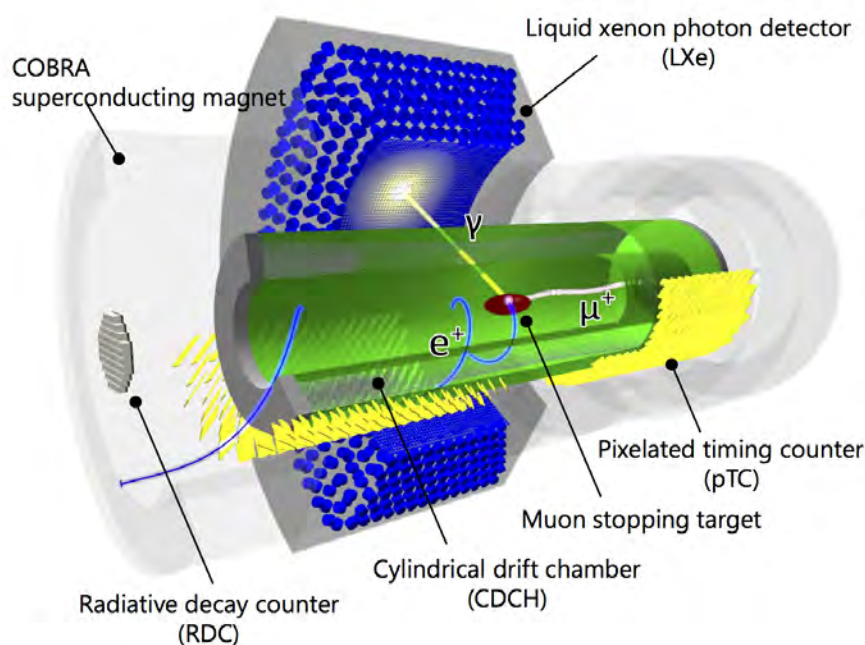


Figure 3.9: A schematic drawing of the MEG II detector.

#### 3.5.2.1 COBRA Superconducting Solenoid

The COBRA superconducting symmetric-gradient solenoidal magnet generates a gradient magnetic field in both positive and negative directions along the beam axis, centered on the stopping target, with a maximum magnetic field of 1.27 T at the center and falling-off to 0.47 T at the edges, such that the bending radius of a 53 MeV positron is roughly independent of the emission angle, as well as sweeping away so-called “re-curlers” (positrons emitted close to  $90^\circ$  with respect to the target) more efficiently than in a constant solenoidal field, so reducing the occupancy in the tracking volume.

Two large diameter, normal conducting compensation coils ensure the magnetic field at the calorimeter photomultiplier location does not influence their performance.

### **3.5.2.2 Cylindrical Drift Chamber**

A cylindrical drift chamber (CDCH) has been designed and optimized for measuring the momentum of 53 MeV positrons originating from the central target region, covering the full  $2\pi$  in  $\phi$  and 1.9 m in length. The CDCH is composed of 10 concentric layers where each layer contains two layers of criss-crossing cathode wires surrounding a central anode wire with read-out on both ends, and filled with a 90% helium 10% isobutane ( $C_4H_{10}$ ) gas mixture, giving a per track-turn thickness in radiation lengths of  $1.58 \cdot 10^{-3} X_0$ . An image of the CDCH with all layers mounted is shown in Figure 3.10a.

### **3.5.2.3 Pixelated Timing Counter**

The pixelated timing counter (pTC) has been designed to measure the positron timing with a resolution of 30 ps through the use of 512 scintillation tiles (split into 256 upstream and 256 downstream) read-out by SiPMs on two sides. The pTC is situated in the lower volume between the CDCH and COBRA covering the full angular acceptance of the positrons originating from  $\mu^+ \rightarrow e^+\gamma$  decay where the photon enters the calorimeter. A schematic drawing of the upstream portion of the pTC is shown in Figure 3.10b.

### **3.5.2.4 Liquid Xenon Calorimeter**

A 900 L C-shaped liquid xenon calorimeter (LXe) dedicated to detecting the high energy  $\gamma$  is situated outside the COBRA magnet and defines the 10% solid angle acceptance. The LXe has been upgraded from the original MEG design to improve the photon position and energy resolutions by replacing the inner face UV-sensitive PMTs with high granularity SiPMs, giving a more uniform coverage and enabling pile-up suppression of background events. An image of the inner face with SiPMs and side wall with PMTs inside the LXe calorimeter is shown in Figure 3.10c.

### **3.5.2.5 Radiative Decay Counter**

An auxiliary detector dedicated to monitoring the RMD process called the Radiative Decay Counter (RDC) has been developed and installed on the downstream

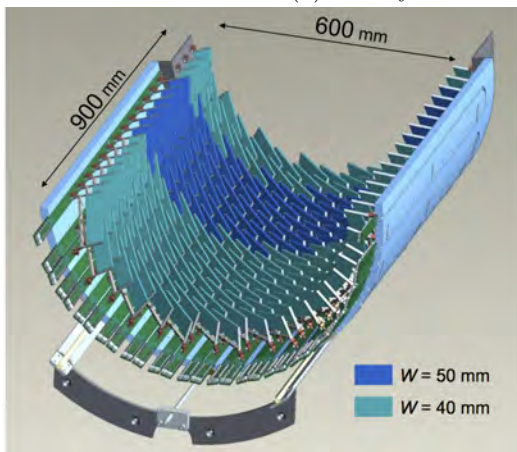
end of the MEG apparatus. The RDC is a two component detector consisting of 76 LYSO crystals each read-out by a single SiPM to measure in coincidence the energy of a low-energy positron associated with a high-energy RMD photon in the calorimeter, and covered on the upstream face by 12 plastic scintillator bars read-out by SiPMs to detect the timing of the incoming positron. A schematic drawing of the RDC is shown in Figure 3.10d.

### **3.5.2.6 Trigger and Data Acquisition System**

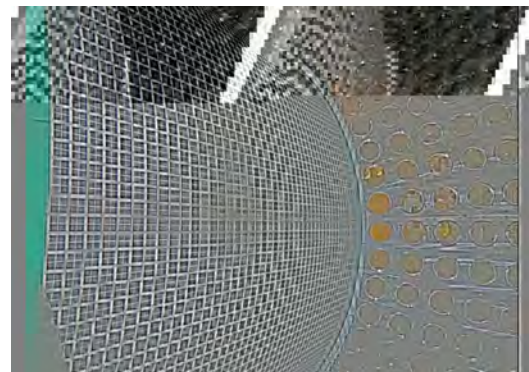
Additionally, the entire detector trigger and data acquisition system (TDAQ) has been significantly improved, through the use of the newly developed WaveDream waveform digitizer board, to handle the factor two increase in muon stopping rate and factor three increase in read-out channels.



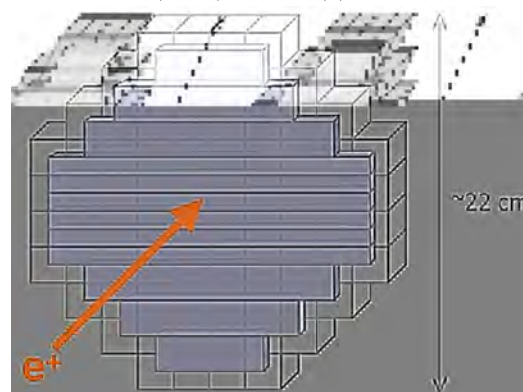
(a) The cylindrical drift chamber (CDCH).



(b) The pixelated timing counter (pTC).



(c) The liquid xenon calorimeter (LXe).



(d) The radiative decay counter (RDC).

Figure 3.10: The sub-detectors of the MEG II experiment.

### 3.6 The Mu3e Experiment

The Mu3e Phase I experiment will search for the decay  $\mu^+ \rightarrow e^+e^-e^+$  at a sensitivity level  $\mathcal{O}(10^{-15})$  [42]. The current best limit on this decay was set by the SINDRUM experiment in 1988 at  $\text{BR}(\mu^+ \rightarrow e^+e^-e^+) < 1.0 \cdot 10^{-12}$  @ 90% CL [30]. The Mu3e experiment will be constructed in two phases, the first with an improvement on the sensitivity over the previous experiment by three orders of magnitude, and the second improving by another factor 10. The experiment will run in the front section of the  $\pi\text{E5}$  area, using a novel Compact Muon Beam Line (CMBL) to accommodate near simultaneous existence of MEG II and Mu3e [43]. The Phase-II experiment will require a further order of magnitude increase in muon beam rate, which is currently not available anywhere worldwide. Therefore, the HiMB project has been undertaken to develop a new muon production target station at PSI capable of delivering the muon rate necessary for Mu3e Phase-II [44]. The Mu3e experiment is currently in the final stages of R&D and will begin data-taking in the coming years. The sensitivity over time for the expected running period for Mu3e Phase-I experiment is shown in Figure 3.11.

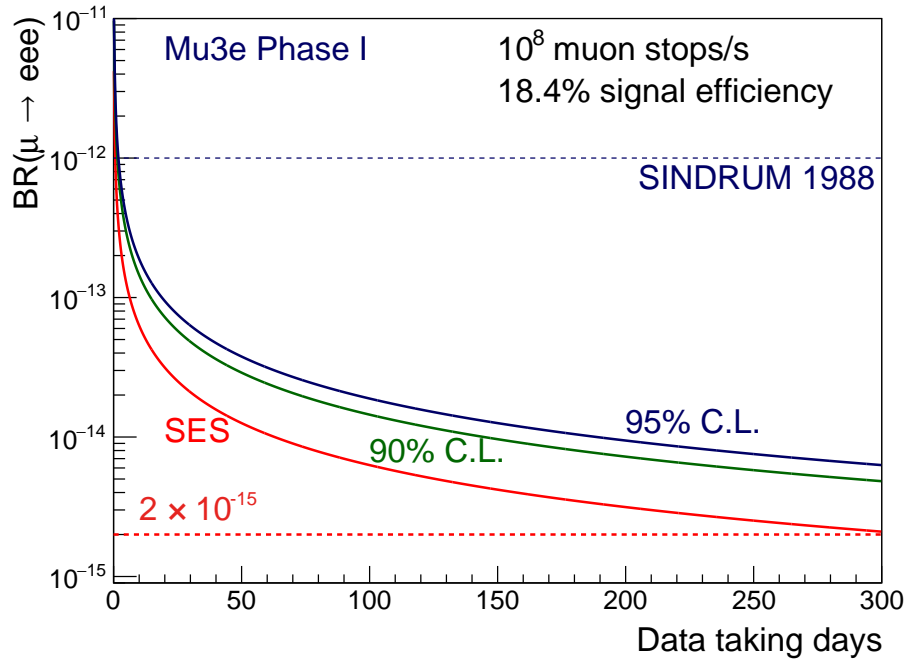


Figure 3.11: The single event sensitivity (SES) and corresponding 90% and 95% confidence level (CL) upper limits on the branching ratio versus time for the Mu3e Phase-I experiment.

### 3.6.1 Signal and Background for $\mu \rightarrow eee$

The signal event kinematics of the decay  $\mu^+ \rightarrow e^+e^-e^+$  is two positrons and an electron in time coincidence, sharing a common vertex and by momentum conservation the sum of all momenta should equal zero, also implying co-planarity, while by energy conservation their energies should sum to the muon mass ( $m_\mu = 105.658 \text{ MeV}/c^2$ ) [45]. Again, there are two categories of backgrounds, irreducible and accidental. The irreducible background comes from the radiative decay with internal conversion  $\mu^+ \rightarrow e^+\bar{\nu}_\mu\nu_e e^+e^-$  which becomes a serious background when the neutrinos carry away only a small amount of energy. The branching ratio as a function of the missing energy carried away by the neutrinos is shown in Figure 3.13, where this process combined with the momentum resolution on the  $e^+e^-e^+$  effectively sets the sensitivity of the experiment [46]. The accidental backgrounds come from the coincidence of an  $e^+$  from normal muon Michel decay with an uncorrelated  $e^+e^-$  pair. These uncorrelated  $e^+e^-$  with a common vertex can originate from Michel positrons or beam positrons that undergo Bhabha scattering with electrons in the target material. Additionally,  $e^+e^-$  pairs can originate from external conversion of the photon from normal radiative muon decay. Schematic diagrams for the signal and background processes in the Mu3e experiment are shown in Figure 3.12. Significant attention has been given to minimizing the total material budget to reduce  $e^+e^-$  production and multiple scattering and energy loss that would distort the reconstructed momentum.

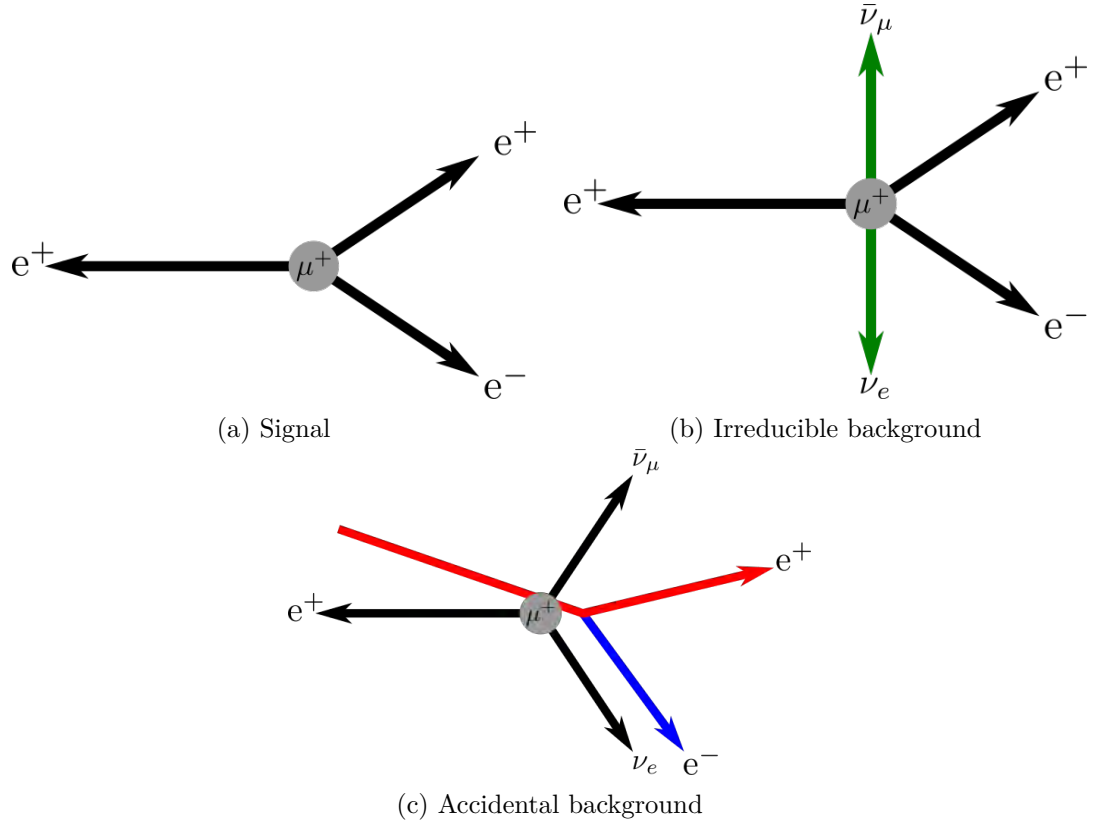


Figure 3.12: Schematics of the signal and background processes in the Mu3e experiment.

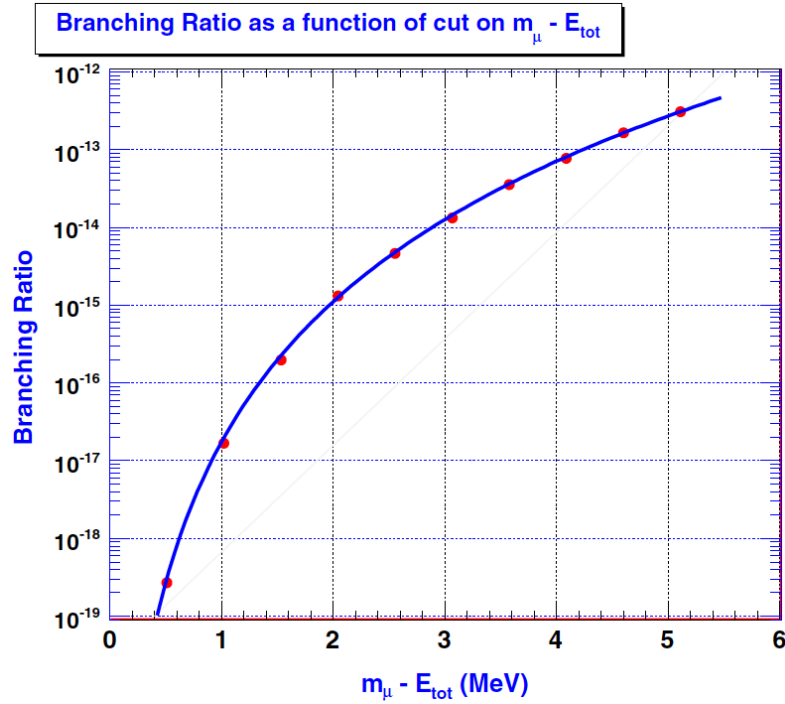


Figure 3.13: The branching ratio of  $\mu^+ \rightarrow e^+ \bar{\nu}_\mu \nu_e e^+ e^-$  as a function of the missing energy carried away by the neutrinos [46].

### 3.6.2 The Mu3e Detector

The Mu3e detector apparatus consists of three complimentary detector systems measuring the positron and electron energies and their associated timing and is described in detail in [27]. A schematic drawing of the Mu3e experiment including each detector system is shown in Figure 3.14.

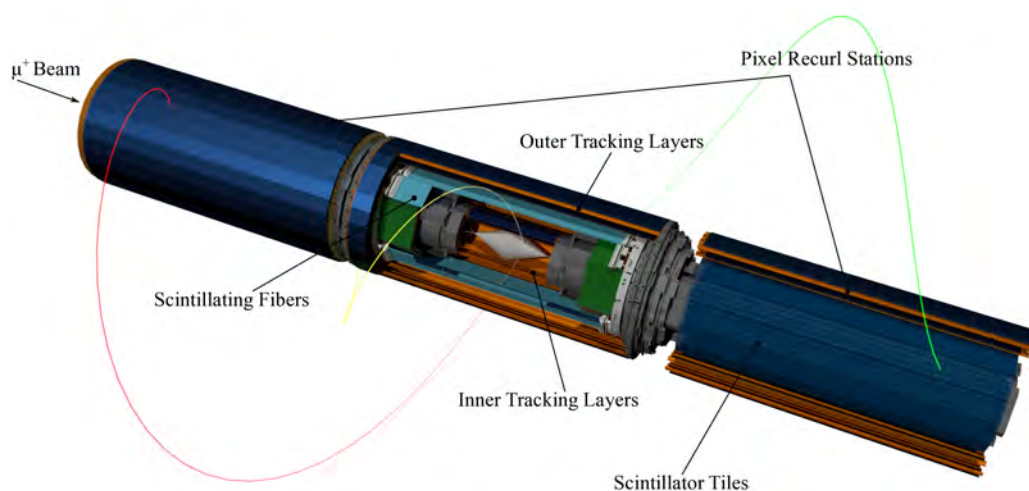


Figure 3.14: A rendering of the Mu3e detector.

#### 3.6.2.1 Magnet and Stopping Target

All detector components have a cylindrical symmetry and are contained within the central bore of the 1 T homogeneous-field solenoidal magnet. The muon beam rate of  $\mathcal{O}(10^8) \mu^+/s$  is stopped in a, thin double hollow cone stopping target of 19 mm radius, located at the center of the magnet. The target material is MYLAR, and the upstream portion of the stopping target is  $75 \mu\text{m}$  thick, whereas the downstream portion is  $85 \mu\text{m}$  thick, such that the muon stopping distribution is approximately centered on the target with the decay vertices spread-out as much as possible to reduce pileup and to allow an even occupancy in the inner tracking layers. An image of the Mu3e stopping target with a 1 CHF coin is shown in Figure 3.15a.

### **3.6.2.2 Silicon Vertex Tracker**

Immediately surrounding the target are two silicon vertex tracking layers based on High Voltage Monolithic Active Pixel Sensors (HV-MAPS) thinned to  $50\ \mu\text{m}$  with  $80\times 80\ \mu\text{m}$  pixel size. The vertex tracker samples each track as it leaves the target region, providing the information necessary for precise vertex reconstruction at the target. Two outer tracking layers are placed just outside the scintillating fiber ribbon layer. An additional two tracking stations, known as “recurl” stations, extend in the up- and downstream direction at the same radius as the outer tracking layer, and provide additional precise momentum measurements for recurling tracks. A rendering of the inner and outer tracking layers, and recurl stations are shown in Figure 3.15b.

### **3.6.2.3 Scintillating Fiber Timing Tracker**

A timing detector based on three to four layers of  $250\ \mu\text{m}^2$  scintillating fibers providing timing information for positrons and electrons leaving the target region placed at a 6 cm radius surrounding the inner tracking layer. The plastic fibers are read-out on each end using SiPM arrays, and provide a timing resolution on the order of a few hundred ps. A rendering of half the scintillating fiber timing tracker ribbons is shown in Figure 3.15c.

### **3.6.2.4 Scintillating Tile Timing Counter**

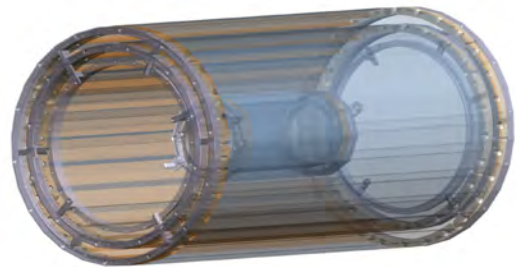
At the up- and downstream recurl stations and within the radius of the tracking double-layers is the second timing detector which is comprised of arrays of  $6.5\times 6.0\times 5\ \text{mm}^3$  plastic scintillator tiles. Each tile in the array is read-out with directly attached SiPMs and provides a timing resolution better than 100 ps. The two complementary timing detector systems (fibers and tiles) provide combinatorial background suppression by efficiently identifying coincident positron/electron tracks. A rendering of a single scintillating tile timing counter module is shown in Figure 3.15d.

### **3.6.2.5 Data Acquisition and Online Reconstruction**

The Mu3e experiment is run in a triggerless mode, with 50 ns frames of all tracks in the detector, therefore track reconstruction must be done online to effectively reduce data rates. This is accomplished using massively parallel track reconstruction in a GPU based filter farm.



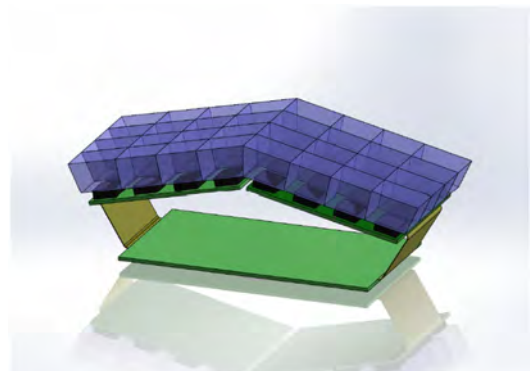
(a) The double hollow-cone stopping target.



(b) The inner and outer silicon vertex tracking layers.



(c) The scintillating fiber ribbons of the timing tracker.



(d) A scintillating tile timing counter module.

Figure 3.15: The target and sub-detectors of the Mu3e experiment.

---

## Characterization and Optimization of Surface Muon Production

---

The Mu3e Phase II experiment aims for a sensitivity level  $\mathcal{O}(10^{-16})$  on the decay  $\mu^+ \rightarrow e^+e^-e^+$  and will require a muon beam rate greater than  $\mathcal{O}(10^9)$   $\mu^+/s$  [42]. This rate is not currently available at PSI nor at any other muon facility worldwide, implying that a new target and beamline installation is necessary. The High Intensity Muon Beam project (HiMB) currently underway at PSI aims to deliver muon rates at  $\mathcal{O}(10^{10})$   $\mu^+/s$  through the design of a new target station and beam transport system [44]. The HiMB project began with the idea of developing a new beamline utilizing the SINCQ spallation neutron source as a muon production target. Due to space constraints from the moderator tank of SINCQ reducing the muon acceptance, the HiMB project shifted to the development of a new target station replacing Target M in the PSI proton beamline together with two solenoidal transport channels delivering muons for both particle physics and materials science.

The characterization of the current Target E began as a means of validating a new simulation toolset G4BEAMLIN [47] primarily for the development of HiMB. Understanding the current production target and the corresponding muon rates is critical to the design of an upgraded or new production target. Therefore, a complete simulation of the muon production chain is required, beginning with protons on target, pion production inside the target volume, and subsequently muon production from pion decay. The simulation study undertaken also provided a muon rate estimation from Target E to act as a normalization to the expected increased secondary beam rates from the HiMB facility.

### 4.1 Pion Production in the Target

The 590 MeV proton beam delivered by the ring cyclotron is, after having passed through the thin target station M, directed on to the thick Target E to produce pions through one of several nucleon-nucleon interaction in the target material. Protons impinging on the target with energies above 290 MeV can produce Delta baryons, with a mass of 1232 MeV/c<sup>2</sup> and decay width of 117 MeV/c<sup>2</sup> and four charge states

$(\Delta^0, \Delta^+, \Delta^-, \Delta^{++})$ , which then quickly decay via the strong interaction to nucleons and pions.

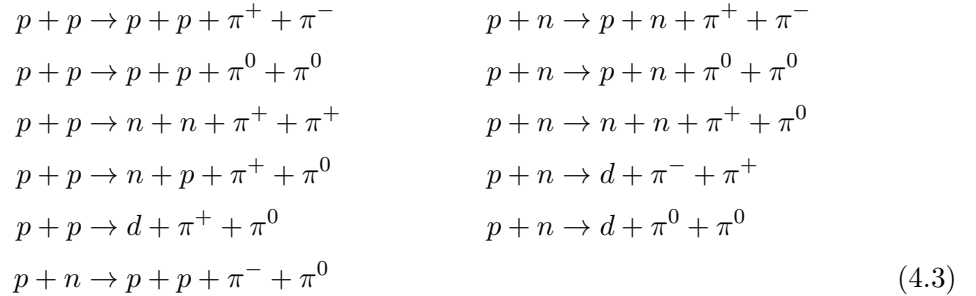
Below the threshold of 600 MeV, single pion production via Delta baryon decay can occur through the following channels to produce positive pions:



and for negative and neutral pions the following channels are available:



Beyond a proton energy of 600 MeV the creation of pairs of pions becomes possible via the following channels:



The charged pions subsequently decay to muons and neutrinos either after stopping inside the target or in-flight either in the region surrounding the target or after being captured by a secondary beamline. These pions and muons are extracted through various secondary beamlines and used in fundamental physics and materials science applications.

#### 4.1.1 Parameterized Pion Production Cross Sections

The first dedicated meson production facilities designed and constructed in the 1970s such as SIN (now PSI), LAMPF, and TRIUMF, collected extensive data on pion production cross sections at proton energies of 585 MeV and 730 MeV [48, 49, 50, 51, 52]. Critical to the understanding and characterization of surface muon production are those measurements at low pion energies.

Simulation frameworks such as GEANT4 [53] utilize hadronic physics models that are capable of modeling the pion production reactions given in Equations (4.1) to (4.3). However, several models perform rather poorly and even models that perform well at a certain pion energy, scattering angle and target material perform poorly in other circumstances when compared to the data available. Figure 4.1 shows a comparison of data with the results of a GEANT4 simulation with various hadronic models. The two models BERT (the default GEANT4 hadronic model) and INCLXX differ greatly to one another and to the data by almost a factor 10.

It is clear that in order to accurately simulate pion production as a first step in understanding surface muon production, a more reliable model is required. For this reason a new parameterized cross section for pion production was developed based on the methods of [54] and [55] using the data available from PSI and LBNL to build a parameterized model which is valid for all proton energies, production angles, and target materials [56]. Using low and high energy contributions, the combined parameterized differential cross section with a smooth transition at 40 MeV is given by

$$\begin{aligned} \frac{d^2\sigma}{d\Omega dT_{\pi^+}}(T_{\pi^+}, \theta) &= (1 - f_t) f_s \frac{d^2\sigma_{\text{LE}}}{d\Omega dT_{\pi^+}}(T_{\pi^+} - T_{\pi^+}^0, \theta) \\ &+ f_t \frac{d^2\sigma_{\text{HE}}}{d\Omega dT_{\pi^+}}(T_{\pi^+}, \theta). \end{aligned} \quad (4.4)$$

where  $T_{\pi^+}$  is the pion kinetic energy,  $T_{\pi^+}^0$  is the shift in kinetic energy due to Coulomb repulsion by the nucleus,  $f_t$  is the transition function, and  $f_s$  is a scale factor. The full parameterization procedure is described in detail in Appendix A. This model (called simply the HiMB model) was integrated into GEANT4 as an extension to the existing physics models. Two examples are shown in Figure 4.2a and Figure 4.2b for a graphite target, demonstrating the robustness of the HiMB model relative to the currently available production models in GEANT4 as this is a parameterized model driven by data. The cross section's model has an accuracy on the order of 10% which is dominated by the uncertainty on the available cross section measurements.

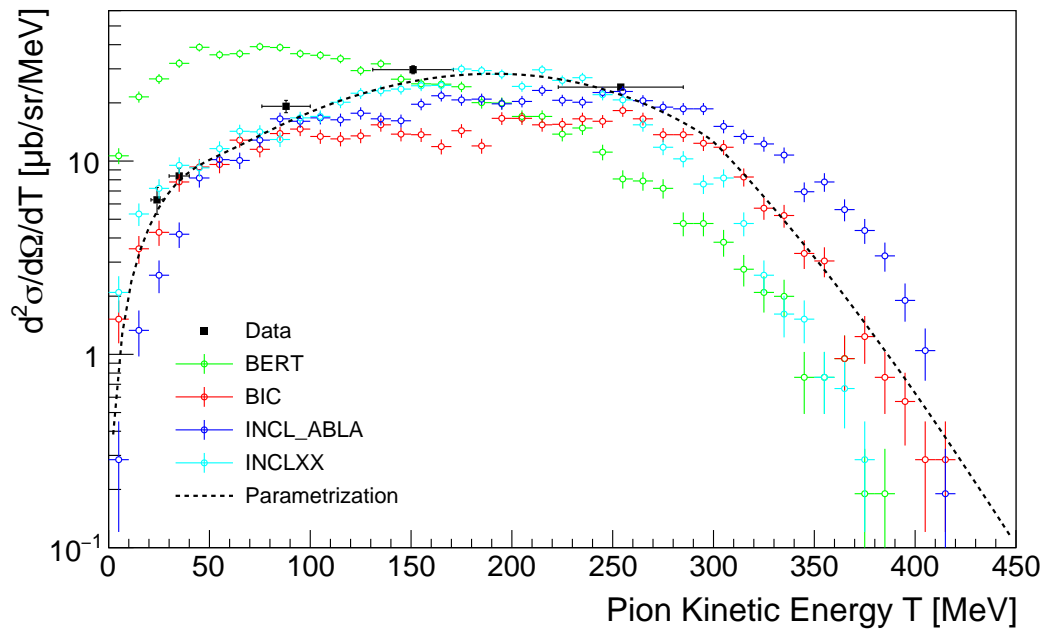
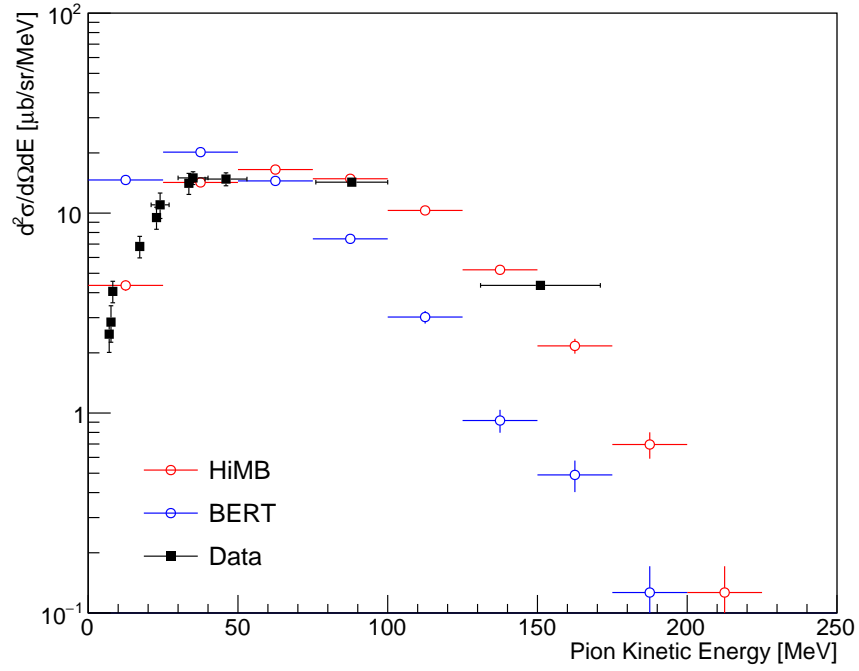
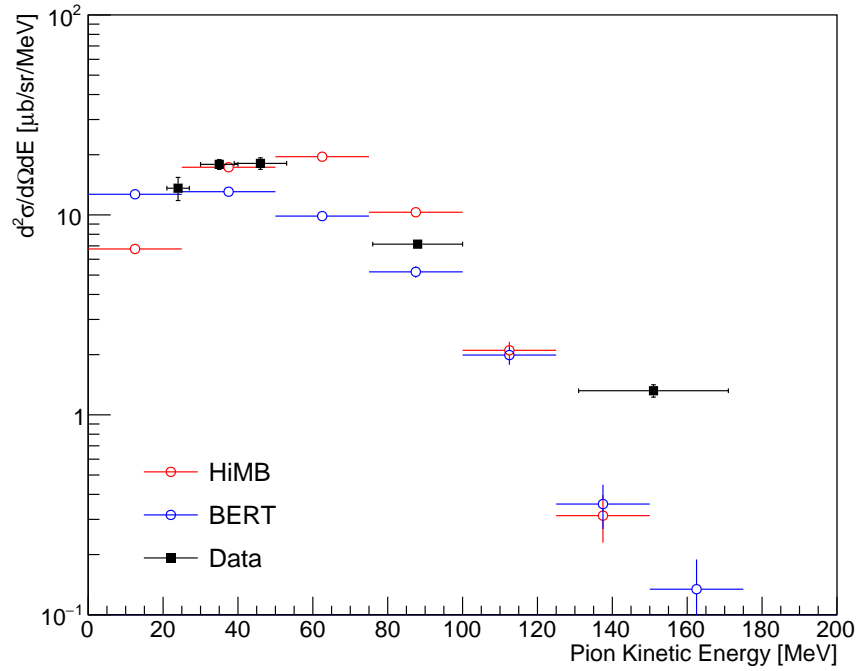


Figure 4.1: Differential cross section comparison of the various hadronic models available in GEANT4 for pion production on carbon at  $22.5^\circ$  with a proton energy of 585 MeV. There is a large difference between available data and the hadronic models contained within GEANT4, especially at low energies.



(a) Differential cross section comparison for pion production at  $90^\circ$  in a graphite target with a proton energy of 585 MeV.



(b) Differential cross section comparison for pion production at  $135^\circ$  in a graphite target with a proton energy of 585 MeV.

Figure 4.2: Differential cross section comparison of the GEANT4 standard BERT hadronic model, Data, and parameterized cross section model (HiMB) for pion production. The parameterized model shows good agreement with data across the pion energy range.

### 4.1.2 Pion Decay and Muon Production Overview

Pions produced inside the target will either be stopped inside the target or have sufficient energy to leave the target volume completely. The pions that exit the target volume can be captured by surrounding beamlines for use as pion beams or directed through a decay solenoid to produce a secondary muon beam. Those pions with sufficiently low momentum will be stopped inside the target and depending on the charge state, have very different kinematics inside the target leading to different final states for stopped pions. The various paths pions can take through the target volume is shown in Figure 4.3. Negative charged pions will lose energy while traversing the target and inevitably be captured in an atomic orbit around a nucleus. The pion will rapidly cascade down to the 2P or 1S level, and due to the large wave function overlap the pion is quickly absorbed (on the order of picoseconds) by the nucleus, producing protons and neutrons.

In contrast, positive charged pions will not form pionic atoms but may stop in the atomic interstitial region and decay. The pion stop distribution inside the target volume follows the proton beam envelope and is shown in Figure 4.4. The peak of the stop distribution is near the center of the target and decreases toward the outer surface of the target. The decay of pions can result in three classes of positive muons, determined by their momentum and consequently where they originate.

- Cloud muons
- Surface muons ( $26 < P_\mu < 29.79 \text{ MeV}/c$ )
- Sub-surface muons ( $P_\mu < 26 \text{ MeV}/c$ )

Cloud muons originate from pion decay in flight, typically inside the target volume or in the region surrounding the target. Additionally, high energy pions can be captured by a nearby beamline and transported in a long solenoid, allowing the pion to decay creating what is known as “decay muons”. These cloud and decay muons will have momenta across the full momentum range with a maximum near 90 MeV/c. Surface muons originate from the surface layer of the production target from stopped pions in the target and carry a unique kinetic energy (4.12 MeV) due to the pion decay kinematics. The details and kinematics of surface muon production is discussed in Section 4.2. Sub-surface muons are also created in the decay of stopped pions inside the target volume, but from deeper within the target than surface muons. These muons have a lower momentum (typically below 26 MeV/c) as a result of the increased material these muons must pass through before exiting the target.

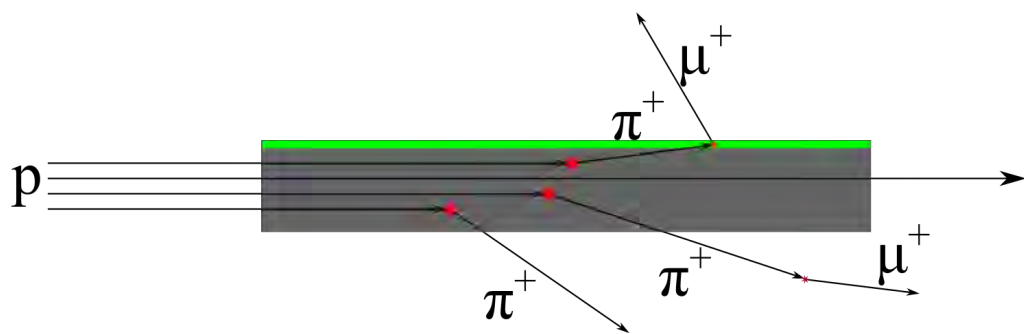
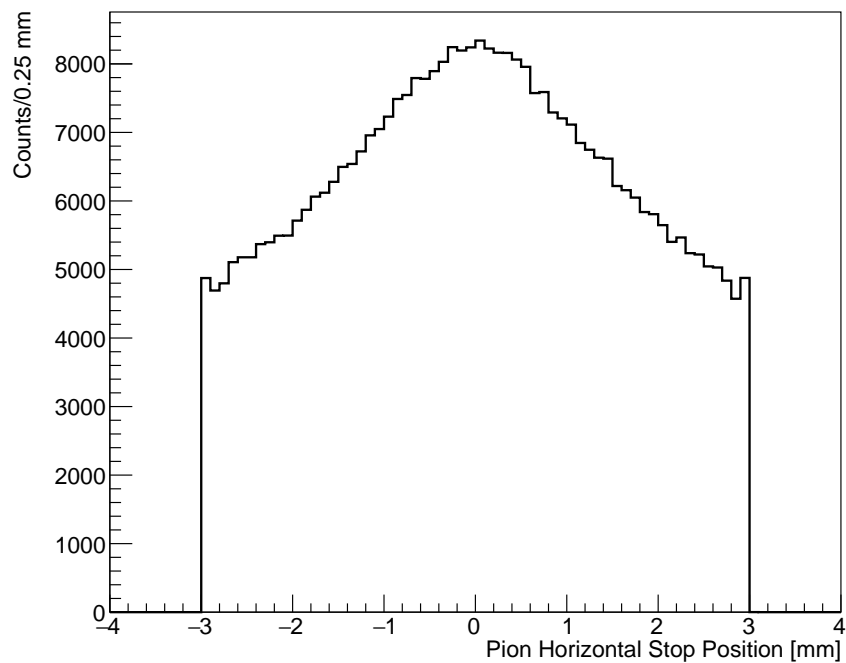
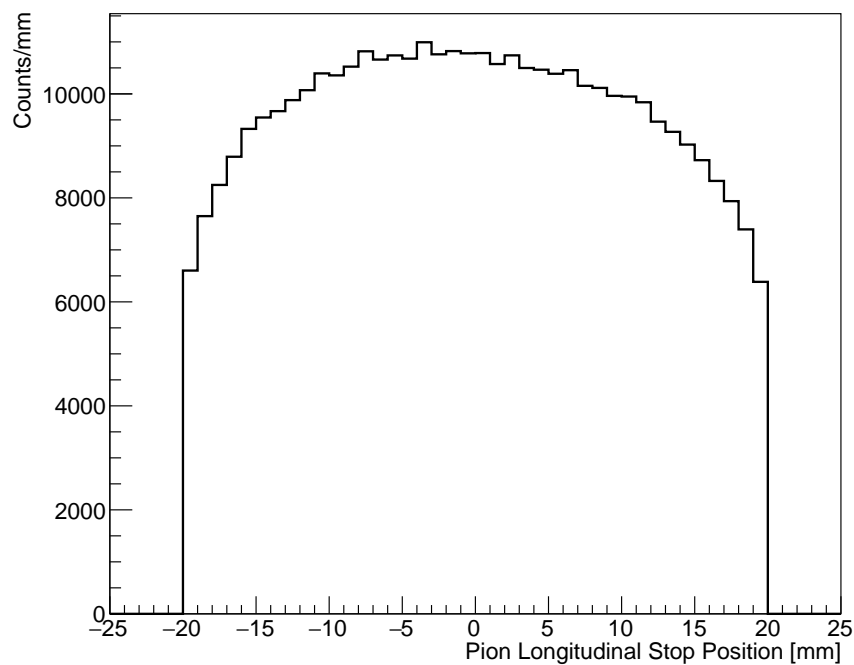


Figure 4.3: A drawing of pion and muon production inside or outside the target volume. Pions either decay outside the target volume leading to cloud muons, or are captured in a decay channel to produce decay muons. The thin green section along the surface represents the volume from which surface muons originate from the stopped pions.



(a) The transverse pion stop distribution inside the Target E volume in G4Beamline using the HiMB pion production model. There is almost a factor two difference in the pion stop density between target center and surface.



(b) The longitudinal pion stop distribution inside the Target E volume simulated in G4Beamline using the HiMB pion production model. The pion stop density is peaked near the center of the target volume.

Figure 4.4: The transverse and longitudinal pion stop distribution for the Target E geometry using G4Beamline and the HiMB pion production model.

## 4.2 Surface Muon Production

The phenomenon of surface muons arises from the decay of these stopped positive pions, through the process  $\pi^+ \rightarrow \mu^+ \nu_\mu$ , near the surface of the target. This is a simple two body decay that results in isotropic production of mono-energetic, spin-polarized positive muons. The concept of using these muons as a high intensity source of low energy muons was first developed by Pifer et. al in 1976 and the unique characteristics of a surface muon beam have made these muons a critical component to many particle physics experiments for decades [57].

### 4.2.1 Muon Production Kinematics

The mono-energetic surface muon momentum is calculated from the two-body decay in the rest frame of the pion assuming zero neutrino mass  $m_\nu$  ( $m_\nu < 0.19$  eV @ 90%CL [45]), in the following way:

$$\begin{aligned}
 P_\mu + P_{\nu_\mu} &= P_\pi \\
 P_\mu^2 &= P_\pi^2 + P_{\nu_\mu}^2 - 2(E_\pi E_{\nu_\mu} - \vec{p}_\pi \cdot \vec{p}_{\nu_\mu}) \\
 m_\mu^2 &= m_\pi^2 + m_\nu^2 - 2(E_\pi(E_\pi - E_\mu) - 0) \\
 &= m_\pi^2 + 0 - 2(E_\pi^2 - E_\pi E_\mu) \\
 &= m_\pi^2 - 2(m_\pi^2 - 2m_\pi E_\mu) \\
 \frac{m_\pi^2 + m_\mu^2}{2m_\pi} &= E_\mu
 \end{aligned} \tag{4.5}$$

with a pion mass  $m_\pi = 139.5706$  MeV/c<sup>2</sup> and a muon mass  $m_\mu = 105.6584$  MeV/c<sup>2</sup> [45]. The momentum is therefore  $P_\mu = 29.792$  MeV/c, with a total energy  $E_\mu = 109.7783$  MeV, and a kinetic energy  $KE_\mu = 4.1199$  MeV.

The charged pion has zero spin, and in the rest frame of the decaying pion, the charged lepton and the neutrino are emitted in opposite directions to conserve linear momentum and with their spins equal and opposite to satisfy angular momentum conservation. This results in the neutrino having a left-handed helicity and chirality state and as a consequence the charged lepton must also have left-handed helicity, as shown in Figure 4.5. The reason for this lies in the electroweak interaction which is a chiral theory where parity is not conserved and as a consequence the weak gauge bosons couple only to the left chirality states of particles and the right chirality states of antiparticles. This can be demonstrated by comparing the two dominant pion decay modes,  $\pi^+ \rightarrow \mu^+ \nu_\mu$  and  $\pi^+ \rightarrow e^+ \nu_e$ . For the case of a relativistic positron being emitted, it will have only a small right handed chiral component, whereas in the

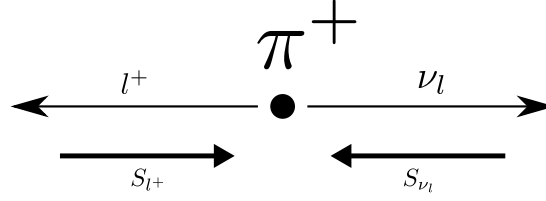


Figure 4.5: The helicity states of the neutrino ( $\nu_l$ ) and lepton ( $l^+$ ) emitted in charged pion decay. The pion has no spin and therefore to conserve angular momentum the neutrino and charged lepton spins must be equal and opposite.  $S_{l^+}$  and  $S_{\nu_l}$  are the spin vectors for the emitted lepton and neutrino respectively.

case of a positive muon which is non-relativistic, it will carry a larger right-handed chiral component. The right-handed chiral component for a left-handed helicity state is proportional to  $(\frac{m}{E})^2$  and since the muon is more than 200 times heavier than the positron, the positron decay mode is “helicity suppressed” leading to a relative enhancement of muons to positrons from pion decay. The relative branching ratio for positrons to muons from pion decay is  $\frac{\Gamma(\pi^+ \rightarrow e^+ \nu_e) + \Gamma(\pi^+ \rightarrow e^+ \nu_e \gamma)}{\Gamma(\pi^+ \rightarrow \mu^+ \nu_\mu) + \Gamma(\pi^+ \rightarrow \mu^+ \nu_e \gamma)} = 1.23 \times 10^{-4}$  [45].

The muon momentum spectrum is shown in Figure 4.6 where the dominant peak near 30 MeV/c is from surface muons with a sharp drop at the kinematic edge. The low energy tail of this distribution comes from muon energy loss in the target material and has here a  $P^{2.5}$  fall below 30 MeV/c. This  $P^{2.5}$  dependence is equivalent to the generally known  $P^{3.5}$  dependence [57] due to the binned histogram of Figure 4.6, which shows counts per momentum as a function of momentum, rather than the direct function. This surface muon peak sits atop the “cloud” muon continuum originating from pion decay-in-flight in the region surrounding the target.

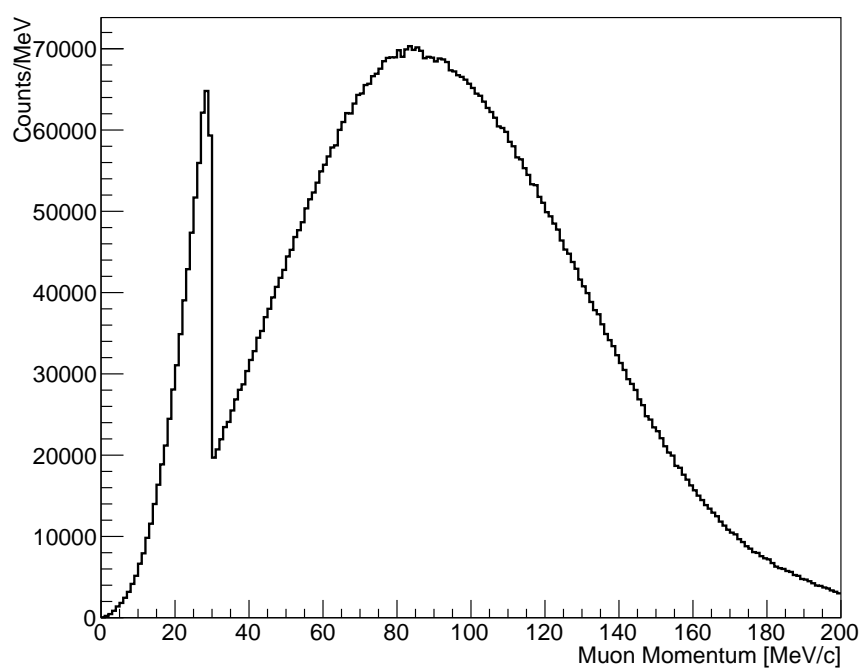


Figure 4.6: The momentum spectrum of all positive muons within the geometric acceptance of a nearby beamline. The peak near 30 MeV/c is the kinematic edge of surface muon production with a characteristic low momentum tail due to energy loss in the target. The surface muon spectrum sits atop a broad cloud muon continuum.

### 4.2.2 Selection Depth

Surface muons are as the name implies a surface phenomenon of the target geometry and therefore one would expect the rate to scale with the surface area of the target. In reality, the secondary beamlines surrounding the target extract surface muons at the production peak in momentum but with varying momentum-bytes and acceptances. The momentum-byte corresponds to an energy loss of the muon as it exits the target volume and therefore a larger momentum-byte selects muons originating from pion stops deeper in the target volume. Therefore the rate of surface muons for a particular beamline depends on the target surface area seen by the beamline and the selection depth given by its momentum-byte. Altogether this creates what is known as the “surface-volume”.

The momentum acceptance chosen by the extraction beamlines effectively selects the acceptance depth for muons and is given by

$$\Delta d = \beta_{\mu} \Delta P \left( \frac{dE}{dx} \right)^{-1} \quad (4.6)$$

where  $\beta_{\mu}$  is the muon velocity,  $\Delta P$  is the selected momentum-byte, and  $\left( \frac{dE}{dx} \right)^{-1}$  is the stopping power of the target material. For a muon beam at 28 MeV/c, from a graphite production target, and a momentum-byte of 3.0%, this depth ( $3\sigma$ ) or equivalent path length is approximately 0.42 mm. Several target geometries are investigated to exploit this surface muon production phenomenon and increase the muon rate delivered to the beamlines.

### 4.2.3 Surface Muon Distribution

Surface muons have a relatively low energy and therefore come from a thin layer of material near the surface on all faces of the target. The surface muon distribution is therefore determined solely by pion stops in this region. In Figure 4.4 it is evident there is nearly a factor two fewer pions near the surface relative to the center of the target. The initial pion kinetic energy of those pions that stop in the volume near the surface of the target is shown in Figure 4.7 with a peak at approximately 15 MeV demonstrating that these pions only travel a few millimeters (7 mm in graphite) before stopping. The initial x-position of muons in the target that are within the geometric and momentum acceptance of a secondary beamline is shown in Figure 4.8. The distribution decreases towards the target center, only reaching 0.4 mm inside, even though the pion stop density is still increasing toward the center. This drop is due to the muon energy loss exiting the target and therefore puts them out of the beamline acceptance.

### 4.3 Geometry Optimization

The optimization of the target geometry begins with the characterization of pion production, stopping distribution and muon production in the standard Target E to identify and exploit efficient production regions. The simulation is based on the G4BEAMLIN package incorporating the newly developed parameterized pion production cross section model to simulate the full chain of pion production from inelastic proton scattering interactions with nucleons as well as subsequent pion decay with muon and neutrino production. The model also incorporates a biasing mechanism where a user-defined number of additional pions and muons are created randomly within the allowed phase space for every primary interaction. This process substantially reduces the required time to generate a statistically significant number of surface muons necessary for any geometry comparisons. These alternate geometries were developed solely to exploit the phenomenon of surface muons in a graphite target, with the only restraint being that the primary proton beam phase space and losses are to be conserved downstream of the target, minimizing any effects at the SINQ target.

#### 4.3.1 Standard Target E

The primary meson production target at PSI, Target E (E for *épais*, French meaning thick), consists of polycrystalline graphite with a density of  $1.84 \text{ g/cm}^3$ . The geometry of Target E is that of a truncated hollow cone with 40 mm length, a 6 mm transverse width, and a diameter of 450 mm. The proton beam enters on the narrow face, passing through the full length of the target volume. The target is separated in 12 individual segments with 1 mm spacing to allow for thermal expansion and deformations, and the entire ring rotates at 1 Hz to facilitate radiative cooling [37]. A picture of Target E is shown in Figure 4.9 [58]. In the optimization simulations only a relatively small section of the target volume is simulated since the bulk of pion production occurs near the region where the proton beam passes through the target. This reduced geometry is a box of 40 mm length, a 6 mm width, and 40 mm height and is sufficient to accurately model pion production within the target volume. A schematic drawing of the target position relative to the beamlines considered in this study is shown in Figure 4.10, with sizes proportional to their geometric acceptance which are listed in Table 4.1.

The initial positions of muons at the target that are detected at the geometric acceptances of surrounding beamlines is shown in Figure 4.11, Figure 4.12, and Figure 4.13. The upstream and side faces of the target have different yields depending on the extraction angle of the beamline. For the sideways direction ( $90^\circ$  extraction) corresponding to a  $\mu\text{E4}$  acceptance, nearly all muons originate from the side face of the target, whereas in the backward direction ( $165^\circ$  extraction) corresponding to the  $\pi\text{E5}$

acceptance, the side face contributes approximately two-thirds and the upstream face contributes one-third of the total muon rate. The transverse and vertical phase space of surface muons from the standard target geometry at the geometric acceptance of  $\mu$ E4 and  $\pi$ E5 beamlines are shown in Figure 4.14 and Figure 4.15 respectively. In the phase space plots the coordinates have been transformed to match the corresponding beamline axis.

Table 4.1: The solid angle acceptance of secondary beamlines used in this simulation

	Distance from Target Center [mm]	Solid Angle Acceptance [msr]
$\pi$ E5	440.8	144
$\mu$ E4	540.0	135
$\pi$ E1	500.0	32

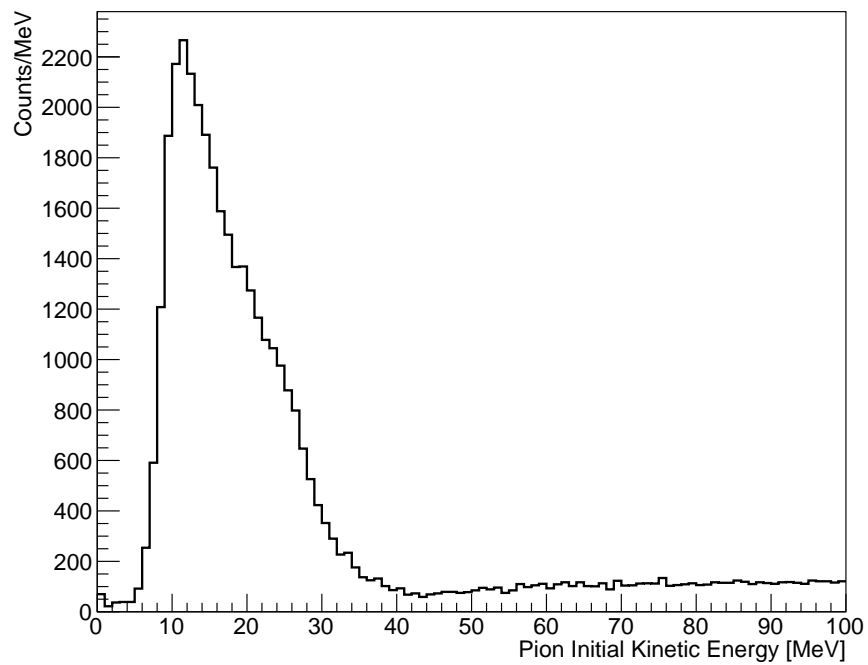


Figure 4.7: The initial energy spectrum of those pions that subsequently stop in a layer near the target surface. The peak near 15 MeV indicates that these pions only travel a few millimeters before stopping.

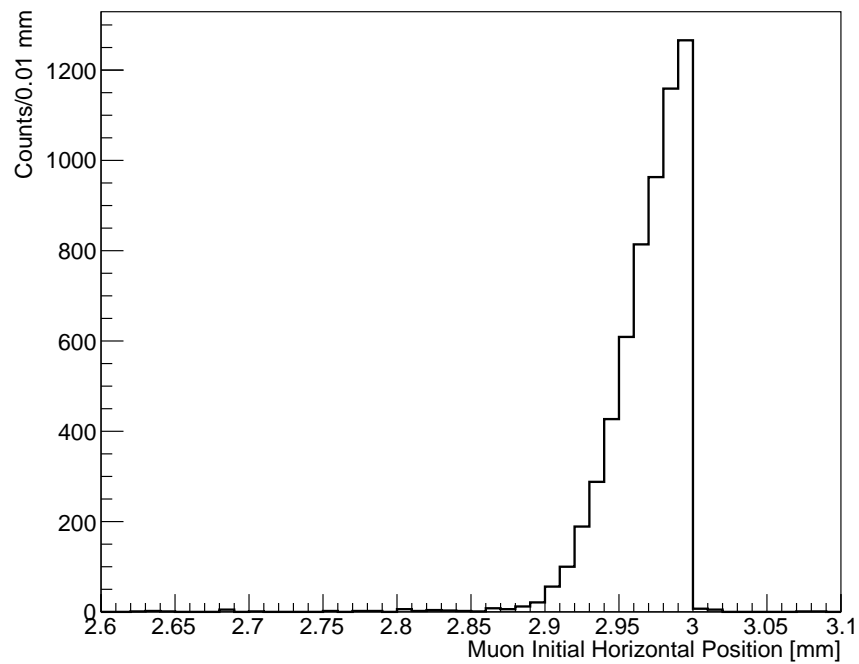


Figure 4.8: The initial  $x$ -positions of muons that are within the geometric and momentum acceptances of a nearby beamline. The target material ends at 3 mm. The decrease toward the interior is due to muon energy loss, resulting in those muons being outside the beamline acceptance after exiting the target material.



Figure 4.9: A picture of the actual Target E. Each of the twelve segments is separated by a 1 mm gap to allow for thermal expansion and deformations.

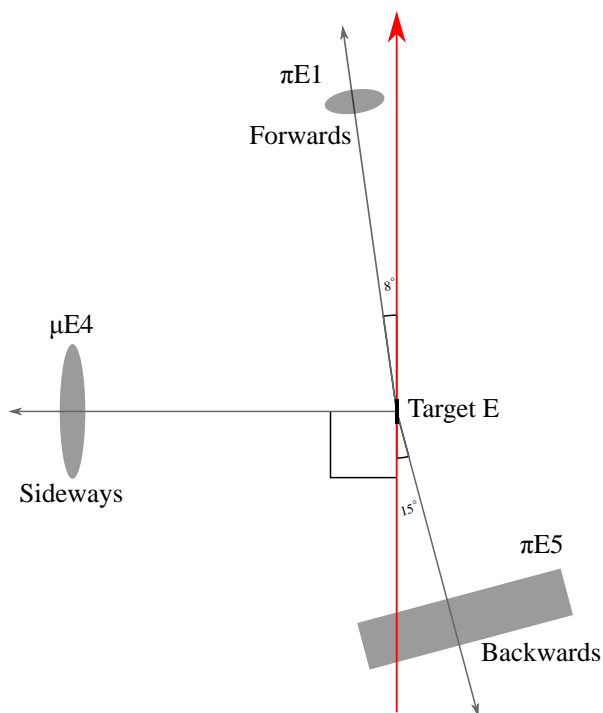


Figure 4.10: A schematic drawing of the target position relative to surrounding beamlines with sizes proportional to their geometric acceptance.

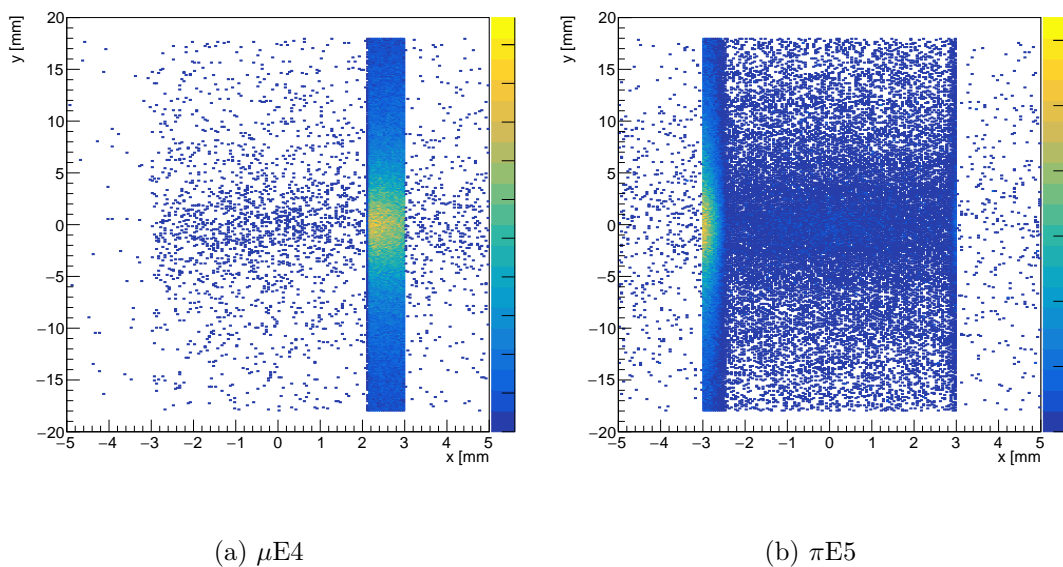


Figure 4.11: The initial x-y positions of muons from the standard target geometry that reach the geometric acceptance of the  $\mu E4$  and  $\pi E5$  beamlines.

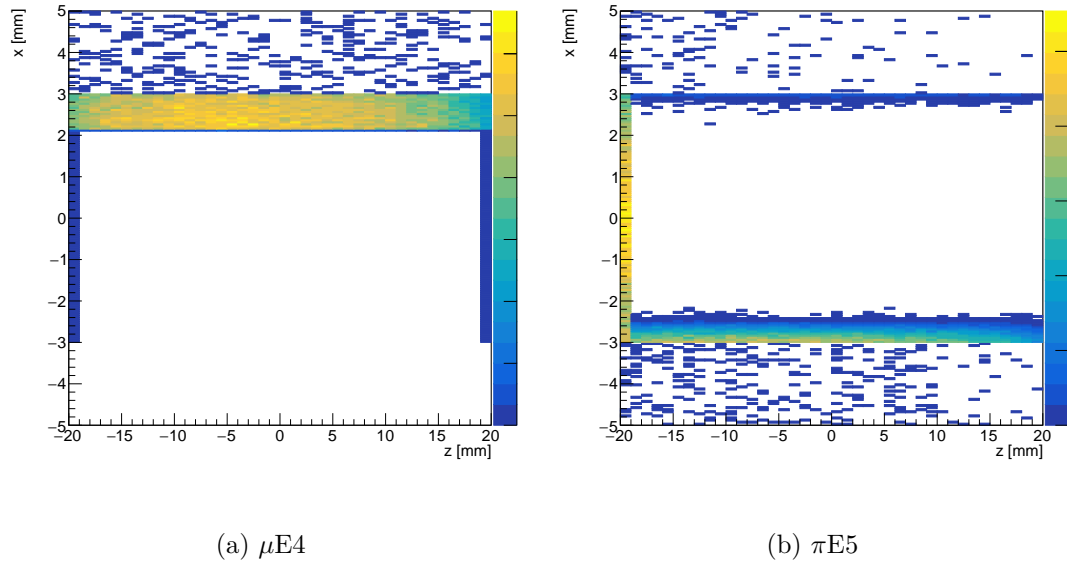


Figure 4.12: The initial x-z positions of muons from the standard target geometry that reach the geometric acceptance of the  $\mu E4$  and  $\pi E5$  beamlines

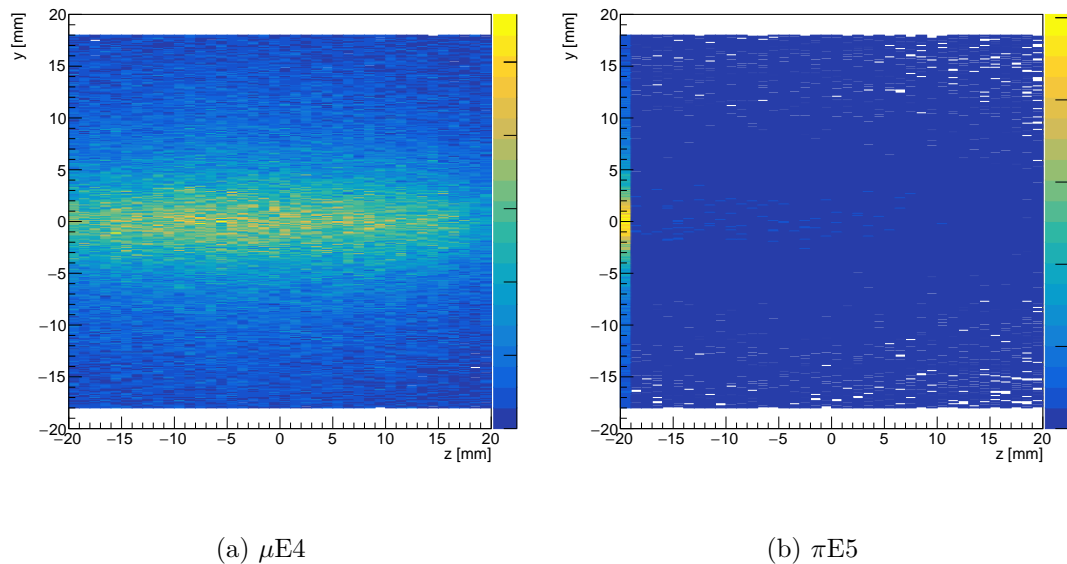


Figure 4.13: The initial y-z positions of muons from the standard target geometry that reach the geometric acceptance of the  $\mu E4$  and  $\pi E5$  beamlines

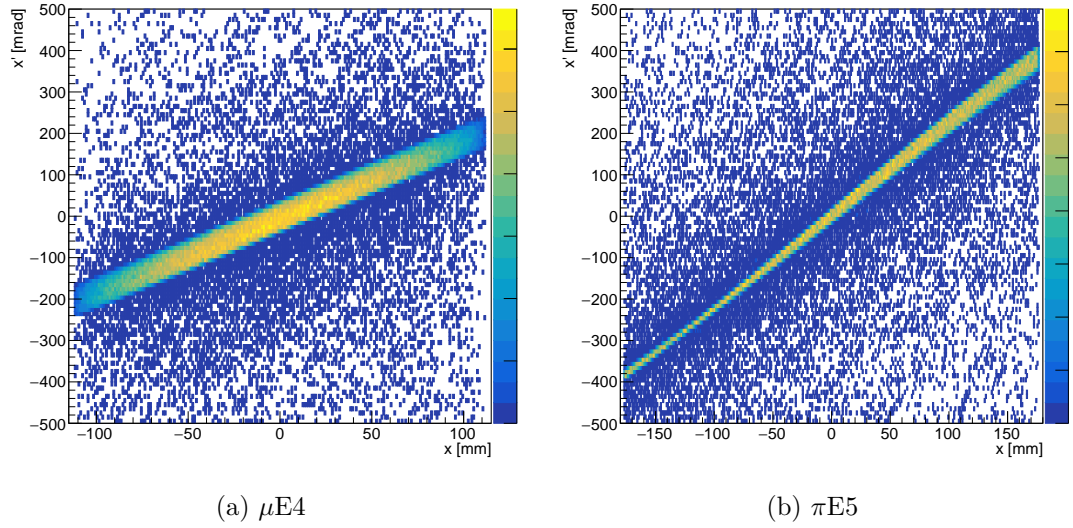


Figure 4.14: The horizontal phase space of surface muons from the standard target geometry at the geometric acceptance of the  $\mu E4$  or  $\pi E5$  beamlines.

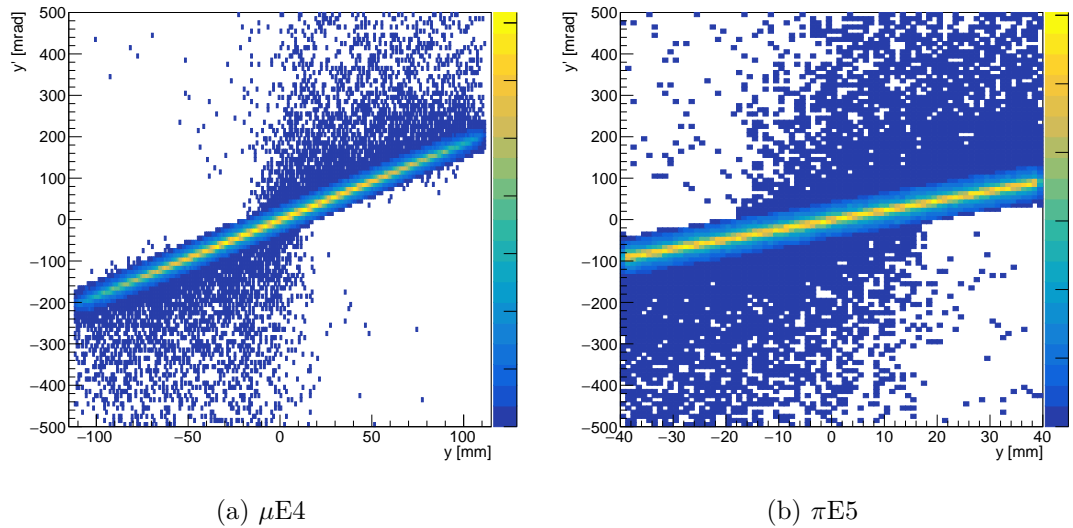


Figure 4.15: The vertical phase space of surface muons from the standard target geometry at the geometric acceptance of the  $\mu E4$  or  $\pi E5$  beamlines.

### 4.3.2 Radial Grooved Target

It is expected that by increasing the surface volume (surface area times acceptance depth) in which pions are stopped along the side face of the target, that the surface muon rate would increase proportionally. One method of increasing this surface volume is by forming grooves in the target surface parallel to the proton beam direction [59]. For a grooved target this surface volume is proportional to the semi-circular surface area of the groove, and is expressed as  $\frac{\pi}{2}((R_g + \Delta d)^2 - R_g^2)$ , where  $R_g$  is the radius of the groove and  $\Delta d$  is the thickness of the semicircle. The corresponding surface volume in a flat rectangular target is simply  $2 \times (R_g + \Delta d) \times \Delta d$ . A visual comparison between a flat and grooved target surface volumes is shown in Figure 4.16. The ratio of these surface areas is given by

$$\epsilon = \frac{\pi (2R_g + \Delta d)}{4 (R_g + \Delta d)} \quad (4.7)$$

and numerical values are listed for several groove radii in Table 4.2.

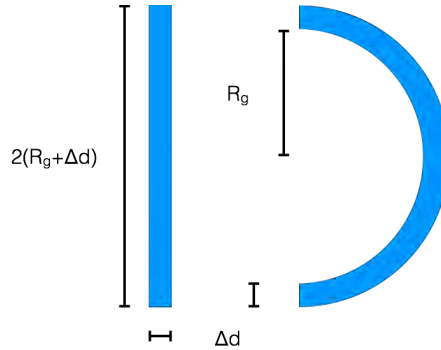


Figure 4.16: A visual comparison of the surface volume for a flat target (left) and a grooved target (right).

Table 4.2: The expected enhancement of surface muons due to increased surface volume compared to the equivalent gain by increasing the proton beam current from the present 2.2 mA.

Groove Radius [mm]	Enhancement Ratio $\epsilon$	Equivalent Proton Current [mA]
1.0	1.35	2.8
1.5	1.40	3.1
2.0	1.45	3.2

A grooved target is constructed in the simulation as a graphite box with dimensions: 40 mm length, 40 mm height, and  $R_g+6$  mm width, where  $R_g$  is the radius of the groove. The grooves are half-cylinders of radius  $R_g$  and length 40.0 mm that are subtracted from both box-target y-z surfaces, with a center-center groove spacing equal to  $2\times(R_g+\Delta d)$ . The groove centers of one side are offset in the y-axis from the opposite side by  $R_g+\Delta d$  such that the transverse target width is approximately 6 mm everywhere. A model of this grooved target is shown in Figure 4.17. The initial x-y position of muons detected in each beamline is shown in Figure 4.18, where one can see the layer of surface muons in each groove. The initial x-z position of muons detected in each beamline is shown in Figure 4.19. The initial y-z position of muons detected in each beamline is shown in Figure 4.20, where one sees two regions of surface muons production in the target, one from the flat section between grooves and another inside the groove closest to the target center. The simulation results of the muon rate in the respective beamlines are shown in Table 4.3.

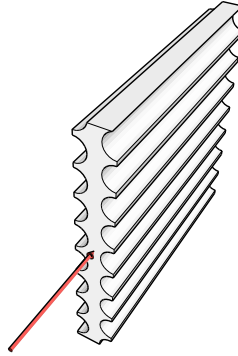


Figure 4.17: A model of the target section with grooves along the outside surface. The direction of the incident proton beam is shown with a red arrow.

There is minimal improvement in the  $\mu E4$  beamline and no improvement for the  $\pi E5$  beamline. This is in stark contrast to the 45% enhancement expected from a geometric argument. This lack of enhancement can be attributed to the geometric properties of the groove whereby it reduces the solid angle from which muons can escape and be accepted into a surrounding beamline. There is also a loss of upstream surface volume as seen by the  $\pi E5$  beamline which contributes to the muon rate loss. The minimal increase of the muon rate as seen by the  $\mu E4$  beamline is a result of the groove cutting deeper into the target where the pion stop density is higher. A closer inspection of the groove shows that surface muons originate only from a crescent shaped volume and not the full semi-circular volume as expected.

Table 4.3: The simulated muon rate enhancement from a radially grooved target in the  $\mu$ E4 and  $\pi$ E5 beamlines.

Groove Radius [mm]	$\mu$ E4 Enhancement Ratio	$\pi$ E5 Enhancement Ratio
1.0	1.02	0.99
1.5	1.02	1.02
2.0	1.04	0.99

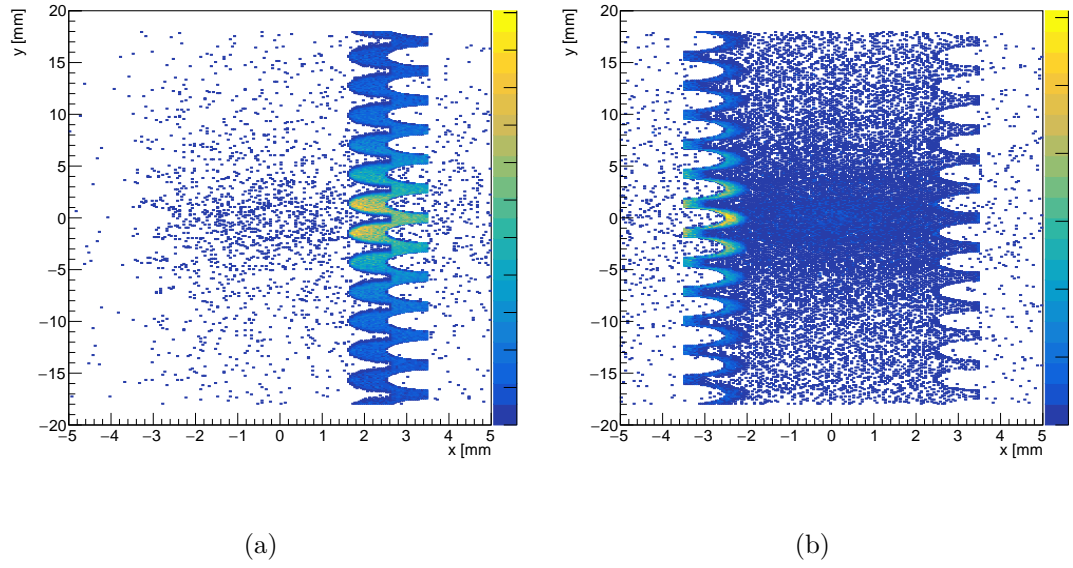


Figure 4.18: The initial x-y position of muons detected in the  $\mu$ E4 and  $\pi$ E5 beamlines for a 2 mm radius grooved target.

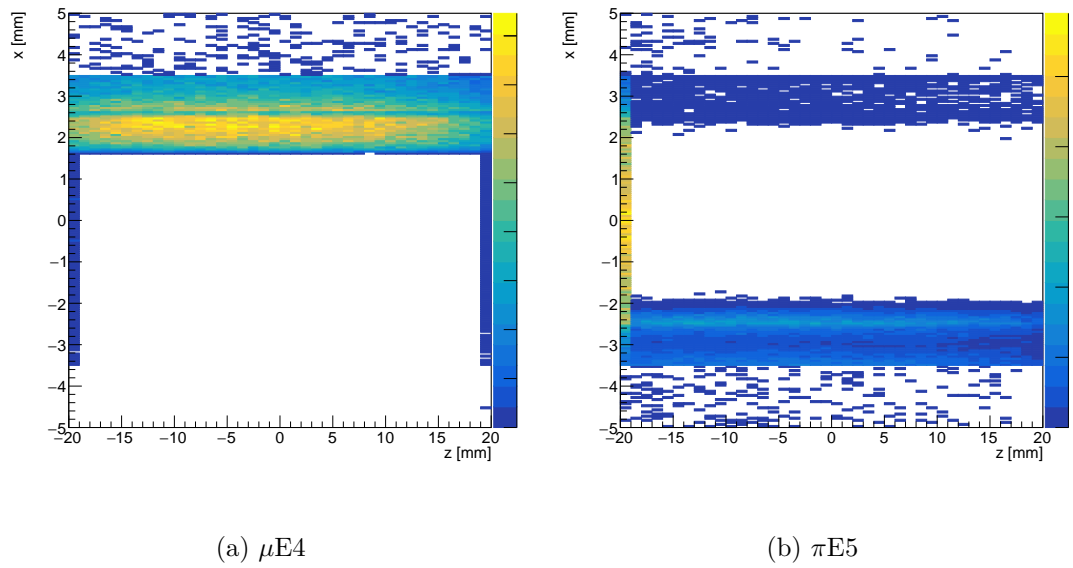


Figure 4.19: The initial x-z position of muons detected in the  $\mu$ E4 and  $\pi$ E5 beamlines for a 2 mm radius grooved target.

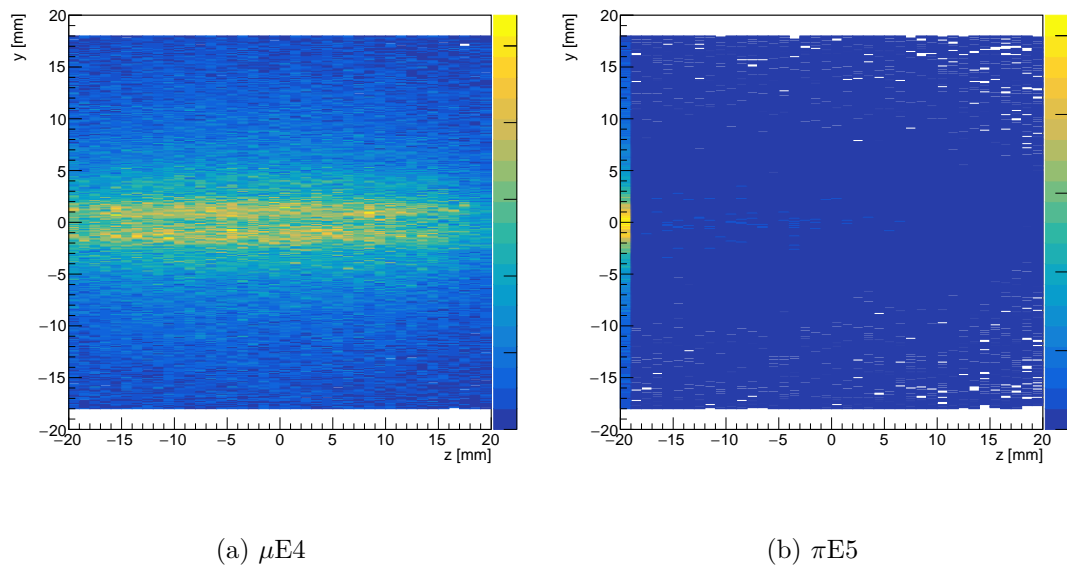


Figure 4.20: The initial  $y$ - $z$  position of muons detected in the  $\mu$ E4 and  $\pi$ E5 beamlines for a 2 mm radius grooved target.

### 4.3.3 Trapezoidal Target

From the grooved target one sees that the groove structure exposes the increased pion stop density toward the center of the target yielding a few percent enhancement in the  $\mu$ E4 beamline acceptance. A trapezoidal shaped target would lead to higher surface pion stop density toward the upstream direction and exploit this enhancement for both beamlines considered. This trapezoidal target is constructed in the simulation as a symmetric graphite trapezoid with dimensions: 40 mm length, 40 mm height, with a downstream width of 6 mm and an upstream width which is varied between 2 mm to 4 mm. A model of the 2 mm upstream width trapezoidal target is shown in Figure 4.21. The results of the muon rate in the respective beamlines is shown in Table 4.4. The initial x-y position of muons detected in each beamline is shown in Figure 4.22. The initial x-z position of muons detected in each beamline is shown in Figure 4.23, where it is seen that for both beamlines the density of collected surface muons increases towards the upstream section of the target. The initial y-z position of muons detected in each beamline is shown in Figure 4.24.

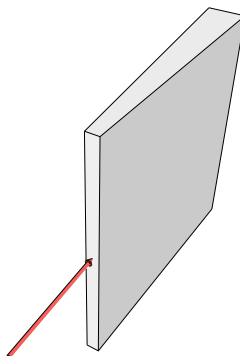


Figure 4.21: A model of the trapezoidal target with a narrow upstream width and nominal 6 mm downstream width. The direction of the incident proton beam is shown with a red arrow.

There is a 13% enhancement in the  $\mu$ E4 beamline but a small loss in the  $\pi$ E5 beamline for the 2 mm upstream width trapezoidal target configuration. There is effectively no gain in the  $\pi$ E5 beamline for any trapezoidal target configuration. This is due to the loss of the upstream face surface volume, and subsequently fewer surface muons. The average width of the 2 mm trapezoidal target is 4 mm and therefore the 13% enhancement on the  $\mu$ E4 side of the target. This enhancement is compatible with the expected 13% improvement from a 1 mm horizontal proton beam offset.

Table 4.4: Simulated muon rate enhancement from a trapezoidal target in the  $\mu$ E4 and  $\pi$ E5 beamlines.

Upstream Width [mm]	$\mu$ E4 Enhancement Ratio	$\pi$ E5 Enhancement Ratio
2.0	1.13	0.96
3.0	1.08	1.02
4.0	1.08	1.00

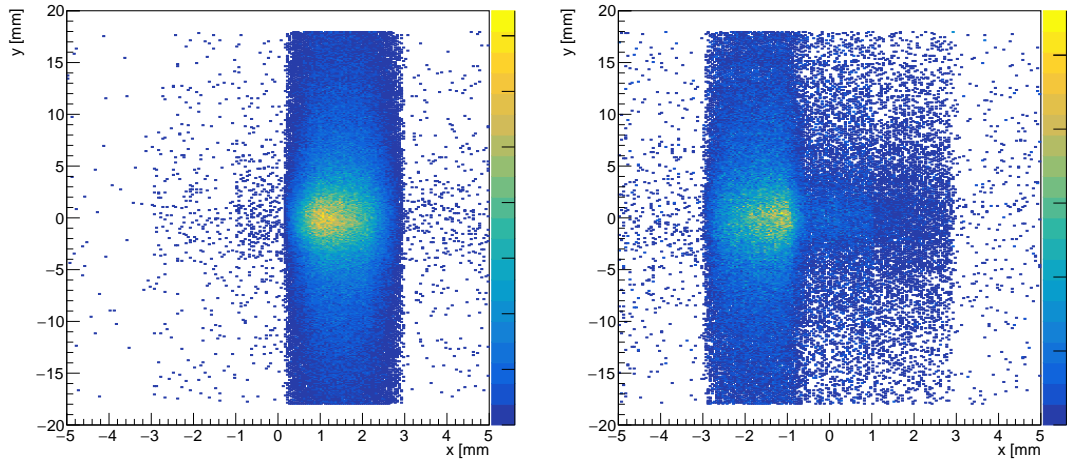
(a)  $\mu$ E4(b)  $\pi$ E5

Figure 4.22: The initial x-y position of muons detected in the  $\mu$ E4 and  $\pi$ E5 beamlines for a 2 mm upstream width trapezoidal target.

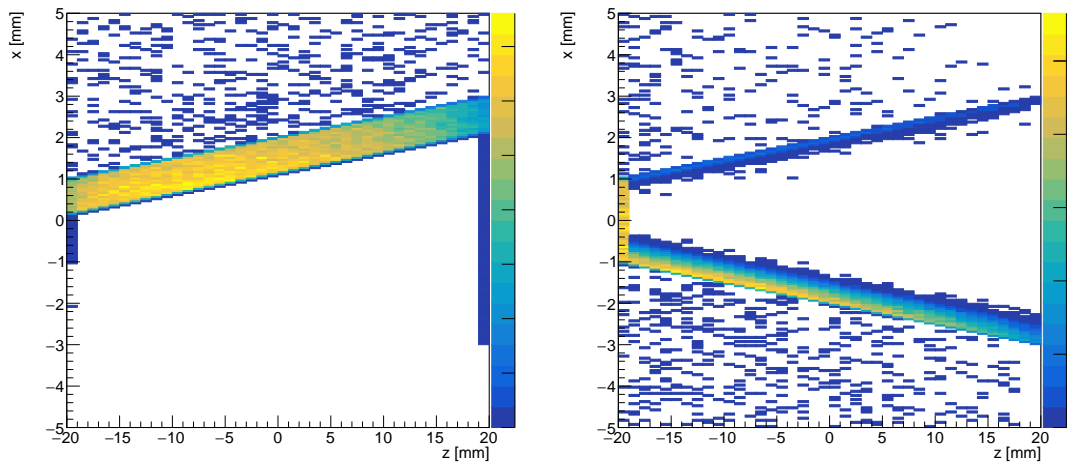
(a)  $\mu$ E4(b)  $\pi$ E5

Figure 4.23: The initial x-z position of muons detected in the  $\mu$ E4 and  $\pi$ E5 beamlines for a 2 mm upstream width trapezoidal target.

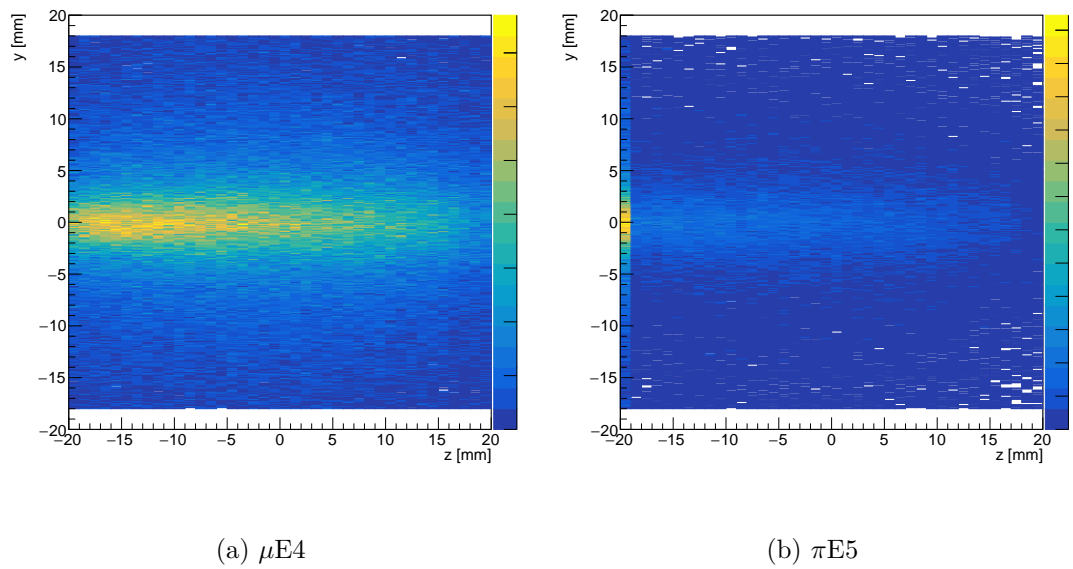


Figure 4.24: The initial  $y$ - $z$  position of muons detected in the  $\mu$ E4 and  $\pi$ E5 beamlines for a 2 mm upstream width trapezoidal target.

#### 4.3.4 Forked Target

From the trapezoidal target, one sees an increase in surface muon rates as expected from the higher pion stop density. Though the outer region of the proton beam does not pass through the full 40 mm length of the target due to the tapered width, the surface pion stop density is not uniform along the z-axis. Therefore a forked target geometry was developed to resolve these inefficiencies. This forked target is constructed in the simulation as three separate graphite boxes each with dimensions: 40 mm length, 40 mm height, and a varying central and side target width, constrained such that the sum of all target section widths is 6 mm. The two side boxes are offset in the proton beam direction by 40 mm downstream. A model of the 2 mm center target width forked target is shown in Figure 4.25.

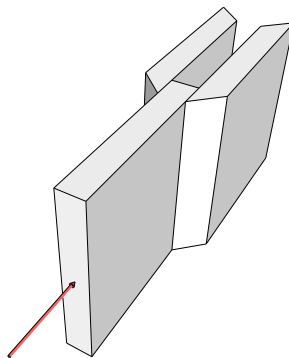


Figure 4.25: A model of the fork target with 2 mm widths for all three target sections such that the total target width is the nominal 6 mm. The direction of the incident proton beam is shown with a red arrow.

The forked target structure leads to considerable gains in the muon rates. Nearly 50% enhancement is seen in the  $\mu$ E4 beamline and a consistent 20% in the  $\pi$ E5 beamline for differing central target widths. This enhancement is attributed to the narrow width of the central target that exposes the high pion stop density at the center of the target. The downstream outer target sections contribute an additional 20% muon rate to the central target. The results of the muon rate in the respective beamlines are shown in Table 4.5. The initial x-y position of muons detected in each beamline is shown in Figure 4.26. The initial x-z position of muons detected in each beamline is shown in Figure 4.27, where it is seen that for both beamlines the majority of muons originate from the central target section. The initial y-z position of muons detected in each beamline is shown in Figure 4.28.

Table 4.5: Simulated muon rate enhancement from a forked target in the  $\mu$ E4 and  $\pi$ E5 beamlines.

Center Target Width [mm]	$\mu$ E4 Enhancement Ratio	$\pi$ E5 Enhancement Ratio
2.0	1.48	1.20
3.0	1.35	1.20
4.0	1.27	1.20

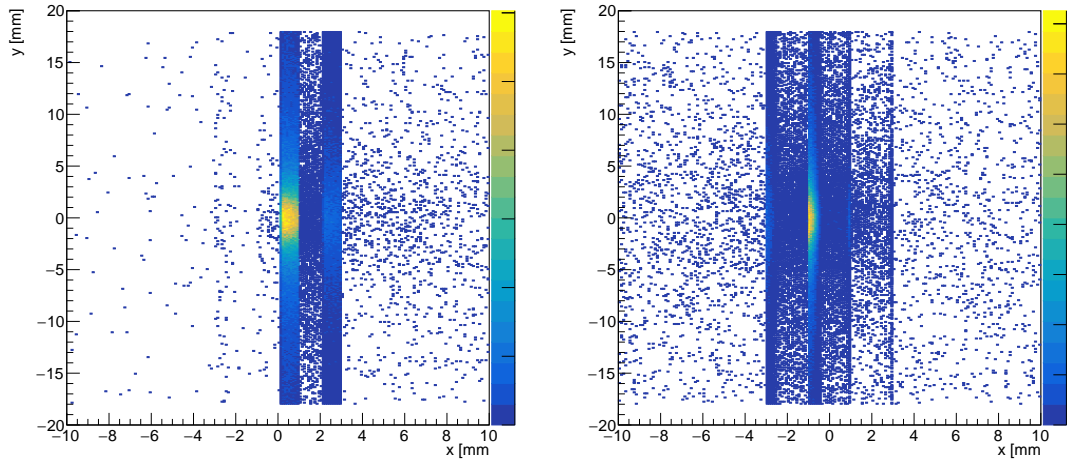
(a)  $\mu$ E4(b)  $\pi$ E5

Figure 4.26: The initial x-y position of muons detected in the  $\mu$ E4 and  $\pi$ E5 beamlines from a forked target with a 2 mm central target section.

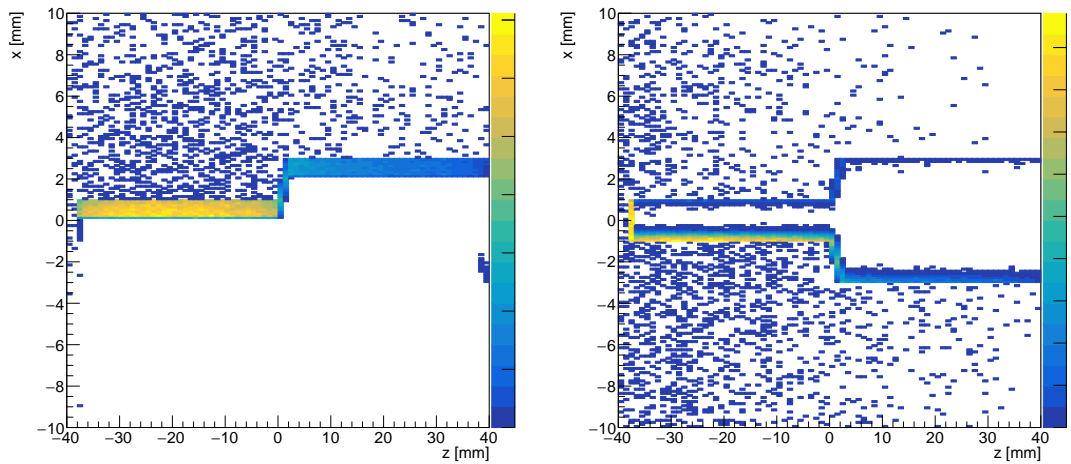
(a)  $\mu$ E4(b)  $\pi$ E5

Figure 4.27: The initial x-z position of muons detected in the  $\mu$ E4 and  $\pi$ E5 beamlines from a forked target with a 2 mm central target section.

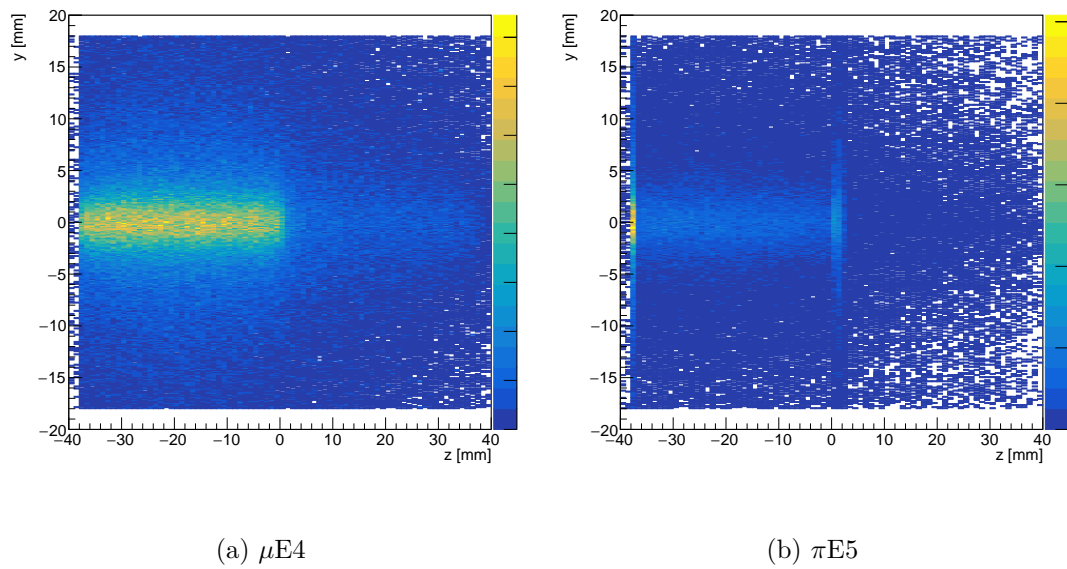


Figure 4.28: The initial  $y$ - $z$  position of muons detected in the  $\mu$ E4 and  $\pi$ E5 beamlines from a forked target with a 2 mm central target section.

### 4.3.5 Rotated Slab Target

The final target geometry investigated is a large slab-like target rotated about the y-axis. The length of target material along the proton beam axis of 40 mm is maintained regardless of rotation angle. Therefore, the width must increase with increasing rotation to maintain the material length. The total length and height are independent so long as the longitudinal length is maintained, therefore the largest realistic dimension is desired and chosen to be 150 mm. A model of the rotated slab target is shown in Figure 4.29, with relative proton beam direction shown with a red arrow. The initial x-y position of muons detected in each beamline is shown in Figure 4.30, the initial x-z positions are shown in Figure 4.31, and the initial y-z position is shown in Figure 4.32 for a 150 mm long target at 10° rotation.

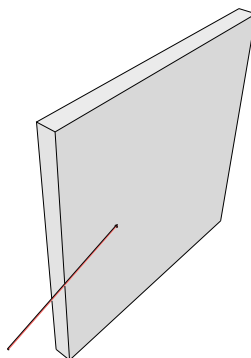


Figure 4.29: A model of the rotated slab target. The direction of the incident proton beam is shown with a red arrow.

The surface muon yield as a function of the target rotation is highly dependent on the beamline extraction direction as shown in Figure 4.33a. An increase of between 30-60% for all beamlines is seen for a shallow rotation of 10°. The yield increases for forward and backward directions but decreases for the sideways direction with increasing target rotation. This is simply a geometric effect due to a reduced effective surface volume for the sideways extraction. Additionally, the surface muon yield is roughly independent of the overall target length beyond about 100 mm as shown in Figure 4.33b. The relative rates for each beamline at rotation angles from 5° to 45° are listed in Table 4.6 and for increasing target length from 50 to 100 mm at a fixed 10° rotation in Table 4.7.

A target rotation angle between 5° and 10° offers large surface muon rate enhancements relative to the standard geometry for all surrounding beamlines. For the case of a 10° target rotation, a significantly increased muon yield to backward and sideways beamlines is seen, with enhancements of 35% sideways and 30% in the backward direction. This configuration has minimal impact on the proton beam while simultaneously

providing a very large surface volume which yields a significant increase in surface muons. Further enhancement of more than 150% are seen for the forward direction in case of large rotation angles, but simultaneously leading to significant losses in the sideways direction.

Table 4.6: Simulated muon rate enhancement in the  $\mu$ E4,  $\pi$ E5, and  $\pi$ E1 beamlines from a slab target with increasing rotation angle and a fixed 150 mm length .

Rotation Angle [ $^{\circ}$ ]	$\mu$ E4 (Sideways) Enhancement Ratio	$\pi$ E5 (Backwards) Enhancement Ratio	$\pi$ E1 (Forwards) Enhancement Ratio
5	1.45	1.14	1.24
10	1.35	1.30	1.56
15	1.25	1.44	1.83
25	1.09	1.64	2.20
35	0.92	1.80	2.43
45	0.77	1.90	2.60

Table 4.7: Simulated muon rate enhancement in the  $\mu$ E4,  $\pi$ E5, and  $\pi$ E1 beamlines from a slab target at a fixed  $10^{\circ}$  rotation angle and increasing overall length

Target Length [mm]	$\mu$ E4 (Sideways) Enhancement Ratio	$\pi$ E5 (Backwards) Enhancement Ratio	$\pi$ E1 (Forwards) Enhancement Ratio
50	1.06	1.19	1.42
60	1.13	1.23	1.57
75	1.20	1.20	1.49
100	1.27	1.32	1.52
125	1.32	1.32	1.55
150	1.35	1.35	1.59

This geometry has an additional secondary benefit due to the transverse size of the target relative to the standard Target E in that if the proton beam deviates from the central trajectory, which happens during alignment of the beam on Target E, the beam still passes through the full length of target material. This protects the SINQ target downstream from, at any time, receiving the full intensity of the proton beam, which could be considerably destructive. This together with significant enhancements to the surface muon yield for all surrounding beamlines suggests the slab target is the optimal target geometry of those investigated. The comparison of pion stop distributions for of all previous geometries is shown in Figure 4.34, where the benefit of the large surface area of the rotated slab target can be seen in the extended horizontal and longitudinal stop distributions.

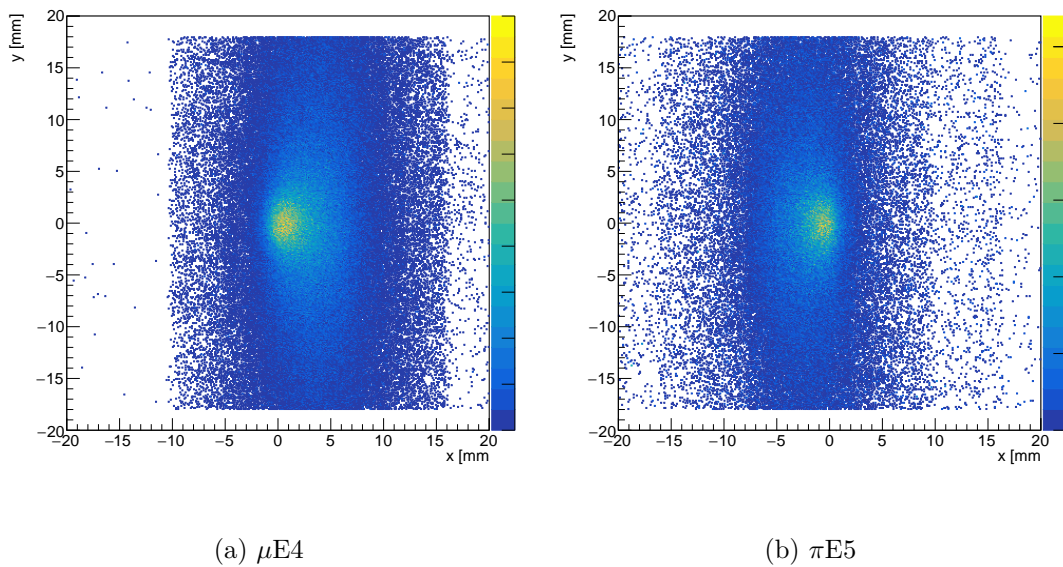


Figure 4.30: The initial x-y position of muons detected in the  $\mu E4$  and  $\pi E5$  beamlines from a slab target with a  $10^\circ$  rotation.

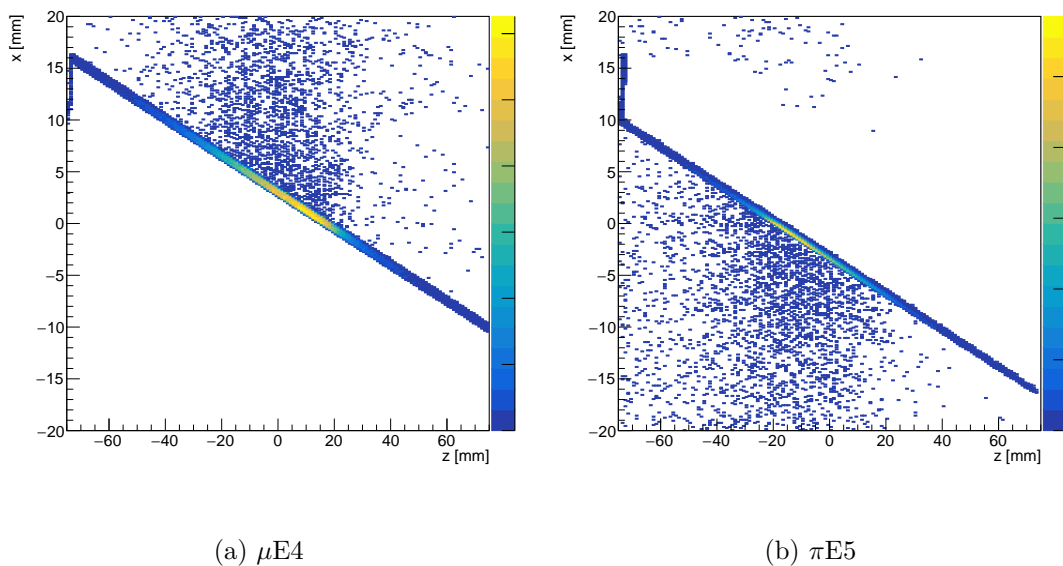


Figure 4.31: The initial x-z position of muons detected in the  $\mu E4$  and  $\pi E5$  beamlines from a slab target with a  $10^\circ$  rotation.

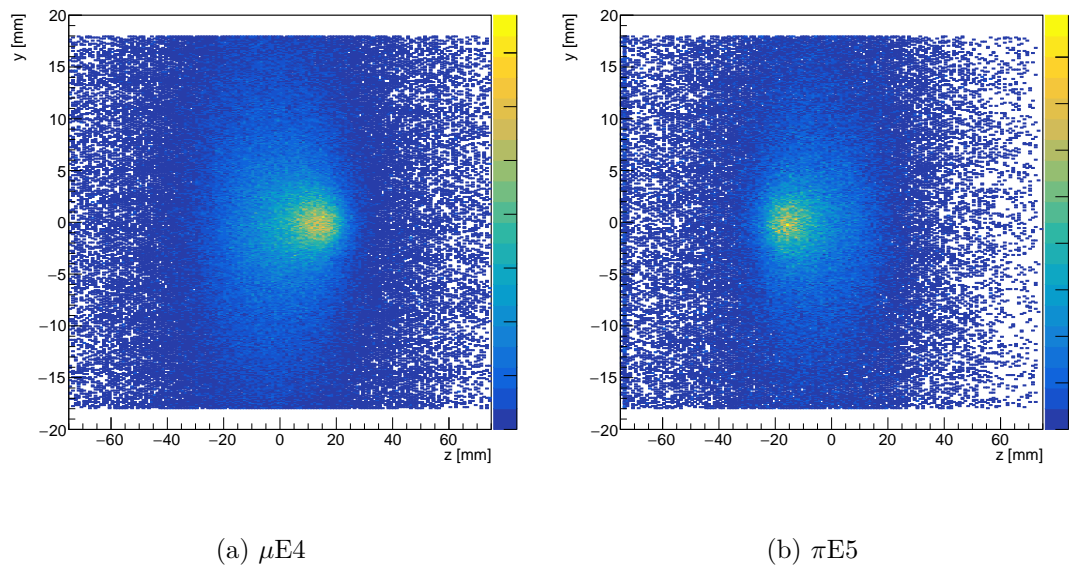
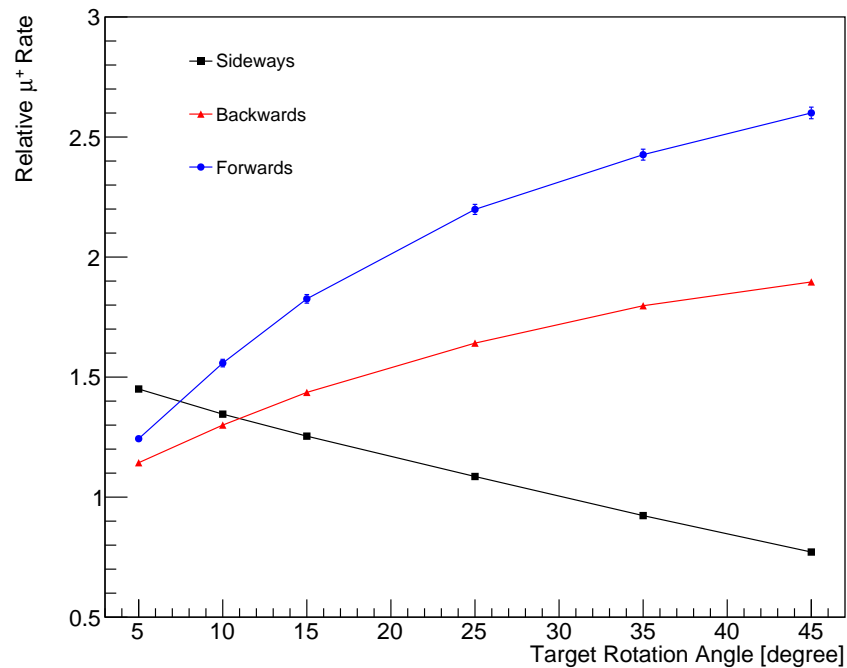
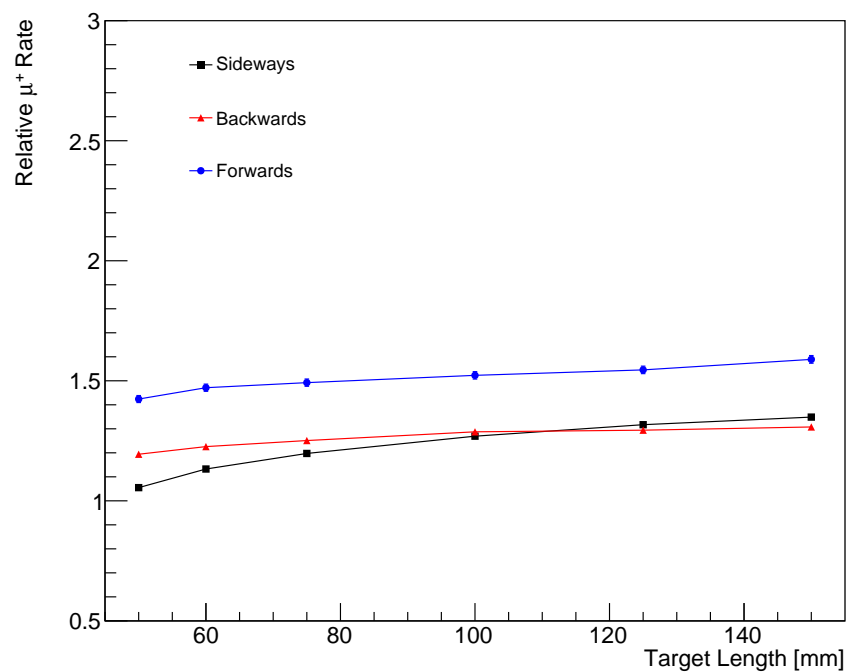


Figure 4.32: The initial  $y$ - $z$  position of muons detected in the  $\mu E4$  and  $\pi E5$  beamlines from a slab target with a  $10^\circ$  rotation.

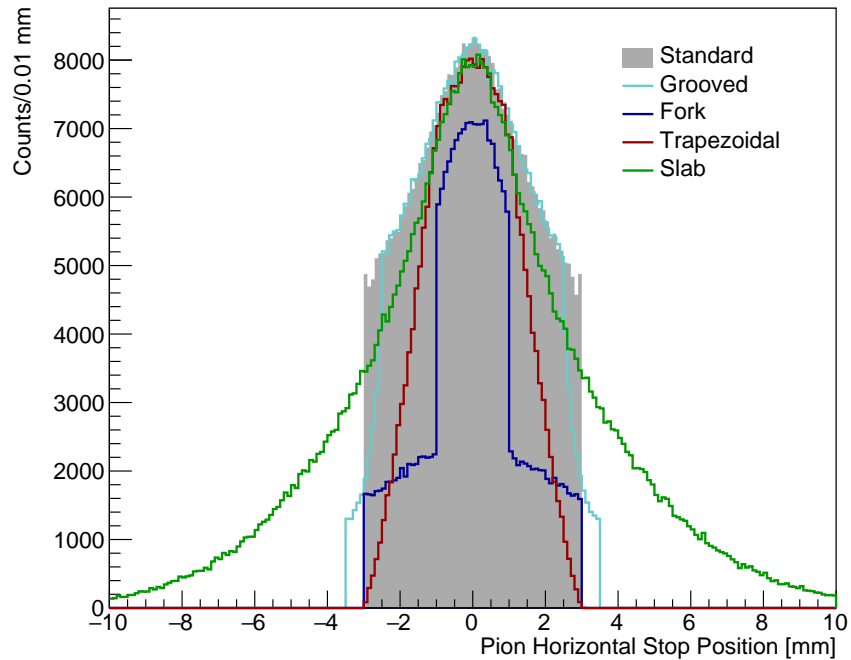


(a) The dependance of simulated muon rate enhancements for a rotated slab target with respect to the target rotation angle. Each beamline responds differently to the target rotation.

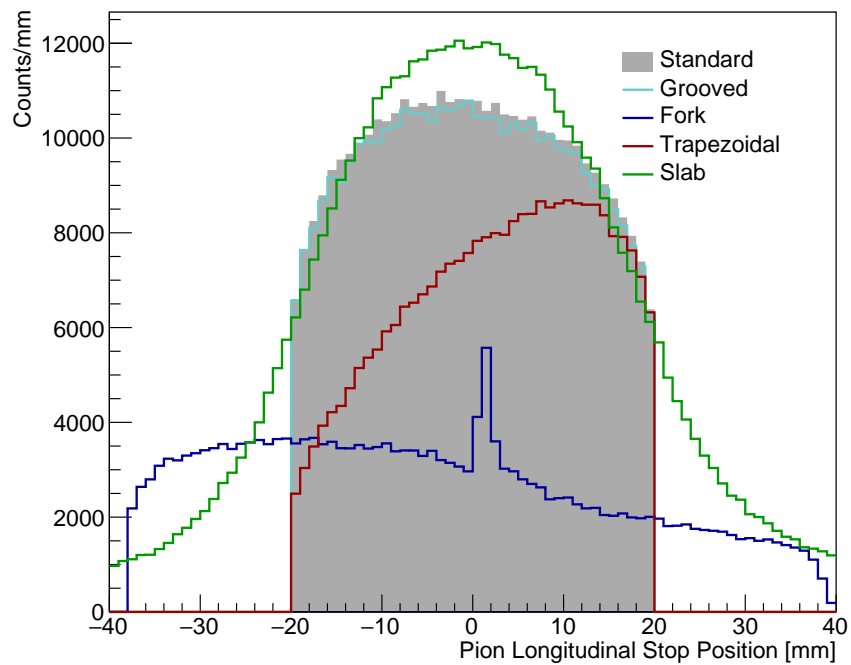


(b) The dependance of simulated muon rate enhancements for a rotated slab target with respect to the target length. Beyond 100 mm the rate remains relatively constant for increasing target length for all surrounding beamlines.

Figure 4.33: The dependance of simulated muon rate enhancements for a rotated slab target with respect to the target rotation angle and target length.



(a) Horizontal Pion Stop Distribution



(b) Longitudinal Pion Stop Distribution

Figure 4.34: Comparison of the longitudinal and horizontal pion stop distributions for all target geometries considered.

#### 4.4 Target Geometry Effects on the Proton Beam

All of the geometry optimizations focused equally on maximizing the surface muon yield and simultaneously minimizing any impact on the proton beam parameters downstream of the target station. Those protons that do not pass through the full target volume will have a higher momentum downstream of the target, and therefore deposit more energy in the SING target. It is obvious that changes in the geometry to enhance pion or surface muon production will have some effect on the proton beam, but the greatest concern was focused on maintaining beam intensity and divergences, i.e. the transmitted beam power.

The total proton momentum downstream of the target station for each target geometry is shown in Figure 4.35 and it is clear that each geometry has a slightly different effect. The grooved target allows parts of the proton beam to completely bypass the target volume, leading to the high momentum tail. The fork target has two effects: one where the proton beam passes through the upstream section and is then scattered into one of the downstream sections, which results in the low momentum tail, and a second effect where the proton beam hits the a downstream section and then is scattered into the empty region between the sections, effectively only passing through a small total length of target material. The trapezoidal target has the largest high momentum tail due to the overall material length being less at the outer edges of the target. The slab target also has two effects: primarily from protons that scatter in the direction of the target rotation, thereby effectively increasing the length of material the proton traverses and secondly from protons that scatter away from the target rotation direction, reducing the effective material length. This effect is proportional to  $\frac{\sin(\theta)}{\sin(\theta-\phi)}$ , for a target rotation angle  $\theta$  and proton scattering angle  $\phi$ . For positive scattering angles in the direction of the target rotation, this leads to an increased effective target length, whereas for negative scattering angles this results in a reduced effective target length. Since most scattering angles are small, this effect is minimal. The proton beam power downstream of the target for each target geometry is listed in Table 4.8. The slab target has the best performance relative to the standard target geometry, with minimal excess loss in energy and no additional transmitted energy combined with the largest muon yield gain.

Table 4.8: The proton beam power downstream of the target for each target geometry.

Target Geometry	Beam Power @ 2.2 mA [MW]	Relative to Standard [ $\times 10^{-4}$ ]
Standard	1.24991	-
Grooved	1.24994	0.24
Trapezoidal	1.25114	9.84
Fork	1.24918	-5.84
Slab	1.24979	-0.96

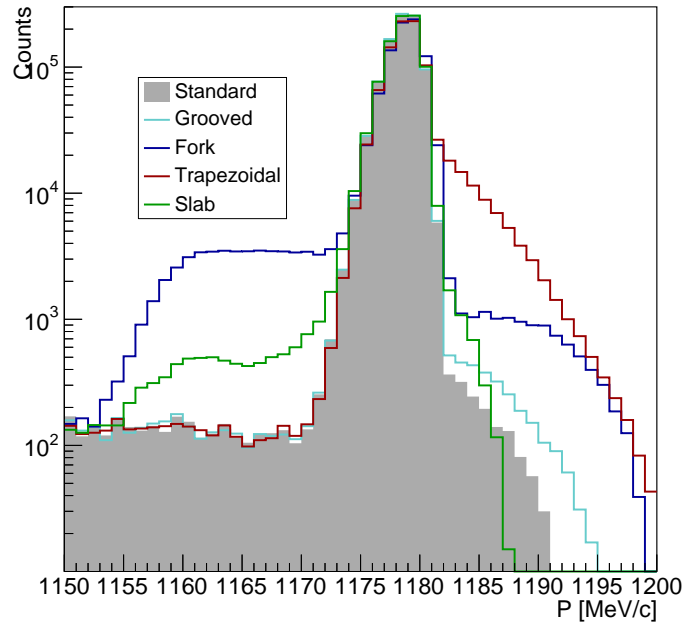


Figure 4.35: The total proton momentum downstream of the target station for various target geometries. Maintaining the proton beam power while simultaneously minimizing any additional energy downstream of the target is critical to maintaining SINQ operations and safety.

## 4.5 Alternate Materials

The surface muon rate is effectively determined by the pion stop density and the muon range for a given target material. The contribution of these quantities in relation to the relative surface muon yield for an equivalent length target is given by

$$\begin{aligned} \text{Relative } \mu^+ \text{ Yield} &\propto \pi^+ \text{ Stop Density} \times \mu^+ \text{ Range} \times \text{Relative Target Length} \\ &\propto n \cdot \sigma_{\pi^+} \cdot \left( \frac{dE}{dx} \right)_{\pi^+} \times \left( \frac{dE}{dx} \right)_{\mu^+}^{-1} \times \frac{\rho_C (Z/A)_C}{\rho_x (Z/A)_x} \end{aligned} \quad (4.8)$$

The pion yield is proportional to the atomic number density ( $n$ ) times the pion production cross section ( $\sigma_{\pi^+}$ ) as shown in Appendix A. The pion production cross section scaling with atomic number  $Z$  is

$$\begin{aligned} \sigma_{\pi^+}(2 \leq Z < 12) &= \sigma_{12}(T_p) (Z/6)^{1/3} (0.77 + 0.039Z) \\ \sigma_{\pi^+}(Z > 11) &= \sigma_0(T_p) Z^{1/3} \\ \sigma_{\pi^+}(Z = 1) &= \sigma_1(T_p) \end{aligned} \quad (4.9)$$

where  $\sigma_0$ ,  $\sigma_1$ , and  $\sigma_{12}$  are parameterization coefficients depending on the initial proton energy. The pion yield multiplied by the pion stopping power ( $\frac{dE}{dx}$ ) is therefore proportional to the pion stop density. The pion stopping power scales linearly with  $Z$ , whereas the muon range is inversely proportional to the stopping power and therefore scales as  $\frac{1}{Z}$ . The target length is also scaled by  $(\rho \frac{Z}{A})^{-1}$  such that the proton beam sees the same surface electron density and maintains beam losses similar to the current target and is given by the following,

$$t_x = t_C \frac{\rho_C (Z/A)_C}{\rho_x (Z/A)_x} \quad (4.10)$$

where  $t_C$  is the target length in carbon,  $\rho_C$  is the nominal Target E graphite density,  $\rho_x$  and  $(Z/A)_x$  is the new target material density and atomic number to mass ratio respectively. It should be noted that this scaling is an approximation to the effect of energy loss through the medium using the dominant material parameters relationship in the Bethe-Bloch equation.

Due to the similar masses of the pion and muon and similar energies in relation to surface muon production, the energy loss portions will effectively cancel. Together, this results in a relative muon yield that scales as  $Z^{-2/3}$ . The pion yield as a function of atomic number is shown in Figure 4.36, where the main structure is dominated by the number density of the material. The relative surface muon yield as a function of atomic number is also shown in Figure 4.36, for the case that the target material budget must be maintained.

It is evident that the lowest  $Z$  materials result in the highest surface muon yield for targets that maintain the proton beam parameters, i.e. material budget. Most materials below carbon would be rather technically difficult to consider as a meson production target, either due to chemical reactivity, environmental concerns, or the need for an enclosing volume. One material that shows promising results is Boron Carbide ( $B_4C$ ) which has an effective atomic number of 5.2, lower than carbon, and subsequently a higher surface muon yield. Initial studies have shown a 10% improvement for  $B_4C$  over the current Carbon graphite target. Another material considered is Beryllium Carbide ( $Be_2C$ ) with an effective atomic number of 4.67, lower than both carbon and  $B_4C$ . Initial studies for  $Be_2C$  have shown a 14% improvement relative to Carbon. Some material properties for Carbon,  $B_4C$ , and  $Be_2C$  are listed in Table 4.9.

Material	Density [g/cm <sup>3</sup> ]	Melting Point [K]	Thermal Conductivity @1000 K [W/mK]	Equivalent Target Length [mm]
Carbon	1.84	4600	83.6	40.0
$Be_2C$	1.90	2150	2.8	41.5
$B_4C$	2.52	3036	8.5	31.0

Table 4.9: Material properties for Carbon,  $B_4C$ , and  $Be_2C$  relevant to the use as a meson production target. [60, 61, 62, 63, 64]

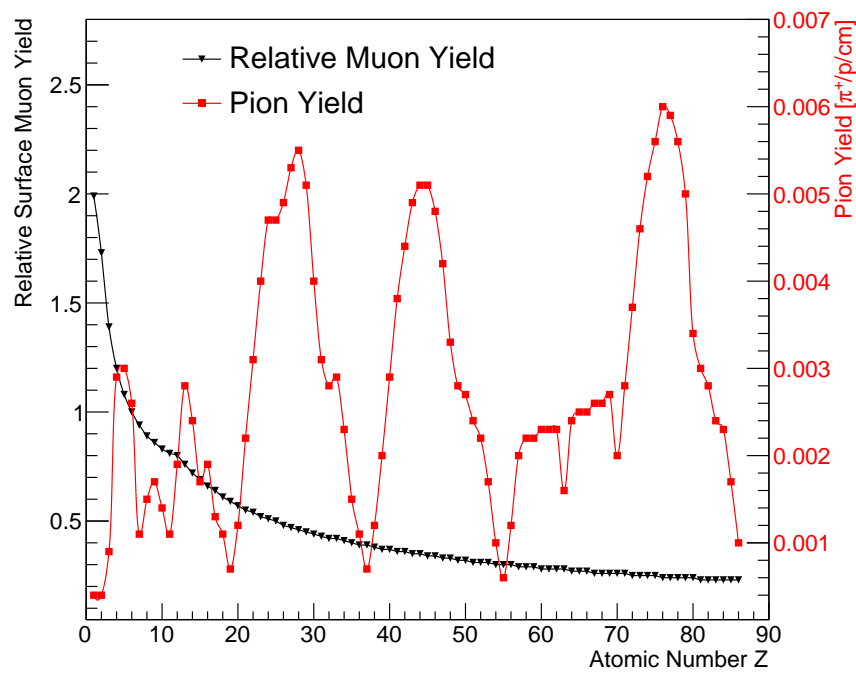


Figure 4.36: The pion yield and normalized surface muon yield for a proton energy of 585 MeV relative to carbon as a function of atomic number  $Z$ . Due to the constraint of maintaining the proton beam parameters downstream of the target, lower  $Z$  materials yield more surface muons. The discontinuity in the black points at  $Z = 12$  is a result of the piecewise parameterization of the pion production cross section.

## 4.6 Summary

The pion production cross sections from models employed by GEANT4 show large differences to measured data from meson production facilities by up to a factor of 10. A new model was developed to overcome these discrepancies by parameterizing the data currently available. This model was then used to fully characterize the current meson production target at PSI, Target E, in the context of normalization to the new High Intensity Muon Beam (HiMB) currently under development. Additionally, a full geometry and material optimization of Target E was undertaken resulting in enhancements to the surface muon rates in the beamlines surrounding Target E. Investigation of the rotated slab target geometry has shown, in simulation, rate enhancements between 30-60% depending on beamline and target orientation. An analysis of target materials showed that given the constraints on maintaining the proton beam phase space and losses downstream of the target, the lowest  $Z$  materials yield the highest number of surface muons. Additional enhancement to these rates is expected from a material choice of low  $Z$  carbides such as  $B_4C$  or  $Be_2C$  yielding an additional 10-14%. Further careful study is required to understand complications arising from the additional energy and radiation deposition in the target and vicinity. Nevertheless, the simulations for a new target design have shown surface muon yield enhancements equivalent to raising the current proton beam intensity from 2.2 mA to between 2.9-3.5 mA depending on orientation.

---

## Beam-Correlated Backgrounds in the Mu3e Experiment

---

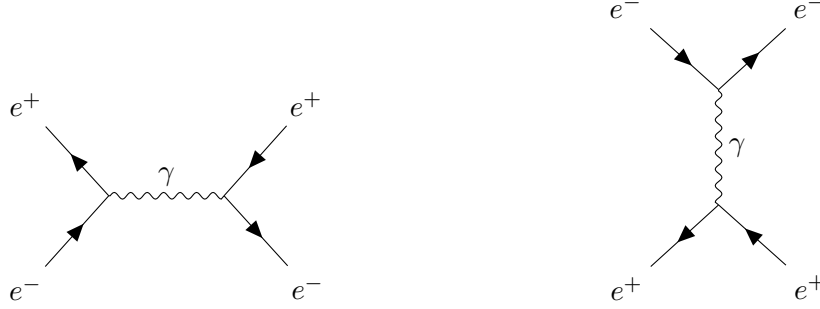
The success of the Mu3e experiment and the ability to achieve the final sensitivity goal relies on the reduction of background events in the detector volume. The two categories of backgrounds in the experiment, irreducible and accidental, are described in Chapter 3 and of principle concern to the beam delivery is the contribution from accidentals which scale with beam intensity. Positrons and pions are created in the primary production target and transported to the experiment as an undesired contamination to the muon beam and therefore significant effort has been devoted to the measurement and reduction of these particle rates and estimating their impact on the sensitivity of the Mu3e experiment.

### 5.1 Background Production from the Muon Beam in Mu3e

Reduction of backgrounds is paramount for high sensitivity searches such as Mu3e, and to eliminate combinatorial background events, excellent timing and vertex resolutions on individual tracks are required. Moreover, reducing or eliminating the positrons that contribute to Bhabha scattering is a way of further reducing background events. The production of positrons from the standard Michel decay  $\mu^+ \rightarrow e^+ \bar{\nu}_\mu \nu_e$  is a main process contributing to accidental backgrounds, but does not directly produce the negatively charged electron necessary for the  $\mu^+ \rightarrow e^+ e^- e^+$  signal. Therefore, Michel positrons can contribute to backgrounds when reconstructed in combination with other processes that do produce negatively charged tracks, such as radiative muon decay with  $\gamma$  conversion, Compton scattering, or  $e^+ e^- \rightarrow e^+ e^-$  scattering with electrons in the target material from either Michel positrons or positrons delivered with the muon beam (beam positrons). These beam positrons originate in the production Target E and are time correlated with the proton RF structure. Neutral pions are created in the target through proton beam interaction, and immediately decay within the target volume due to their  $8.52 \cdot 10^{-17}$  second lifetime. The decay modes and corresponding branching fractions of the  $\pi^0$  are listed in Equation (5.1). The dominating decay modes produce one or two photons, and within the material of the target these quickly convert to  $e^+ e^-$  pairs. Therefore up to two positrons are created in  $\pi^0$  decays.

$$\begin{aligned}
\Gamma(\pi^0 \rightarrow \gamma\gamma) &= 98.823 \pm 0.034 \% \\
\Gamma(\pi^0 \rightarrow \gamma e^+ e^-) &= 1.174 \pm 0.035 \% \\
\Gamma(\pi^0 \rightarrow e^+ e^- e^+ e^-) &= 3.34 \pm 0.16 \cdot 10^{-5} \% \\
\Gamma(\pi^0 \rightarrow e^+ e^-) &= 6.46 \pm 0.33 \cdot 10^{-8} \%
\end{aligned} \tag{5.1}$$

The  $e^+e^-$  scattering process was originally described by H. J. Bhabha in 1935 [65] and the Feynman diagram for this Bhabha scattering is shown in Figure 5.1. Bhabha scattering is the dominant background process in Mu3e, involving two Michel positrons, and therefore any additional sources of Bhabha scattering such as beam positrons will further increase the background rate in the experiment.



(a) Feynman diagram for the s-channel annihilation contribution to  $e^+e^-$  Bhabha scattering.

(b) Feynman diagram for the t-channel scattering contribution to  $e^+e^-$  Bhabha scattering.

Figure 5.1: The Feynman diagrams for s- and t-channel contributions to Bhabha scattering.

The derivation for the differential cross section for unpolarized  $e^+e^-$  scattering in the laboratory frame to leading order can be found in [66] and is given by the following

$$\left(\frac{d\sigma}{d\Omega}\right)_{lab} = \frac{m_e^4}{\pi^2} \frac{\cos^2 \theta'_1}{(E + m_e - (E - m_e) \cos^2 \theta'_1)^2} |M_{fi}|^2 \tag{5.2}$$

where  $E$  is the incoming positron energy,  $\theta'_1$  is the scattering angle, and  $|M_{fi}|^2$  is the electron-positron scattering matrix element. The scattering matrix element can be expressed using Mandelstam variables  $s$ ,  $t$ , and  $u$  by the following expressions,

$$|M_{fi}|^2_{Bhabha} = (4\pi)^2 e^4 \frac{1}{8m_e^4} \left( \frac{1}{t^2} \bar{A}_{sc} + \frac{1}{s^2} \bar{A}_{an} - \frac{1}{ts} \bar{A}_{in} \right) \tag{5.3}$$

and

$$\bar{A}_{sc} = (u - 2m_e^2)^2 + (s - 2m_e^2)^2 + 4m_e^2 t \quad (5.4)$$

$$\bar{A}_{an} = (u - 2m_e^2)^2 + (t - 2m_e^2)^2 + 4m_e^2 s \quad (5.5)$$

$$\bar{A}_{in} = - (u - 2m_e^2) (u - 6m_e^2) \quad (5.6)$$

where  $\bar{A}_{sc}$  is the matrix element contribution from scattering (t-channel),  $\bar{A}_{an}$  is the matrix element contribution from annihilation (s-channel), and  $\bar{A}_{in}$  is the matrix element contribution from interference.

Pion decays such as  $\pi^+ \rightarrow e^+e^+e^-\nu_e$  and  $\pi^+ \rightarrow \mu^+\nu_\mu\gamma$  with subsequent photon conversion in the detector volume can be identical to signal events if the momenta of the final state particles sum to the invariant muon mass. Considering the small branching fractions  $\Gamma(\pi^+ \rightarrow e^+e^+e^-\nu_e) = 3.2 \cdot 10^{-9}$  and  $\Gamma(\pi^+ \rightarrow \mu^+\nu_\mu\gamma) = 2.0 \cdot 10^{-4}$ , and the low pion contamination from the beam at this momentum, negligible rates in the signal region are expected.

### 5.1.1 Bhabha Production in Mu3e

The two sources of beam correlated positrons come from muon decays either in flight or once stopped, and beam positrons transmitted along the beamline from Target E. There are four distinct combinations of a Bhabha pair with a positron that leads to a  $e^+e^-e^+$ -like signal in the detector volume. The following notation is used to differentiate between beam positrons and those positrons originating from muon decay,

- $e_B^+ \longleftrightarrow$  beam positron
- $e_\mu^+ \longleftrightarrow$  Michel positron, from muon decay

**Process A**, the combination of a Michel positron with a Bhabha pair from an additional Michel positron has been studied extensively in preparation of the Mu3e Technical Design Report and is shown in Figure 5.2. The maximum energy of the Michel positron, coming from a stopped muon, is 52.83 MeV, and any Michel positron undergoing Bhabha scattering can lead to a  $e^+e^-$  invariant mass of 52.83 MeV. Therefore the invariant mass of a Michel positron combined with a Bhabha pair coming from another Michel positron is exactly the muon mass. This process is an irreducible background, and requires excellent vertex and timing resolution to reject.

**Process B** involves the overlap of a Michel positron with a Bhabha pair coming from an incident beam positron and is shown in Figure 5.3. As before the maximum energy of the Michel positron is 52.83 MeV, but the beam positron has the same momentum as the incident muon beam, and therefore has an energy of approximately

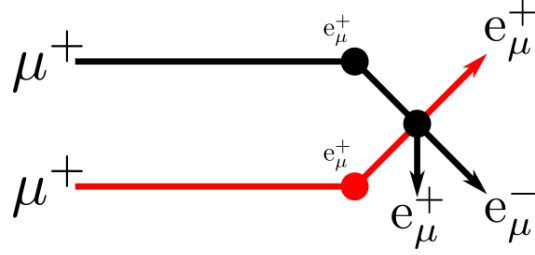


Figure 5.2: **Process A** - The combination of a Michel positron with a Bhabha pair from an additional Michel positron.

28 MeV. At  $3\sigma$  of the nominal CMBL momentum byte, the beam positron energy is 30.6 MeV. If this high energy beam positron undergoes Bhabha scattering, and overlaps with a Michel positron of 52.8 MeV, the invariant mass is  $83.4 \text{ MeV}/c^2$ , much less than the muon mass and well outside the expected resolution of the Mu3e spectrometer. Nevertheless, if instead the positron originates from a muon decay-in-flight, the Michel positron will receive a boost in the lab frame. Due to the decay asymmetry of the muon, the positron is preferentially emitted in the direction of the muon spin. Using the inverse Lorentz boost, the positron energy in the lab frame is given by the following,

$$E_e^{\text{lab}} = \gamma_\mu (E_e^{\text{com}} + \beta_\mu P_e^{\text{com}}) \quad (5.7)$$

where  $\gamma_\mu$  is the muon Lorentz factor,  $\beta_\mu$  is the muon velocity,  $E_e^{\text{com}}$  and  $P_e^{\text{com}}$  are the positron energy and momentum in the center of mass frame, respectively. For a spin polarized surface muon at the kinematic edge,  $P_\mu = 29.79 \text{ MeV}/c$ , decaying in flight and the positron being emitted in the forward direction, this results in a maximum positron energy of  $P_e^{\text{lab}} = 69.79 \text{ MeV}/c$ . Therefore the invariant mass of a decay-in-flight Michel positron with a high energy beam positron is  $100.4 \text{ MeV}/c^2$ , which is nearly  $5\sigma$ , in terms of the reconstruction mass resolution, from the muon mass and at the edge of the acceptance to the signal region.

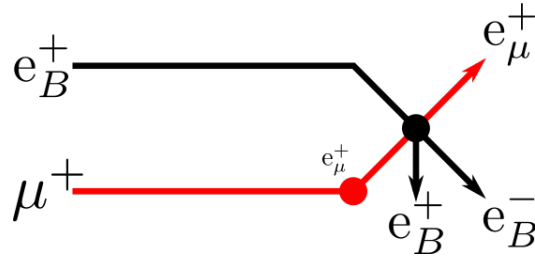


Figure 5.3: **Process B** - The combination of a Michel positron with a Bhabha pair coming from an incident beam positron

**Process C** involves the overlap of two beam positrons, where one undergoes Bhabaha scattering and is shown in Figure 5.4. This process is possible, but

from the maximum energy of beam positrons, the invariant mass of this interaction ( $61.2 \text{ MeV}/c^2$ ) lies far outside the signal region of the Mu3e experiment.

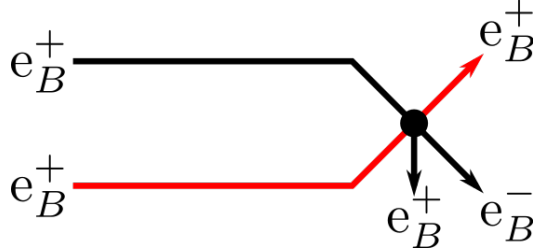


Figure 5.4: **Process C** - The combination of two beam positrons, where one undergoes Bhabha scattering

The final combination, **process D**, is analogous to process B and involves the overlap of a beam positron with a Michel positron originating from a stopped muon, that subsequently undergoes Bhabha scattering. This process is shown schematically in Figure 5.5. The invariant mass from a Michel positron at the maximum energy of the Michel spectrum with a high energy beam positron is again  $83.4 \text{ MeV}/c^2$  and well outside the kinematic constraints for  $e^+e^-e^+$ -like events. Again, if the Michel positron originates from a muon decay-in-flight and then undergoes Bhabha scattering in the nearby material, the maximum invariant mass of the  $e^+e^-$  pair is  $69.79 \text{ MeV}/c^2$ . If this Bhabha pair overlaps with a high energy ( $30.6 \text{ MeV}/c$ ) beam positron, the maximum invariant mass of the  $e^+e^-e^+$  from a decay-in-flight Michel positron with a high energy beam positron is  $100.4 \text{ MeV}/c^2$

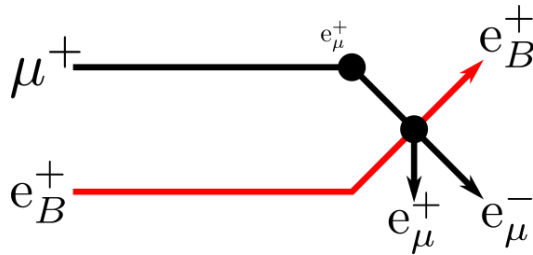


Figure 5.5: **Process D** - The combination of a beam positron with a Michel positron that undergoes Bhabha scattering

## 5.2 The $\pi E5$ Channel

The  $\pi E5$  beam channel begins in the region of Target E with the dipole magnet AHSW41 that momentum selects charged particles originating from the production

target and towards  $\pi E5$  at  $165^\circ$  relative to the longitudinal axis of the primary proton beam. The next section of the beamline consists of eight quadrupoles and four sextupoles as well as one vertical and two horizontal slit systems that further shape and define the beam “momentum-byte”. Two sequential dipoles magnets AST41 and ASC41 direct the beam to the Z-branch of  $\pi E5$  and provide additional momentum selection. This front section of the beamline is described in Section 3.2 and a schematic drawing is shown in Figure 3.4 A 195 kV  $E \times B$  Wien Filter (SEP41) is situated between two quadrupole triplets (TI and TII) and provides the ability to separate particles of equal momentum based on velocity differences. Downstream of TII is a circular lead collimator system with 120 mm inner diameter, placed at an optical double focus of the beam and intended to remove undesired particles from the beam. From this position the beamline is connected to either the MEG COBRA spectrometer magnet via the superconducting Beam Transport Solenoid (BTS) or to the Mu3e solenoid via a newly developed beamline extension. The  $\pi E5$  beamline layout in the MEG II configuration is shown in Figure 5.6, extending from Target E to the MEG COBRA spectrometer magnet.

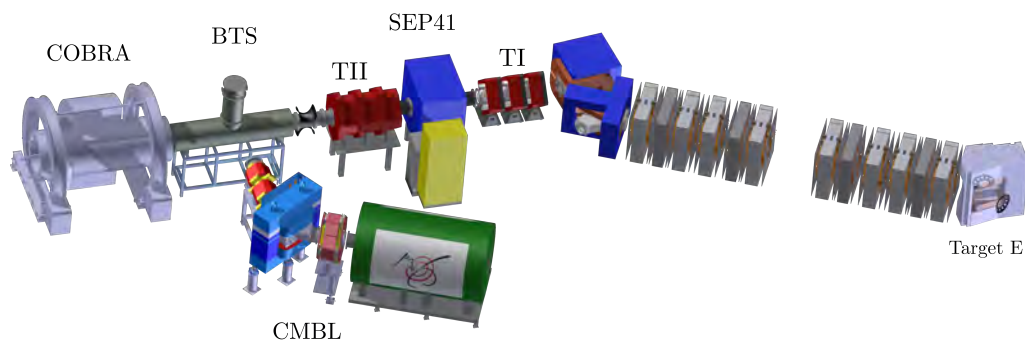


Figure 5.6: The  $\pi E5$  beamline, MEG beamline elements, and Mu3e extension in the MEG configuration.

### 5.2.1 The Compact Muon Beamline

The Mu3e Phase-I experiment will require muon intensities  $\mathcal{O}(10^8)$  muons per second and therefore the  $\pi E5$  channel at PSI is the only facility in existence delivering these rates as a continuous source. The  $\pi E5$  beam channel and experimental area has been dedicated almost exclusively to the MEG experiment including permanent infrastructure installed in the rear area of  $\pi E5$ . In the future, this beam channel and some associated infrastructure will be shared with the Mu3e experiment. In order to minimize downtime during operational switchover between the MEG II and Mu3e experiments, a new Compact Muon Beamline (CMBL) has been developed to allow for the coexistence of MEG II and Mu3e in the  $\pi E5$  area. For an extensive overview on the development of the CMBL, see the thesis by F. Berg [43].

The CMBL exists as an extension to the existing  $\pi E5$  and MEG beamline elements, including the two quadrupole triplets TI and TII, the Wien filter SEP41, and 120 mm collimator system. This compact beamline allows the 3.2 m long Mu3e solenoid to be placed in the front part of the  $\pi E5$  area. Beginning at the collimator, a  $90^\circ$  dipole bending magnet ASL41 replaces the BTS, and the next four beamline elements together form a “split triplet” solution via a quadrupole doublet QSO41 and QSO42, a  $65^\circ$  dipole ASK41, and the final quadrupole singlet QSK41 leading to the injection of the Mu3e solenoid. Figure 5.7 shows the final layout of the CMBL along with the Mu3e solenoid.

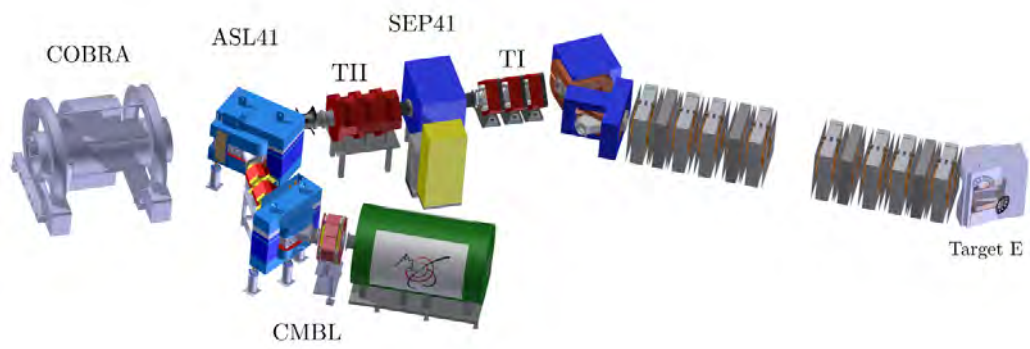


Figure 5.7: The  $\pi E5$  beamline, MEG beamline elements, and Mu3e extension in the CMBL configuration.

### 5.3 Simulation of $\pi$ E5 Channel

Simulation of the  $\pi$ E5 channel in the context of estimating the muon rate and associated positrons and pions is divided in two parts, production and transport. The first simulation begins with protons hitting the primary production target with a total of  $10^9$  protons simulated corresponding to approximately 0.16 nA·s. Obviously this is only a small fraction of the nominal 2.2 mA proton current delivered by HIPA, but nonetheless it is adequate to estimate particle rates at the end of the  $\pi$ E5 channel. The second simulation is primarily focused on optimizing the beamline elements for muon transmission to the Mu3e solenoid. Finally, the transmission efficiency, phase space, and rate of muons, positrons, and pions from production to injection to the Mu3e solenoid can be estimated. It is important to note these simulations are done with the standard 40 mm long Target E, whereas the measurements of the beam were conducted using a 60 mm long target.

#### 5.3.1 Muon and Positron Production at Target E

The production simulation at Target E was done using the HiMB parameterized model described in Chapter 4 and Appendix A. A large 300 mm radius virtual detector was placed 150 mm downstream of Target E in the direction of the  $\pi$ E5 channel, upstream of the AHSW41 dipole bending magnet. This virtual detector collects all muons, positrons, and pions exiting the target with longitudinal momentum centered around the  $165^\circ$  direction relative to the proton beam axis. The AHSW41 current was set to the nominal 97.5 A to optimally select surface muons at 28 MeV/c. A plot of the rates per second versus momentum of positive charged particles at Target E, in the direction of  $\pi$ E5, is shown in Figure 5.8, normalized to 2.2 mA of proton beam current. An equivalent plot for negative charged particles is shown in Figure 5.9, but since the HiMB model only applies to positive pions these spectra were generated using the BIC physics model [67]. In Figure 5.8, one sees a peak at 30 MeV/c in the muon spectrum, corresponding to the surface muons. Additionally, the positron spectrum has two main components, the Michel spectrum extending to 53 MeV/c and the continuum that decreases with momentum corresponding to beam positrons produced from  $\pi^0$  decays. From Figure 5.8 the surface muon rate reaches  $10^{10}$  per second at 2.2 mA of proton beam current in the vicinity of Target E, whereas the positron rate in the same momentum region can be up to an order of magnitude higher.

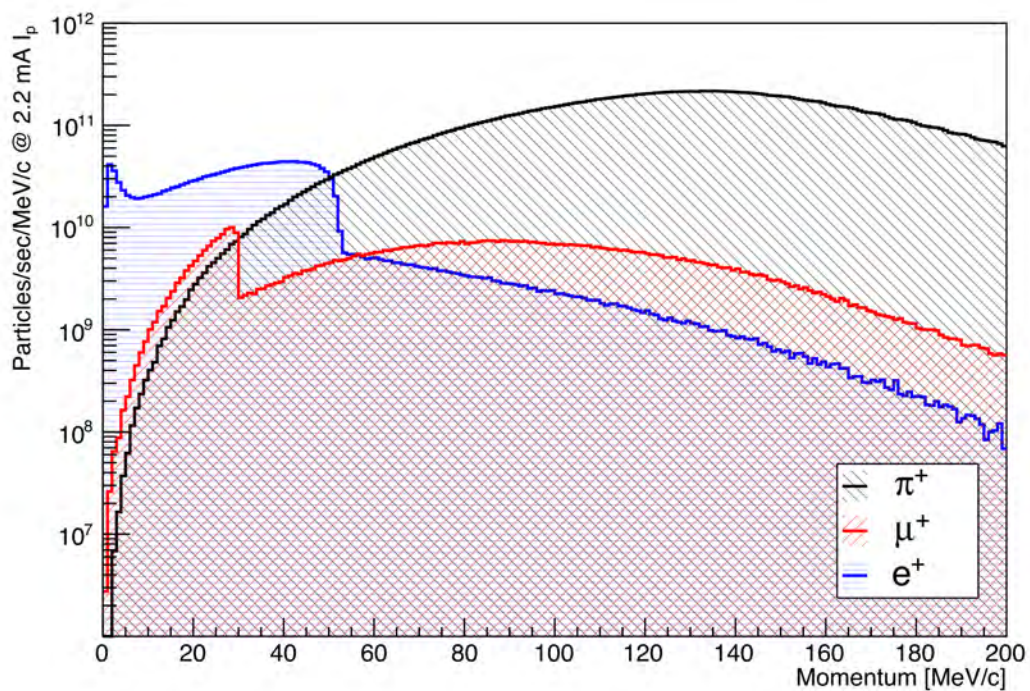


Figure 5.8: The momentum spectrum of positively charged particles produced in Target E, 150 mm downstream in the direction of the  $\pi$ E5 channel.

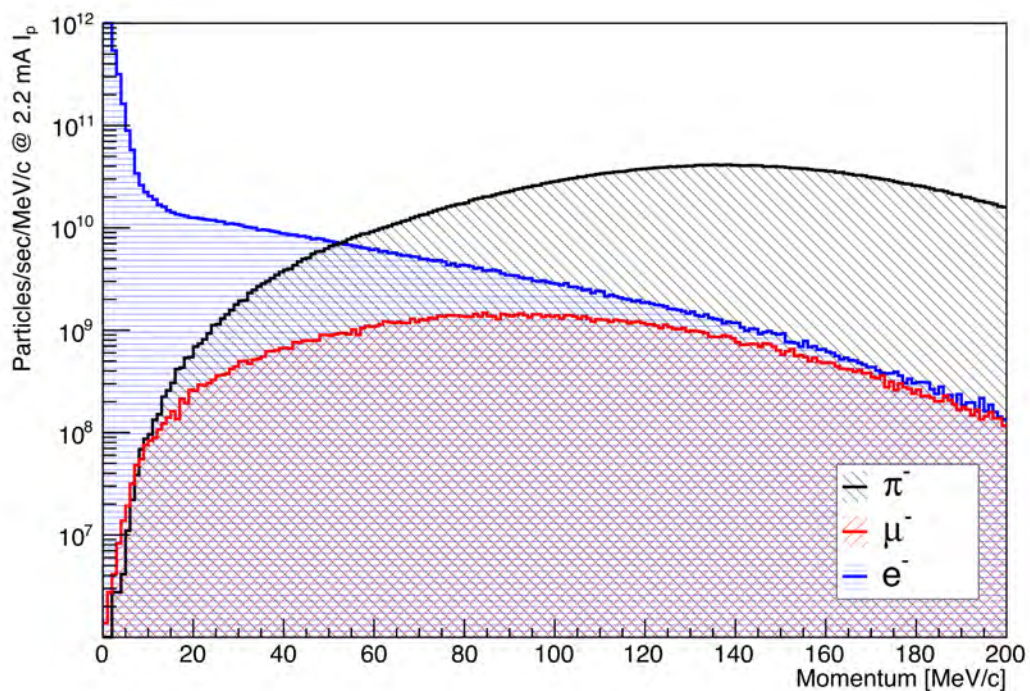


Figure 5.9: The momentum spectrum of negatively charged particles produced in Target E, 150 mm downstream in the direction of the  $\pi$ E5 channel.

### 5.3.2 Transport in the $\pi$ E5 Channel

Particles that are captured by the first few elements in the  $\pi$ E5 channel can be effectively transmitted to the end of the beamline. Since the magnetic field generated by a given magnet current is not known exactly, many elements within the channel must be tuned to optimize transmission. This can be a very time consuming and CPU intensive process requiring many iterations to converge to a solution. In order to achieve a good compromise between optimization and expediency, the first section of the channel from the AHSW41 and the eight quadrupoles and four sextupoles of  $\pi$ E5 are set to the current values found during the optimization of the true beamline during the MEG setup. This leaves the two dipole magnets AST41 and ASC41, the two triplets TI and TII, and the CMBL available for optimization.

The optimization of the  $\pi$ E5 channel uses only muons originating from Target E in the momentum band  $0 < P_\mu < 40$  MeV/c, no emphasis is placed on reducing other particle rates. Furthermore, the optimization is done in segments such that the solution can be guided in a desired way. For instance, the AST41 - ASC41 optimization can be applied to an infinite number of solutions since one dipole can compensate for the other. A starting point for the dipole optimization was achieved by utilizing the built-in G4BL tune command, requiring the transverse beam momentum to be minimized at the exit of the ASC41 and the distance from the optical axis of the reference 28 MeV/c  $\mu^+$  particle minimized at a point several meters downstream at the collimator. Tuning of the beamline was then carried out using the full muon beam generated from Target E and optimizing for rate on a virtual detector placed at critical locations along the beamline. Further iterations of the optimization routine progressively included additional downstream elements, the elements included in each iteration and the optimization position are listed in Table 5.1.

Beamline Elements Optimized	Initial Beam Position	Optimization Position
AST41, ASC41	Target E	collimator
TI	Target E	collimator
TI,TII	Target E	collimator
TII,SML41,CMBL	DS TI	Mu3e Injection

Table 5.1: Positions and beamline elements included for the several stages of optimization of the  $\pi$ E5 channel.

### 5.3.3 Estimated Background Rates from Simulation

The rates of positrons reaching critical points along the beamline can be estimated in the simulation beginning with protons on Target E producing muons, positrons,

and pions and transmitting them through the  $\pi$ E5 channel and CMBL. Additionally, a certain percentage of the muons traveling down the beamline will decay before reaching the measurement point, producing Michel positrons.

Following the initial loss at QSF41, the muon loss throughout the beamline to the Mu3e injection leads to an approximate 10% transmission. The positions of greatest loss are at the FSH42 slit system, the AST41/ASC41 dipoles, and downstream of the ASL41. The transmission of muons from Target E to the Mu3e solenoid injection is shown in Figure 5.10 as well as the mean position and sigma width. The majority of losses occur in the first few elements and are associated with the phase space acceptance of  $\pi$ E5 channel, the additional losses in the vicinity of the FSH42 are associated with the fact that the upstream  $\pi$ E5 elements have not been optimized for transmission and can therefore be expected. The large fluctuations in  $\bar{x}$  and  $\sigma_x$  near AST41 and ASC41 are artifacts due to tracking deficiencies of G4BL z-ntuples through nearby corner arcs. The  $\bar{y}$  is especially stable through the length of the channel, with minimal deviation through SEP41.

The transmission of positrons from Target E to the Mu3e solenoid injection is shown in Figure 5.11a and shows three orders of magnitude reduction of positrons reaching the final focus of the CMBL. The beam positron loss through the  $\pi$ E5 channel up to the SEP41 is nearly identical to the muon loss. The majority of positrons created in the region near the Target E are not captured by the  $\pi$ E5 channel, and therefore to reduce the size on disk of the initial positron beam used in the simulation, only the positrons that make it to the entrance of QSF41 are recorded. The same method is not applied to muons, since the muon rate is many times less than the positrons. Thus, the significant difference in initial beam content is due to the initial positron starting location being further downstream from Target E, which includes the phase space acceptance of ASHW41. There is a 90% loss following the SEP41 and the QSK41. A further 70% loss at the collimator downstream of QSK43. The remaining losses are due to the large y-deflection angle the positron beam experiences due to being far off-axis when passing through the TII quadrupoles. The positron transmission efficiency from QSF41 to the Mu3e solenoid injection is 0.1%.

The absolute rates of pions is difficult to determine due to the short 26.03 ns lifetime of the  $\pi^+$ . At the Mu3e solenoid injection, there are zero pions detected in the simulation for  $10^9$  protons on target. This is equivalent to  $10^{11}$  protons on target using the HiMB model splitting factor of 100. A limit on the expected pion rate can be set to  $<3.45 \cdot 10^5 \pi^+/\text{sec}$  @ 90% C.L..

The final rates of all three particle types from the simulation beginning with protons hitting Target E and being transmitted independently along the  $\pi$ E5 channel and CMBL and sampled at the collimator and Mu3e solenoid injection positions are shown in Table 5.2. The rates from a second simulation including the positron-stopper placed in TII are shown in Table 5.3. The positron-stopper was a simple test solution to an

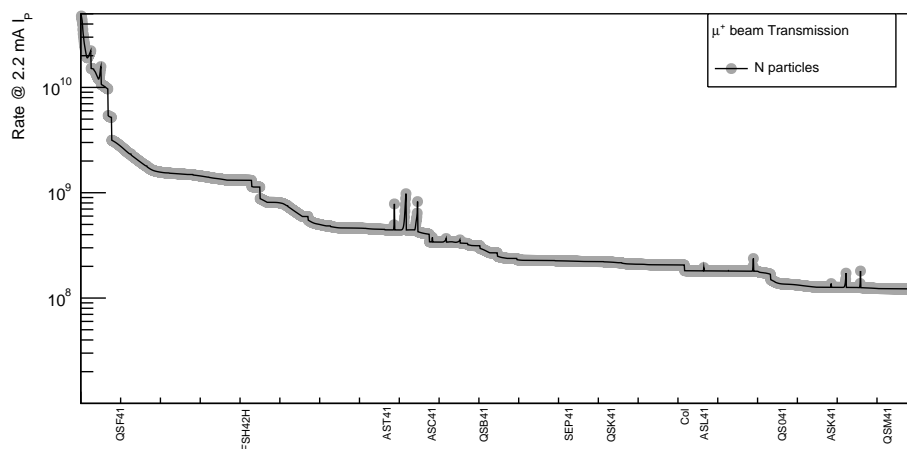
unexpected enhanced positron transmission in TII, caused by a re-centering of the off-axis beam positrons after the SEP41 Wien filter by the vertical focusing element QSK42 of TII. The positron-stopper gives approximately a 20% reduction in beam positrons transmitted to the Mu3e Injection with negligible impact on the muon rate.

	Collimator Position	Mu3e Injection
$\mathcal{R}_{\mu^+}$	$1.82 \cdot 10^8$	$1.22 \cdot 10^8$
$\mathcal{R}_{e^+}$	$8.77 \cdot 10^7$	$2.189 \cdot 10^7$
$\mathcal{R}_{\pi^+}$	$< 3.45 \cdot 10^5$ @ 90% C.L.	same

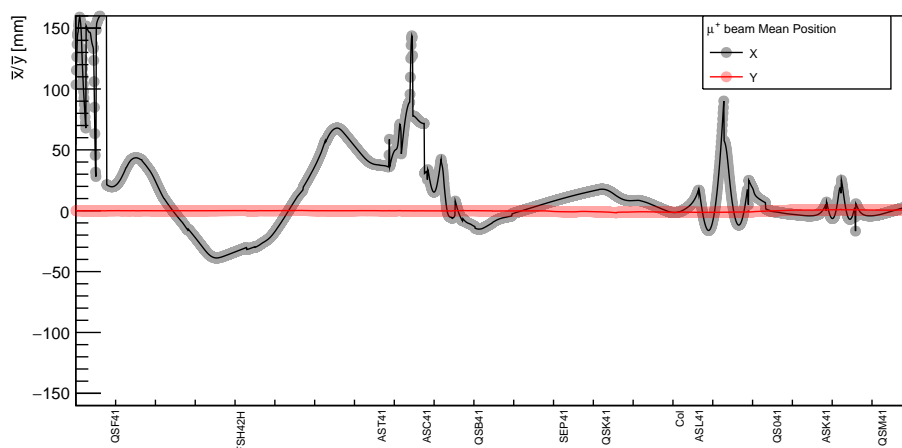
Table 5.2: Beam particle rates from simulation optimized for muon rate transmission to Mu3e Injection without  $e^+$  stopper in TII. Rates are for a 40 mm Target E normalized to 2.2 mA  $I_p$ .

	Collimator Position	Mu3e Injection
$\mathcal{R}_{\mu^+}$	$1.76 \cdot 10^8$	$1.21 \cdot 10^8$
$\mathcal{R}_{e^+}$	$4.87 \cdot 10^7$	$1.842 \cdot 10^7$
$\mathcal{R}_{\pi^+}$	$< 3.45 \cdot 10^5$ @ 90% C.L.	same

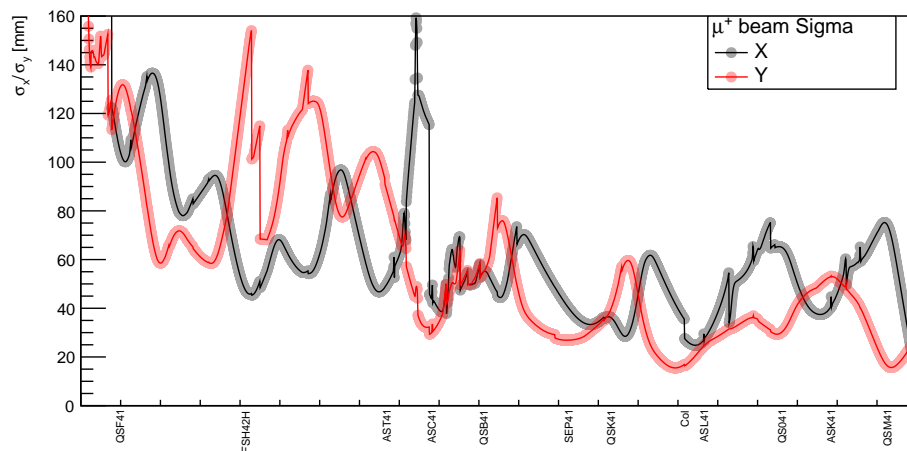
Table 5.3: Beam particle rates from simulation optimized for muon rate transmission to Mu3e Injection with  $e^+$  stopper in TII. Rates are for a 40 mm Target E normalized to 2.2 mA  $I_p$ .



(a) Muon beam rate.

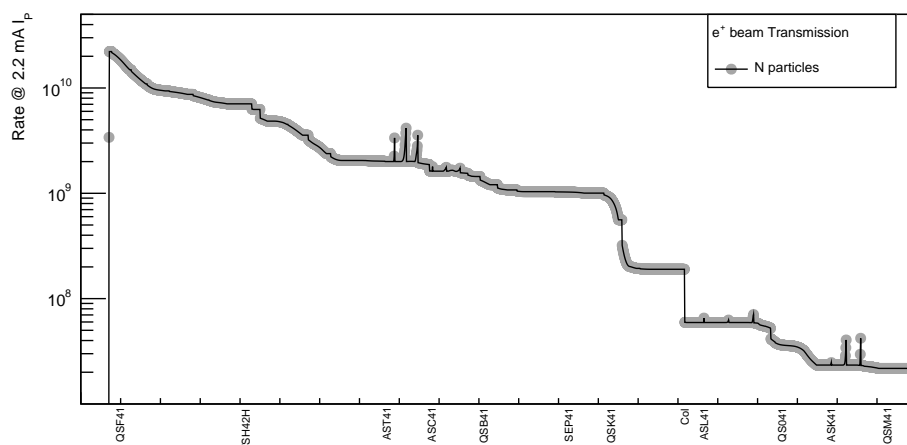
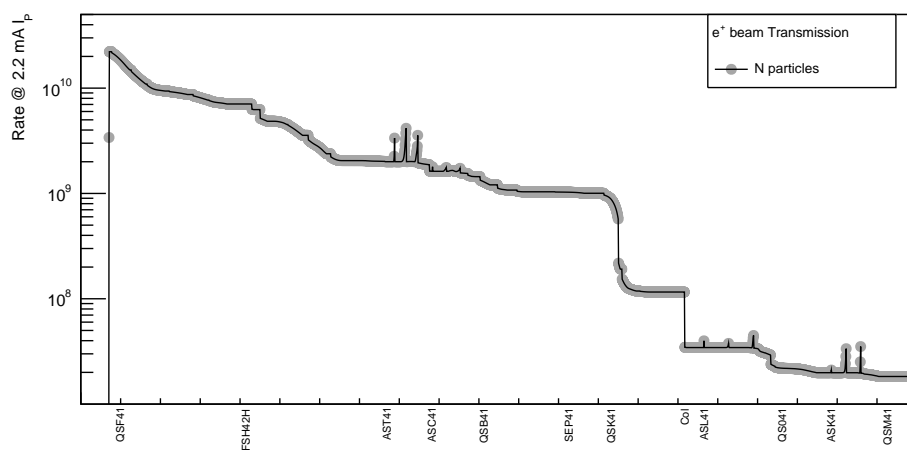


(b) Muon beam centroid position.



(c) Muon beam size.

Figure 5.10: Muon beam transmission and profile through the  $\pi$ E5 channel and CMBL.

(a) Positron transmission in the  $\pi$ E5 channel and CMBL.(b) Positron transmission in the  $\pi$ E5 channel and CMBL with the positron-stopper in TII.Figure 5.11: Positron beam transmission through  $\pi$ E5 channel and CMBL.

### 5.3.4 Modified Wien Filter

The SEP41 Wien Filter is a beamline element generating orthogonal electric and magnetic fields to deflect particles based on velocity. For typical beamline elements consisting solely of a magnetic field, the charged particles will take a circular path within the uniform field region with a radius of curvature proportional to the momentum and inversely proportional to the magnetic field, given by the following expression

$$\rho = \frac{mv}{qB} \quad (5.8)$$

where  $\rho$  is the radius of curvature,  $q$  is the electric charge,  $v$  is the particle velocity,  $m$  is the particle mass, and  $B$  is the magnetic field.

A Wien filter generates electric and magnetic fields such that the total force acting on the particle is zero for a given velocity. From the Lorentz force equation  $\mathbf{F} = q(\mathbf{E} + \mathbf{v} \times \mathbf{B})$  the total force is zero when the force from the electric field is equal and opposite to the force due to the magnetic field. A diagram with the proper field configuration for a positively charged particle and the various paths it will take based on velocity is shown in Figure 5.12. Therefore the particle velocity for which the total force acting on it is zero is given by the following

$$\begin{aligned} qv_z B_x &= qE_y \\ v_z &= \frac{E_y}{B_x} \end{aligned} \quad (5.9)$$

where  $q$  is the electric charge,  $E_y$  is the electric field component,  $B_x$  is the magnetic field component perpendicular to the electric field, and  $v_z$  is the particle velocity in the direction orthogonal to  $E_y$  and  $B_x$ .

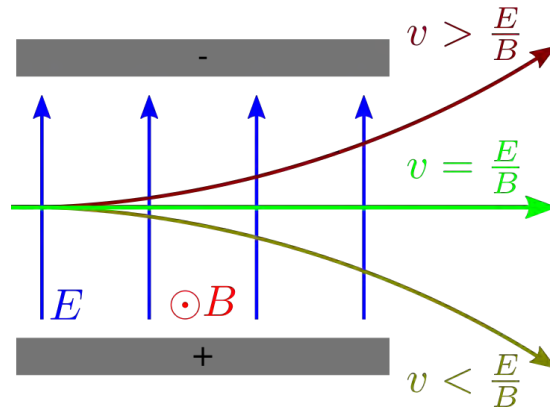


Figure 5.12: Schematic of the working principle of a Wien Filter velocity separator.

The standard SEP41 is operated with the top plate on 195 kV negative potential and the bottom plate on ground. For this field configuration, the magnetic and electric fields calculated with OPERA [68] are shown in Figure 5.13 and Figure 5.14 respectively. Within the majority of the SEP41 volume, the electric field is oriented along the y-axis, but due to the asymmetric potential there is a non-zero z-component of the electric field at the entrance and exit to the SEP41. This additional electric field component leads to an acceleration along the z-axis as the particle enters, and deceleration on exiting, the SEP41, resulting in non-optimal velocity separation. A symmetric plate configuration with equal and opposite potential on each plate will lead to a z-component cancelation and improved transmission through SEP41. This can be easily tested in the G4BL simulation by using the original fieldmap and inverting in the x-y plane and applying a negative current.

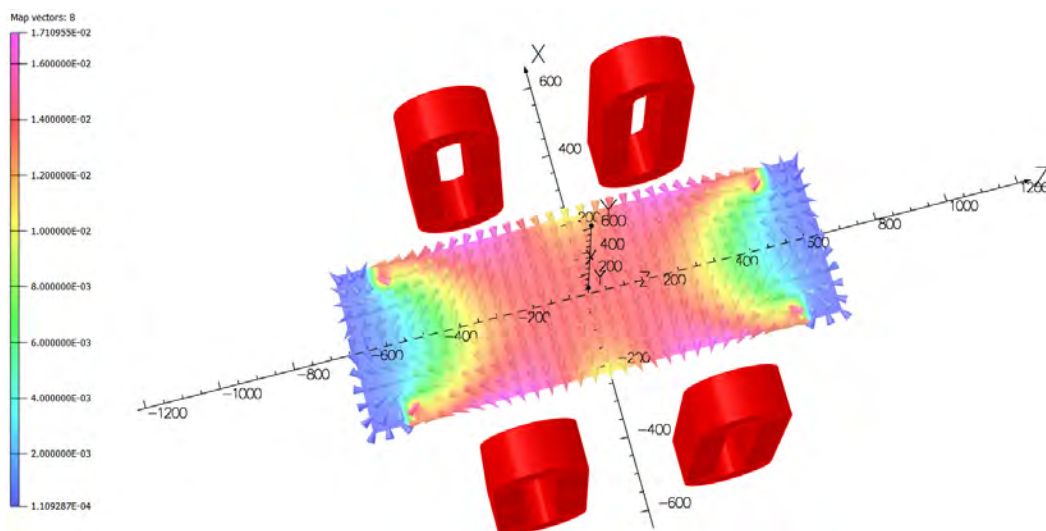


Figure 5.13: The magnetic field along the z-axis at  $y = 0$  in SEP41 calculated using OPERA.

Additionally, it was seen that the SEP41 does not provide enough separation power to force the positrons to hit the iron of QSK41. Instead the positrons enter the lower region of the quadrupole and along with deflections in QSK42 and QSK43 lead to the positrons returning to the beam axis at the collimator. The optical solution for maximum muon transmission is slightly different between MEG and CMBL configurations. The field strength of the final quadrupole magnet in the TII, QSK43, is of primary interest because in the MEG configuration, this element directs positrons not lost immediately after SEP41 into the 120 mm diameter lead collimator. This results in the effective elimination of any beam positron contamination in the MEG experiment. Since the field strength of QSK42 is slightly lower in CMBL configuration, the positrons are not lost in the collimator but are transmitted through the CMBL.

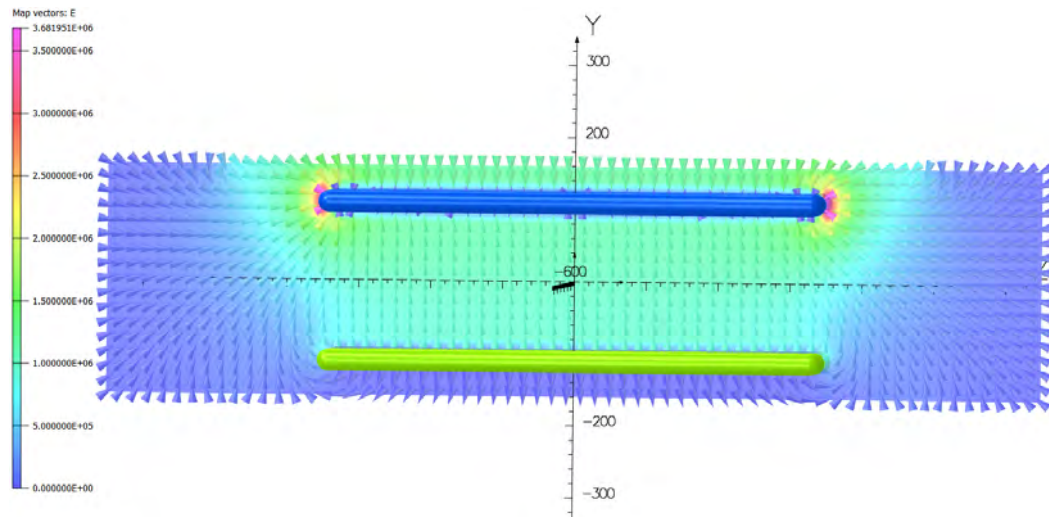


Figure 5.14: The electric field along the  $z$ -axis at  $x = 0$  in SEP41 calculated using OPERA.

The separation power in SEP41 is determined by the maximum electric and magnetic fields that can be generated. The SEP41 is limited to 200 kV potential by the high-voltage electrical configuration which only allows for a single power supply, but in the G4BL simulation higher potentials can be explored. The OPERA calculated electric field for a symmetric potential is shown in Figure 5.15. Increasing the electric field requires also increasing proportionally the magnetic field to maintain the same muon velocity selection and positron separation. The particle rates at the end of the CMBL are listed in Table 5.4, and using the configuration with a symmetric potential leads to slightly better transmission as seen in the increased muon and positron rates for the equivalent standard separation power. The rates in Table 5.4 are without optimization of downstream beamline elements, as it was assumed the effect is negligible for muons. A doubling of the electric potential with a symmetric potential results in a factor 500 reduction in positrons reaching the Mu3e solenoid injection and a slightly increased muon rate due better transmission through the separator. The beam positron rate can be effectively eliminated without the use of a lead collimator positron-stopper by introducing a symmetric potential SEP41 with a doubling of the electric potential.

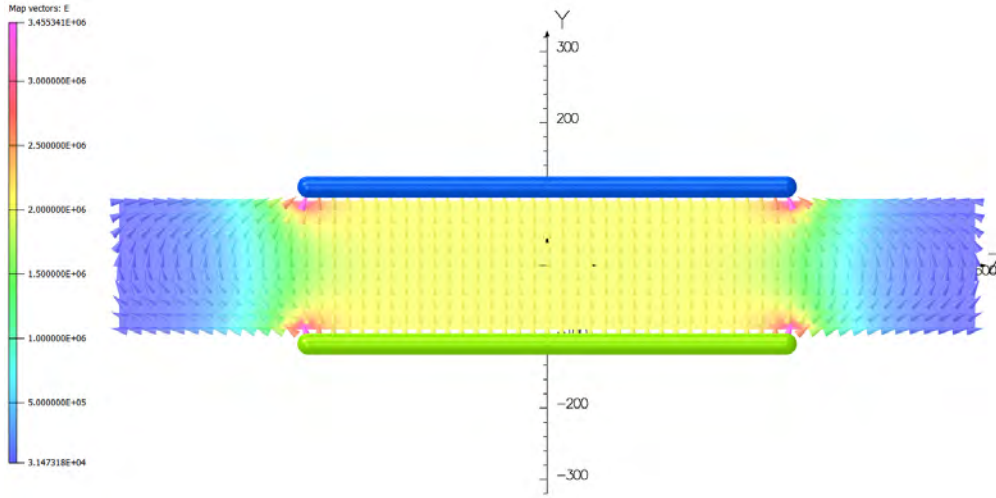


Figure 5.15: The electric field along the  $z$  axis at  $x = 0$  in SEP41 for a symmetric potential, calculated using OPERA.

	HV=195 kV $I_B=42.55$ A standard	HV=195 kV $I_B=42.55$ A symmetric	HV=292.5 kV $I_B=63.82$ A symmetric	HV=390 kV $I_B=85.09$ A symmetric
$\mathcal{R}_{\mu^+}$	$1.76 \cdot 10^8$	$1.81 \cdot 10^8$	$1.84 \cdot 10^8$	$1.86 \cdot 10^8$
$\mathcal{R}_{e^+}$	$8.77 \cdot 10^7$	$9.03 \cdot 10^7$	$2.41 \cdot 10^7$	$1.72 \cdot 10^5$

Table 5.4: Muon and Positron rates at the Mu3e Injection point with a standard, symmetric potential, and an enhanced symmetric potential SEP41.

## 5.4 Beam Measurements at the $\pi$ E5 Beamline

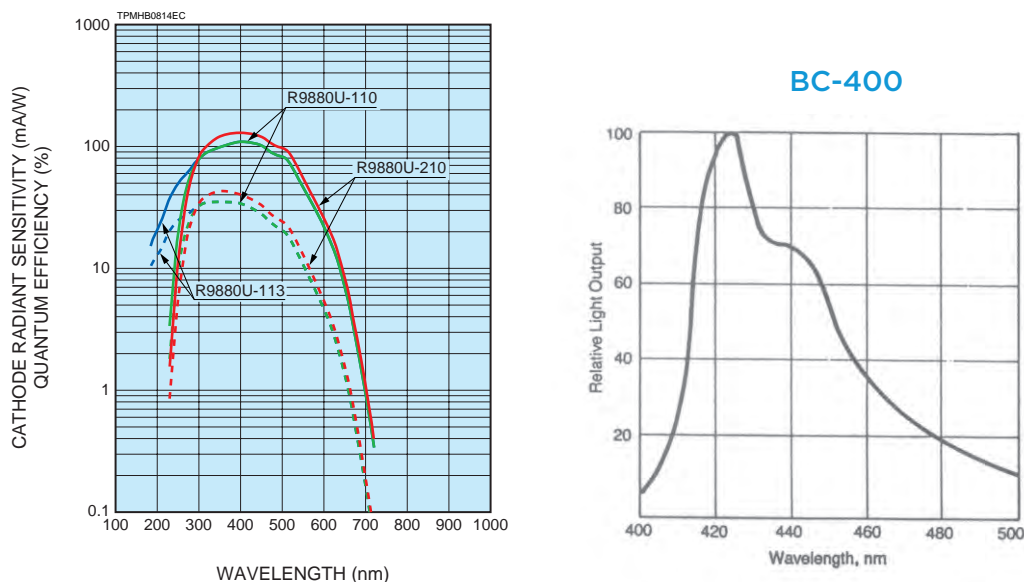
Muon beam measurements are carried out at two critical locations in the  $\pi$ E5 experimental area, to fully characterize the beam as it enters the experimental area and at the injection to the Mu3e experiment. The first location is downstream of the 120 mm diameter lead collimator, situated between QSK43 and either the BTS or ASL41 dipole magnet depending on the beamline configuration. The measurements at the collimator serve as a transmission efficiency normalization to the maximum beam rate expected as well as the contamination of the beam due to undesired positrons. The second set of measurements at the Mu3e solenoid injection yield the maximum expected rate and positron contamination expected for the Mu3e experiment. The measurement of muons and positrons at both locations is conducted with the same mini-PMT pill scanner, to minimize systematic effects associated with the detector system. A panoramic view of the front  $\pi$ E5 area in CMBL configuration is shown in Figure 5.16.



Figure 5.16: Panoramic view of the  $\pi$ E5 front area, in CMBL configuration.

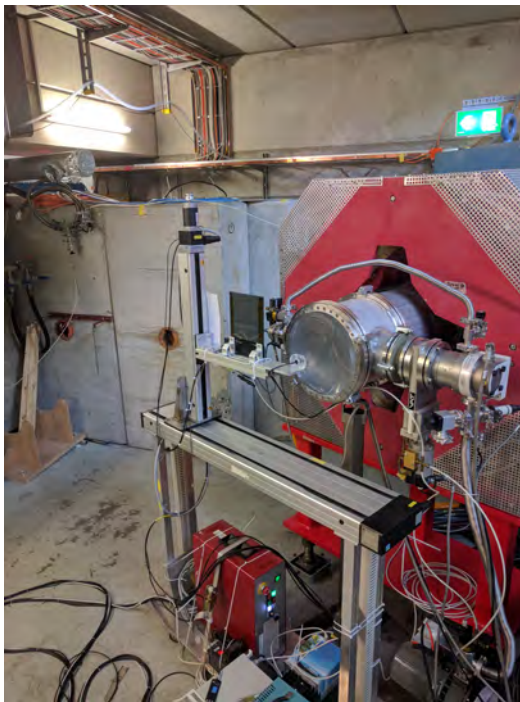
### 5.4.1 The Pill Scintillator Scanner System

Measurements of the muon and positron beams as well as optimization of the beamline are conducted using a small detector mounted on a two dimensional scanner system. The detector is a miniature photomultiplier tube with small plastic scintillator mounted to the PMT window using optical coupling grease. The PMT is a high gain, fast response, compact Hamamatsu R9880U-110 series with 10 dynode stages operated at 650 V and peak QE at 400 nm. The R9880U-110 spectral response is shown in Figure 5.17a. The scintillator is a cylindrical 2 mm thick, 2 mm diameter, NE-102A (BC-400 equivalent), general purpose organic plastic scintillator sensitive to low energy charged particles and with a peak light emission at approximately 425 nm, well matched to the PMT QE. The emission spectrum for BC-400 is shown in Figure 5.17b. The detector is mounted in acrylic glass for stability, which is then mounted on the scanner platform and placed downstream of the 190  $\mu\text{m}$  thick MYLAR beam pipe window. The scanner system is built from two linear actuators with independent spindle drive units and 0.02 mm precision, mounted orthogonally to each other. The scanner system is shown placed at the end of the CMBL in Figure 5.18a, whereas the detector mounting is shown in Figure 5.18b. The corresponding signal electronics using NIM standard modules for high and low threshold discrimination and other hardware are shown in Figure 5.19.

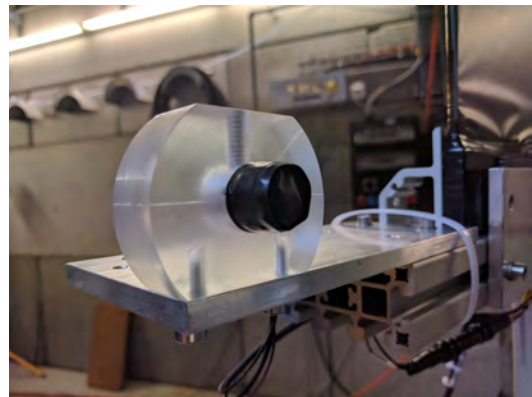


(a) The spectral response for the Hamamatsu R9880U-110 shown in green. The solid line is the cathode radiant sensitivity, the dashed line is the quantum efficiency [69]. (b) The emission spectrum for BC-400 [70].

Figure 5.17: Detector characteristics for the beam scanner detector system.



(a) The two dimensional XY beam scanner system placed at the end of the CMBL.



(b) The mini-PMT with a 2 mm diameter scintillator, covered with TEDLAR and mounted in acrylic glass.

Figure 5.18: Beam Scanner System and mini-PMT.

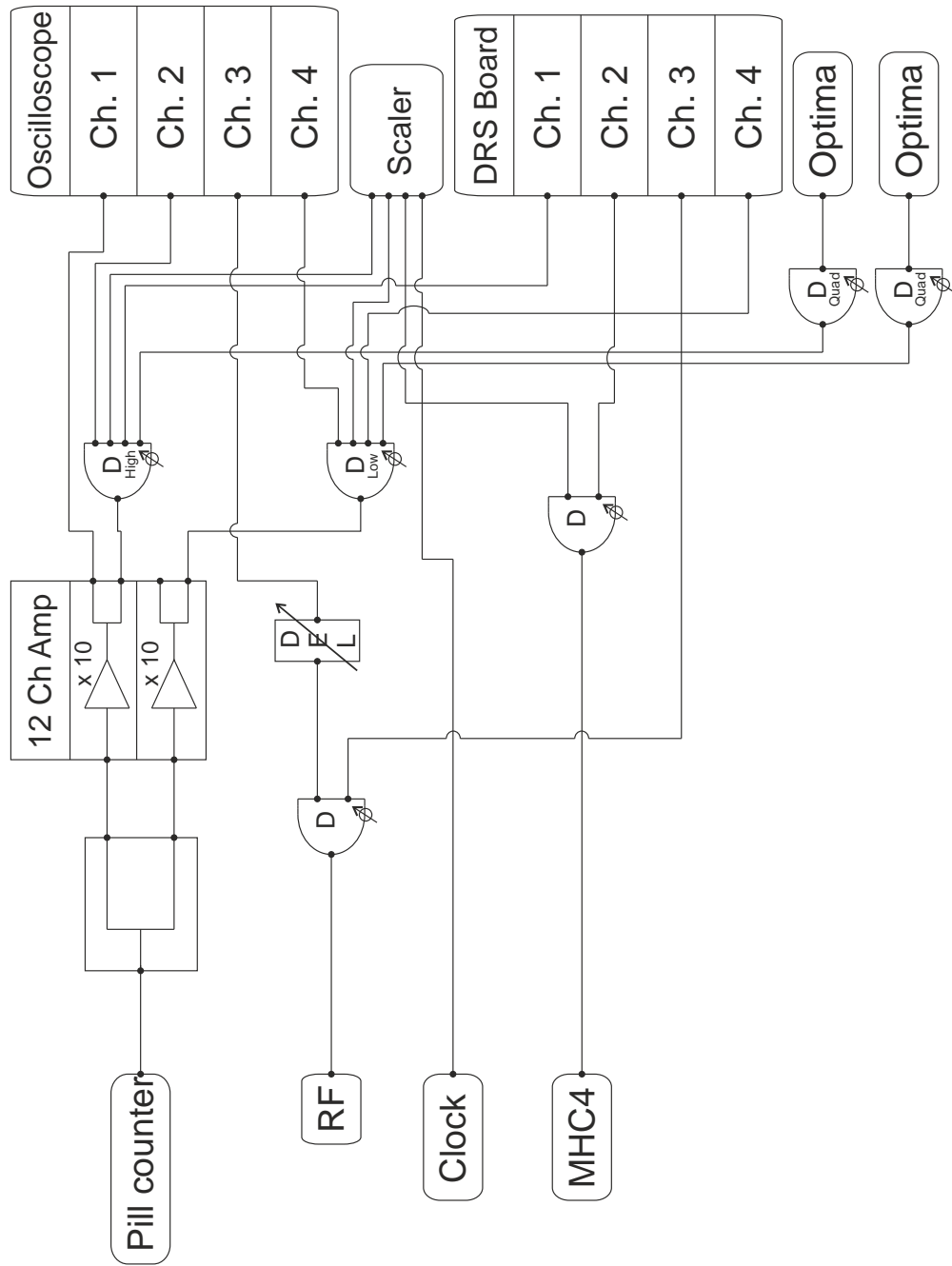


Figure 5.19: Basic electronics schematic for the Pill Scintillator Scanner System. Not shown is the extra RF-coincidence circuitry for the beam background measurement Section 5.4.4.

### 5.4.2 Beam Measurements and Data Analysis

Optimization of the  $\pi E5$  channel is focused solely on maximizing the muon rates delivered to the running experiments. Significant attention has been dedicated to reducing the beam positron content delivered to those experiments through the use of SEP41 and in conjunction with the 120 mm lead collimator system. Nevertheless, some beam positrons will be transmitted through the beamline, and estimates of these rates and steps to further minimize this are considered.

Two types of measurements were conducted: The first aims to characterize the momentum aspects of the beam, such as the central momentum and momentum-byte. These results are obtained from an extensive measurement of the muon momentum spectrum at the collimator system. The results serve as a means of determining the central momentum giving the maximum surface muon yield and a measure of the momentum-byte transmitted, both of which are essential for the simulation of the beamline. An independent, high-resolution muon range curve was also collected, which substantiated the muon momentum spectrum results. These measurements were taken with a 40 mm thick Target E during the 2015/2016 test beam measurements.

The second type of measurement was dedicated to the beam phase-space characteristics and associated beam-correlated background, an essential detail for a high-sensitivity experiment. These latter measurements were conducted during a period with an extended 60 mm Target E, and therefore rates for all particles are increased. Due to the extraction angle of the  $\pi E5$  channel, this yields approximately 30% more surface muons but 50% more beam positrons relative to the standard 40 mm Target E. In order to measure the muon and beam positron rates as well as the CMBL transmission efficiency, measurements were conducted at the collimator focus position between QSK43 and ASL41 and at the Mu3e solenoid injection at the end of the CMBL. Optimization of the beamline at the collimator position and later at the end of the CMBL resulted in two solutions, one for the muon beam focus at the collimator, and a second for the muon transmission through the CMBL. The muon rate and beam profile are considerably different for each case and are therefore treated separately.

### 5.4.3 Fundamental Momentum Characteristics of the Beam

The momentum of the  $\pi E5$  channel is selected by the first dipole magnet ASHW41 situated at  $165^\circ$  relative to the proton beam, near Target E. The selection of a new beamline central momentum is controlled by the HIPA accelerator control room crew as the AHSW41 field has a strong influence on the proton beam centering at Target E. The ASHW41 dipole magnet field as well as all other beamline elements have a linear

momentum dependence, and therefore when adjusting the magnet currents for a new momentum, all elements must be scaled by the ratio of momenta. The SEP41 is treated separately, as both the magnetic and electric fields must be scaled proportionally to maintain the correct velocity separation. Measurements of the muon momentum spectrum therefore require many adjustments to the magnet current for the ASHW41 and all other  $\pi$ E5 elements. The  $\pi$ E5 channel contains two slit systems FSH41 and FS42 which allow for intensity regulation and momentum-byte selection, and during typical operations are at maximum opening to allow for maximum rate transmission.

The fit of the muon spectrum uses the expected surface muon rate relation  $P^{3.5}$  from Pifer et al. [57] with a cutoff at the kinematic edge, which sits atop an exponentially increasing cloud muon continuum and is given by the following expression,

$$\mathcal{R} = A \cdot (1 - \Theta(P - P_{edge})) \left( \frac{1}{P_{edge}^{3.5}} \cdot P^{3.5} \right) + be^{cP} \quad (5.10)$$

where  $\mathcal{R}$  is the muon rate,  $\Theta(x)$  is the Heaviside step function,  $A$  is a scale factor,  $P_{edge}$  is the momentum of the kinematic edge for surface muon production,  $b$  and  $c$  correspond to the rising cloud muon contribution to the absolute muon rate. The momentum function is then convoluted with a gaussian resolution function with a width  $\sigma_P$  that represents the momentum-byte of the beam. The  $\pi$ E5 momentum spectrum from 24 MeV/c to 34 MeV/c along with the fit using Equation (5.10) is shown in Figure 5.20. The fit of the momentum spectrum results in a surface muon kinematic edge at  $P_{edge}=30.06\pm 0.02$  MeV/c and a channel momentum-byte of  $\sigma_P=0.95$  MeV/c, or 3.4% at 28 MeV/c. The systematic shift in momentum due to magnet hysteresis and other effects is estimated to be  $-0.05\pm 0.05$  MeV/c. Therefore the mean kinematic edge is  $\bar{P}_{edge}=30.01\pm 0.05$  MeV/c. These results are consistent with the central momentum and momentum-byte obtained using range curve measurements described in Chapter 6.

Additionally, as a cross check, the pion mass can be determined from the kinematic edge of the muon spectrum. This is essentially the same as Equation (4.5), inserting the muon energy for  $E_\mu$  and solving for  $m_\pi$  gives the following expression,

$$m_\pi = E_\mu + \sqrt{E_\mu^2 - m_\mu^2} \quad (5.11)$$

where  $E_\mu=109.837$  MeV is the muon energy taken from the fit of Figure 5.20, the muon mass  $m_\mu=105.658$  MeV/c<sup>2</sup> is taken from the PDG [45], and assuming zero neutrino mass. This yields a pion mass  $m_\pi=139.85\pm 0.08$  MeV/c<sup>2</sup> with a 0.20 % difference to the PDG value of  $m_\pi=139.5706$ .

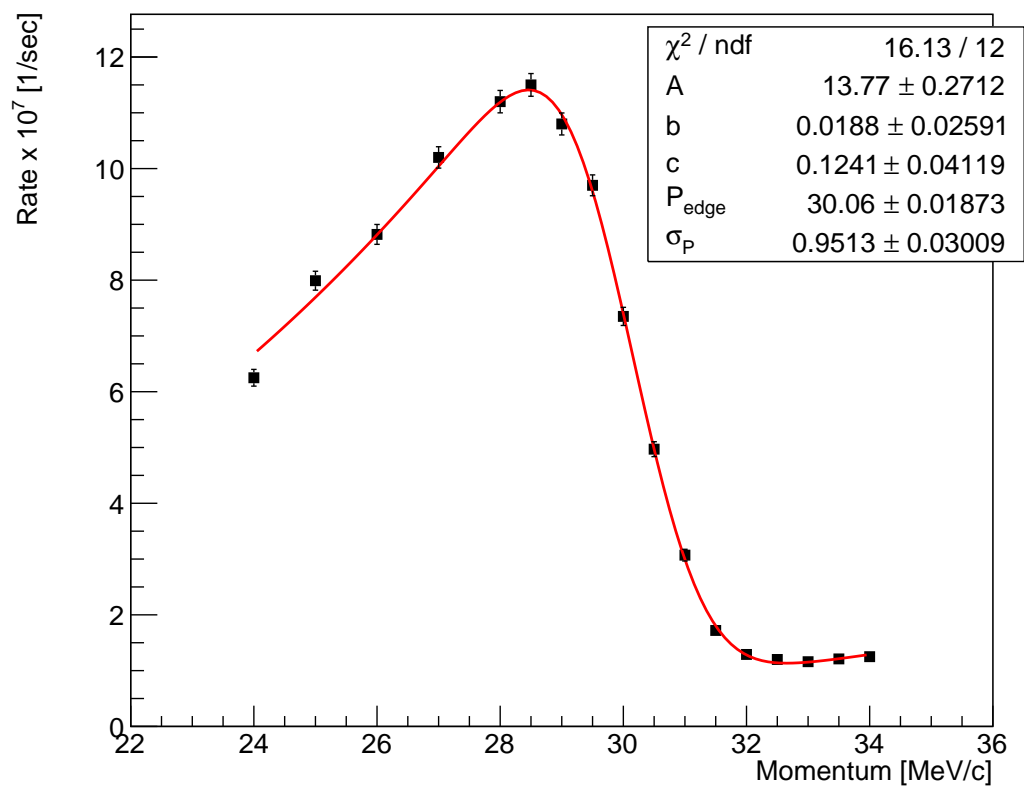


Figure 5.20: Momentum Spectrum in the  $\pi E5$  channel near the surface muon kinematic edge.

### 5.4.4 Beam-Correlated Background Measurements

Muon beam measurements were carried out at two critical locations in the  $\pi E5$  experimental area, to fully characterize the beam as it enters the experimental area and at the injection to the Mu3e experiment. Once the muon beam optimization is completed, the absolute muon rates and beam positron rates can be determined. Typically throughout the optimization procedure the muon rate is estimated using one dimensional scans of the horizontal and vertical axes of the beam profile (cross scan). A gaussian distribution is fitted to the data to obtain the horizontal and vertical beam widths independently. The rates are estimated using the integrated cubic spline interpolation of the data points. An example of the output of the scanner software for a cross scan with a high threshold discriminator (muons only) is shown in Figure 5.21a. A simultaneous scan using a low threshold discriminator (muons and positrons) is shown in Figure 5.21b.

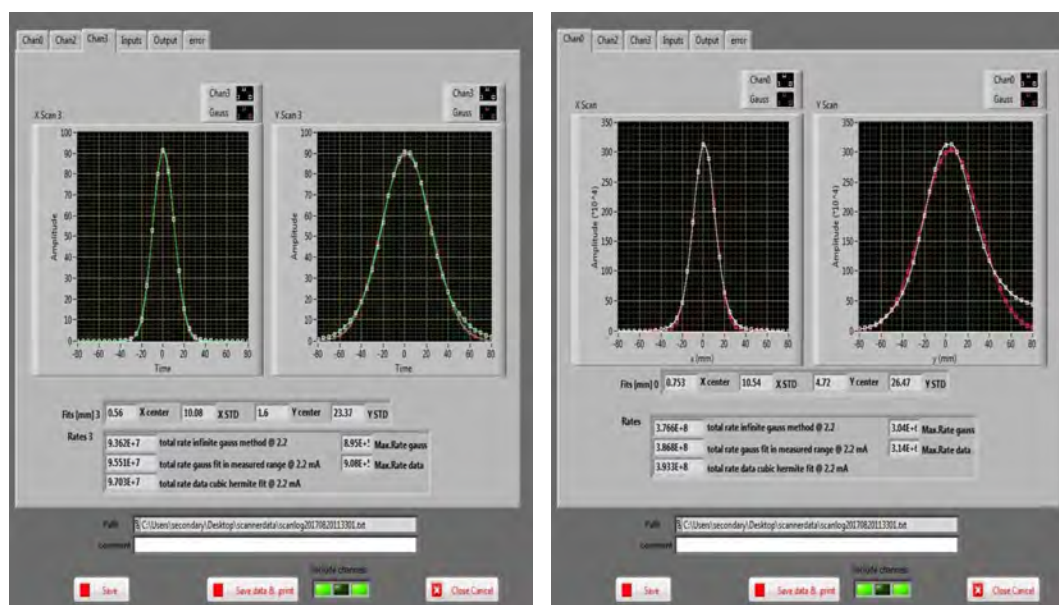


Figure 5.21: Beam scan software output

In order to achieve a more accurate and clearer estimate of the beam positron content in the muon beam, the muon beam was completely stopped in a thin 1.92 mm sheet of  $(C_2H_4)_n$  polyethylene. The stopped muons will decay, creating a large solid angle, low intensity, and nearly gaussian shaped spot of Michel positrons. Since the beam positrons are highly relativistic, they experience minimal energy loss or scattering in the polyethylene. Therefore, downstream of the polyethylene is a nearly pure positron beam with some Michel background. Further reduction of the Michel background is

achieved via a time coincidence trigger of the correlated beam positrons with the RF signal associated with the HIPA ring cyclotron and the production at the target.

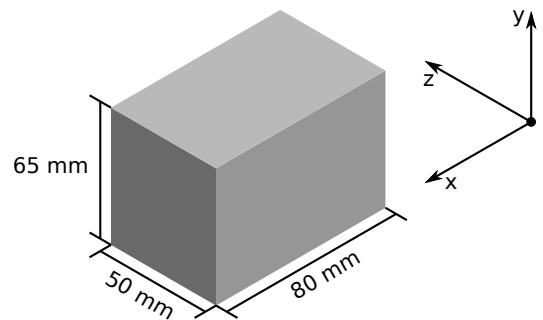
Measurements at the Mu3e Injection point showed that for maximal muon transmission down the CMBL, the beam positron rate exceeded expectations, especially relative to typical MEG operations. Comparison with simulation indicated the positron beam that is initially deflected off-axis vertically by SEP41 and additionally by QSK41 (vertically defocusing) is eventually returned back on-axis by QSK42 (vertically focusing). In order to further reduce the beam positron content without significantly altering the beamline optics, the positrons must be stopped before reaching QSK42. A small lead collimator positron-stopper was placed in the lower section of the cross-shaped vacuum chamber of the TII in the gap between QSK41 and QSK42, as a test, where the vertically defocusing quadrupole field strength is greatest. A picture of the positron stopper and the placement orientation is shown in Figure 5.22.

For both configurations with and without the positron-stopper, at the collimator focus and Mu3e solenoid injection, the following scans were conducted

- Without  $(C_2H_4)_n$ 
  - High Threshold Raster Scan (only  $\mu^+$ )
  - Low Threshold Raster Scan (Michel + Beam  $e^+$  and  $\mu^+$ )
- With  $(C_2H_4)_n$ 
  - Low Threshold Raster Scan (Michel + Beam  $e^+$ )
  - Low RF coincidence Threshold Raster Scan (Beam  $e^+$  and reduced Michel  $e^+$ )



(a) A picture of the positron-stopper inside the cross-shaped vacuum chamber of TII in the gap between QSK41 and QSK42.



(b) A diagram of the lead collimator positron-stopper indicating the size and orientation relative to the beam axis coordinate system.

Figure 5.22: The lead collimator positron-stopper.

During the raster scan with polyethylene covering the beam pipe window, the scaler rates of both low threshold positrons (**A**) and low threshold in RF coincidence (**B**)

are collected. The bin-to-bin ratio ( $\mathbf{R}$ ) of  $\mathbf{A}$  to  $\mathbf{B}$  provides a classifier on whether that bin is Michel positron or beam positron dominated. The histogram of  $\mathbf{R}$  bin values has a peak associated with the majority of the bins being dominated by Michel positrons only, as lower  $\mathbf{R}$  corresponds to more events in  $\mathbf{B}$  relative to  $\mathbf{A}$ . This is only true if one assumes that the majority of the raster scan bins are dominated by Michel positrons and there is a small, localized beam positron contamination. A gaussian distribution is fitted to this peak to obtain the mean  $\bar{R}$  and width  $\sigma_R$  of the bin value distribution. The beam positron classifier is then defined as  $\alpha = \bar{R} - 2\sigma_R$ . A new raster  $\mathbf{D}$  is filled with the value of  $A_{ij}$  for  $R_{ij} < \alpha$ . Another raster  $\mathbf{F}$  is filled with the value of  $A_{ij}$  for  $R_{ij} > \alpha$ , corresponding to bins filled predominantly with Michel positrons. A 2D gaussian distribution  $f(x, y)$  is fitted to  $\mathbf{F}$  to estimate the underlying Michel positron content of  $\mathbf{D}$ . The final beam positron rate estimate  $\mathcal{R}_{e^+}$  is calculated using the following

$$\mathcal{R}_{e^+} = \mathcal{N} \sum_{ij} A_{ij} - f(x(i, j), y(i, j)) \quad (5.12)$$

where  $A_{ij}$  is the  $\mathbf{A}$  bin value at point  $ij$ ,  $f(x(i, j), y(i, j))$  is the gaussian fit function evaluated at point  $x, y$  corresponding to bin  $ij$ , and  $\mathcal{N}$  is the conversion factor from counts to rate.

An example of this procedure is shown in the following, as applied to beam measurements at the collimator using the beamline magnet optics set to focus at the collimator. The  $\mathbf{A}$  and  $\mathbf{B}$  raster scans are shown in Figure 5.23a and Figure 5.23b respectively. The ratio  $\mathbf{R}$  is shown in Figure 5.23c and the histogram of the bin values is shown in Figure 5.23d. The raster  $\mathbf{F}$  with bins of  $\mathbf{A}$  classified as Michel positrons is shown in Figure 5.24a, while the raster  $\mathbf{D}$  with bins of  $\mathbf{A}$  classified as beam positrons are shown in Figure 5.24b. The final raster from which the beam positron rate is calculated is shown in Figure 5.25.

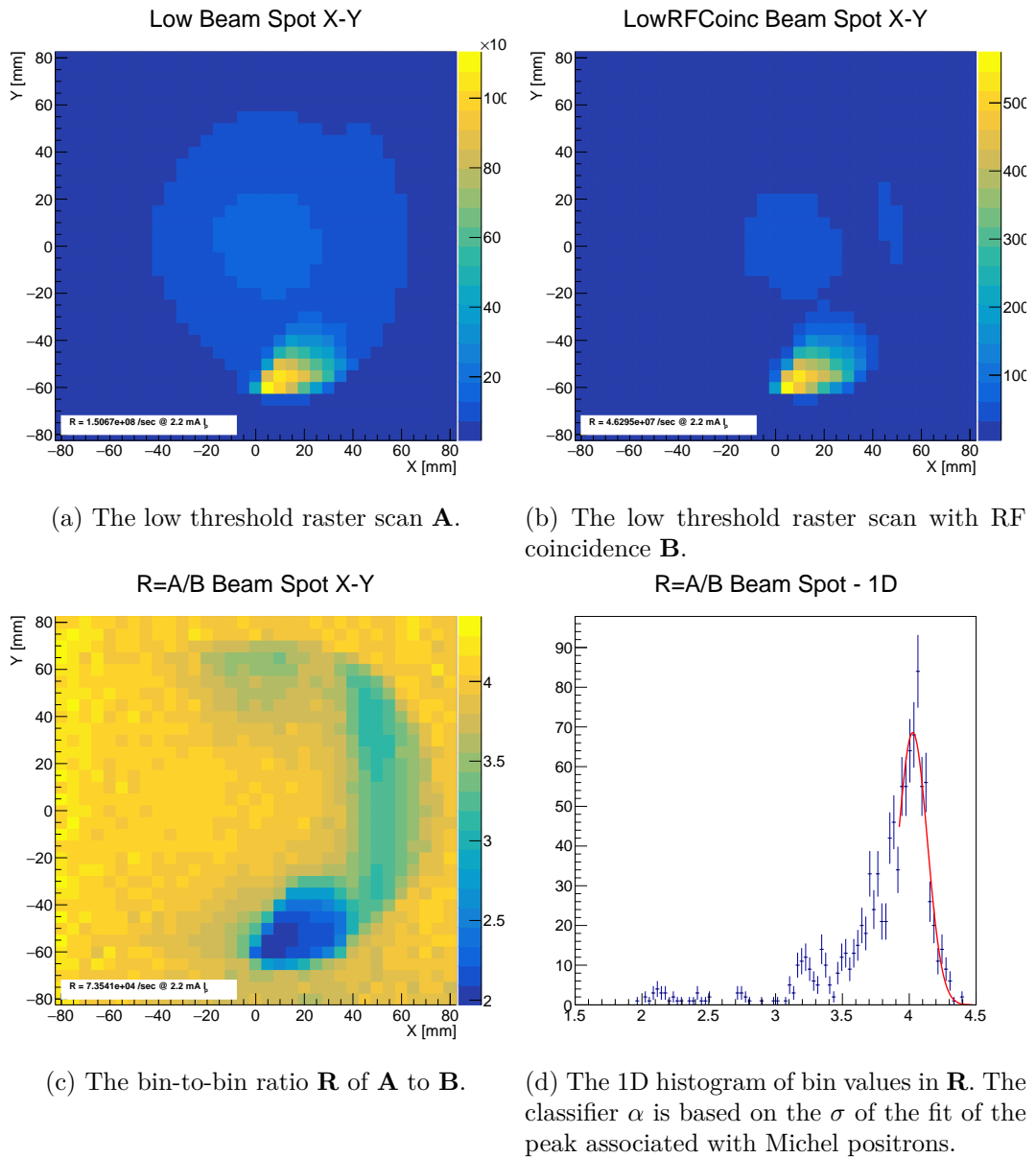
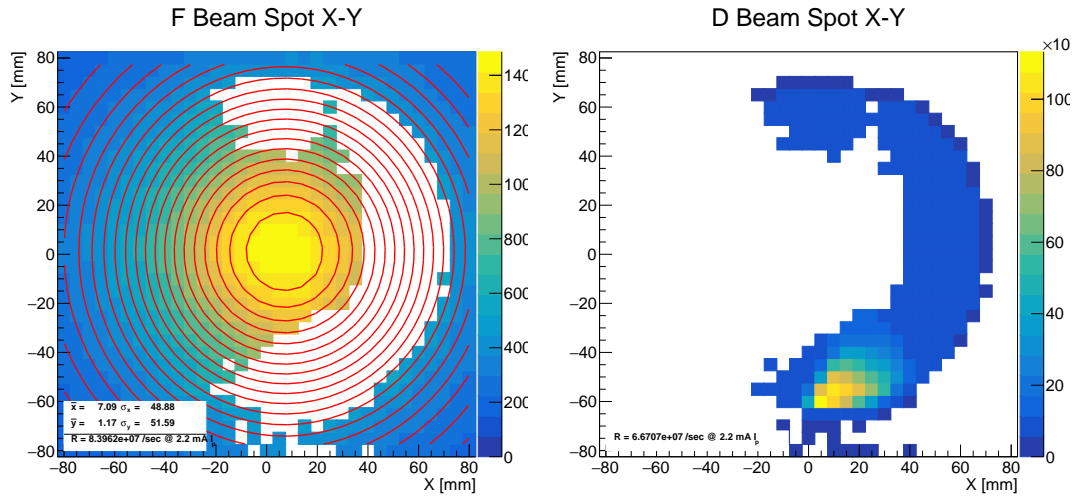


Figure 5.23: The measured raster scans using polyethylene to stop muons and extract the underlying beam positron contamination. The ratio of the two simultaneous scans provides a classifier on the amount of beam positrons within that bin.



(a) The **F** raster generated by filling bins of **A** classified as Michel positrons. (b) The **D** raster generated by filling bins of **A** classified as beam positrons.

Figure 5.24: The rasters for Michel and beam positrons, generated by filling bins of **A** based on the classifier  $\alpha$ .

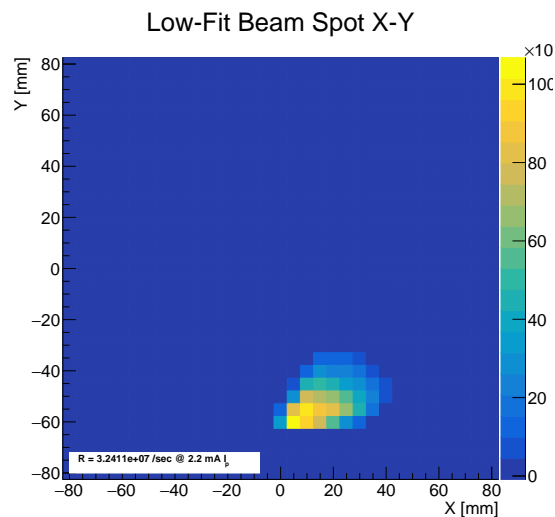


Figure 5.25: The final calculated raster for beam positrons, after subtracting the fit of the Michel positron background.

### 5.4.5 Measurement at the Collimator System

The measurements at the collimator system were conducted downstream of the QSK43 and the 120 mm lead collimator, in the air gap between the beam pipe vacuum window and the ASL41 vacuum chamber entrance. The measurements at the collimator position were conducted after the measurements at the Mu3e solenoid injection using the beamline magnet values for optimized transmission to the Mu3e solenoid. There was an exchange of Target E between the measurements at the Mu3e injection point and those at the collimator position, but since this involved the replacement of a 6 cm long target with another 6 cm target it is assumed this does not affect the absolute particle rates. The distance between the pill detector and window flange is 28 mm, and 83 mm to the center of the MYLAR beam pipe vacuum window. Due to space constraints between the collimator beam pipe and the ASL41 vacuum chamber, a long arm was attached to the Y-axis scanner platform to place the detector system in the gap between beamline elements.

The muon beam cross scans at the beam center, using a high threshold trigger are shown in Figure 5.26. The muon rate with beamline optics associated with transmission through the CMBL (“QSM-optics”) is determined via the high threshold cross scans, and the integrated cubic spline gives  $\mathcal{R}_{\mu^+} = 1.70 \cdot 10^8 \mu^+/\text{sec} @ 2.2 \text{ mA } I_p$ . A full 2D raster scan of the beam gives additional information and more accurate estimate of the absolute muon rate. The muon beam as measured at the collimator without the positron-stopper installed has a non-gaussian shape and is slightly asymmetric as shown in Figure 5.27a. The low threshold scan after subtracting the high threshold scan to remove the muon component is shown in Figure 5.27b, and shows a bright spot below the muon spot, suggesting positron contamination. The muon rate at the collimator position for beamline optics associated with transmission through the CMBL using QSM optics is  $\mathcal{R}_{\mu^+} = 1.42 \cdot 10^8 \mu^+/\text{sec} @ 2.2 \text{ mA } I_p$ .

The deflection of the muons and positrons in the SEP41 can be controlled by reducing the current supplied to the SEP41 dipole bending magnet. Therefore one can effectively sweep the muon and positron beams across the detector downstream. The low threshold scan of the SEP41 magnet current from 60 A to 0 A is shown in Figure 5.28. A SEP41 magnet current of 43.5 A corresponds to maximum muon transmission, and 11.2 A corresponds to maximum positron transmission. The ratio of the integral of the positron distribution to the muon distribution in the SEP41 scan is 2.36, but this does not correspond to the actual positron to muon ratio, as this measurement is made at low discriminator threshold and therefore the muon peak also contains the contribution from Michel decays, whereas the beam  $e^+$  peak consists of beam  $e^+$  only. This scan is a measure of the separation quality between muons and beam  $e^+$ . This ratio is only a measure of the instantaneous rate at the center of the beam spot where the pill detector is located, and since the beam distribution will

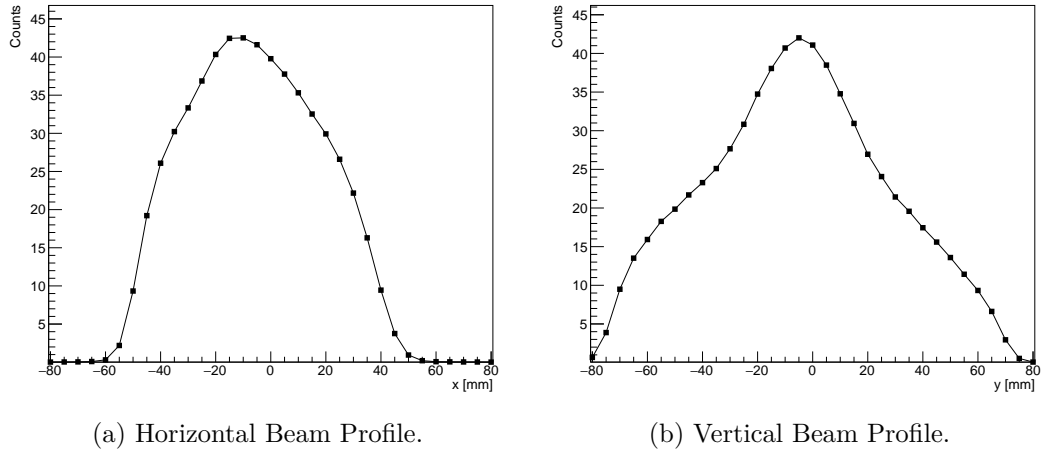


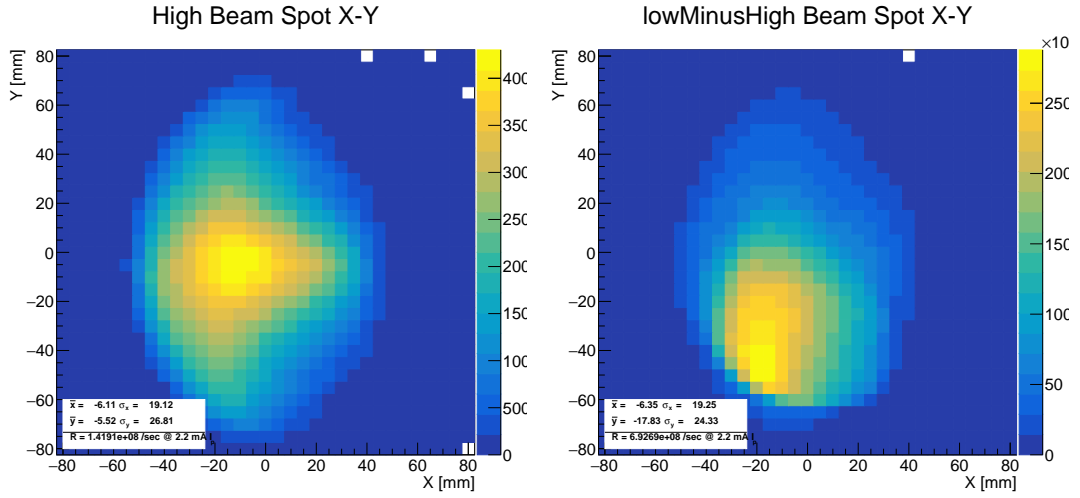
Figure 5.26: QSM final focus optics measured at the collimator system showing the horizontal and vertical beam profile measured with the pill scanner system and using the high threshold discriminator.

change as the beam travels through the stronger field region off-axis in the quadrupoles of TII so will the rate at the center of the beam spot. A true measure of the total beam  $e^+$  content in the beam prior to the separator can be obtained from a cross scan when the SEP41 magnet current is tuned to transmit only beam  $e^+$  at 11.2 A.

Another check of the absolute muon to positron ratio is having the full muon and full positron beam together in one raster scan. This can be achieved by reducing the separation power of SEP41 through the reduction of both the magnetic and electric fields. If the SEP41 was completely off, the muon and positron beams would overlap, and it would be difficult or impossible to separate the Michel positrons from beam positrons. Therefore, a reduced SEP41 maintains some spatial separation of the beams downstream at the measurement position.

The reduced SEP41 dipole magnet current was set to 14 A and the SEP41 electric potential between the plates was set to 105 kV. The high threshold discriminated muon beam raster scan is shown in Figure 5.29a and the low threshold raster scan after subtracting the associated muon component is shown in Figure 5.29b. The total muon rate in this configuration is  $\mathcal{R}_{\mu^+} = 1.50 \cdot 10^8 \mu^+/\text{sec} @ 2.2 \text{ mA } I_p$ .

The polyethylene sheet was then placed over the vacuum pipe window, and for the same reduced SEP41 settings a low threshold raster scan, which is shown in Figure 5.30a and with the RF coincidence shown in Figure 5.30b. The bins classified as predominantly Michel positrons using Figure 5.30c is shown in Figure 5.30d fitted with a 2D gaussian distribution. The bins with Michel positrons are shown in Figure 5.31a whereas those bins dominated by beam positrons are shown Figure 5.31b. The final beam positron contribution after subtracting the estimated Michel contribution is shown in Figure 5.32. The beam positron rate with reduced SEP41 power is  $\mathcal{R}_{e^+} = 1.54 \cdot 10^9 e^+/\text{sec} @ 2.2 \text{ mA } I_p$ , giving a ratio of positrons to muons of  $\mathcal{R}_{e^+}/\mathcal{R}_{\mu^+} = 10.1$



(a) Raster scan of muon beam using a high threshold discriminator. (b) Raster scan of muon beam using low threshold discriminator.

Figure 5.27: Raster scan of the beam at the collimator position using QSM optics.

consistent with the ratio from production at Target E seen in Figure 5.8. This test with the full positron beam along with the muon beam using reduced separation power in the SEP41 shows the method is capable of separating the two beam types with a factor 10 difference in rate.

For the optimized beamline magnet currents for transmission through the CMBL, and the SEP41 operated at maximum separation power, the beam is then measured at the intermediate focus downstream of the 120 mm lead collimator system. The raster scans with  $(C_2H_4)_n$  placed on the beam pipe vacuum window using low threshold and low threshold with an RF-coincidence are shown in Figure 5.33a and Figure 5.33b respectively. The ratio of these scans is shown in Figure 5.33c. The bins classified as predominantly Michel positrons using Figure 5.33d is shown in Figure 5.34a fitted with a 2D gaussian distribution. The bins dominated by beam positrons is shown Figure 5.34b. The final beam positron contribution after subtracting the estimated Michel contribution is shown in Figure 5.35. The estimated beam positron rate at the Collimator using beam optics for optimal transmission through the CMBL without a positron-stopper in TII is  $\mathcal{R}_{e^+} = 3.58 \cdot 10^8 \text{ e}^+/\text{sec} @ 2.2 \text{ mA } I_p$ . This positron rate is far in excess of what was expected and is due to the re-centering of off-axis particles after SEP41, in TII.

In order to both confirm the off-axis re-centering hypothesis and demonstrate the effect of a positron-stopper in reducing the beam positron content, the previously mentioned positron-stopper in the form of a lead collimator (in in Section 5.4.4) was placed between QSK41 and QSK42. The muon rate at the collimator using beam optics for optimal transmission through the CMBL with the positron-stopper in TII is  $\mathcal{R}_{\mu^+} = 1.62 \cdot 10^8 \text{ e}^+/\text{sec} @ 2.2 \text{ mA } I_p$ . The raster scans with  $(C_2H_4)_n$  placed on

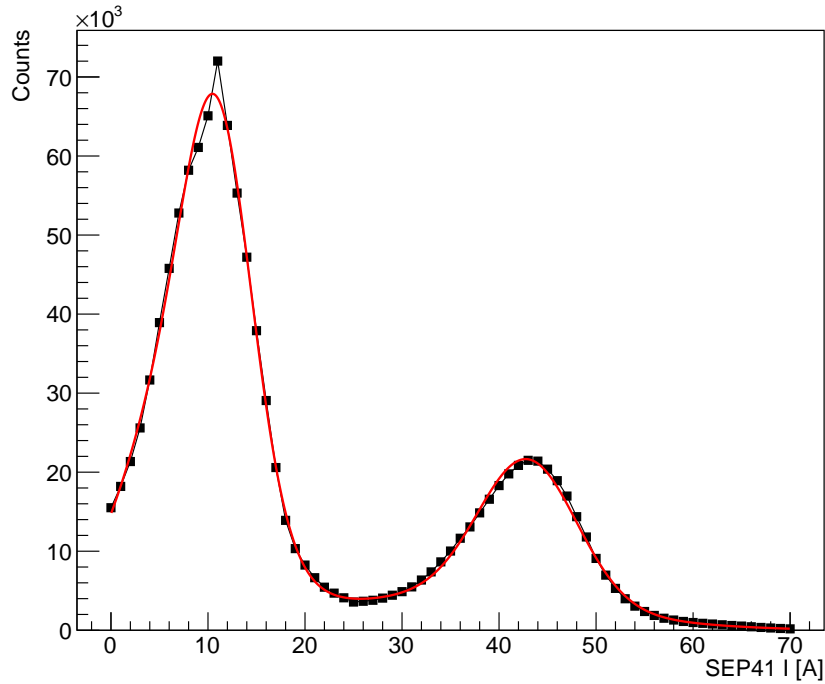
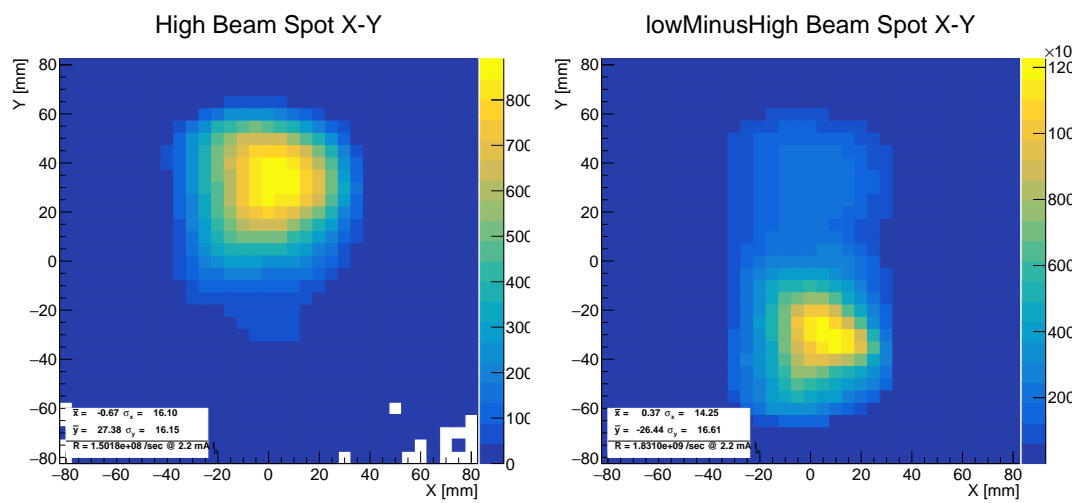


Figure 5.28: The scan of SEP41 magnet current from 60 A to 0 A. The peak at 11 A corresponds to beam positrons, whereas the peak at 44 A corresponds to muons and Michel positrons. Since the SEP41 provides a vertical deflection, this scan sweeps the beam across the pill detector.

the beam pipe vacuum window and with low threshold and low threshold with an RF-coincidence are shown in Figure 5.36a and Figure 5.36b respectively. The ratio of these scans is shown in Figure 5.36c. The bins classified as predominantly Michel positrons using Figure 5.36d are shown in Figure 5.37a fitted with a 2D gaussian distribution. The bins dominated by beam positrons are shown Figure 5.37b. The final beam positron contribution, after subtracting the estimated Michel contribution, is shown in Figure 5.38. The estimated beam positron rate at the collimator using beam optics for optimal transmission through the CMBL with the positron-stopper in TII is  $\mathcal{R}_{e^+} = 1.16 \cdot 10^7 \text{ e}^+/\text{sec} @ 2.2 \text{ mA } I_p$ . This is more than a factor 30 reduction of beam positrons at the collimator position.



(a) The high threshold raster scan during reduced separation power in SEP41. (b) The low threshold raster scan after subtracting the high threshold component during reduced separation power in SEP41. The Michel positrons associated with muons stopping in the detector can be seen in the same upper positions as the muons in the high threshold scan. The lower spot is the beam positrons.

Figure 5.29: The high and low threshold raster scans during reduced separation power of SEP41. This provides an opportunity to check the absolute positron to muon ratio.

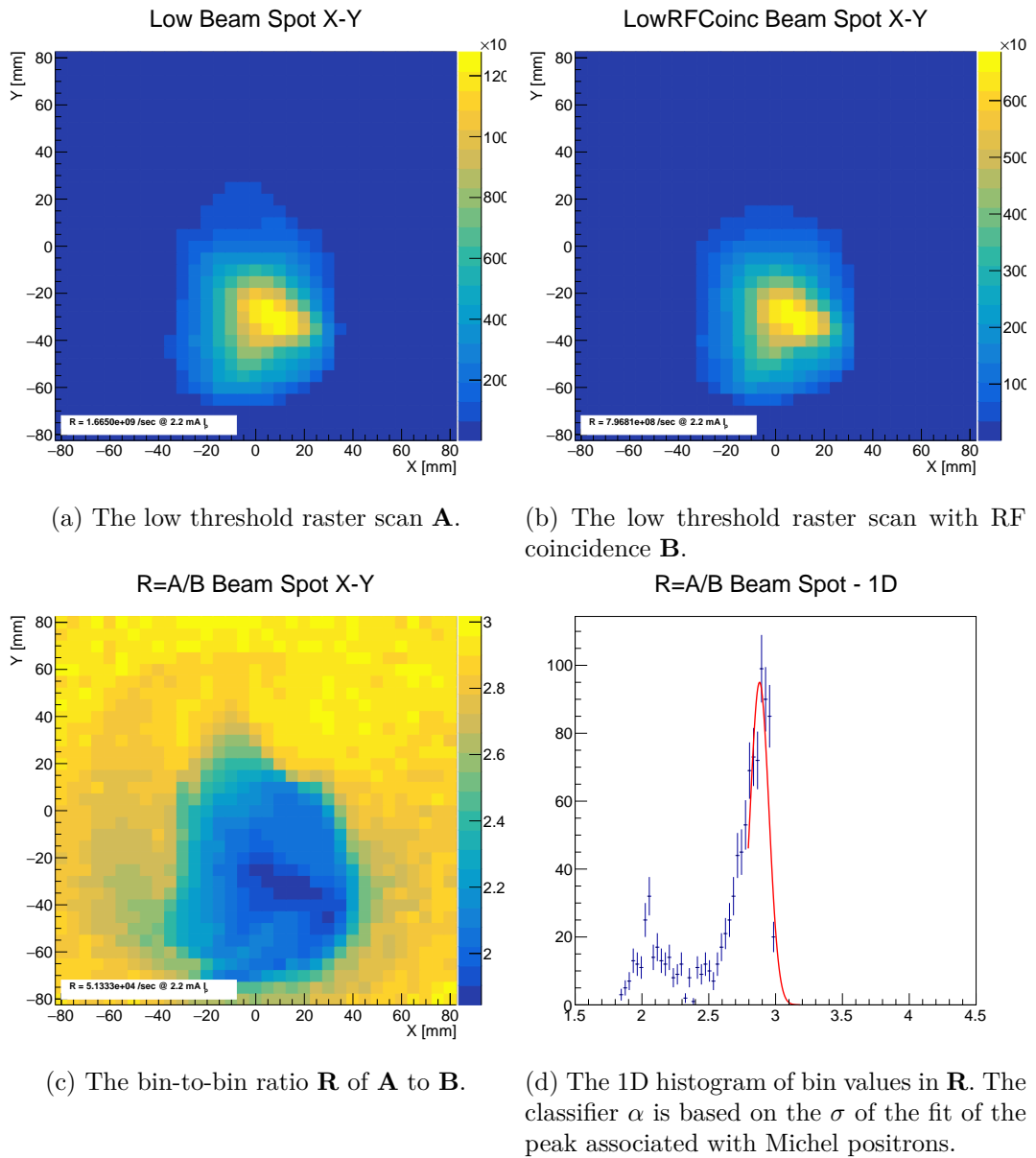
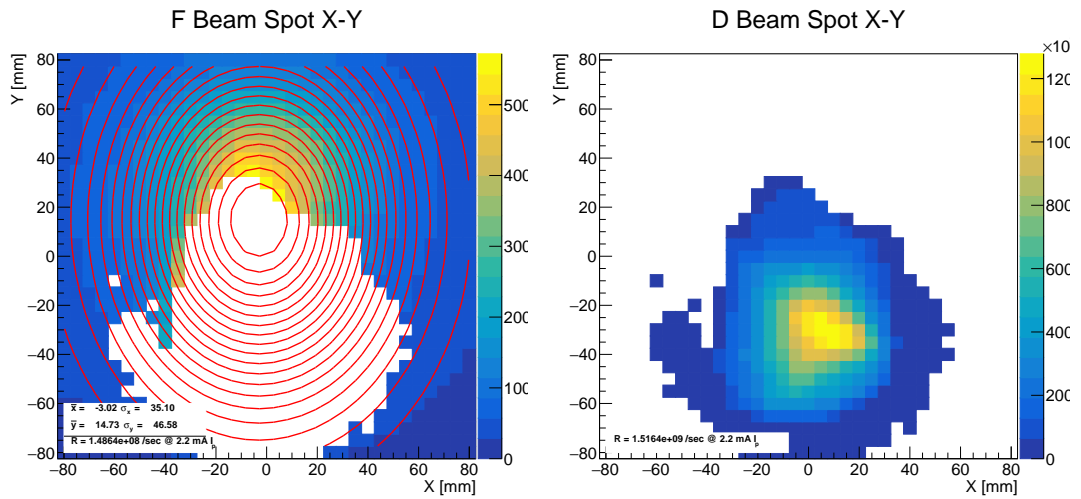


Figure 5.30: The measured raster scans at the collimator focus, using reduced separation power of SEP41, using polyethylene to stop muons and extract the underlying beam positron contamination.



(a) The **F** raster generated by filling bins of **A** classified as Michel positrons. (b) The **D** raster generated by filling bins of **A** classified as beam positrons.

Figure 5.31: The rasters for Michel and beam positrons at the collimator focus, using reduced separation power of SEP41, generated by filling bins of **A** based on the classifier  $\alpha$ .

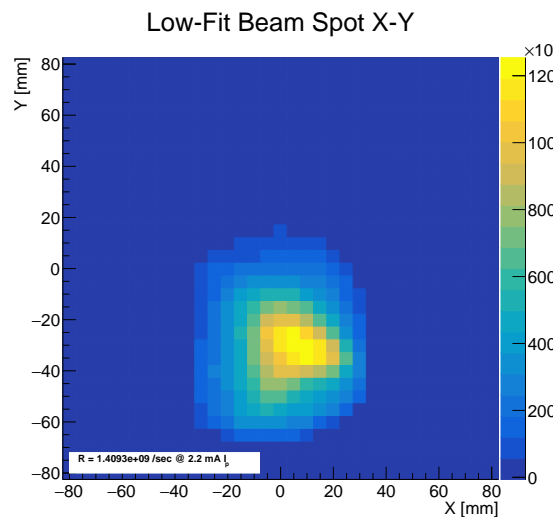


Figure 5.32: The final calculated raster for beam positrons using reduced separation power of SEP41, with the polyethylene sheet.

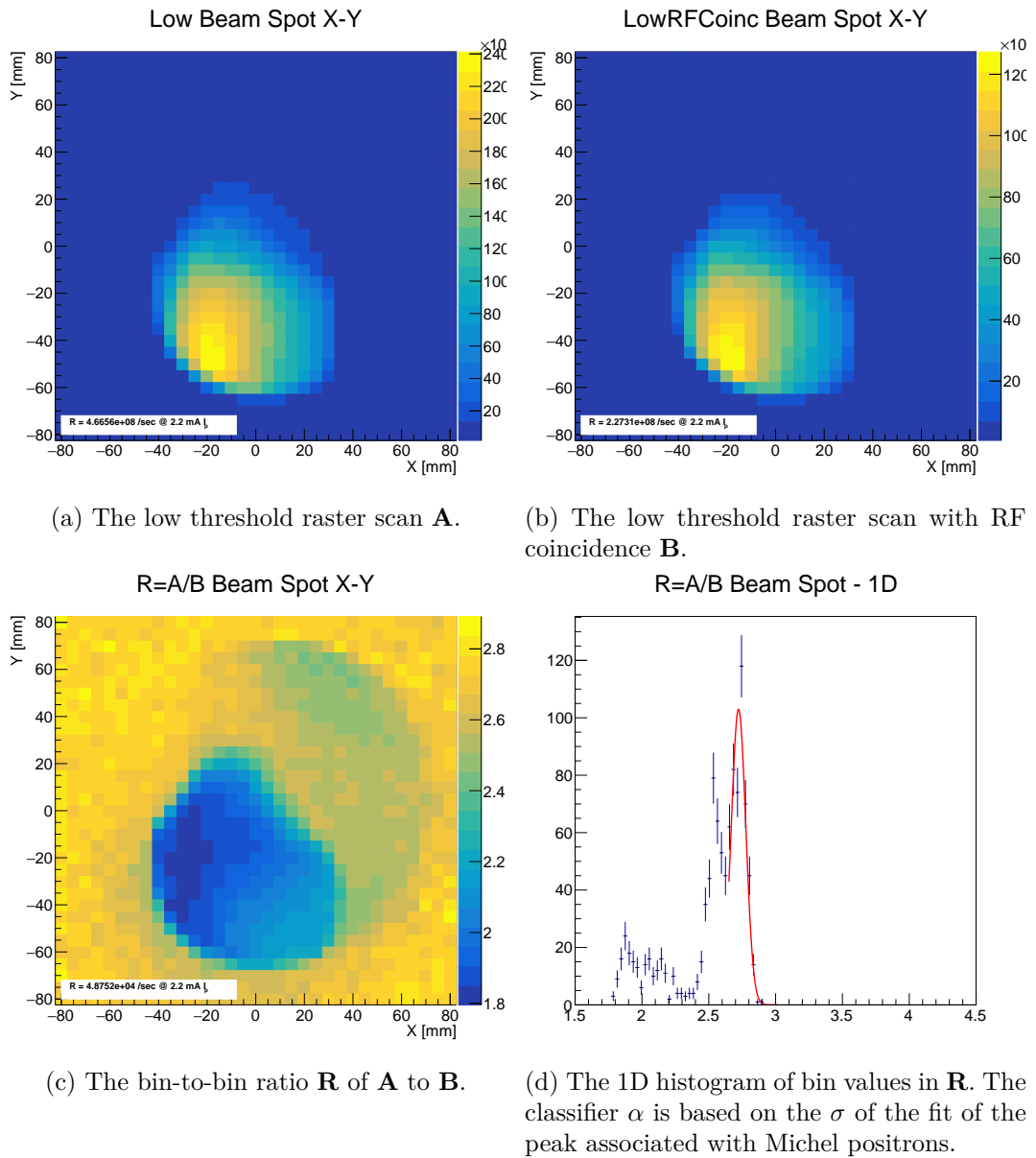
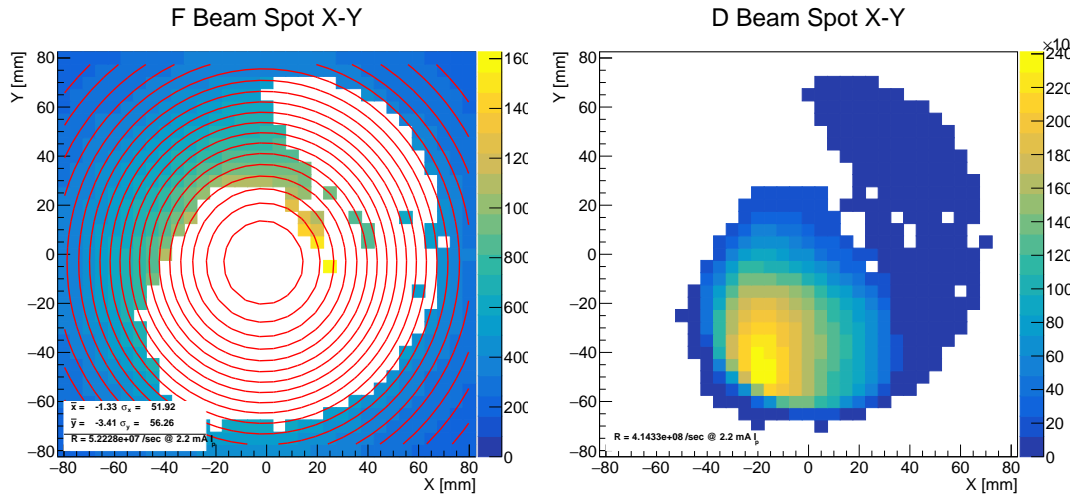


Figure 5.33: The measured raster scans at the collimator focus, without the positron-stopper, using polyethylene to stop muons and extract the underlying beam positron contamination.



(a) The **F** raster generated by filling bins of **A** classified as Michel positrons. (b) The **D** raster generated by filling bins of **A** classified as beam positrons.

Figure 5.34: The rasters for Michel and beam positrons at the collimator focus, without the positron-stopper, generated by filling bins of **A** based on the classifier  $\alpha$ .

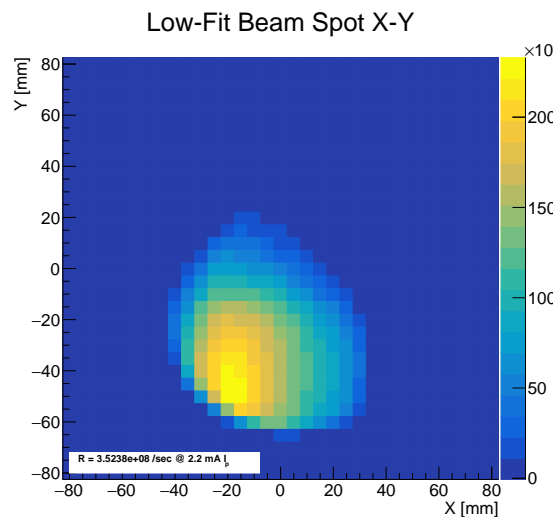


Figure 5.35: The final calculated raster for beam positrons with the polyethylene sheet at the collimator focus.

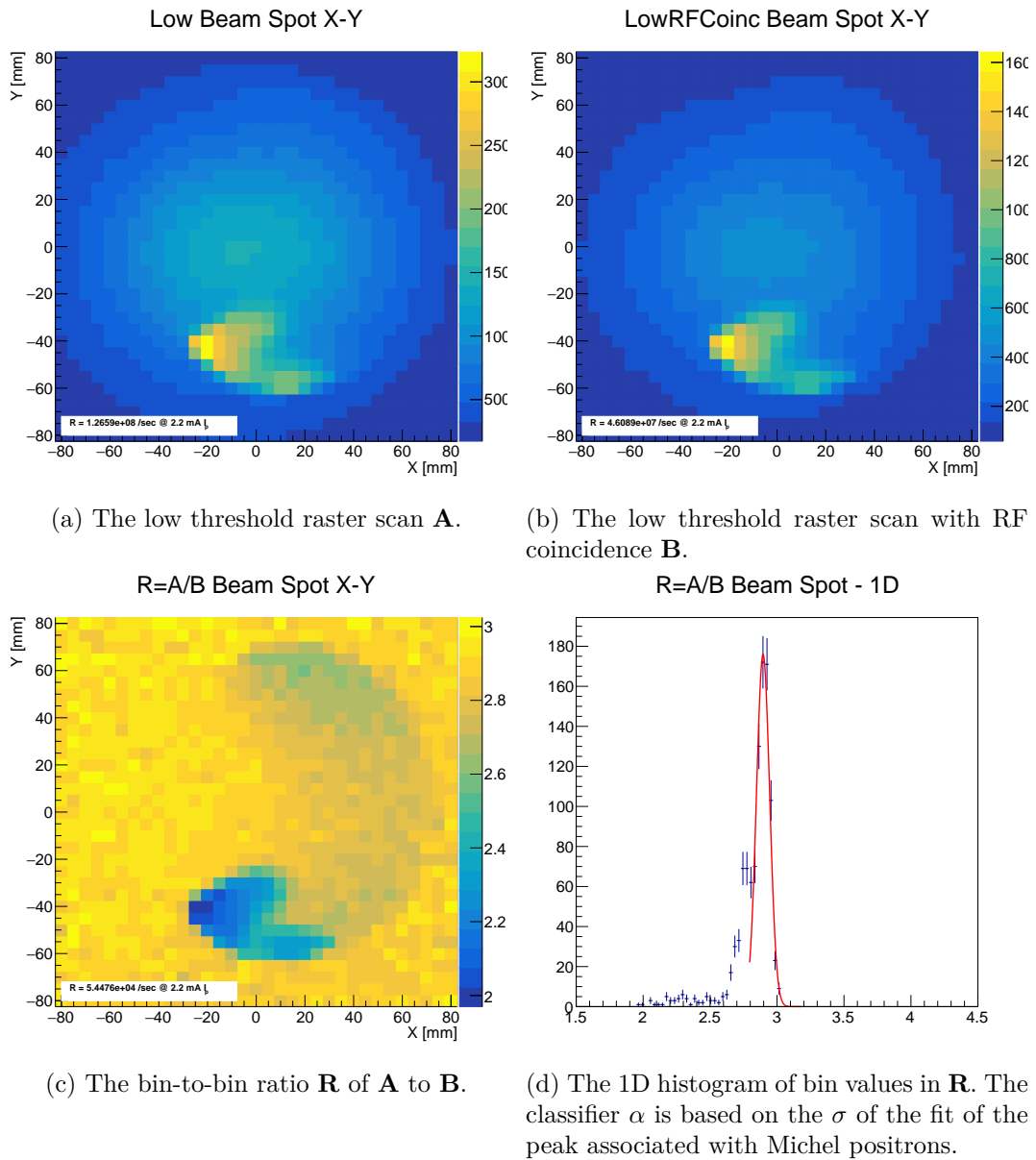
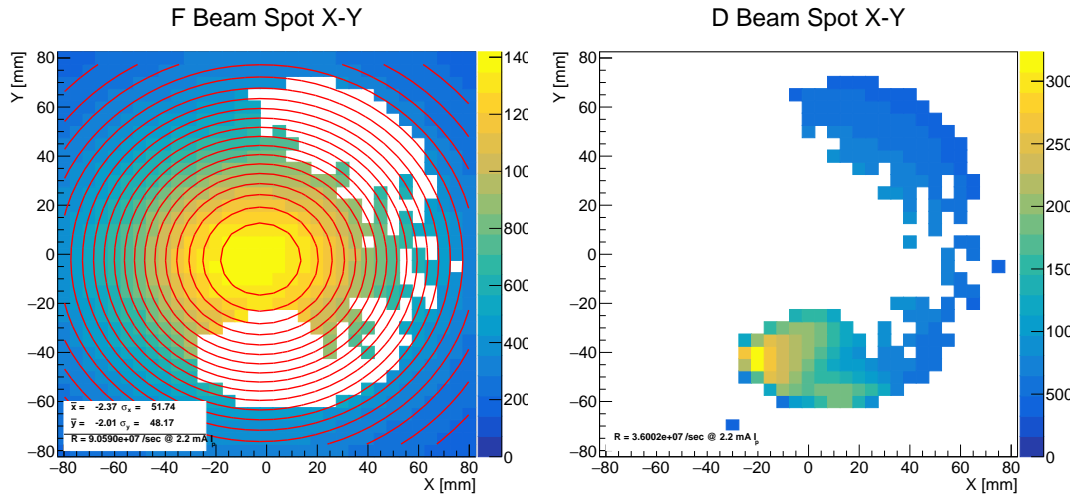


Figure 5.36: The measured raster scans at the collimator focus, with the positron-stopper, using polyethylene to stop muons and extract the underlying beam positron contamination.



(a) The **F** raster generated by filling bins of **A** classified as Michel positrons. (b) The **D** raster generated by filling bins of **A** classified as beam positrons.

Figure 5.37: The rasters for Michel and beam positrons at the collimator focus, with the positron-stopper, generated by filling bins of **A** based on the classifier  $\alpha$ .

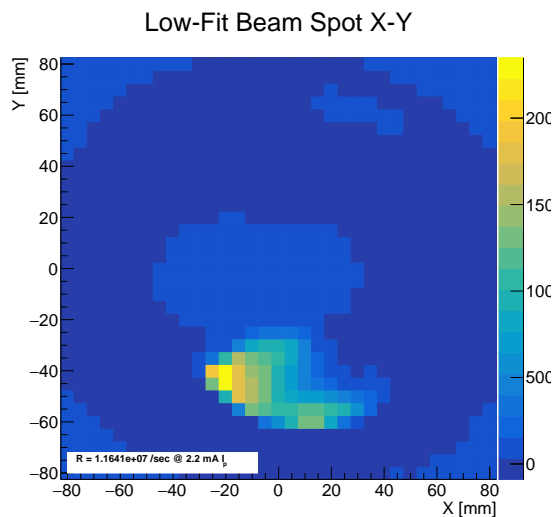
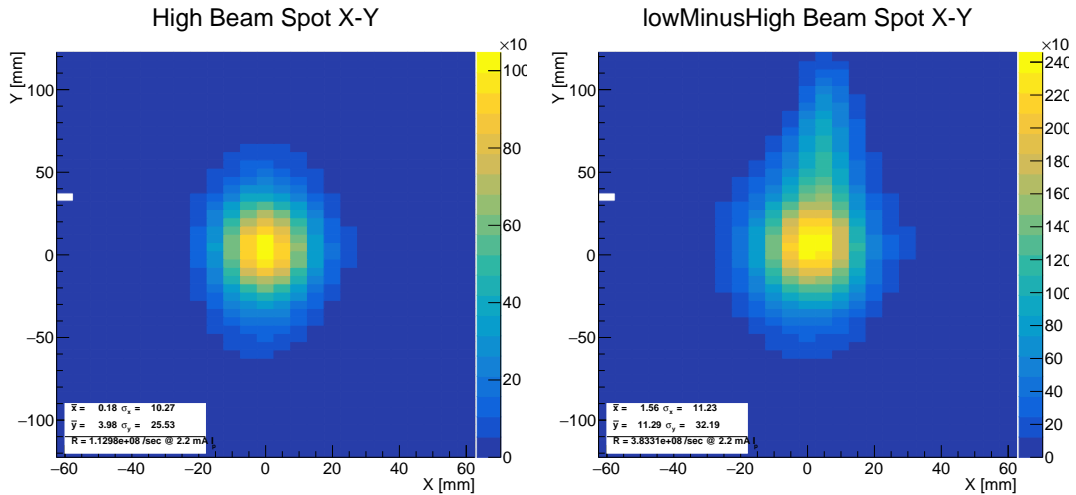


Figure 5.38: The final calculated raster for beam positrons with the polyethylene sheet at the collimator focus with the lead collimator positron-stopper in TII.

### 5.4.6 Measurement at the Injection to the Mu3e Solenoid

Measurements were conducted at the injection to the Mu3e solenoid downstream of the QSM43 in air, to determine the maximum muon rate deliverable for the Mu3e experiment. Additionally, further investigations and minimization of beam positron contamination were carried out. For the measurements at the Mu3e injection position, the distance between the pill detector and window flange was 98 mm, corresponding to 153 mm of air to the center of the MYLAR beam pipe vacuum window. The muon beam as measured at the Mu3e injection without the positron-stopper installed has a gaussian shape but is vertically wide as shown in Figure 5.39a. The muon rate at the Mu3e injection position for beamline optics associated with transmission through the CMBL is  $\mathcal{R}_{\mu^+} = 1.13 \cdot 10^8 \mu^+/\text{sec} @ 2.2 \text{ mA } I_p$ . The low threshold scan after subtracting the high threshold scan to remove the muon component is shown in Figure 5.39b, and shows a long vertical tail above the muon spot, indicating a positron contamination.



(a) Raster scan of muon beam using a high threshold discriminator. (b) Raster scan of muon beam using low threshold discriminator after subtracting the high threshold component.

Figure 5.39: Raster scan of the beam at the Mu3e solenoid injection position without the positron-stopper installed in TII.

The raster scans with  $(C_2H_4)_n$  placed on the beam pipe vacuum window with low threshold and low threshold with an RF-coincidence are shown in Figure 5.40a and Figure 5.40b respectively. The ratio of these scans is shown in Figure 5.40c. The bins classified as predominantly Michel positrons using Figure 5.40d are shown in Figure 5.41a fitted with a 2D gaussian distribution. The bins dominated by beam positrons are shown Figure 5.41b. The beam positron spot is extended along the y-axis and covers the central portion of the Michel distribution, nevertheless the bin

ratio classifier method is able to separate the two and allow the Michel spot to be fitted accurately. The final beam positron contribution after subtracting the estimated Michel contribution is shown in Figure 5.42. The estimated beam positron rate at the Mu3e solenoid injection using beam optics for optimal transmission through the CMBL without a positron-stopper in TII is  $\mathcal{R}_{e^+} = 9.50 \cdot 10^7 \text{ e}^+/\text{sec} @ 2.2 \text{ mA } I_p$ .

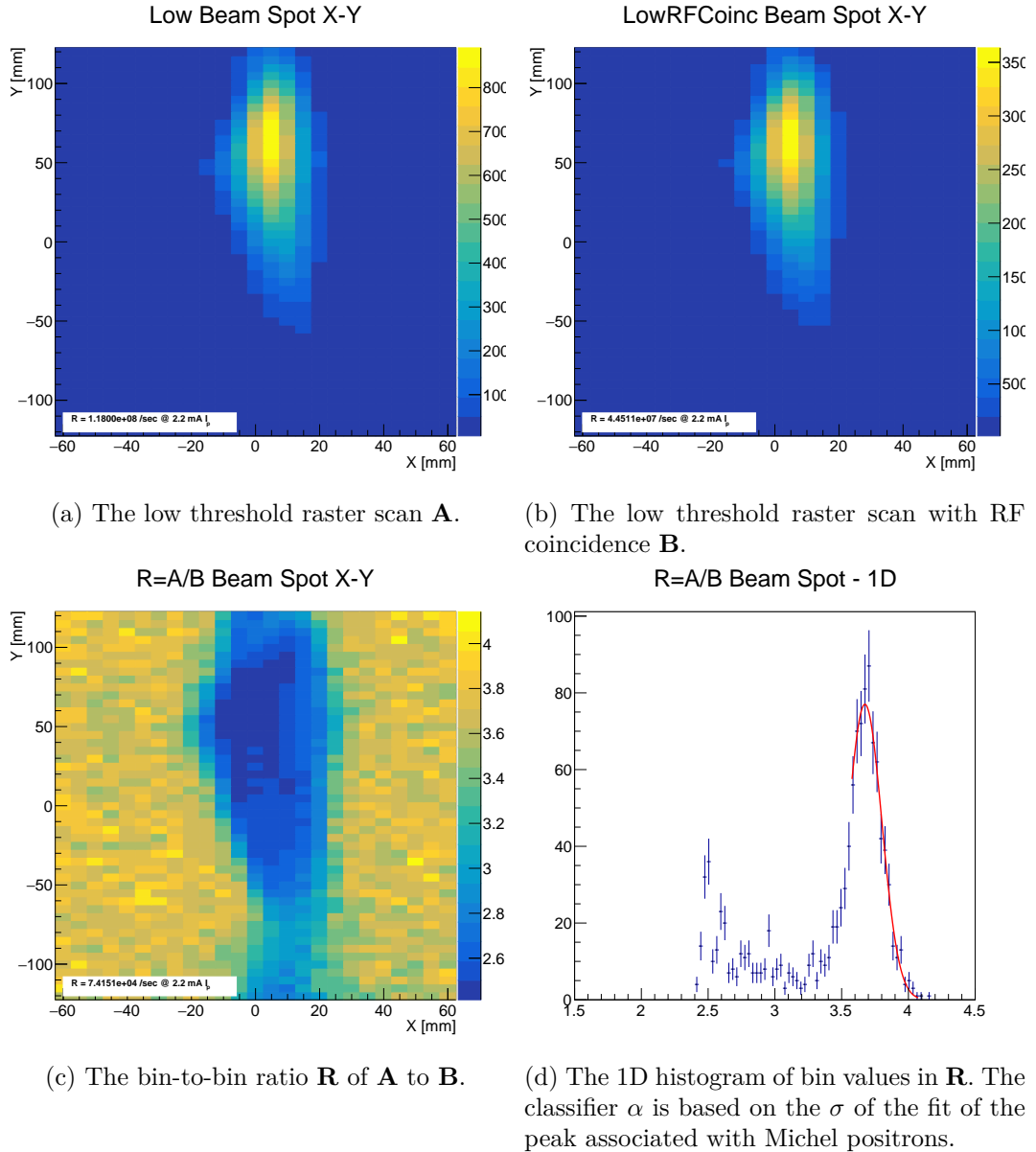
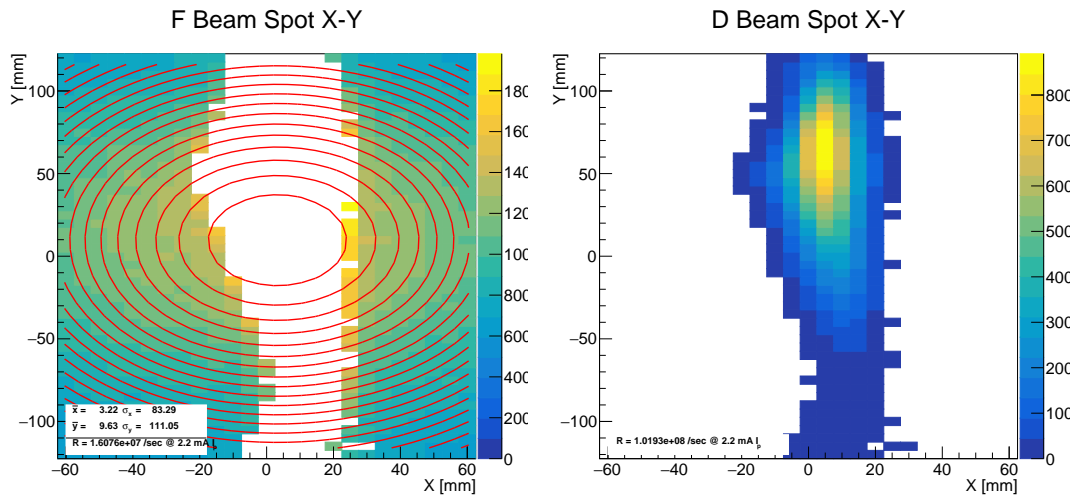


Figure 5.40: The measured raster scans at the Mu3e solenoid injection focus, without the positron-stopper, using polyethylene to stop muons and extract the underlying beam positron contamination.



(a) The **F** raster generated by filling bins of **A** classified as Michel positrons. (b) The **D** raster generated by filling bins of **A** classified as beam positrons.

Figure 5.41: The rasters for Michel and beam positrons at the Mu3e solenoid injection focus, without the positron-stopper, generated by filling bins of **A** based on the classifier  $\alpha$ .

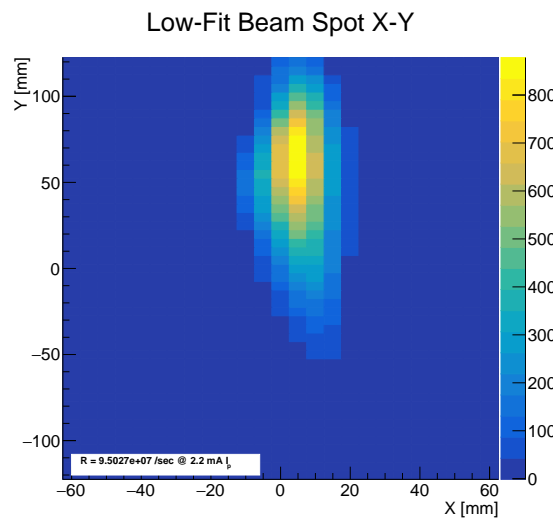
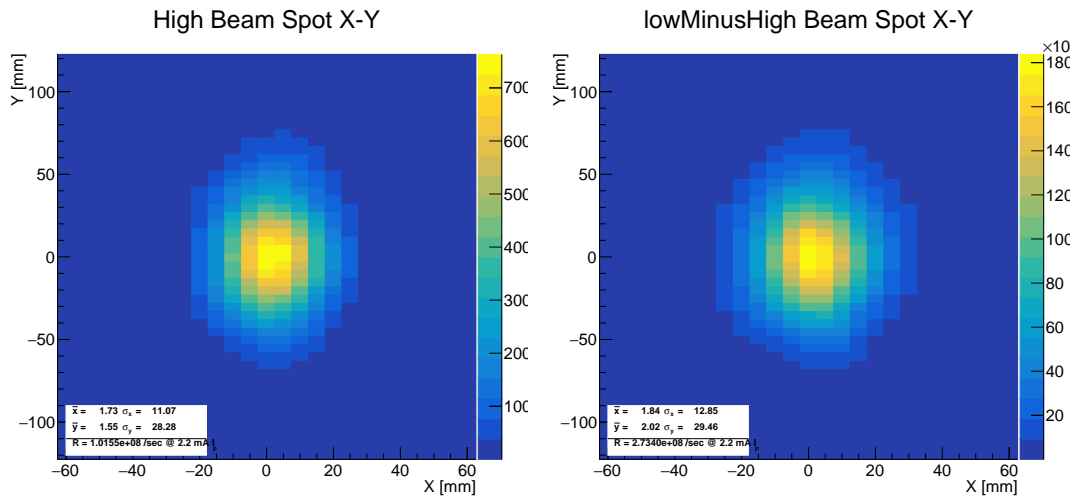


Figure 5.42: The final calculated raster for beam positrons with the polyethylene sheet at the Mu3e solenoid injection point, after subtracting the fit of the Michel positron background.

The muon beam at the Mu3e injection position using a high threshold discriminator and with the positron-stopper installed in the QSK43 vacuum chamber is shown in Figure 5.43a and the associated low threshold scan is shown in Figure 5.43b where the previous vertical tail associated with beam positrons is now gone. The muon rate with the positron-stopper installed is  $\mathcal{R}_{\mu^+} = 1.02 \cdot 10^8 \mu^+/\text{sec} @ 2.2 \text{ mA } I_p$ . The influence of the positron-stopper in the final positron contamination is shown by the raster scans with  $(\text{C}_2\text{H}_4)_n$  placed on the beam pipe vacuum window, and measured with low threshold and low threshold with an RF-coincidence are shown in Figure 5.44a and Figure 5.44b respectively. The ratio of these scans is shown in Figure 5.44c. The bins classified as predominantly Michel positrons using Figure 5.44d are shown in Figure 5.45a fitted with a 2D gaussian distribution. The bins dominated by beam positrons are shown Figure 5.45b. Again, the beam positron spot is extended along the y-axis covering the Michel spot, but the bin ratio classifier method is still capable of separating the two. The final beam positron contribution after subtracting the estimated Michel contribution is shown in Figure 5.46. The estimated beam positron rate at the Mu3e solenoid injection using beam optics for optimal transmission through the CMBL with the positron-stopper in TII is  $\mathcal{R}_{e^+} = 6.53 \cdot 10^6 e^+/\text{sec} @ 2.2 \text{ mA } I_p$ . This is a factor 15 reduction of beam positrons reaching the Mu3e detector region, compared to no positron-stopper or a factor 54 reduction to the number of beam  $e^+$  at the collimator without stopper.



(a) Raster scan of muon beam using a high threshold discriminator. (b) Raster scan of muon beam using low threshold discriminator after subtracting the high threshold component.

Figure 5.43: Raster scan of the beam at the Mu3e solenoid injection position with the positron-stopper installed in TII.

The muon and beam positron rates are listed in Table 5.5 without the lead positron-stopper and in Table 5.6 with the stopper. Both the rates at the collimator intermediate focus position and final focus position before injection to the Mu3e solenoid are given.

The positron-stopper reduces the rate of beam positrons reaching the Mu3e solenoid injection by 93%. The increase in the muon rate between to setups is a result of slightly better optimization of some beamline elements.

An extensive study of the beam-correlated background in the CMBL showed an unexpectedly high transmission for beam  $e^+$  at the collimator, which was not seen at the same location for the MEG beam optics. Investigation showed that for the high transmission optics for the CMBL an unacceptably large number of beam  $e^+$  were re-centered after the separator due to the TII focusing properties. A simple test solution using a lead positron-stopper in TII reduced this background at the Mu3e injection point by a factor 54 compared to the rate at the collimator without stopper. From this the method of stopping the muons in  $(C_2H_4)_n$  has been developed along with an analysis technique to extract the beam positron content from Michel positrons. This procedure can be repeated at the beginning of each Mu3e run period during the typical beam setup, to ensure a good beam quality. The impact of the residual contamination on the Mu3e experiment is investigated in the following section.

	Collimator Position	Mu3e Injection
$\mathcal{R}_{\mu^+}$	$1.42 \cdot 10^8$	$1.13 \cdot 10^8$
$\mathcal{R}_{e^+}$	$3.52 \cdot 10^8$	$9.50 \cdot 10^7$

Table 5.5: Beam particle rates measured in  $\pi E5$  channel optimized for muon rate transmission to Mu3e Injection without  $e^+$  stopper in TII. Rates are for a 60 mm Target E and normalized to 2.2 mA  $I_p$ .

	Collimator Position	Mu3e Injection
$\mathcal{R}_{\mu^+}$	$1.62 \cdot 10^8$	$1.02 \cdot 10^8$
$\mathcal{R}_{e^+}$	$1.16 \cdot 10^7$	$6.53 \cdot 10^6$

Table 5.6: Beam particle rates measured in  $\pi E5$  channel optimized for muon rate transmission to Mu3e Injection with  $e^+$  stopper in TII. Rates are for a 60 mm Target E and normalized to 2.2 mA  $I_p$ .

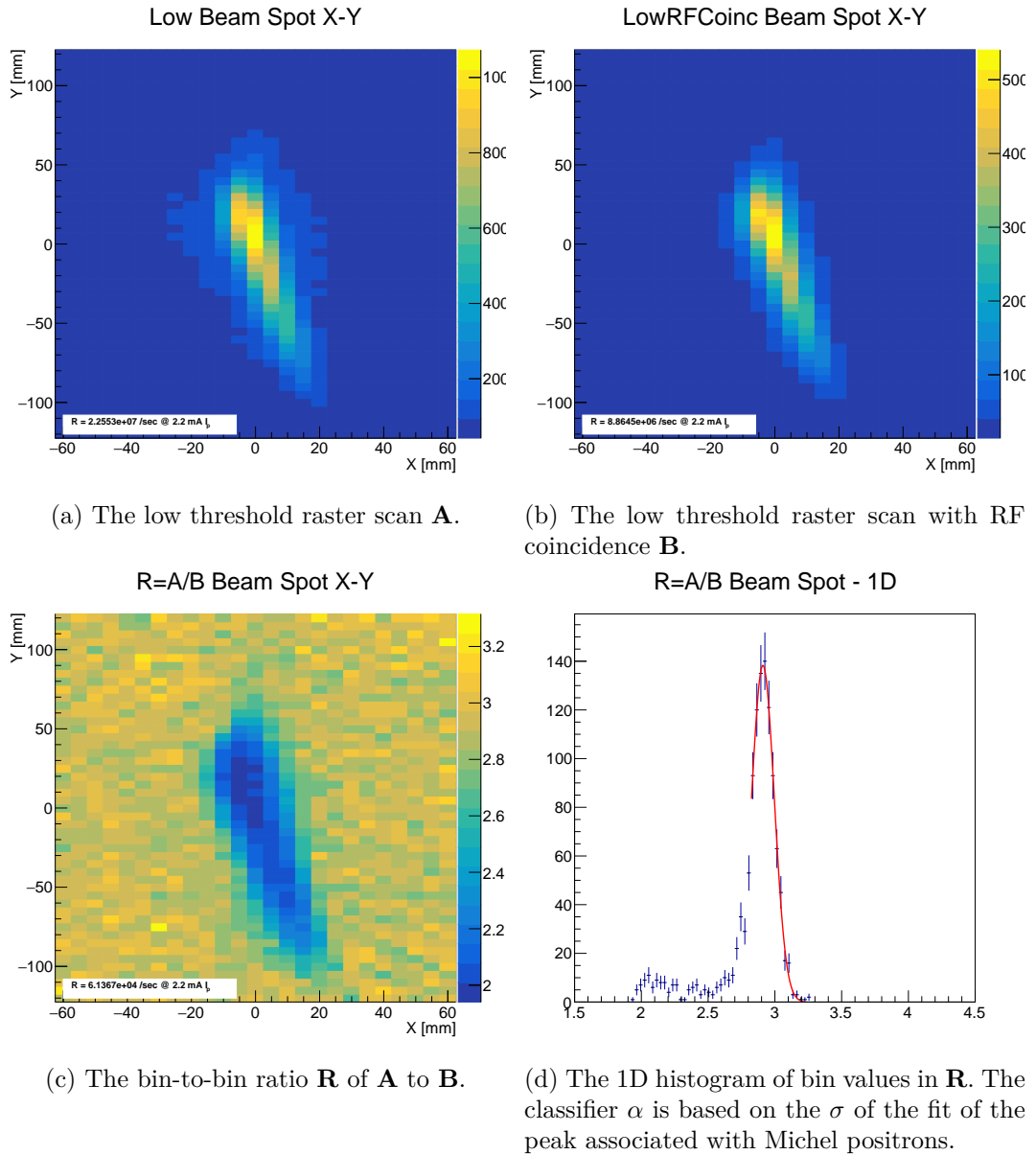
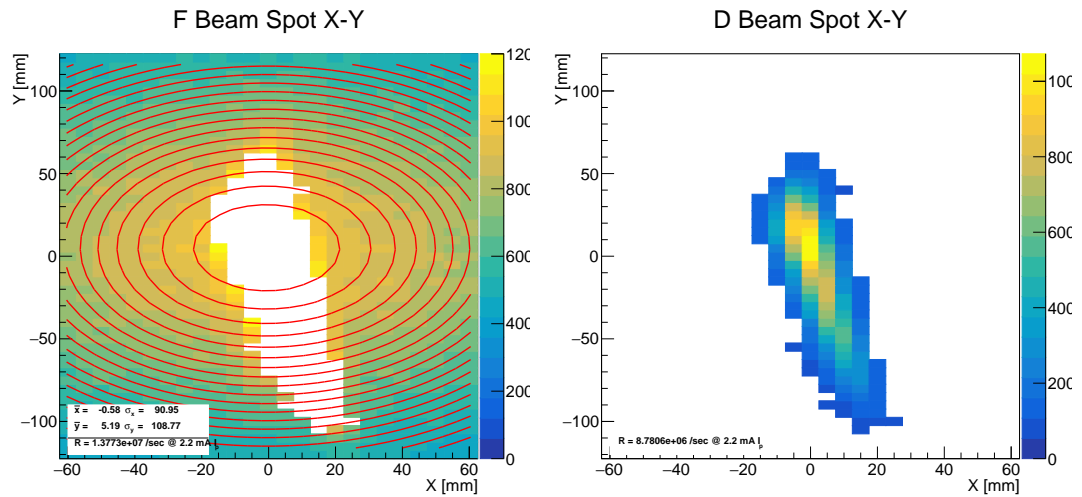


Figure 5.44: The measured raster scans at the Mu3e solenoid injection focus, with the positron-stopper, using polyethylene to stop muons and extract the underlying beam positron contamination.



(a) The **F** raster generated by filling bins of **A** classified as Michel positrons. (b) The **D** raster generated by filling bins of **A** classified as beam positrons.

Figure 5.45: The rasters for Michel and beam positrons at the Mu3e solenoid injection focus, without the positron-stopper, generated by filling bins of **A** based on the classifier  $\alpha$ .

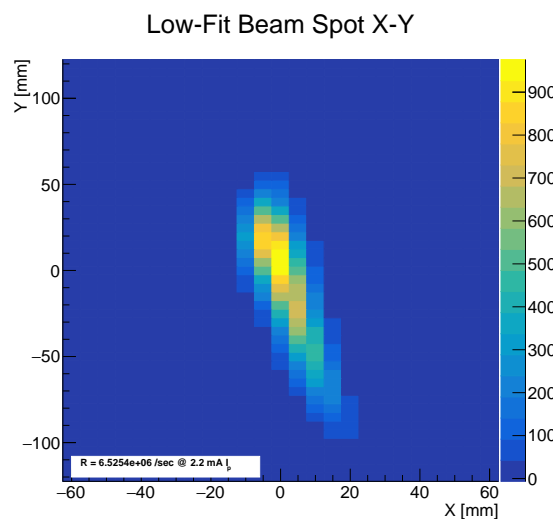


Figure 5.46: The final calculated raster for beam positrons with the polyethylene sheet at the Mu3e solenoid injection point with the positron-stopper in TII, after subtracting the fit of the Michel positron background.

## 5.5 Impact on the Mu3e Sensitivity

The impact of beam positrons delivered to the experiment as an undesired beam contamination is determined by the number of additional Bhabha pairs generated in the Mu3e muon stopping target region. Background events in the Mu3e detector are minimized through a multifold suppression in timing, kinematics, and common vertex requirements. A simplified simulation in G4Beamline is used, including the Mu3e solenoid, muon stopping target, and placeholder structures for the inner layers of vertex tracker without full track reconstruction. The reconstruction efficiency and background suppression performance is taken from previous simulations done using the full Mu3e simulation framework. The number of additional Bhabha pairs that contribute to background events is determined relative to the number of beam positrons reaching the target.

Due to the kinematic constraints on the  $e^+e^-e^+$  invariant mass, the only contributions beam positrons have to background events is through their combinations with muon decay-in-flight. Each of the beam-correlated background processes and beam positron combinations in Bhabha pair production are described in Section 5.1.1.

The probability for an  $e^+e^-e^+$  signature with invariant mass within the Mu3e signal region for a positron originating from a muon decay-in-flight and overlaps with a high energy beam positron that undergoes Bhabha scattering, **Process B**, is given by the following expression,

$$\mathcal{P}_{e_\mu^+ e_B^+ \rightarrow e^+ e^- e^+}^B = \mathcal{P}_{2e_\mu^+ \rightarrow e^+ e^- e^+} \frac{\mathcal{P}_{e_B^+ \rightarrow e^+ e^-} \mathcal{R}_{e_B^+} \mathcal{P}_{e_\mu^+} (E > 64 \text{ MeV})}{\mathcal{P}_{e_\mu^+ \rightarrow e^+ e^-} \mathcal{R}_{\mu^+} \mathcal{P}_{e_\mu^+} (E < 52.8 \text{ MeV})} \quad (5.13)$$

and the probability for the analogous **Process D**, whereby a positron from decay-in-flight undergoes Bhabha scattering and overlaps with a high energy beam positron, is given by the following expression,

$$\mathcal{P}_{e_\mu^+ e_B^+ \rightarrow e^+ e^- e^+}^D = \mathcal{P}_{2e_\mu^+ \rightarrow e^+ e^- e^+} \frac{\mathcal{R}_{e_B^+} \mathcal{P}_{e_\mu^+} (E > 64 \text{ MeV}) \mathcal{P}_{e_B^+} (E > 30.6 \text{ MeV})}{\mathcal{R}_{\mu^+} \mathcal{P}_{e_\mu^+} (E < 52.8 \text{ MeV}) \mathcal{P}_{e_B^+} (E < 30.6 \text{ MeV})} \quad (5.14)$$

where

- $\mathcal{P}_{2e_\mu^+ \rightarrow e^+ e^- e^+}$  is the probability of two Michel positrons from stopped muons, one of which undergoing Bhabha scattering, and all are seen in the Mu3e detector with common timing and vertex.
- $\mathcal{P}_{e_\mu^+ \rightarrow e^+ e^-}$  is the probability of a Michel positron from a stopped muon undergoing Bhabha scattering, where both  $e^+e^-$  hit the inner tracking layer and originate from the target region

- $\mathcal{P}_{e_B^+ \rightarrow e^+e^-}$  is the probability of a beam positron undergoing Bhabha scattering and both  $e^+e^-$  hit the inner tracking layer and originate from the target region
- $\mathcal{P}_{e_\mu^+}$  ( $E > 64$  MeV) is the probability of a high energy positron originating from decay-in-flight hitting the inner tracking layer and originate from the target region and  $\mathcal{P}_{e_\mu^+}$  ( $E < 52.8$  MeV) is the probability of a positron from stopped muon decay hitting the inner tracking layer and originate from the target region
- $\mathcal{P}_{e_B^+}$  ( $E > 30.6$  MeV) is the probability of a high energy beam positron hitting the inner tracking layer, and  $\mathcal{P}_{e_B^+}$  ( $E < 30.6$  MeV) is the probability of a standard beam positron hitting the inner tracking layer
- $\mathcal{R}_{\mu^+}$  is the muon rate on target
- $\mathcal{R}_{e_B^+}$  is the beam positron rate on target

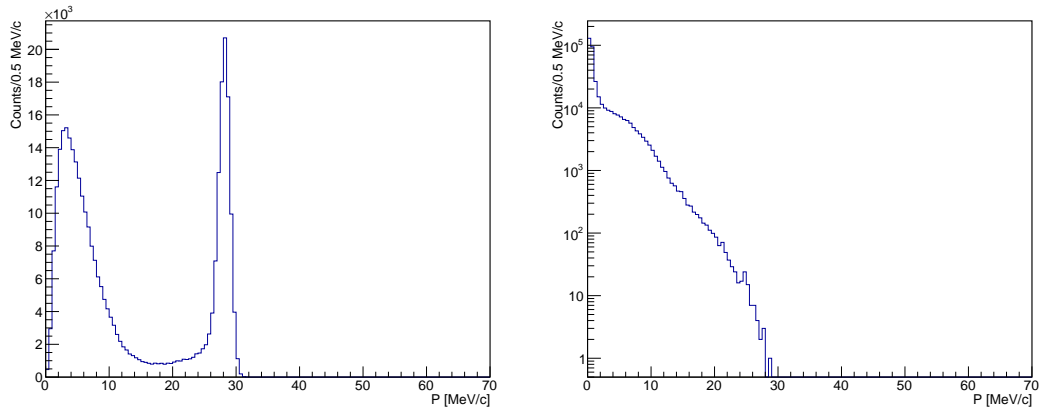
The number of Michel positrons that produce a Bhabha pair in the target region which are then seen by the first silicon vertex layer is taken from [27] and is  $7.8 \cdot 10^{-5}$  per stopped muon. Using the full reconstruction framework, the expected number of background events from an overlapping Bhabha pair and an additional Michel positron is  $\mathcal{P}_{2e_\mu^+ \rightarrow e^+e^-e^+} < 3.342 \cdot 10^{-15}$  @ 90% CL per stopped muon. Using a simplified simulation of the Mu3e detector in G4BL, a 28 MeV/c positron beam with 0.84 MeV/c momentum spread in a spatial distribution with  $\sigma_x=10$  mm and  $\sigma_y=23.5$  mm which begins 1.5 m upstream of the target center. The momentum of positrons and electrons that originate from a Bhabha scattering event from a beam positron and both particles are seen by the inner silicon tracking layer are shown in Figure 5.47. From the simulation with  $6.1 \cdot 10^9$  beam positrons incident on the muon stopping target, there are no Bhabha pairs with transverse momentum greater than 10 MeV/c hitting the first silicon vertex tracker layer and originating from the target region. The probability for a beam positron below 30.6 MeV/c hitting the inner tracking layer is  $\mathcal{P}_{e_B^+}$  ( $E < 30.6$  MeV) =  $4.394 \cdot 10^{-2}$  per incident beam positron. The high-side tail of the beam positron momentum spectrum that hits the inner tracking layer is shown in Figure 5.48a for those hits above 30.6 MeV/c. The probability for a high energy beam positron hitting the inner tracking layer is  $\mathcal{P}_{e_B^+}$  ( $E > 30.6$  MeV) =  $2.319 \cdot 10^{-5}$  per beam positron on target. The probability for Michel positron below 52.8 MeV/c from the target region hitting the tracking layer is  $\mathcal{P}_{e_\mu^+}$  ( $E < 52.8$  MeV) = 1.079 per incident muon. This probability is greater than unity due to the normalization of muons reaching the target region is recorded by a virtual detector with the same radius of the target (19 mm), 1 mm upstream of the upstream section target cone tip. Muons with a helical path that does not intersect this virtual detector can still travel inside the target region and decay. The high side tail of Michel positron tracks hitting the inner tracking layer is shown in Figure 5.48b, and for  $4.6 \cdot 10^7$  muons on target there are no

Michel positrons above 64 MeV from muon decay-in-flight originating from the target region and seen by the inner tracking layer.

From this, and using the measured muon and beam positron rates of  $\mathcal{R}_{\mu^+} = 1.02 \cdot 10^8 \mu^+/\text{s}$  and  $\mathcal{R}_{e_B^+} = 6.53 \cdot 10^6 e^+/\text{s}$ , the upper limit on the probabilities for the two primary beam-correlated backgrounds are set at

- $\mathcal{P}_{e_\mu^+ e_B^+ \rightarrow e^+ e^- e^+}^B < 5.38 \cdot 10^{-28}$  @ 90% CL per beam positron on target
- $\mathcal{P}_{e_\mu^+ e_B^+ \rightarrow e^+ e^- e^+}^D < 5.55 \cdot 10^{-27}$  @ 90% CL per beam positron on target

This is twelve orders of magnitude below the dominant background process of Bhabha production from Michel positrons and will therefore have no impact on the sensitivity of the Mu3e Phase-I experiment.



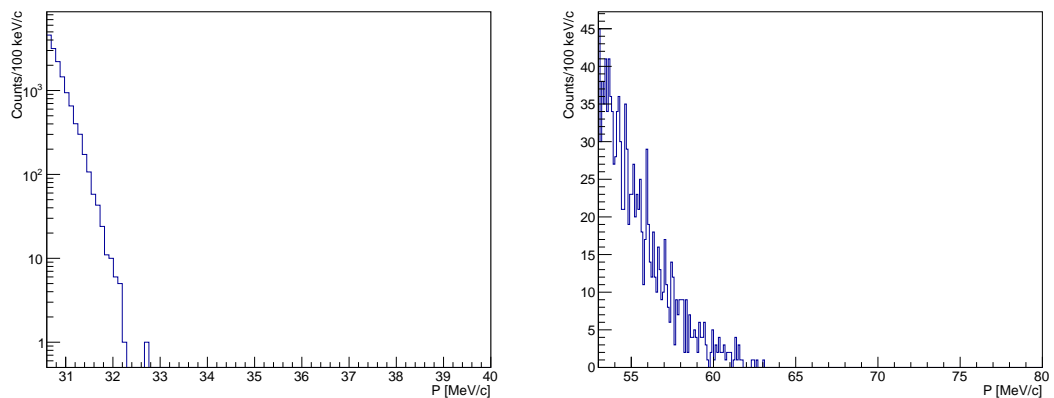
(a) The momentum spectrum of beam positrons that Bhabha scatter and are seen by the inner tracking layer. The low momentum peak is due to beam positrons passing through the material of the collimator in the beampipe upstream.

(b) The momentum spectrum of electrons that originate from Bhabha scattering of beam positrons and are seen by the inner tracking layer.

Figure 5.47: The momentum spectrum of positrons and electrons that participate in Bhabha scattering as a result of beam positrons and are subsequently seen by the inner tracking layer.

Beam positrons can however have an additional influence on the experiment by increasing the hit rate on the inner silicon tracking layers. The total number of beam positrons hitting the inner tracking layer is  $2.85 \cdot 10^{-3}$  per beam positron upstream of the collimator in the Mu3e beam pipe. Additionally, the collimator can act as source of electrons as a result of muons and beam positrons passing through the lead. The number of electrons or positrons originating from the muons passing through the collimator that hit the inner tracking layer is  $3.89 \cdot 10^{-3}$  per incident muon. The number of electrons or positrons originating from the beam positrons passing through the collimator that hit the inner tracking layer is  $3.92 \cdot 10^{-3}$  per incident positron. The relative contribution of hits in the inner tracking layer from beam positrons is

approximately equal to those from muons, but because the beam positron rate is two orders of magnitude lower, the absolute contribution will be negligible.



(a) The falling momentum spectrum above 30.6 MeV/c of beam positrons that hit the inner tracking layer.

(b) The falling momentum spectrum above 52.8 MeV/c of positrons from a muon decay-in-flight that hit the inner tracking layer.

Figure 5.48: Momentum spectra for high momentum positrons in the inner tracking layer.

## 5.6 Summary

The Mu3e experiment is searching for the very rare decay of a muon to two positrons and an electron and there are several processes that can mimic this signal, generating backgrounds for the experiment. The dominating process is the Bhabha scattering of a positron, overlapping in time and space with another positron. Bhabha scattering from Michel positrons is currently the most probable source of backgrounds for Mu3e, but additional sources of positrons, such as beam positrons, could contribute substantially if their rates are high. Reducing or eliminating the beam positrons that can contribute to Bhabha scattering is a way of further reducing background events.

The full  $\pi E5$  beamline has been simulated in G4BL, beginning with pion production via proton collisions in Target E and subsequent muon production and transport through the channel. The beamline has been partially optimized, beginning with the ASC41 and AST41 dipole magnet through to the final focus at the Mu3e solenoid injection. This provided a check on the HiMB pion production cross section as well as providing a possibility to investigate methods to reduce the beam positron transport to the Mu3e detector region, such as a lead collimator positron-stopper in TII and a symmetric potential and enhanced field gradient in the SEP41. The lead collimator positron-stopper does reduce the beam positron content, but the 395 kV symmetric potential SEP41 which eliminated all beam positrons at the Mu3e solenoid injection in the G4BL simulation.

Measurements of the muon rate and beam positron rate at two critical locations in the  $\pi E5$  beamline have been carried out. A method has been developed to separate the beam positrons from Michel positrons in raster scans of the beam through the use of  $(C_2H_4)_n$  polyethylene to stop the muons, and has been tested using the reduced separation power of SEP41 and accurately reproduces the expected positron to muon ratio from production kinematics. The muon rate of  $1.02 \cdot 10^8 \mu^+/\text{sec}$  with the positron stopper in place, meets the requirements for the Mu3e Phase-I experiment, with the planned upgrade of the Wien filter (SEP41) this number is expected to further increase, as demonstrated.. The use of a lead collimator positron-stopper in TII was tested in  $\pi E5$  and shows sufficient reduction in beam positrons reaching the Mu3e solenoid injection to  $6.52 \cdot 10^6 e^+/\text{sec}$ . The impact on the sensitivity of the Mu3e Phase-I experiment due to the current levels of beam positrons is negligible, since the contribution to backgrounds is 12 orders of magnitude below the dominant process of Bhabha production from Michel positrons.

---

### Development of a Ultra-Thin CsI(Tl) Luminophore Foil Muon Beam Monitor

---

The muon beam delivered to the MEG II experiment is in excess of  $7 \times 10^7$  per second and even higher for the Mu3e experiment. Monitoring of the muon beam delivery to the BTS and COBRA or the Mu3e solenoid is critical to the long term operation and continuous data collection of the experiments. Any changes to the muon beam or beam line resulting in a loss of muon stops on target is highly undesirable.

Beamline measurements and characterization for the MEG II experiment are usually scheduled at the beginning of the HIPA operation period to allow for the proper setup and calibration of the beamline and to make any necessary adjustments. A two-dimensional transverse beam profile scanner system combined with a small PMT and plastic scintillator is used to measure the beam rates for both muons and positrons individually, using pulse-height discrimination. Because the scanner system must fit between beamline elements and operate in air, the corresponding beamline section must be removed and a vacuum window installed and therefore the scanner system is a destructive system (in terms of beam transmission). Additionally, during the proton accelerator operations period, the muon production target, Target E, can occasionally experience failure either due to mechanical problems or target degradation and must be replaced. The alignment of the proton beam on the new target following the exchange is not necessarily identical, and can noticeably affect the muon rate and position in the secondary beamlines. Therefore it would be advantageous to have a monitoring of these effects throughout MEG II runs without ceasing data-taking to insert the scanner system.

Beamline optimization before the experimental data collection period consists of adjusting individual or groups of beam line elements and observing the effect it has on the muon rate transmission and profile. A typical beam optimization program consists of iterating through the magnet currents and taking two one-dimensional (horizontal and vertical) scans to obtain rate and spatial size information while adjusting elements to deliver maximum rate. A single cross scan with 5 mm steps across the full beam profile takes at minimum 10 minutes. Because the magnet optimization procedure is iterative, a full optimization of such a beamline can take many hours to days. A more robust measurement of the beam profile is obtained with a full two-dimensional raster

scan with a 5 mm step size which delivers spatial x-y correlation information regarding the beam and a somewhat more accurate estimate of the beam rate. This is especially important if the beam is not perfectly gaussian (e.g. from upstream losses) or slightly rotated. A detailed raster scan requires more than an hour to complete.

To overcome these issues, a new beam monitoring system has been developed using ultra-thin CsI(Tl) luminophore foils and a high performance camera system. This beam monitor has been tested in several configurations and with two camera systems and measurements of various beam criteria have been compared to the standard beam profile scanner system. The luminophore beam monitor has subsequently been installed in the vacuum beam pipe in the  $\pi$ E5 beam line and offers an additional online, in situ measurement and monitoring of the beam delivery during experiment operations.

## 6.1 Scintillation Mechanism of CsI(Tl)

Cesium iodide (CsI) is a compound belonging to the alkali halide family and is a common inorganic scintillator used in many fields including particle physics, medical diagnostics, and x-ray imaging. A complete description of the scintillation mechanisms for inorganic and organic compounds can be found in Birks [71] and Knoll [72]. The production of light in inorganic scintillators is a consequence of the electron energy states due to the crystalline structure of the material. The absorption of energy by an electron can raise the electron into the conduction band and leaving behind a positive hole in the valence band. Holes or electrons can also become trapped at vacant lattice sites where negative ions are missing, common in alkali halides [73]. The three paths for de-excitation are through the following,

1. Luminescence centers, where the de-excitation leads to photoemission.
2. Quenching centers, with de-excitation via radiation-less thermal dissipation.
3. Traps, where electrons are stuck until de-excitation via thermal dissipation or acquire thermal energy back to the conduction band.

In a pure inorganic crystal, the recombination of the electron back in the valence band is associated with the emission of a photon, but approximately the same energy would be required to produce an electron-hole pair as that released when the pair recombines. Therefore this is an inefficient process since the emission and absorption spectra will overlap with significant self-absorption. To overcome this inefficiency, small amounts of an impurity, called activators, are added to inorganic scintillators to enhance the probability of visible photon emission during the de-excitation process. These impurities create energy states within the forbidden gap through which the electron can de-excite back to the valence band and is therefore less than the energy

needed to create the electron-hole pair. As a result the emission spectrum is shifted to longer wavelengths and the crystal can be transparent to the scintillation light [71, 72]. A schematic diagram of the band structure for an impurity activated crystal is shown in Figure 6.1. In the case of CsI(Tl) the effect of the thallium activator concentration on the light yield output from the crystal can be seen in Figure 6.2.

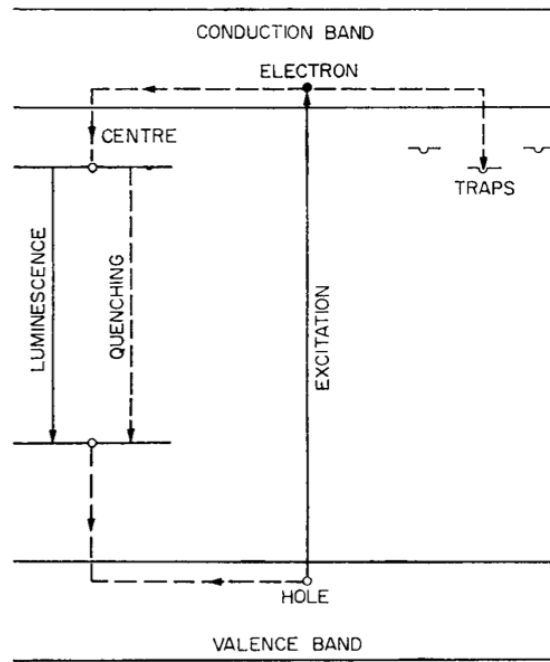


Figure 6.1: The band structure for an impurity activated crystal [71].

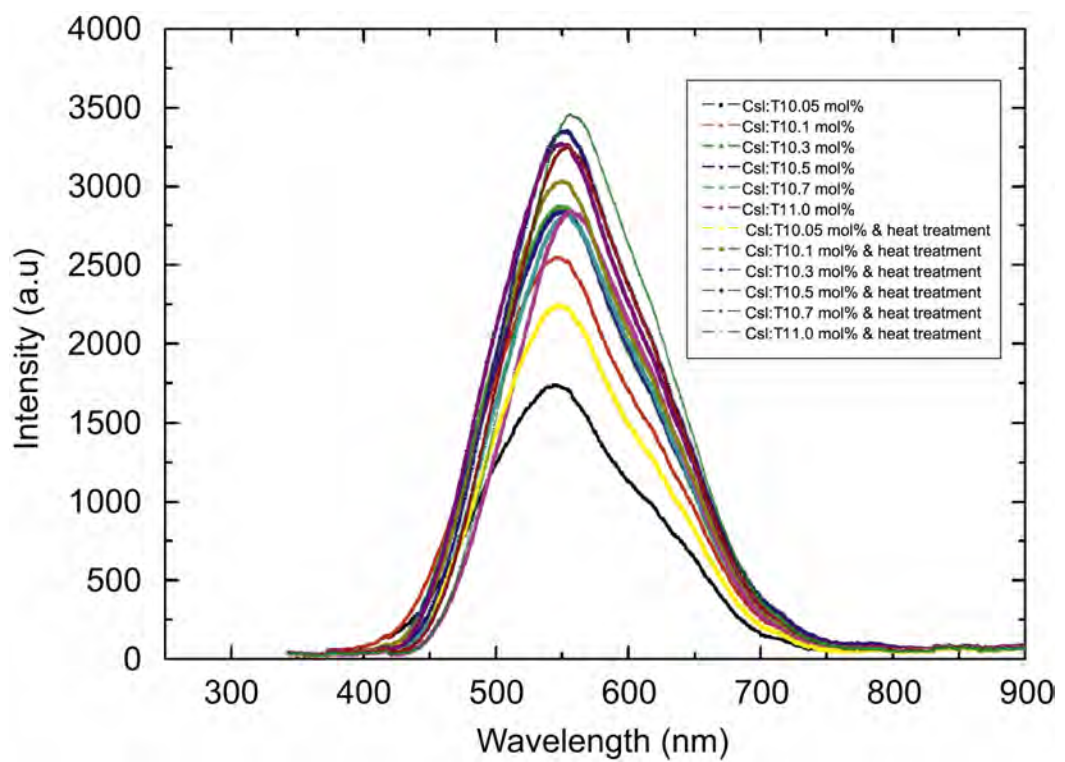


Figure 6.2: The light yield output from a CsI(Tl) crystal with increasing thallium dopant concentrations. Taken from [74]

## 6.2 The CsI(Tl) Foil Muon Beam Monitor

The use of scintillator screens for the detection of particle beams dates back decades, but further development is currently ongoing [75, 76, 77, 78]. As charged particles pass through the active scintillator layer, they will produce scintillation light and the intensity of this light will be proportional to their energy loss. By placing a camera and lens system nearby, some of this light can be collected and imaged using the camera CCD. The spatial distribution of the light generated on the foil provides information on the characteristics of the beam as it passes through. The total light yield in a given time is proportional to the total beam rate. The peak of the distribution is correlated with the peak beam intensity and thus the position of the beam relative to the beamline axis, and the width of the distribution is correlated to the width of the beam passing through.

Typical scintillators are between hundreds of microns to several millimeters thick, enough to highly degrade or stop a low-energy muon. For the use in low-energy muon beams and to be non-invasive, the total material thickness must be significantly reduced, otherwise the beam would be lost in the detector. Additionally, for use in high-rate or continuous monitoring, organic scintillators are generally avoided due to their poor radiation hardness, whereas thin CsI(Tl) foils have proven to be radiation hard up to 75 kGy.

Through the use of chemical vapor deposition, ultra-thin CsI(Tl) layers are possible, reducing the impact on beam transmission [75, 79]. CsI(Tl) can be grown in thin layers on substrates with a columnar microstructure oriented perpendicular to the surface of the layer. Each column has a diameter on the order of 5  $\mu\text{m}$ , and behaves nearly as an optically isolated scintillator [80, 74]. The absolute light yield at room temperature for CsI(Tl) is on the order of 50-60k photons/MeV. Typical layer thicknesses of hundreds of microns are needed for good detection efficiency in X-ray imaging [79]. For low-energy muon detection with CCD imaging, layer thickness on the order of a few microns and integration times of a few seconds are sufficient for good signal collection.

### 6.2.1 The Ultra-Thin CsI(Tl) Foils

The scintillator foils were prepared by MEG collaboration colleagues at BINP in Novosibirsk. The foil production technique followed that described in [81] and were tested using X-rays from the VEPP-3 synchrotron source at BINP. The CsI(Tl) with 0.08 mol% dopant concentration was placed in a tantalum boat reactor where the temperature was raised to 680 C. A low deposition rate of 17  $\text{\AA}/\text{s}$  was set to achieve a homogenous coverage of the scintillator on the rotating glass substrate. The CsI(Tl) film has a granular structure of individual columns with an individual grain size be-

tween 2 and 5  $\mu\text{m}$  and can be seen in Figure 6.3. For use in low-energy muon beams, the glass substrate was replaced with 3  $\mu\text{m}$  MYLAR. Several foils were created with various film thicknesses from 3 to 5.2  $\mu\text{m}$ . An image of one foil with a 5.2  $\mu\text{m}$  layer is shown in Figure 6.4.

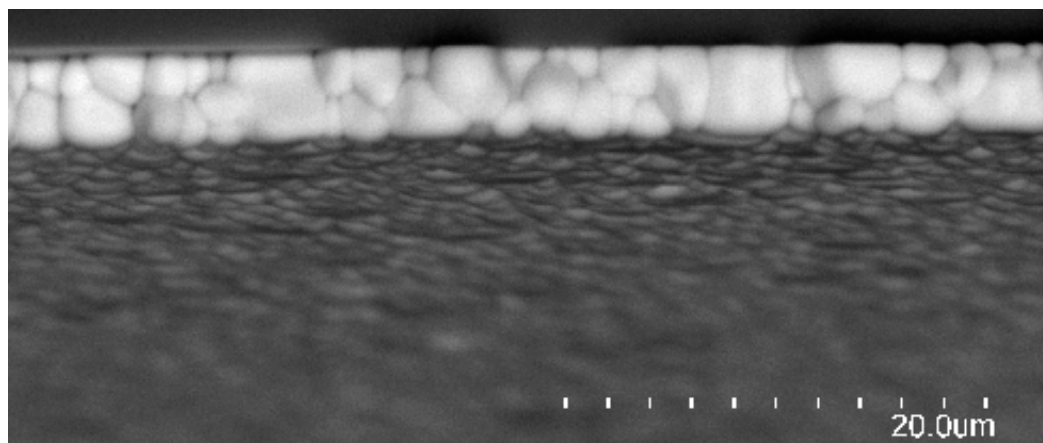


Figure 6.3: The granular structure of a 4.1  $\mu\text{m}$  CsI(Tl) deposited layer on a glass substrate. Individual grain size is on the order of 2-5  $\mu\text{m}$ .

Unlike most scintillator systems that collect their light from the side surfaces, the luminophore foil samples the light through its thinnest dimension and is therefore expected to be less prone to radiation damage effects reducing the attenuation length. An estimate based on the G4Beamline simulation shows an average energy deposition per muon in the CsI(Tl) layer amounts to 20.3 keV. Based on a muon rate of  $10^8 \mu^+ / \text{sec}$  and a  $1\sigma$  beam spot of 20 mm this leads to an absorbed dose of 46 krad per day (460 Gy/day) in the central  $1\sigma$  region of the foil. A fractionated measurement with a 5 MeV electron beam from a ILY-10 industrial accelerator at Novosibirsk, measuring the light yield (LY) after every fractionated dose with a  $^{226}\text{Ra}$   $\alpha$ -source, showed that the LY stayed constant within  $\pm 1.5\%$  up to a integrated dose of 75 kGy, approximately equivalent to one year running time for MEG II.



Figure 6.4: One of the CsI(Tl) luminophore foils used in the muon beam test with a CsI(Tl) layer thickness of  $5.2\mu\text{m}$  on a  $3\mu\text{m}$  MYLAR substrate. The foil diameter is 125 mm.

## 6.2.2 The CCD Camera Systems

Two camera systems were used throughout the development of the beam monitor, and were chosen for convenience and availability and not optimized for the situation of long exposure image capture. Nevertheless, both cameras were adequate for the development of a beam monitor system. A few of the technical specification provided by the manufactures are listed in Table 6.1. The IDS UI-2220SE camera system with a 0.44 MP ICX415AL sensor is a small body, low resolution camera with low performance. The Hammastsu ORCA Flash4.0 model C11440-22C is a high performance, 4 MP, liquid cooled camera system. The ORCA has approximately twice the full well capacity (total charge a pixel can hold before saturation) of the IDS, a critical property for long duration exposures and along with small noise characteristics results in an extended dynamic range. The spectral response for the IDS camera is shown in Figure 6.5a and for the ORCA in Figure 6.5b, where both sensors have a maximum performance between 500 and 600 nm and is well matched with the 560 nm peak emission of CsI(Tl) as shown in Figure 6.2. The ORCA has an internal thermoelectric cooling plate that is regulated using an external water cooling system to maintain the water temperature at 15° C. Both camera systems can be remotely operated by use of an external manually operated trigger that begins the exposure and simultaneously starts a local proton signal scaler. This allows for the normalization of the light intensity to the average proton beam intensity for the duration of the exposure. A raw image of the muon beam taken with the IDS and ORCA cameras are shown in Figure 6.6.

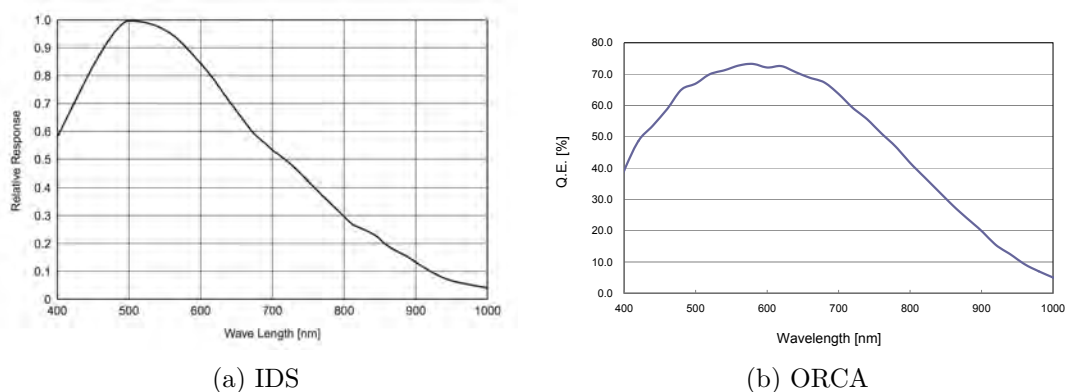


Figure 6.5: The spectral response for the IDS and ORCA camera sensor from 400 to 1000 nm. [82, 83]

Table 6.1: Technical specifications of the IDS and ORCA camera system.

Camera	Resolution [pixels]	Pixel Size [ $\mu\text{m}$ ]	Full Well Capacity [e]	Bit Depth	Peak QE
ORCA C11440-22C	2048 $\times$ 2048	6.5 $\times$ 6.5	30000	16	73% @ 560 nm
IDS UI-2220SE	768 $\times$ 576	8.3 $\times$ 8.3	15300	8	39% @ 533 nm

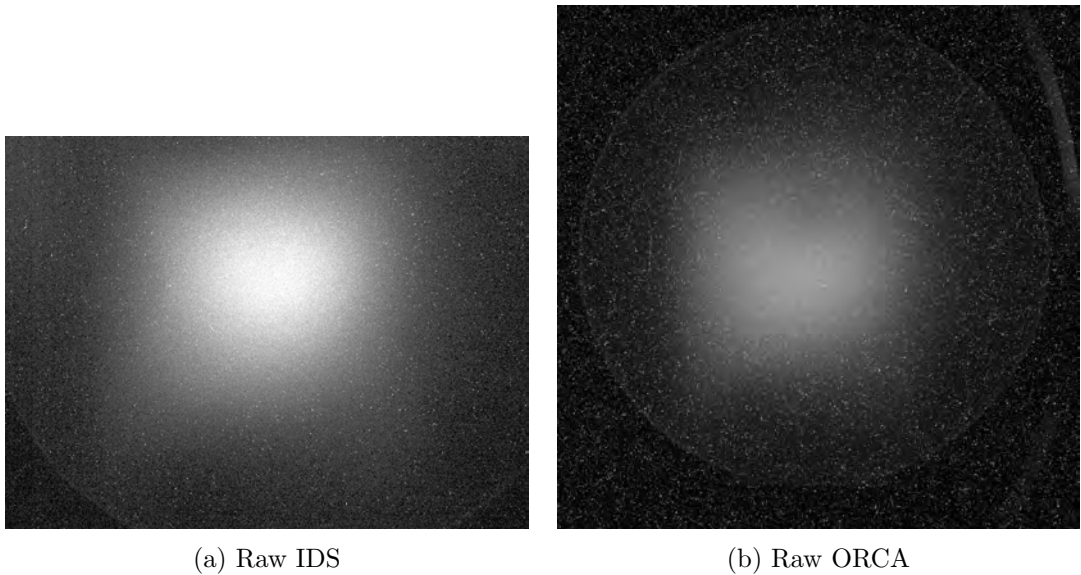


Figure 6.6: Raw images of the muon beam captured from the IDS and ORCA cameras under the same conditions. The contrast and levels have been adjusted to enhance the image visibility.

### 6.2.3 The Detector Setups.

The method employed for muon beam detection using foil imaging with a camera system was developed from an initial setup containing the foil and camera enclosed in a light-tight box, placed in air, downstream of the beam pipe window. A picture of the light-tight box setup is shown in Figure 6.7. The second setup was developed as a semi-permanent installation within the beam pipe allowing a continuous beam monitoring without breaking vacuum. A picture of the luminophore beam monitoring system within the beam pipe is shown in Figure 6.9. The light-tight box setup was also used for the range curve measurements (described below in Section 6.3.4) allowing an increasing number of degrader foils to be inserted into the muon beam in front of the luminophore foil, which would otherwise not be possible when the foil is in the beam pipe under vacuum

The light-tight box was constructed from PVC plastic for the walls and a wooden base plate with all edges sealed with a light tight epoxy. Two perpendicular rail systems were mounted on the base plate allowing for the CsI(Tl) foil and mirror to be fixed along one axis, and the camera system and mirror along the other axis at 90 degrees to the foil-mirror axis. A matte-black cloth was placed on the interior surfaces to reduce light reflection by the metallic structure of the rail system. A calibration grid paper was placed in the foil mount after measurements to determine the pixel-to-millimeter conversion for the corresponding measurement conditions.

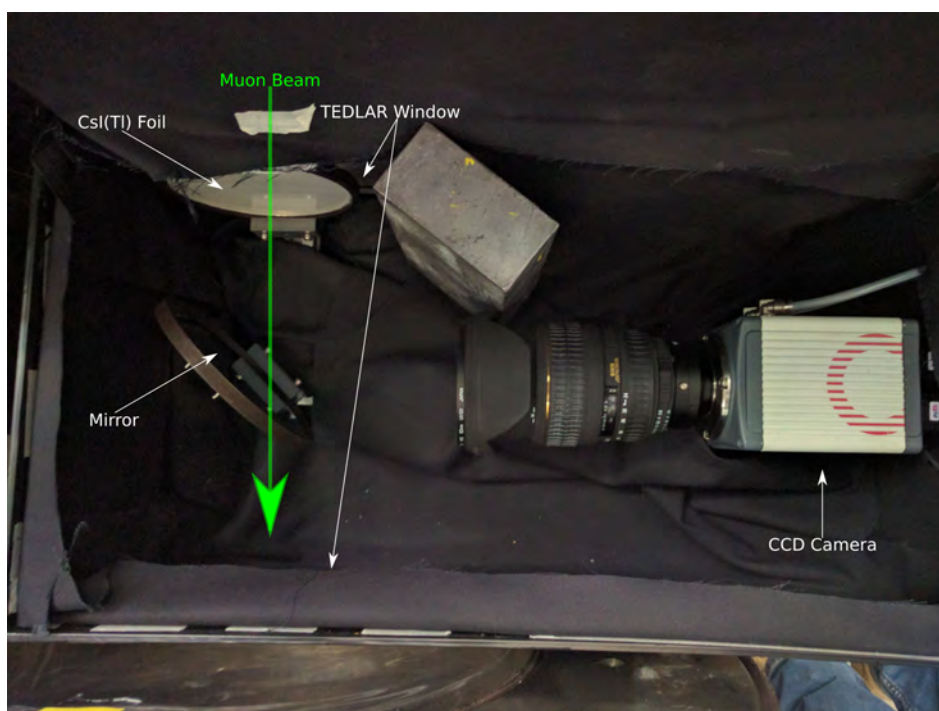


Figure 6.7: The overhead view of the luminophore setup inside the light-tight box.

For measurements in vacuum, a frame was constructed to hold the foil in what was previously a 2 mm thick polyethylene “muon stopper”, immediately upstream of the collimator system currently in place in the MEG beamline, between the TII quadrupole triplet and BTS. The frame is attached to a driveshaft and pulley system that allows one to rotate the foil in and out of the beam via an external hand-knob. A schematic drawing of the luminophore setup in vacuum is shown in Figure 6.8 and photos of the setup in Figure 6.9. A calibration grid design was attached to the surface of the frame which allowed for pixel-to-millimeter conversion at any time during measurements and a corrective perspective transformation due to the angle between mirror and scintillating foil. The scintillating foil and frame were placed inside the beam pipe, under vacuum and imaged with the CCD camera via a mirror system and glass window. The interior of the vacuum pipe can be illuminated with a 285 nm UV LED, which is outside the spectral sensitivity range of the CCD sensors and is used to conduct calibration measurements of the foil and CCD system within the light-tight region. The UV LED can also be used to estimate the scintillation uniformity across the foil. A picture taken with the UV LED showing the fluorescent white paper used for the calibration grid is shown in Figure 6.10. Concurrent and sequential measurements of the muon beam were conducted in air, downstream of the beam window using the pill scanner system described in Chapter 5.

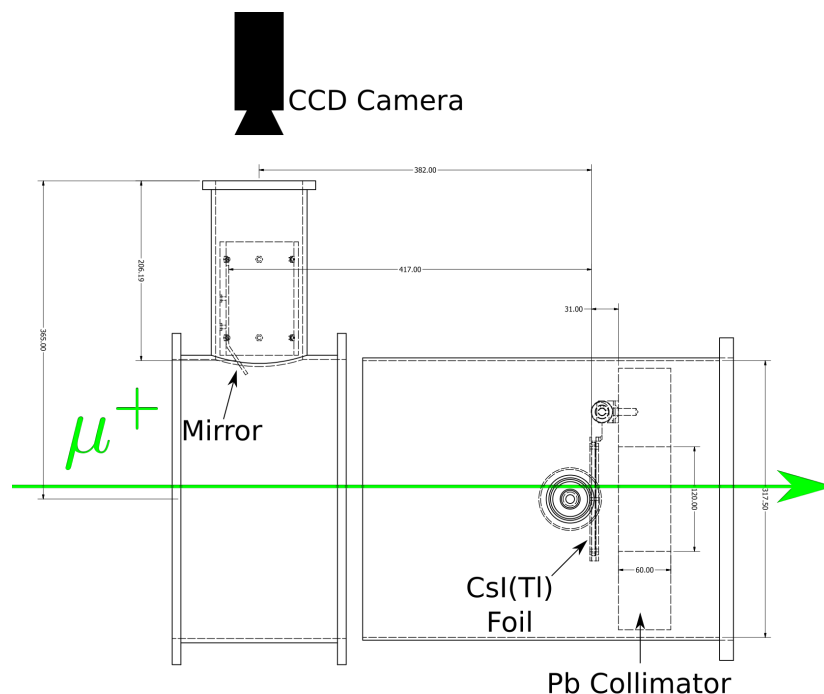


Figure 6.8: Plan-view of the luminophore vacuum setup at the MEG collimator position.



(a) The muon beam monitoring system including the CsI(Tl) foil, rotation mechanism, and mirror to the CCD camera, looking downstream relative to the muon beam. The separate mirror flange and mount are nominally rotated by  $180^\circ$  so that the mirror is on the left-hand side.

(b) The view of the foil in the mirror, along with the mirror mount in the feedthrough flange, as seen from the CCD camera location.

Figure 6.9: Image of the luminophore vacuum setup at the MEG collimator position.

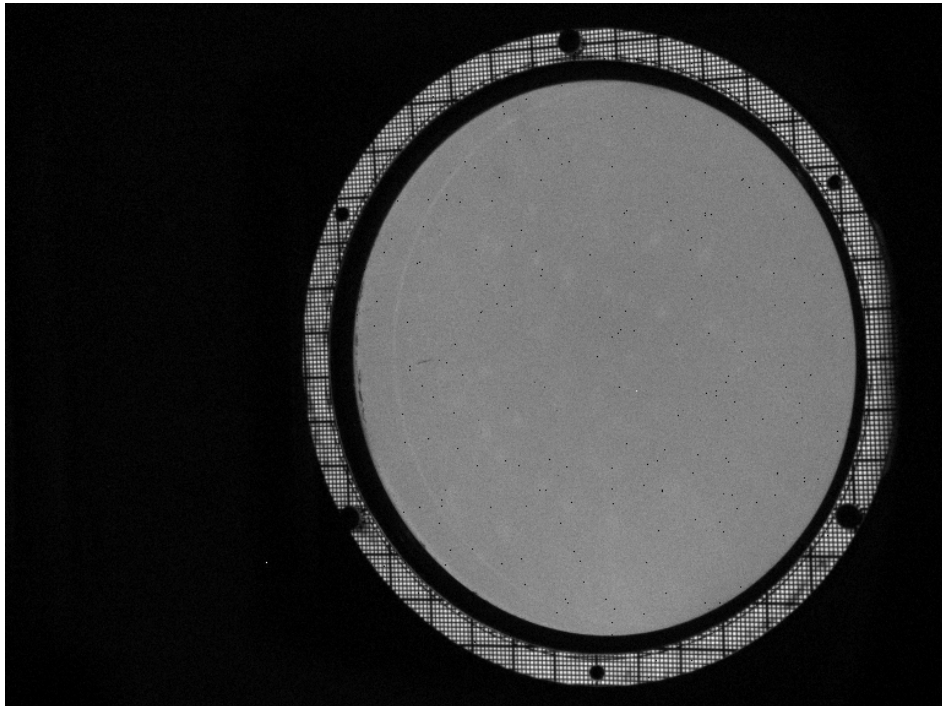


Figure 6.10: Image of the calibration grid using the UV LED installed inside the beampipe. This image was captured with the IDS camera system.

### 6.2.4 Beam Image Analysis

Beam profile imaging consists of taking a set of individual beam exposures and an equivalent set of exposures of the dark current (background) with the muon beam shutter closed, capturing any stray ambient light and the inherent thermal noise of the sensor. The image analysis software is built using the OpenCV library [84] for image manipulation and ROOT [85] for data analysis. Each image is first processed to remove hot-pixels using a simple algorithm that detects individual pixels above the baseline noise and is a relative factor above the surrounding pixels. A perspective transformation is applied to each image, using the transformation matrix determined using the calibration image. Individual pixels are assigned an error using the jackknife resampling technique. The methods for perspective transformation and jackknife resampling are described in Appendix B. The individual pixel values for each image in the set of signal images are summed, normalized to 2 mA proton current and exposure duration, producing a final image for the full exposure.

All signal and background images are summed and averaged to generate a calibrated signal image, which is then reduced to a region of interest excluding the foil frame and support structure. The averaged signal and background images from the set of exposures are given given by the following expressions,

$$\bar{S}_{ij} = \frac{1}{N_{sig}} \sum_k^{N_{sig}} \frac{\epsilon_{sig}}{\epsilon_k} \frac{I_p}{I_{p_k}} S_{ijk} \quad (6.1)$$

$$\bar{B}_{ij} = \frac{1}{N_{bkg}} \sum_k^{N_{bkg}} \frac{\epsilon_{bkg}}{\epsilon_k} B_{ijk} \quad (6.2)$$

where  $N_{sig}$  and  $N_{bkg}$  are the number of signal and background images respectively,  $\epsilon_{sig}$  and  $\epsilon_{bkg}$  is the standard exposure time for signal and background images respectively,  $\epsilon_k$  is the  $k^{th}$  image exposure duration,  $I_p$  is proton current normalization and  $I_{p_k}$  is the average proton current during the image exposure, while  $S_{ijk}$  and  $B_{ijk}$  is the ADC value of the  $i^{th}$  row,  $j^{th}$  column pixel in the  $k^{th}$  signal and background image. The final beam image is then taken as the difference between the average signal image and average background image. Since the number of images for a measurement is low, the individual pixel error is calculated using the jackknife method of error estimation for small samples. The final pixel error is the sum in quadrature of the signal and background error. The final image pixel values and associated errors are given by the following expressions,

$$F_{ij} = \bar{S}_{ij} - \bar{B}_{ij} \quad (6.3)$$

$$\sigma_{ij}^2 = \sigma_{\bar{S}_{ij}}^2 + \sigma_{\bar{B}_{ij}}^2 \quad (6.4)$$

where  $F_{ij}$  is the final value for the  $i^{th}$  row,  $j^{th}$  column pixel and  $\sigma_{ij}$  is the associated pixel variance. This image is then fitted using a 2D correlated gauss function to obtain the central beam position and transverse widths and correlations. The beam profile is fitted using the following expression,

$$f(x, y) = A \cdot e^{-\frac{(a+b-c)}{2(1-\rho^2)}} + C \quad (6.5)$$

$$a = \frac{(x - \bar{x})^2}{\sigma_x^2}$$

$$b = \frac{(y - \bar{y})^2}{\sigma_y^2}$$

$$c = 2\rho \frac{(x - \bar{x})(y - \bar{y})}{\sigma_x \sigma_y}$$

where  $\bar{x}$  is the mean horizontal position,  $\bar{y}$  is the mean vertical position,  $\sigma_x$  is the horizontal width,  $\sigma_y$  is the vertical width,  $\rho$  is the horizontal-vertical correlation describing the beam profile rotation,  $A$  is the scale factor, and  $C$  is a constant offset.

Typical signal and background images for a nominal 100 second exposure using the IDS camera system are shown in Figure 6.11. The background image using the IDS camera has a distinct asymmetry, where the upper left corner has an increased background dark count that is a result of damage from previous use. Since this asymmetry is present in both the background and signal images it will be removed through background subtraction but those pixel will have an increased variance relative to other regions of the sensor. Typical signal and background images for the maximum 10 second exposure using the ORCA camera system are shown in Figure 6.12. The ORCA background image shows a more uniform and flat distribution, which is expected due to the internal thermoelectric cooling of the sensor and the external water cooling as well as the superior sensor.

A constant background can be easily subtracted (while reducing the dynamic range), but the large variance on the background is the limiting factor. The mean signal and background count and background variance for both cameras under the same conditions are listed in Table 6.2. A common measure of the camera performance in digital imaging is the signal to background noise variance ratio which is given by the following expression,

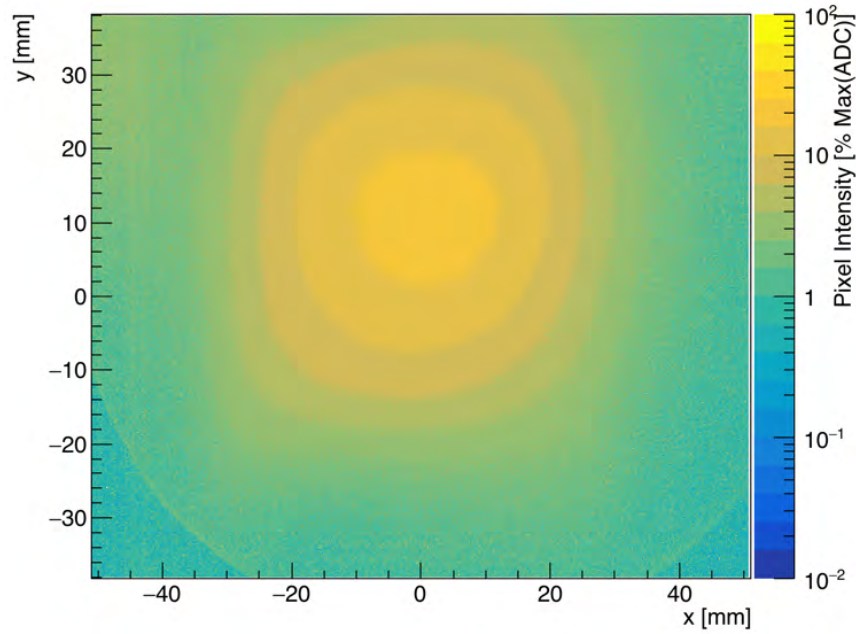
$$S\sigma_N R = 20 \cdot \log_{10} \left( \frac{\bar{S} - \bar{B}}{\sigma_B} \right) \quad (6.6)$$

where  $\bar{S}$  is the mean signal value,  $\bar{B}$  is the mean background value, and  $\sigma_B$  is the variance on the background within the region of interest. Under maximum beam intensity the  $S\sigma_N R_{IDS}=22.8$  dB and  $S\sigma_N R_{ORCA}=47.1$  dB, meaning the ORCA camera has more than a factor 16 higher signal sensitivity. A full scan of the  $S\sigma_N R$  for both cameras was made by varying the muon beam intensity as shown in Figure 6.13, also

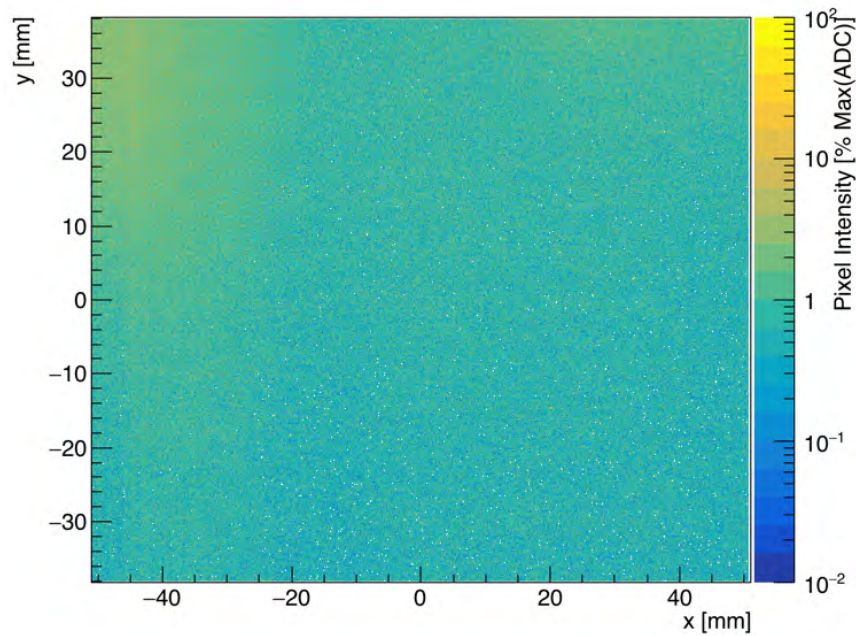
demonstrating that the ORCA outperforms the IDS over the full range of beam intensities. The IDS requires a 10 times longer exposure time to achieve this sensitivity.

	Mean Signal Count [ADC/pixel/sec]	Mean Dark Count [ADC/pixel/sec]	Dark Count Variance [ADC/pixel/sec]
IDS	0.18	0.024	0.012
ORCA	44.5	10.4	0.15

Table 6.2: The mean signal and background count and variance within the region of interest for both the IDS and ORCA cameras.

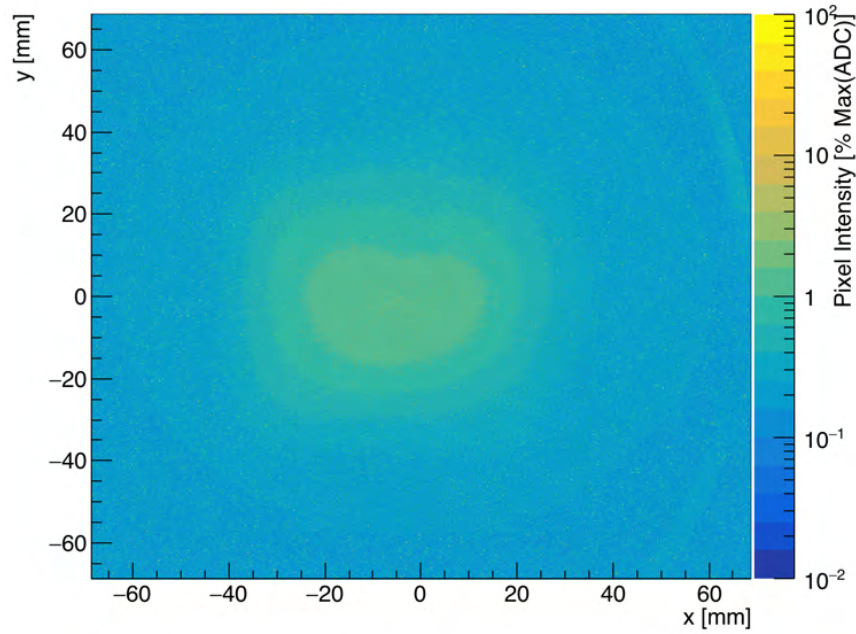


(a) IDS Signal

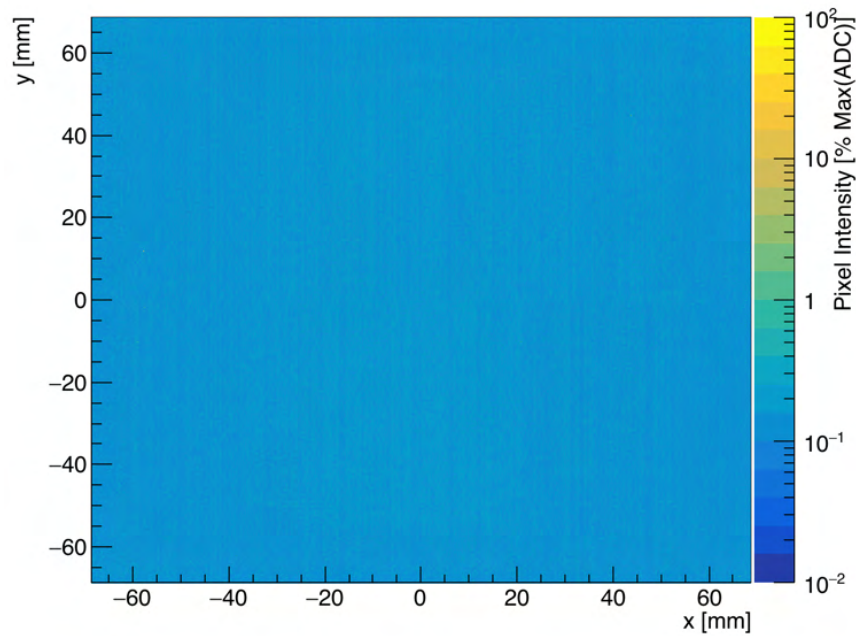


(b) IDS Background

Figure 6.11: The signal and background images captured with the IDS camera system in the light-tight box for a 100 second exposure at nominal muon beam intensity. The pixel values are in percent of the maximum ADC value and shown in log scale.



(a) ORCA Signal



(b) ORCA Background

Figure 6.12: The signal and background images captured with the ORCA camera system in the light-tight box for a 10 second exposure at nominal muon beam intensity. The pixel values are in percent of the maximum ADC value and shown in log scale.

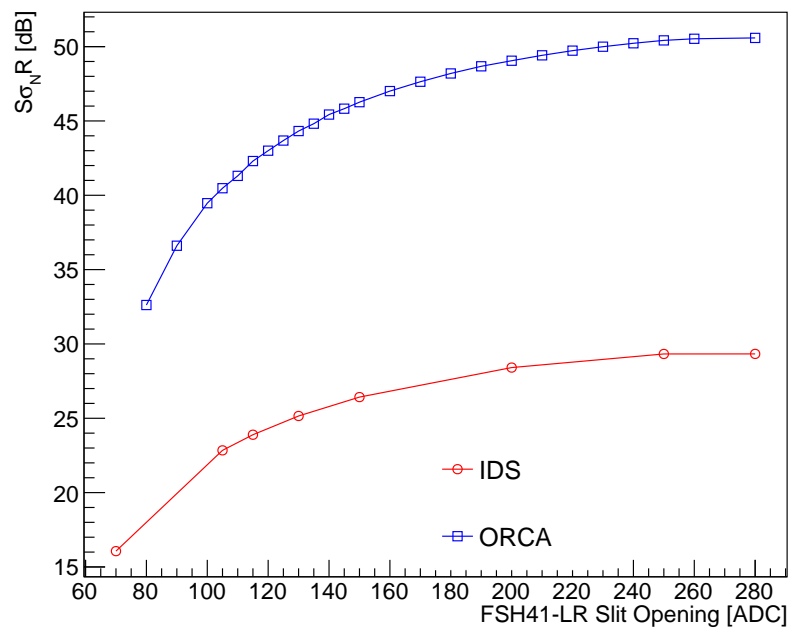
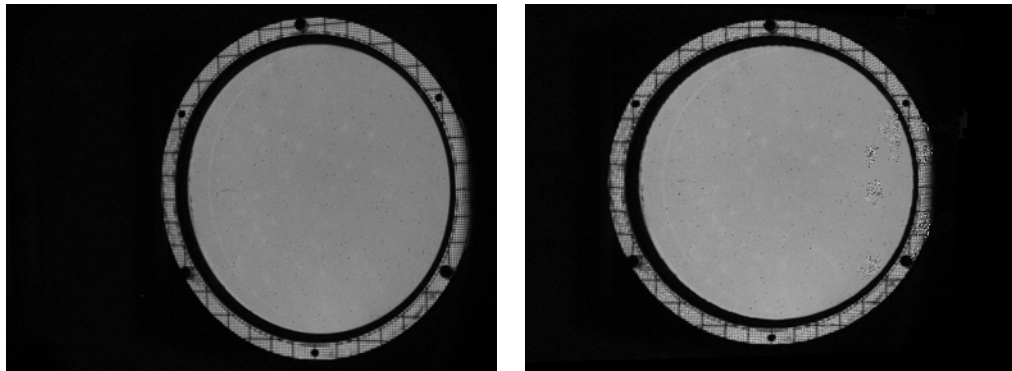


Figure 6.13: The  $S\sigma_N R$  for the IDS and ORCA cameras relative to the muon beam intensity. The muon beam intensity is controlled via the slit system in the middle part of the  $\pi E5$  channel.

### 6.2.5 CsI(Tl) Layer Uniformity

The CsI(Tl) layer uniformity on the foil is estimated by two methods, using the calibration photo taken with UV illumination. The first method relies on the distribution of pixel intensities, and the second uses regional averaging. The perspective transformation is applied to correct for viewing angle and to place the foil near the center of the image. The original and corrected images are shown in Figure 6.14. A background image without UV illumination is subtracted from the signal image to remove hot-pixels. The image is then cut to the region of interest on the foil surface, removing the calibration grid and foil mount from the image.

The two-dimensional spatial histogram of pixel intensities is shown in Figure 6.15, and the associated one-dimensional histogram is shown Figure 6.16. A gaussian fit of the pixel intensity histogram shows a maximum spread in individual pixel intensities of  $18.145 \pm 0.002\%$ . The second method of determining the uniformity relies on the regional averaging of pixel intensities by use of a  $5 \times 5 \text{ mm}^2$  grid overlaying the calibration image. The sum of all pixel intensities within each grid block generates a second two dimensional histogram, and only grid blocks that are fully contained within the region of interest are included. A contour plot of this regionally averaged histogram is shown in Figure 6.17, where the maximum difference between grid blocks is  $13.001 \pm 0.035\%$ . A clear top-bottom asymmetry in pixel intensity is seen in Figure 6.15 and Figure 6.17. Since the UV LED is mounted in a vertical flange on the upper part of the beam pipe to prevent direct illumination, it is possible part of the foil was subject to non-uniform scattered light by the LED and therefore the apparent non-uniformity in the foil light yield response can be attributed in non-uniform illumination from the UV LED. The error on the two uniformity estimates imply they are very underestimated since the layer uniformity from the two methods are incompatible. A dedicated measurement with better uniform illumination of the CsI(Tl) is needed to fully characterize the layer uniformity.



(a) Original image of the CsI(Tl) foil under UV LED illumination.

(b) The image after perspective transformation and centering.

Figure 6.14: The original and corrected images of the luminophore foil in vacuum, under UV LED illumination.

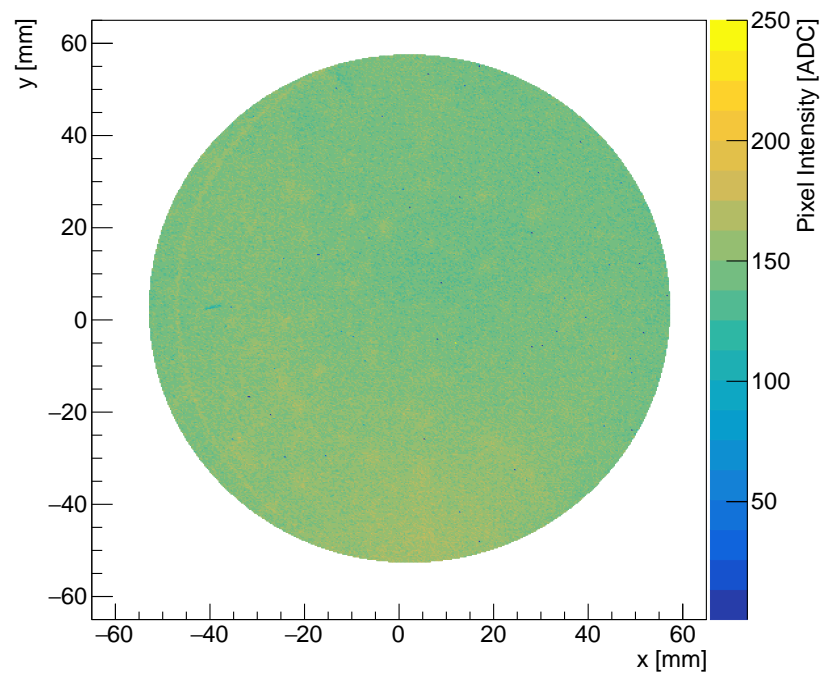


Figure 6.15: The pixel intensity spatial distribution in the region of interest on the CsI(Tl) foil under UV LED illumination.

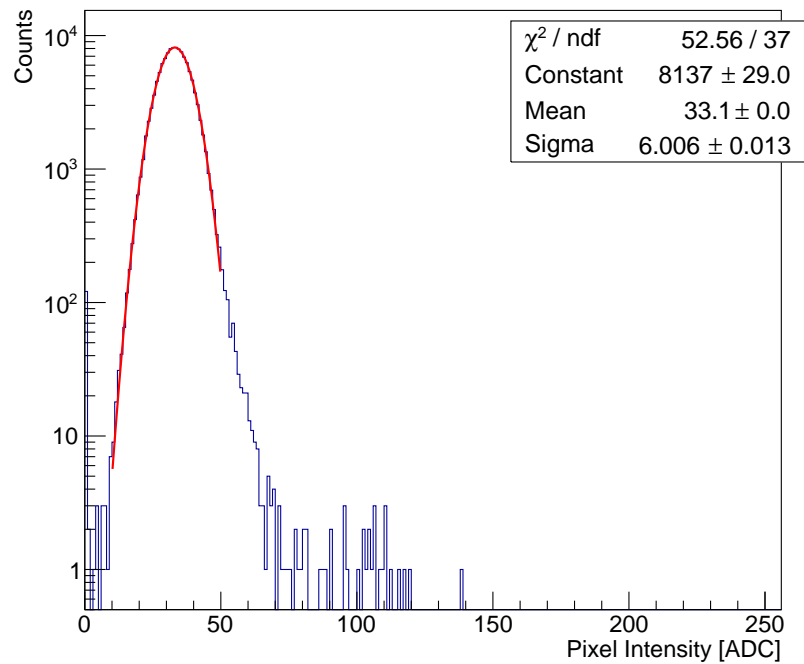


Figure 6.16: The histogram of pixel intensity in the region of interest on the CsI(Tl) foil, and a gaussian fit which indicates the spread in individual pixel intensities. The spread in pixel intensities suggests a uniformity on the order of 18%.

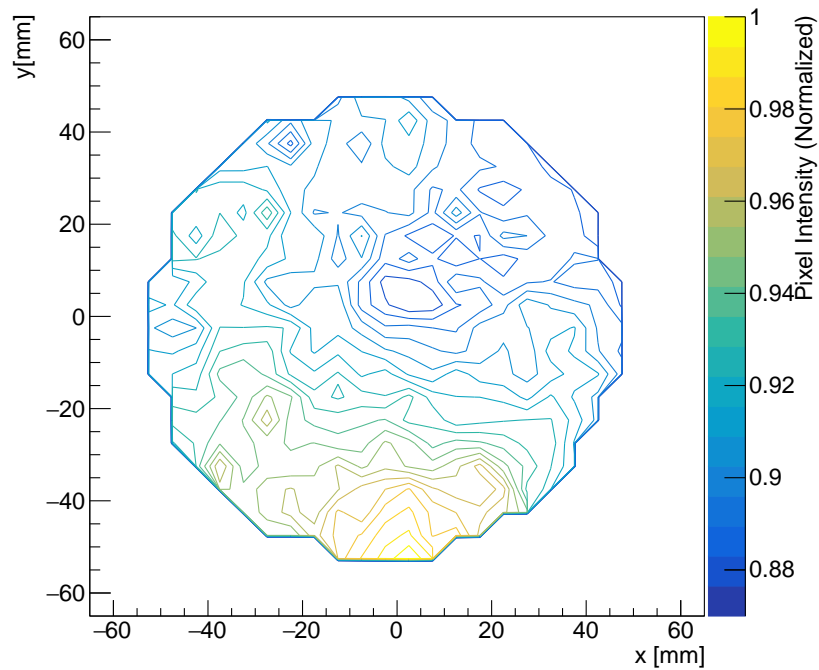


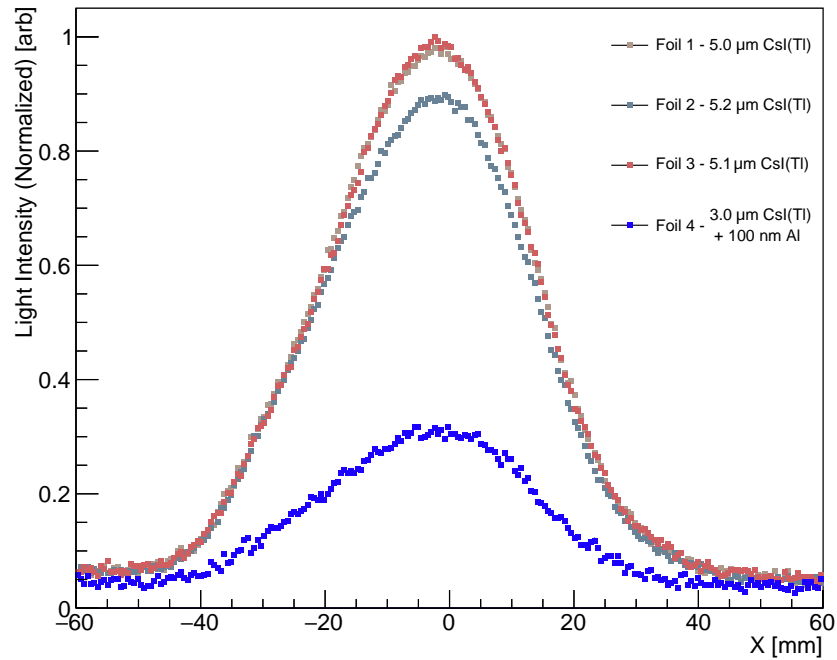
Figure 6.17: The contour plot of regionally averaged pixel intensity spatial distribution using  $5 \times 5 \text{ mm}^2$  grid blocks. The plot is normalized to the maximum grid block intensity, with a 13% difference between minimum and maximum.

### 6.3 Muon Beam Measurements with Thin CsI(Tl) Foils

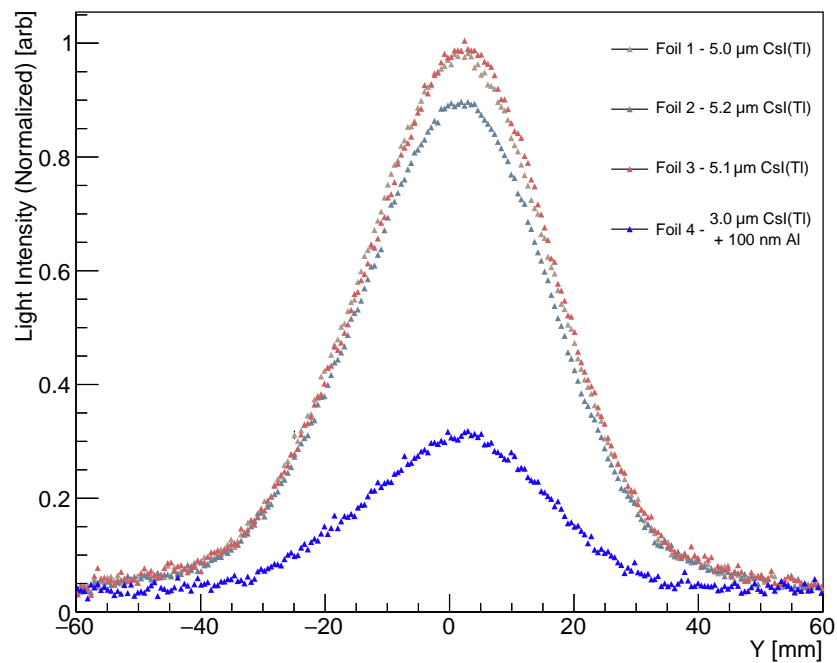
The measurements of the muon beam were carried out using the two different setups (light-tight box and in-vacuum) at two locations along the  $\pi$ E5 channel and CMBL extension. The measurement of muon intensity regulation via the beamline slits was conducted downstream of the QSK43 in air with the light-tight box using the ORCA camera system. The muon range curve measurement to determine the muon central momentum was conducted at the end of the CMBL, downstream of the QSM41, in air with the light-tight box using the ORCA camera system. The muon phase space measurements were conducted downstream of QSK43 using the in-vacuum setup with the IDS camera system. Concurrent and comparative measurements for beam profiles, slit curve, range curve, and phase space were conducted using the pill scanner system.

#### 6.3.1 Beam Profiles

Four separate foils were constructed by our MEG colleagues in BINP using MYLAR as a base structure, with a thin layer of CsI(Tl) applied using chemical vapor deposition. Three foils were created with CsI(Tl) layer thicknesses of 5.0, 5.1, and 5.2  $\mu\text{m}$ , allowing for the comparison and a basic optimization of layer thickness. Additionally, a fourth foil with 100 nm Al layer beneath a 3.0  $\mu\text{m}$  layer of CsI(Tl) was created, such that the Al-layer acts as a mirror to reflect light and increases the total light captured in the camera system. The beam profile projections for all four foils are shown in Figure 6.18a and Figure 6.18b for the x-axis and y-axis respectively. Both horizontal and vertical beam profiles clearly show that foil 2 which has only a 0.1  $\mu\text{m}$  thickness difference to foil 1 and 0.2  $\mu\text{m}$  difference to foil 3, has a 10% lower maximum light yield compared to foils 1 and 3. This suggests that larger thickness differences are required to quantitatively infer the light yield (LY) is proportional to layer thickness and the effect seen here with such small differences in layer thickness are probably due to production variations. Foil 3, due to its LY was chosen as default for the tests. It is uncertain whether the aluminum mirror backing had a significant effect on total light capture, but overall it was considerably lower than any other foil due to the reduced CsI(Tl) layer.



(a) Horizontal Beam Profile



(b) Vertical Beam Profile

Figure 6.18: Comparison of the four foils using the beam profile projection.

Comparison of the beam profile from measurements with the pill scintillator to x-y projections of the luminophore foil image measured in the light-tight box in air are shown in Figure 6.19. Measurements of the beam widths show excellent agreement, whereas differences in the centroid positions is attributed to a misalignment of the foil with respect to the beam line axis during setup.

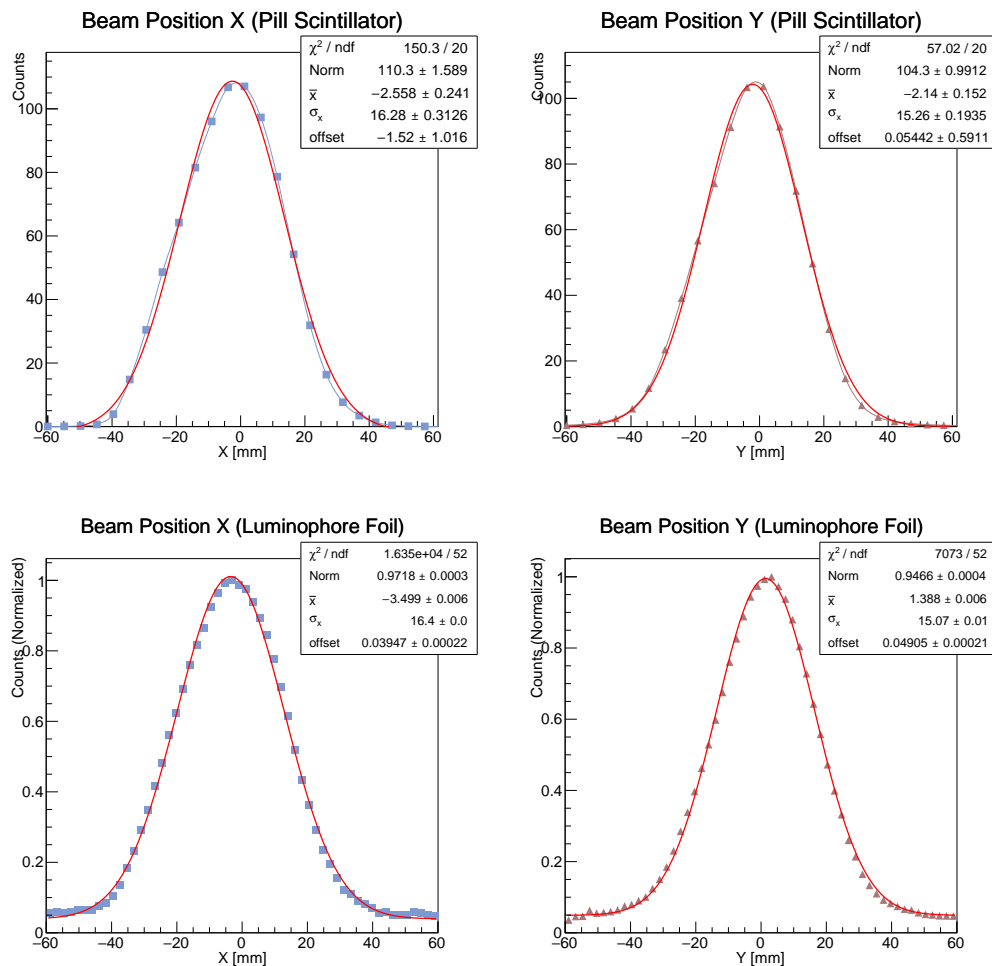
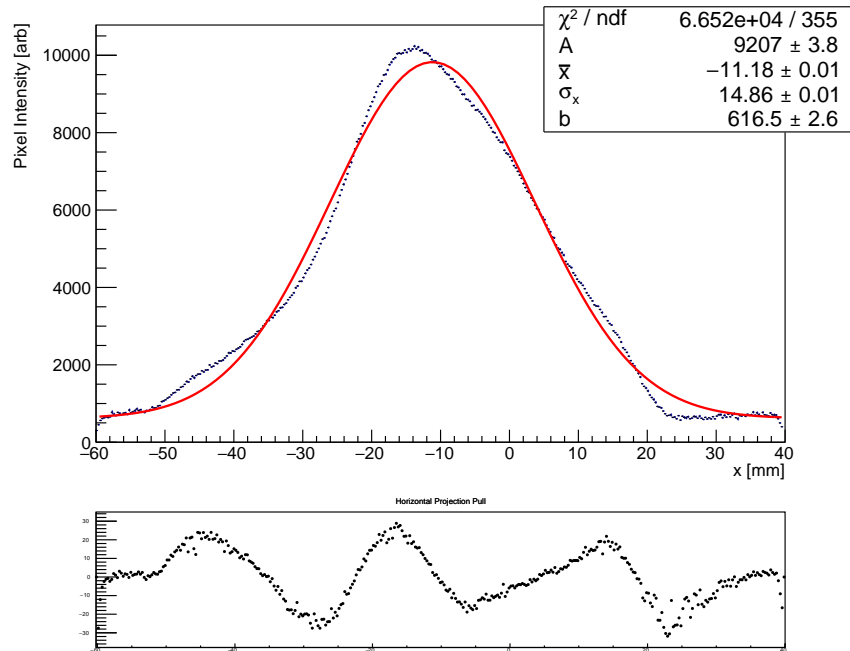


Figure 6.19: The beam profiles in X and Y measured with the pill scintillator in (a) and (b) and the luminophore foil in (c) and (d). Emphasis is on the beam widths, differences in mean positions are attributed to misalignment.

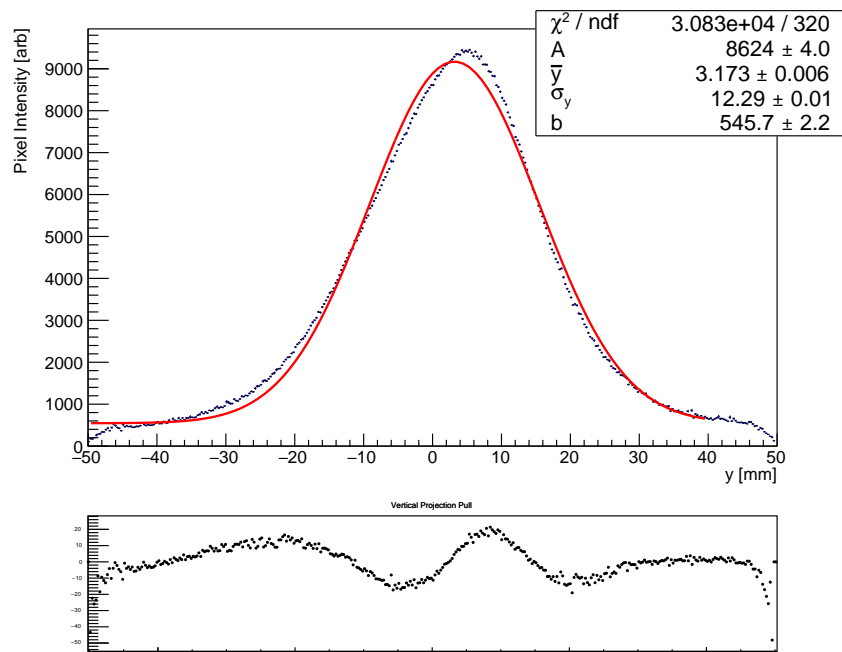
Measurements of the beam profile in vacuum show an interesting beam profile that would otherwise be lost due to the scattering in the beam window and air in front of the detector system. The beam profile and pull for the horizontal and vertical profile projections are shown in Figure 6.20. Both profiles differ significantly from the expected gaussian shape and have a distinctive skew towards the positive x- and y-axes. This suggests higher-order beam aberrations which are normally ‘smeared out’ when measured in air due to the multiple scattering in the vacuum window and air.

The most probable source of a non-gaussian profile is due to chromatic aberration, causing dispersion in the AST41-ASC41 dipole magnets, which affect only on the horizontal plane. Dispersion of muons results from different momenta muons being bent by different amounts as they pass through the magnetic field of the dipoles, and which is not totally compensated for in the remaining downstream elements to give an achromatic focus. This is further supported by the horizontal profile measurements which show significantly more deviation from a gaussian profile than the vertical.

The further usefulness of such a system is demonstrated in Figure 6.21, which shows a pseudo-3D light intensity plot of both the muon beam (small peak) and positron beam spots (large peak) passing through the luminophore foil. Normally the beam-correlated background positron spot is eliminated at this position by the Wien filter and the quadrupole triplet magnets TI and TII. However, here the separation power in the Wien filter (SEP41) has purposefully been reduced such that both spots can be seen simultaneously. This can be used to calibrate online the spatial separation power at the collimator by varying either the electric or magnetic field of SEP41 and measuring the displacement of the spot centroid.



(a) Horizontal beam profile.



(b) Vertical beam profile.

Figure 6.20: Projection of the horizontal and vertical beam profiles measured with the luminophore system in vacuum. The pull of each distribution is shown below the main plot.

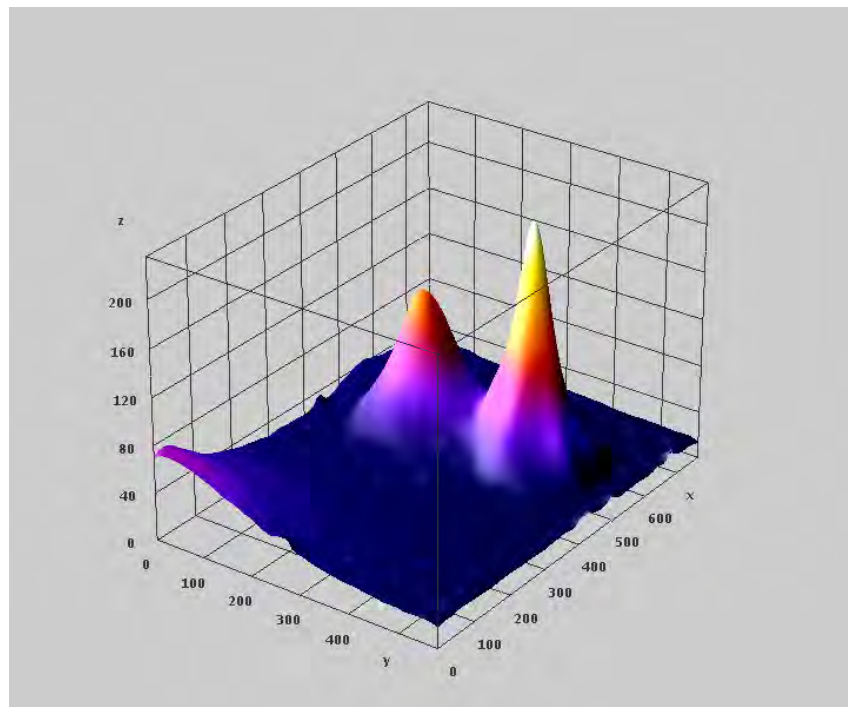


Figure 6.21: A pseudo-3D light intensity plot of both the muon beam (small peak) and positron beam spots (large peak) imaged with the luminophore system with reduced separation power of SEP41.

### 6.3.2 Spatial Resolution

The spatial resolution intrinsic to the luminophore monitoring system was first tested in a qualitative method by a simple muon radiography test shown in Figure 6.22, in which experiment logos formed from solder wire were attached to the outside of the light-tight window of the test box. The reconstructed image of the muon beam spot clearly shows the logos reproduced, by the lack of light from muons stopped in the solder wire. A quantitative measure of the system resolution was estimated using an aluminum grid placed flush against the upstream foil surface to obstruct and stop regions of the muon beam. Those regions where the muon can pass through and strike the luminophore foil are then compared relative to regions blocked to estimate the resolution assuming a step function convoluted with a gaussian. The grid has 0.75 mm thickness along the beam direction, 1 mm wide gratings, with  $4 \times 4 \text{ mm}^2$  gaps between gratings. An image of the beam profile with the aluminum grating placed upstream of the foil is shown in Figure 6.23. The projection of this profile using 31 bins centered on a hole in the grating along the x-axis and y-axis as well as the fit using a step function convoluted with a gaussian are shown in Figure 6.24a and Figure 6.24b respectively. An upper estimate on the resolution of  $544 \mu\text{m}$  was determined by the average of the resolution in x and y, which represents a combined spatial resolution of the camera system, scintillating foil, and muon beam.



(a) The muon radiography setup with the solder wire logos placed on the outside of the light-tight box containing the luminophore foil and camera system.

(b) The reconstructed muon radiograph showing clearly the experiment logos for MEG and Mu3e.

Figure 6.22: Muon radiography using soldering wire and the luminophore system.

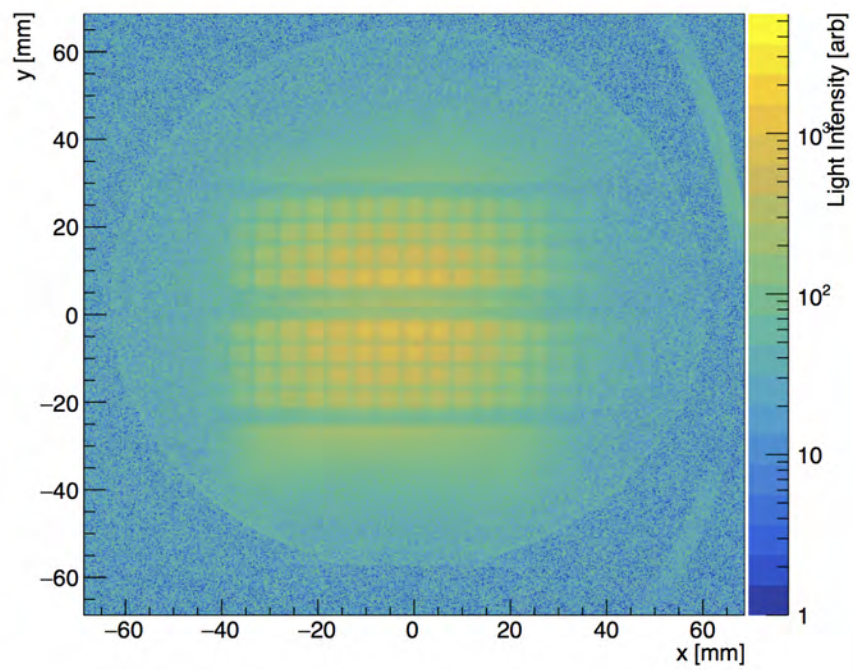
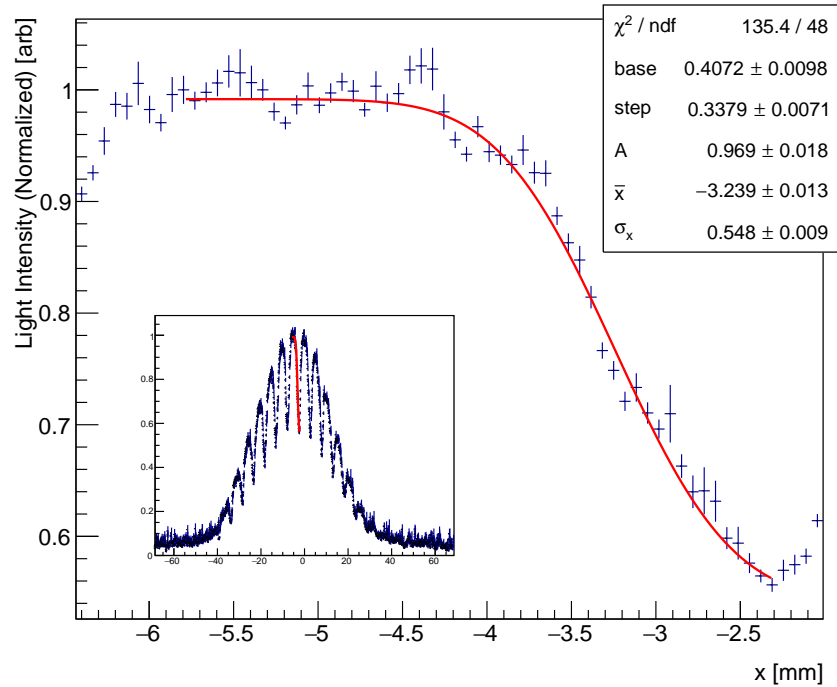
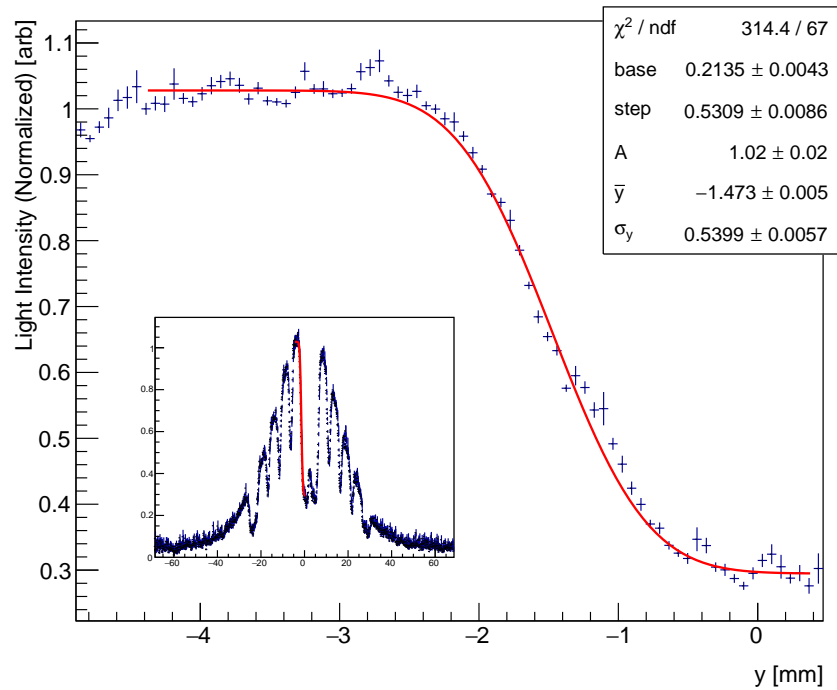


Figure 6.23: Beam profile with an aluminum grating placed on the upstream side of the luminophore foil, stopping muons from hitting the foil. The drop in light intensity near the edge of a grating hole allows the spatial resolution to be determined.



(a) Horizontal Profile Projection



(b) Vertical Profile Projection

Figure 6.24: Spatial resolution test showing the beam profile projections with an aluminum grating placed directly on the upstream side of the luminophore foil.

### 6.3.3 Beam Intensity Regulation via Beam Slits

The  $\pi E5$  beamline has a slit system situated in the middle of the channel which can be operated symmetrically to modify the total beam intensity. See Chapter 5 for a description and overview of the  $\pi E5$  channel and CMBL extension. The pill scintillator measurements are made at a single point on the beam line axis (not a 2D scan). The beam is measured for a given number of proton signals, then the slits are adjusted and the measurement repeated. The measurements using the luminophore were conducted downstream of the beam window, also in air, using the light-tight box and the ORCA camera system. The luminophore measurement contains the full beam profile information and the corresponding light yield integrals along with the rates from the pill scintillator are shown in Figure 6.25. The two sets of measurements show good agreement over the full range of muon beam intensities as well as displaying the same trend that the intensity increases nearly linearly with increasing slit settings and reaches a plateau beyond 250 ADC channels. Slits setting of 80 ADC channels corresponds to approximately 10% transmission and beyond 250 ADC channels the full beam intensity is transmitted. The beam profile width versus slit settings as measured with the luminophore foil is shown in Figure 6.26. A changing beam profile width versus slit settings can be seen, whereby the beam profile becomes smaller with increasing slit opening, and is attributed to increased slit scattering for small apertures. The pill scanner was only used to measure the intensity at a single point and not a full x-y cross scan, whereas the luminophore captures the full beam profile, and therefore includes the changing beam profile width.

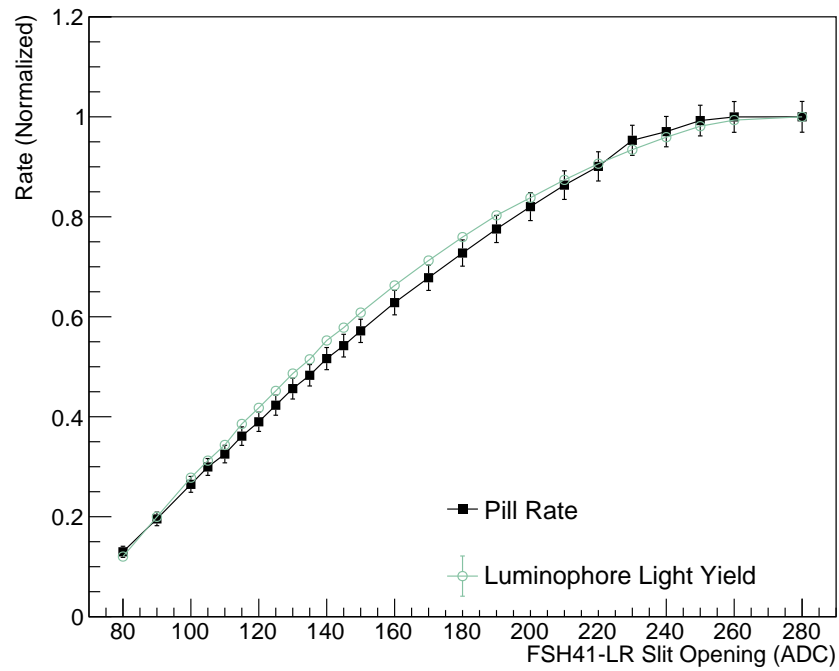


Figure 6.25: The muon rate as a function of the beam line slit opening, measured using the pill scintillator and luminophore foil.

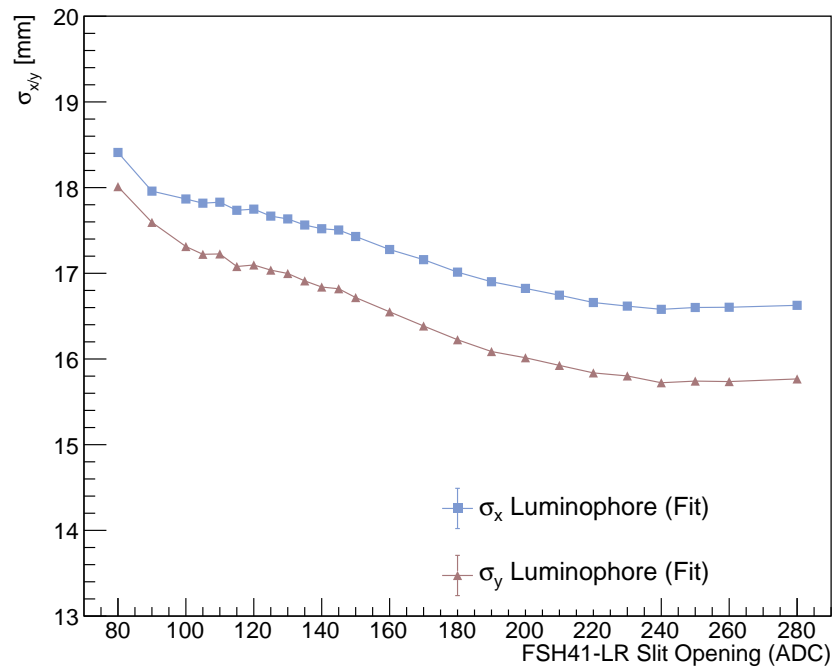


Figure 6.26: The muon beam width as a function of the beam line slit opening, measured using the luminophore foil.

### 6.3.4 Range Curve

The muon beam momentum can be determined by measuring the range curve of the muons in known materials. The range curve is achieved by systematically increasing the material thickness of the degrader in front of the detector and then measuring the number of particles reaching the detector. As the degrader thickness increases, the number of muons that can effectively pass through the degrader and be detected downstream is reduced, as those muons with insufficient energy will be stopped in the degrader. For a perfectly monochromatic beam, the drop-off in beam intensity would be a smeared step function, with the step corresponding to the range limit of muons in that material, and the smearing proportional only to the range straggling.

The range curve can be described by a convolution of two functions, one describing the particle rate hitting the detector for a fixed momentum and a second describing the stochastic fluctuations of the ionization energy loss combined with the momentum-byte of the beam. For the perfectly monochromatic beam with hypothetically no range straggling, the particle rate would be best represented by a Heaviside step function, where the rate drops to zero at the maximum range for that particle in the medium. The range straggling is represented by a gaussian distribution, with the width corresponding the stopping distribution spread in the medium. For a beam with a finite momentum byte, the straggling width is the sum in quadrature of the width of the range straggling distribution ( $\sigma_{RS}$ ) with the range spread due to a momentum-byte ( $\sigma_{RP}$ ), given by the following,

$$\sigma_R^2 = \sigma_{RS}^2 + \sigma_{RP}^2 \quad (6.7)$$

The step function and straggling functions are given by the following expressions,

$$f(t) = (1 - \Theta(t - \bar{t}))(1 - b) + mt + b$$

$$g(t) = Ae^{-\frac{t^2}{2\sigma_R^2}}$$

where  $f(t)$  is the count rate step function,  $g(t)$  is the gaussian straggling-width,  $\Theta(t)$  is the Heaviside step function,  $t$  is the independent parameter corresponding to the total material thickness between vacuum and the detector,  $\bar{t}$  is the position of the step corresponding to the mean range,  $b$  is the base count rate at maximum degrader thickness,  $m$  is the slope of the background count rate, and  $\sigma_R$  is the total range straggling distribution width. The linear background accounts for any beam positrons that are transported along with the muons, as they will experience minimal energy loss in the degrader for the thicknesses used in these measurements. Therefore the count rate  $\mathcal{R}$  in the detector is given by the convolution of  $f$  and  $g$  given by the following,

$$\mathcal{R}(t) = (f * g)(t) = \int_{-\infty}^{\infty} f(t)g(t - \tau)d\tau \quad (6.8)$$

A diagram showing the effect of increasing degrader thickness on the number of stopped particles in the scintillator is shown in Figure 6.27.

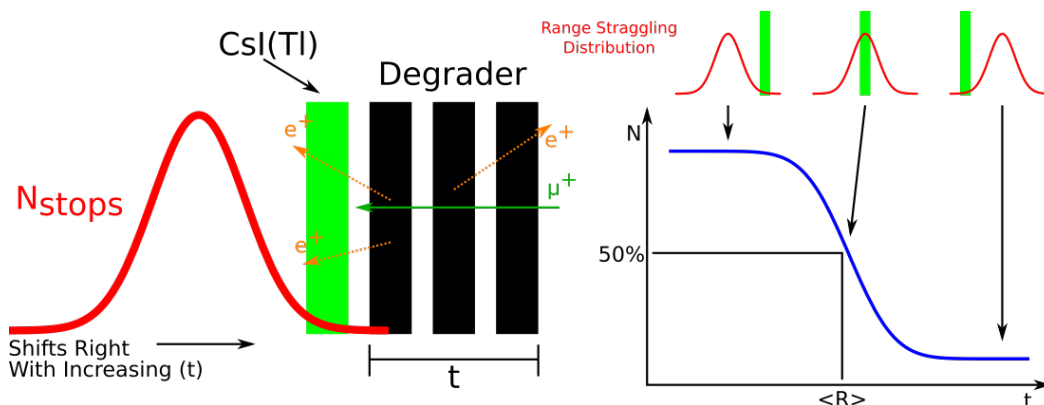


Figure 6.27: A schematic diagram of a range curve with increasing degrader thickness. As more degrader material is added in front of the CsI(Tl) layer, the mean stopping position for muons shifts further to the right. The number of muons that reach the active scintillator layer will begin decreasing as the total material thickness approaches the mean range of the particle in the material.

The pill scanner detector is operated using the low threshold discriminator since the progressively thicker degrader will result in the muon energy deposition in the scintillator being comparable to the energy deposition of Michel positrons. The equivalent energy depositions therefore lead to similar pulse heights of the ADC waveform, making muons and positrons indistinguishable. The pulse height discriminator is therefore operated on low threshold, counting both muons and Michel positrons and corresponding to a minimum energy deposition of approximately 300 keV. The expected contribution from Michel positrons originating in the scintillator from muon stops in or near the scintillator or originating from muon stops in the degrader is proportional to the muon rate. Furthermore, the plastic scintillator thickness of the pill scanner is sufficient to stop all muons whereas Michel positrons above threshold are through-going. A simplified schematic of the pill scanner range curve measurement setup showing the materials involved is shown in Figure 6.28.

Contrary to the pill scanner, the luminophore system does not count individual particles, but instead measures only the scintillation light intensity produced by energy loss in the CsI(Tl) foil. Therefore only relative changes of the light yield associated with a given particle rate can be determined. As a reference the light yield without degrader is taken. The energy of muons reaching the scintillating foil will decrease with increasing degrader thickness, and consequently the energy loss will initially increase and follow the Bethe-Bloch equation Equation (6.9) and the integral of the reciprocal of the energy loss over the energy range  $E_i$  to  $E_f$ , and assuming only ionization energy loss, is the range in the material and is given by Equation (6.10). Correspondingly, the

light yield, which is proportional to the energy loss, increases with increasing degrader thickness until reaching what is known as the Bragg peak where the energy loss is maximal. Once the total material thickness including the degrader is larger than the range of muons, the light yield will drop to zero. A diagram showing the effect of increasing degrader thickness on the energy deposition in the scintillator is shown in Figure 6.29.

$$\left\langle -\frac{dE}{dx} \right\rangle = K \rho z^2 \frac{Z}{A} \frac{1}{\beta^2} \left[ \frac{1}{2} \ln \frac{2m_e c^2 \beta^2 \gamma^2 W_{\max}}{I^2} - \beta^2 \right] \quad (6.9)$$

$$R = \int_{E_i}^{E_f} \frac{1}{\left(-\frac{dE}{dx}\right)} dE \quad (6.10)$$

The range curve measurement using the luminophore system requires continuously modifying the degrader upstream of the scintillating foil, and was carried out using the light tight box in air, as this is the only feasible way to modify the degrader without requiring breaking vacuum and re-pumping the beamline. A simplified schematic of the luminophore system Bragg peak measurement setup showing materials involved is shown in Figure 6.30.

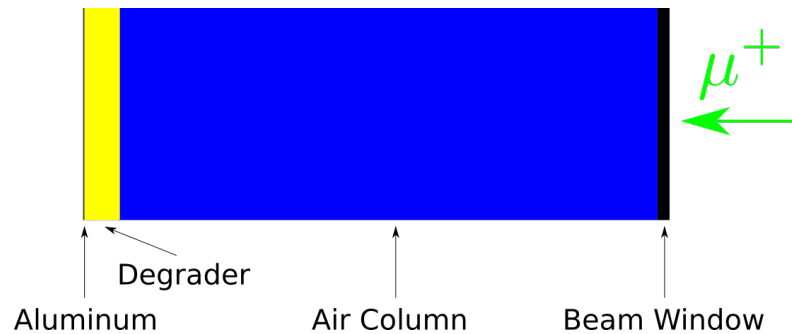


Figure 6.28: A simplified schematic diagram of the materials between the muon beam in vacuum and the pill detector system.

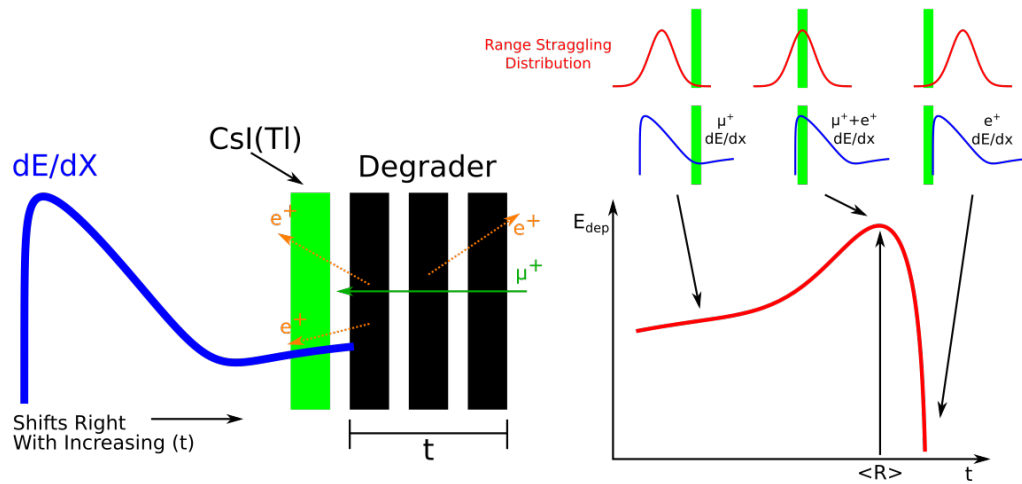


Figure 6.29: A schematic diagram of a Bragg curve with increasing degrader thickness. As more degrader material is added before the CsI(Tl) layer, the energy deposition peak shifts further to the right. This results in more total energy being deposited in the active scintillator layer.

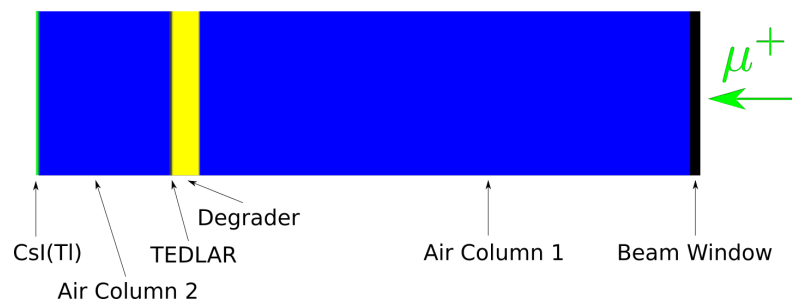


Figure 6.30: A simplified schematic diagram of the materials between the muon beam in vacuum and the CsI(Tl) foil used in the luminophore system.

A first series of G4Beamline simulations were conducted to determine the range-momentum relation for muons in MYLAR. Muons with a momentum from 25 to 32 MeV/c, in 200 keV steps and with no momentum spread, pass through a large block of MYLAR. The mean position of the muon stop distribution is taken as the mean range, and the width of this distribution corresponds to the range straggling. A plot of the muon range as a function of the initial momentum is shown in Figure 6.31, where the error bars correspond to the RMS range straggling. The power law fit yields the same  $P^{3.5}$  as described in Pifer *et al.* [57] and Badertscher *et al.* [86]. By inverting this relationship, the muon momentum can be determined from the range in MYLAR. Muon ranges calculated via integration of Equation (6.10) show consistent agreement across the momentum range.

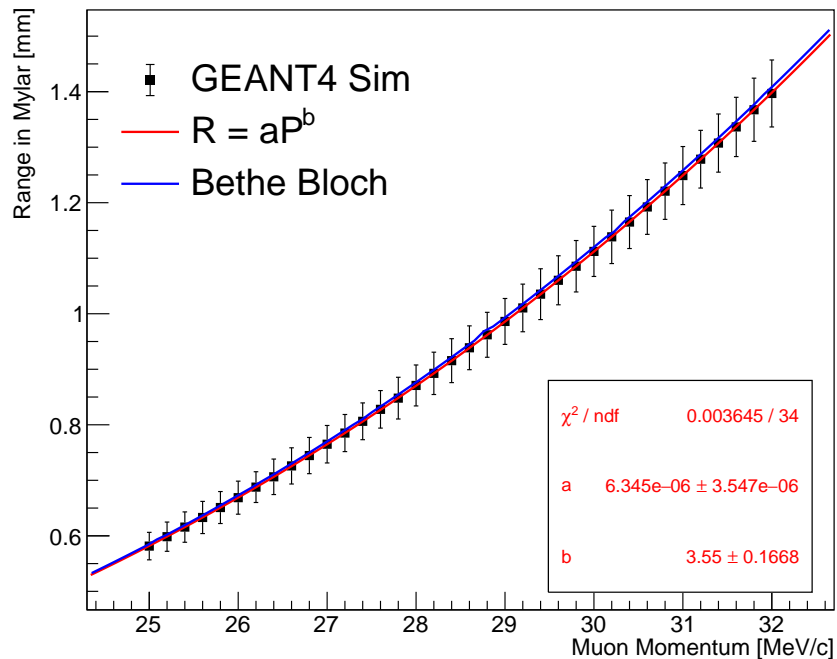


Figure 6.31: The mean range of monochromatic muons in MYLAR as a function of their initial momentum simulated in G4Beamline. The error bars correspond to the width of the stop distribution or range straggling. The power law fit corresponds to the expected  $P^{3.5}$  range relation and matches well with the integration of the Bethe-Bloch equation given by Equation (6.10).

A second series of G4Beamline simulations were conducted to determine the energy deposition in the luminophore CsI(Tl) layer as a function of initial momentum and degrader thickness. A total of 286 combinations of initial muon momentum and degrader thickness were simulated, with degrader thickness ranging from 0 to 1500  $\mu\text{m}$  with varying step size (typically 100  $\mu\text{m}$  and 50  $\mu\text{m}$  near the predicted range) and momentum from 25 to 31 MeV/c in 500 keV steps. A two dimensional plot of the energy deposition in the CsI(Tl) for each combination is shown in Figure 6.32. From this

parameter space, an interpolating function is used to fit the energy deposition based on degrader thickness and determine the associated beam momentum.

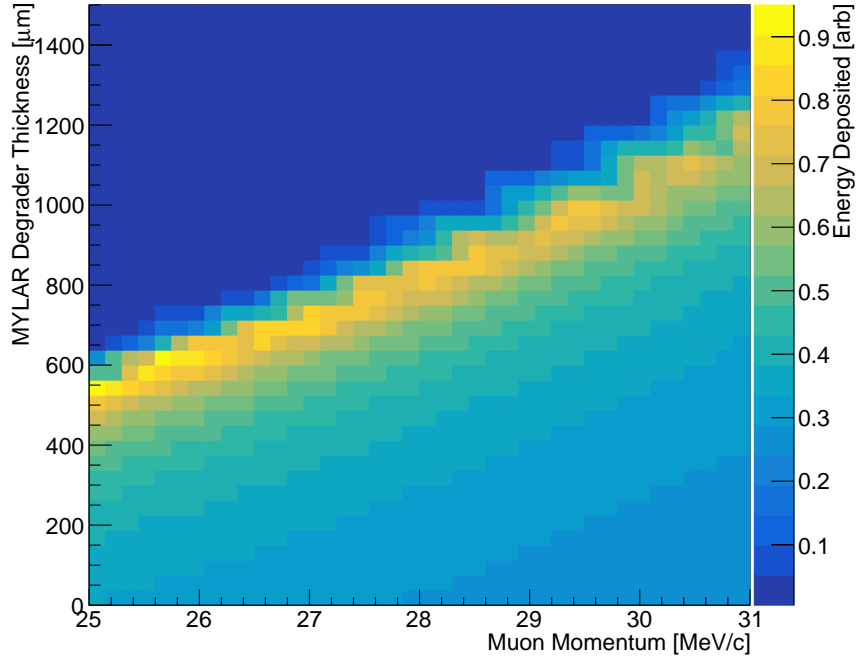


Figure 6.32: The total energy deposited in the CsI(Tl) layer relative to the initial muon momentum and the total thickness of MYLAR degrader material. This is created by 286 individual simulations in G4Beamline and used to generate a fitting function for the light yield data and determine the incoming muon beam momentum.

The range curve measurements were conducted with the luminophore system and the pill scanner system sequentially, at the same location along the beam line, downstream of the final beamline element, the QSM41 quadrupole. The total material thickness for each measurement, including vacuum window, air, TEDLAR window, and MYLAR degrader has been converted to an equivalent MYLAR thickness with density  $1.40 \text{ g/cm}^3$  by scaling the relative stopping power for a 28 MeV/c muon using the following expression,

$$t_2 = t_1 \left( \frac{dE}{dx} \right)_1 / \left( \frac{dE}{dx} \right)_2 \quad (6.11)$$

where  $t_1$  is the true material thickness,  $\left( \frac{dE}{dx} \right)_1$  is its stopping power,  $\left( \frac{dE}{dx} \right)_2$  is the equivalent stopping power in standard MYLAR, and  $t_2$  is the equivalent thickness in standard MYLAR. The materials, densities, thicknesses, and equivalent MYLAR thickness are listed in Table 6.3 for measurements made with the Pill scanner system and in Table 6.4 for measurements made with the luminophore foil and camera system. The beam pipe window is made of  $190 \text{ } \mu\text{m}$  MYLAR and when under vacuum this foil is stretched 55 mm into the beam pipe by the 1 atm. pressure difference. Assuming the window is uniformly stretched to a spherical-cap geometry, the effective longitudinal

thickness through the center of the foil is reduced to  $170 \mu\text{m}$ . Muons traversing this foil at off-axis transverse positions will pass through additional window material and this is not accounted for. Additionally, the material properties for TEDLAR are not fully known as there is no entry for polyvinyl fluoride (PVF) in the PDG or NIST tables. The mean excitation energy and thus  $(\frac{dE}{dx})$  is estimated based on extrapolation from similar materials (PVC, PVDF, PVDC, and PET). The density of TEDLAR has been measured, but does not agree with the density range quoted by DuPont [87]. The mean excitation energy is interpolated based on similar materials (PVC, PVDF, PVDC, and PET).

	Material	Density [g/cm <sup>3</sup> ]	Thickness [mm]	MYLAR Equivalent Thickness [mm]
Beam Pipe Window	MYLAR	1.377	0.170	0.1671
Air Column	Air	$1.205 \cdot 10^{-3}$	78.0	0.0636
Degrader100	MYLAR	1.342	0.100	0.0959
Degrader50	MYLAR	1.338	0.050	0.0478
Degrader25	MYLAR	1.450	0.0125	0.0129
Pill Cover	Aluminum	2.70	0.020	0.0420

Table 6.3: Material thickness for range curve measurement using the Pill Scanner System. The total degrader thickness in multiples of 25, 50, 75, and 100  $\mu\text{m}$  is pieced together using several foils of the various thicknesses and densities. The 25  $\mu\text{m}$  steps are created using two 12.5  $\mu\text{m}$  MYLAR foil layers.

	Material	Density [g/cm <sup>3</sup> ]	Thickness [mm]	MYLAR Equivalent Thickness [mm]
Beam Pipe Window	MYLAR	1.377	0.170	0.1671
Air Column 1	Air	$1.205 \cdot 10^{-3}$	90.0	0.0734
Degrader	MYLAR	1.387	0.050	0.0495
Box Window	TEDLAR	1.167	0.050	0.0388
Air Column 2	Air	$1.205 \cdot 10^{-3}$	24.0	0.0196

Table 6.4: Material thickness for Bragg curve measurements using the luminophore foil and ORCA camera system.

Finally, simulations of the complete luminophore setup, for each corresponding degrader thickness, including the air columns and windows was done with an initial muon beam momentum  $P_\mu=27.466 \text{ MeV}/c$  and momentum-byte  $\Delta P/P_\mu=3\%$  where the momentum was selected based on previous momentum measurements of the muon beam. The mean range in simulation from the fit of the range curve of muons in MYLAR is  $R_\mu=0.7670 \text{ mm}$   $\sigma_{R_P}=0.087 \text{ mm}$ . The fit of the Bragg curve from simulation corresponds to a mean range of  $R_\mu=0.7835 \text{ mm}$   $\sigma_{R_P}=0.076 \text{ mm}$ .

The range curve measurements using the pill scanner along with range curve simulation of the luminophore setup are shown in Figure 6.33. The total degrader thickness in steps of 25, 50, 75, and 100  $\mu\text{m}$  is constructed using several foils of the various thicknesses and densities. The range of muons in MYLAR from measurements with pill scanner is  $R_\mu=0.7971$  mm  $\sigma_{R_P}=0.081$  mm which corresponds to a muon momentum  $P_\mu=27.31$  MeV/c and momentum-byte  $\Delta P_{-0.81}^{+0.75}$  MeV/c. The asymmetric spread in momentum is due to  $R_\mu \pm \sigma$  corresponding to a higher or lower momentum asymmetrically as shown in Figure 6.31. The range of muons in MYLAR from the simulation of the luminophore setup compared to the data from the pill scanner differ by only 30  $\mu\text{m}$ .

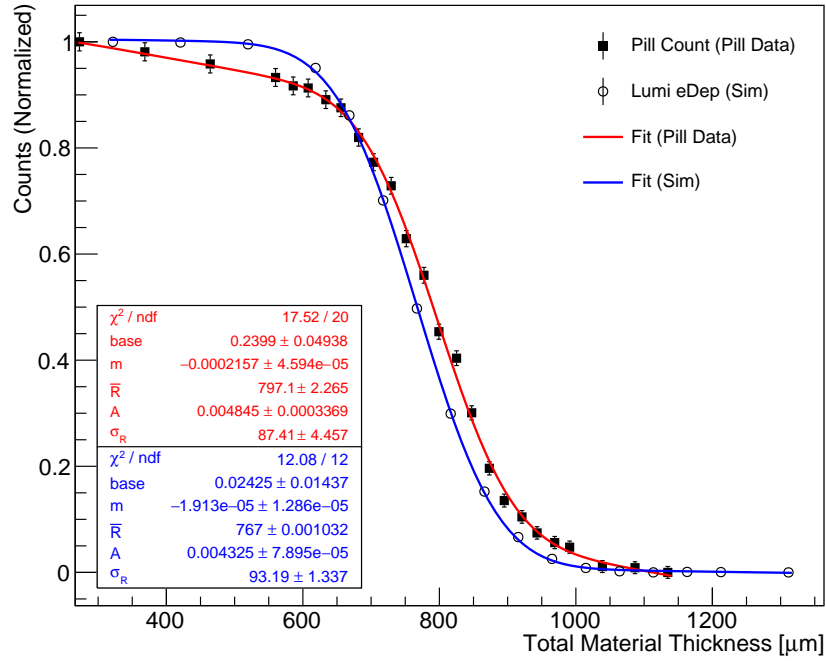


Figure 6.33: Range curve measurements and luminophore simulation for the full degrader thickness range, where total material thickness is converted to equivalent thickness of MYLAR. The fit of the range curve measurements for the pill and the simulation of luminophore differ by 30  $\mu\text{m}$  of material.

The luminophore light yield measurements along with the energy deposition in CsI(Tl) from simulation are shown in Figure 6.34. The fit of luminophore measurements using the interpolated function generated from the simulation results in a mean range and corresponding range straggling width of muons in MYLAR  $R_\mu=0.8565$  mm  $\sigma_{R_P}=0.072$  mm, corresponding to a muon momentum  $P_\mu=27.87$  MeV/c and momentum byte  $\Delta P_{-0.58}^{+0.55}$  MeV/c. The results for both simulation and data are summarized in Table 6.5. The Bragg peak in simulation differs significantly from the observed Bragg peak by approximately 73  $\mu\text{m}$ , more than double the difference using the range curve method of counting particles. This suggest that either the light yield is not

directly proportional to the energy deposition or the material properties are not fully understood. These differences require further investigation through material property measurements and additional range curve measurements. Nevertheless, the two measurements using very different techniques achieve a momentum measurement consistent within 2%.

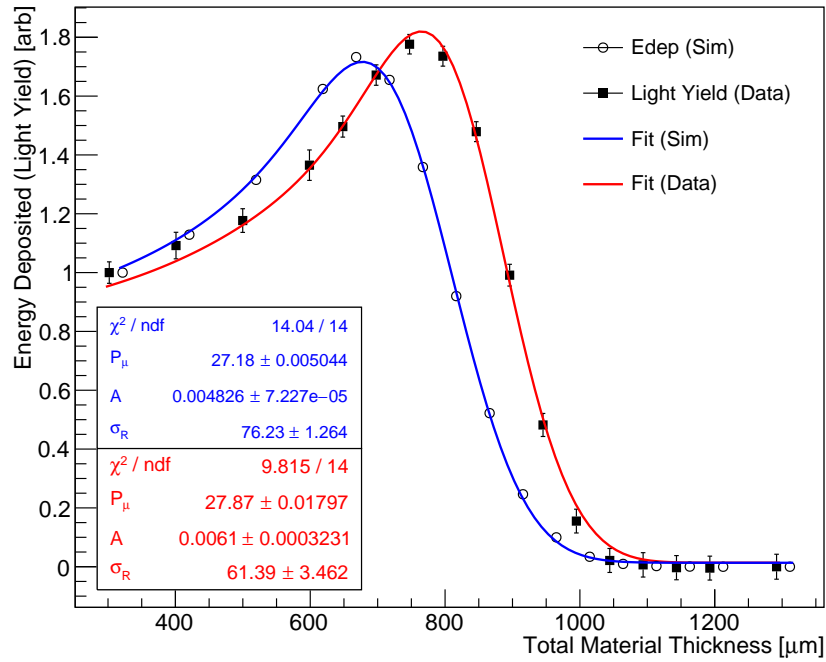


Figure 6.34: Bragg curve measurements using the luminophore foil in the light-tight box and corresponding simulation for the full degrader thickness range. The Bragg curve using the measurement of total light intensity produced by the luminophore system and simulation of energy deposition in the CsI(Tl) layer differ by approximately  $73 \mu\text{m}$ , suggesting either some of the material properties are not fully understood or the light yield is not exactly proportional to energy deposition.

	$P_\mu$ [MeV/c]	$\Delta P$ [MeV/c]	$R_\mu$ [mm]	$\sigma_{RP}$ [mm]
G4BL Sim				
Energy Deposit in CsI(Tl)	27.18	+0.72 -0.77	0.7835	0.076
Luminophore Data				
Light Yield from CsI(Tl)	27.87	+0.55 -0.58	0.8565	0.061
G4BL Sim				
$\mu^+ + e^+$ Count	27.02	+0.83 -0.90	0.7670	0.087
Pill Scanner Data				
$\mu^+ + e^+$ Count	27.31	+0.75 -0.81	0.7971	0.081

Table 6.5: The muon momentum and range in MYLAR in simulation and measurements using the pill scanner and luminophore detector systems.

### 6.3.5 Phase Space

The transverse phase space of the muon beam can for example be determined by scanning the magnetic field strength of the final focusing element in the beam line before the detector system. The transverse beam width is then determined from a gaussian fit of the profile as a function of the quadrupole field strength. The phase space measurements were conducted sequentially with the pill scanner system and luminophore monitoring system in vacuum using the IDS camera system. The measurements with the pill scanner contain an additional scattering contribution, compared to the luminophore measurements in vacuum, due to the MYLAR window and air leading to an enlarged beam profile. The expected scattering contribution is determined via simulation of a muon beam with no transverse width and the correct momentum and momentum-byte passing through the corresponding MYLAR window and air column. This correction factor is not necessary for the luminophore foil, as it is inside the vacuum beam pipe.

The phase space transformation between two points along the beam line is defined by the following expression

$$\begin{pmatrix} x_f \\ x'_f \end{pmatrix} = \mathbf{M} \begin{pmatrix} x_i \\ x'_i \end{pmatrix} \quad (6.12)$$

where  $x_i$  and  $x_f$  are the initial and final positions,  $x'_i$  and  $x'_f$  are the initial and final divergences, and  $\mathbf{M}$  is the transfer matrix describing the transition between the initial and final phase space. For the case of a horizontally focusing quadrupole followed by a drift length, the horizontal transfer matrix is given by the following expression,

$$\mathbf{M} = \begin{pmatrix} 1 & L_D \\ 0 & 1 \end{pmatrix} \cdot \begin{pmatrix} \cos(\sqrt{k}L_Q) & \frac{\sin(\sqrt{k}L_Q)}{\sqrt{k}} \\ -\sqrt{k}\sin(\sqrt{k}L_Q) & \cos(\sqrt{k}L_Q) \end{pmatrix} \quad (6.13)$$

where  $L_D$  is the drift length,  $k$  is quadrupole magnet focusing strength, and  $L_Q$  is the quadrupole effective length. The full beam phase space calculations via transfer matrix formalism are described in Appendix C. A polynomial fit of the profile width vs quadrupole strength is used to determine the transport matrix element parameters and thus the beam phase space. The functions used to fit the beam width versus magnet focusing strength are given by the following expressions,

$$\sigma_{11,f}(k) = \sigma_{11,o}(M_{11}(k))^2 + 2\sigma_{21,o}M_{11}(k)M_{12}(k) + \sigma_{22,o}(M_{12}(k))^2 \quad (6.14)$$

$$\sigma_{33,f}(k) = \sigma_{33,o}(M_{33}(k))^2 + 2\sigma_{43,o}M_{33}(k)M_{34}(k) + \sigma_{44,o}(M_{34}(k))^2 \quad (6.15)$$

where  $\sigma_{11,f}$  and  $\sigma_{33,f}$  are the measured horizontal and vertical beam widths squared respectively,  $\sigma_{ij,o}$  are the elements of the  $2 \times 2$  matrix defining the phase space ellipse, and  $M_{ij}$  is the matrix elements from Equation (6.13).

The Pill Scanner measurements of the QSK43 magnetic focusing strength scan are shown in Figure 6.35 and the corresponding transverse phase space ellipses are shown in Figure 6.36. Corresponding measurements of the QSK43 magnetic focusing strength scan using the luminophore system is shown in Figure 6.37 and the corresponding transverse phase space ellipses shown in Figure 6.38. The horizontal and vertical Twiss phase space parameters [88], also known as Courant-Snyder parameters, relate the area, shape, and orientation of the beam ellipse in the transverse phase space. The transverse phase space measurements in Table 6.6 show good agreement between the two methods, with horizontal emittance approximately 800-1000 mm·mrad, and vertical emittance approximately 400-500 mm·mrad. Differences between emittances can be attributed to higher order effects not accounted for in the first-order transfer matrix formalism such as momentum dispersion. This is evident in the beam profile projections seen in Section 6.3.1 which do not match perfectly to the expected gaussian shape.

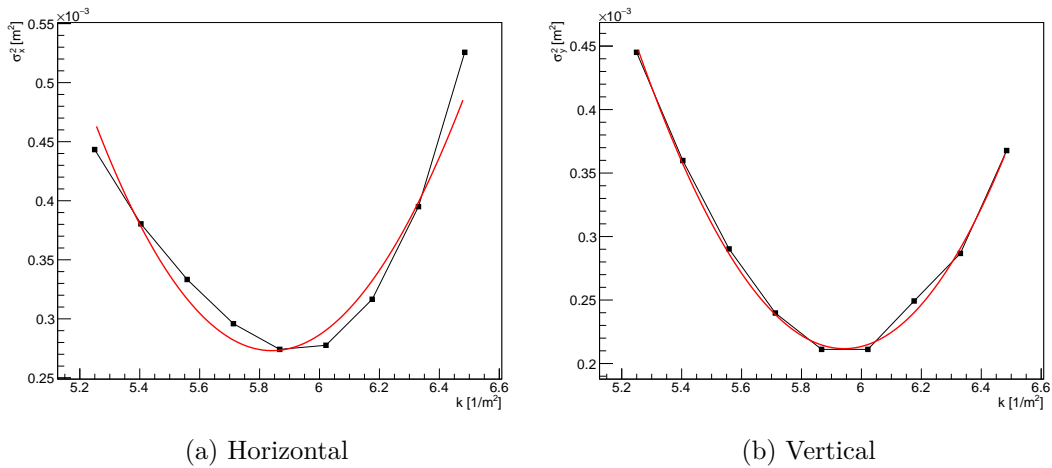


Figure 6.35: Transverse muon beam width measurements using the pill scanner downstream in air and adjusting the QSK43 focusing strength. The fits using Equation (6.14) and Equation (6.15) are shown in red.

	Pill Scanner	CsI(Tl) + IDS
Horizontal Phase Space		
$\alpha_x$	-4.02	-2.57
$\beta_x$ [m]	2.92	2.09
$\epsilon_x$ [mm mrad]	1026.91	775.69
Vertical Phase Space		
$\alpha_y$	17.02	11.44
$\beta_y$ [m]	7.82	5.26
$\epsilon_y$ [mm mrad]	492.86	390.97

Table 6.6: The muon beam transverse phase space Twiss parameters, measured with the pill scanner in air and luminophore system in vacuum.

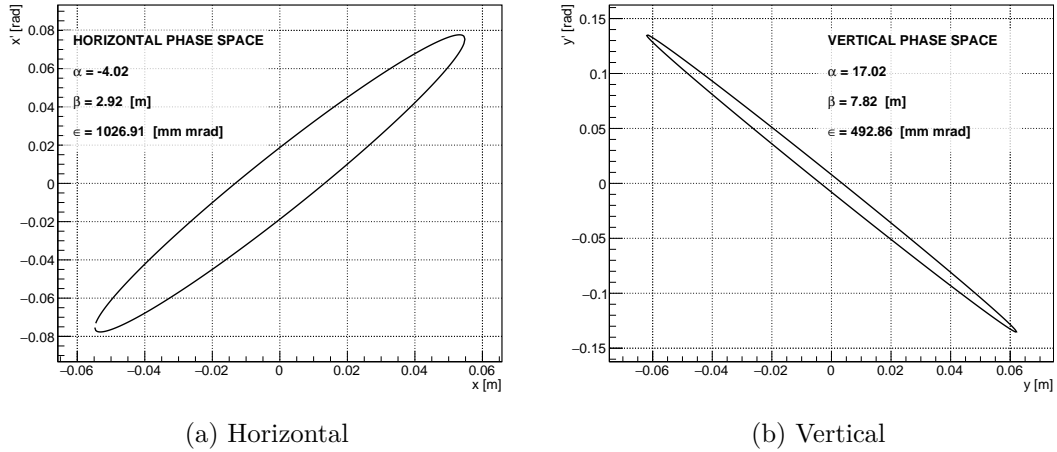


Figure 6.36: Muon beam transverse phase space ellipses using the pill scanner downstream in air.

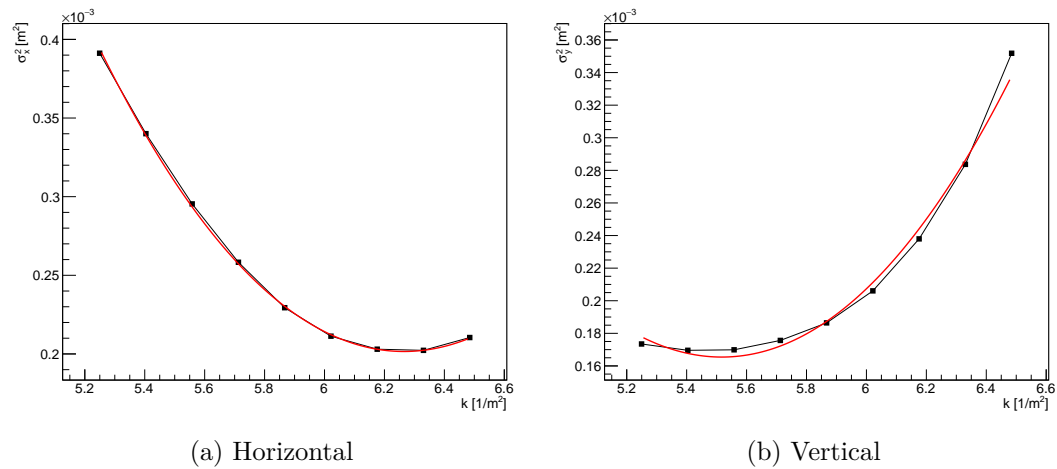
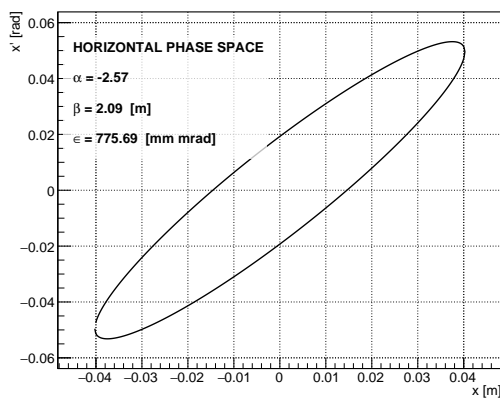
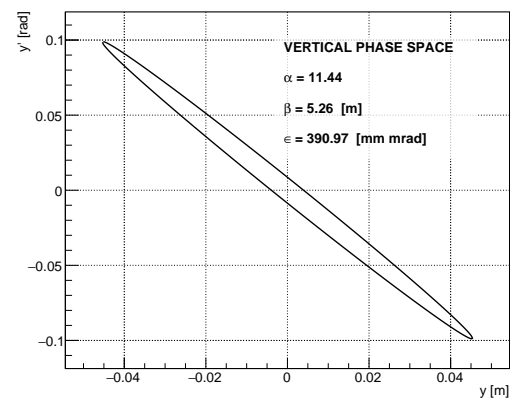


Figure 6.37: Transverse muon beam width measurements using the luminophore foil in vacuum and adjusting the QSK43 focusing strength. The fits using Equation (6.14) and Equation (6.15) are shown in red.



(a) Horizontal



(b) Vertical

Figure 6.38: Muon beam transverse phase space ellipses using the luminophore foil in vacuum.

## 6.4 Summary

A non-invasive, in situ beam monitoring system has been developed for use in the MEG II and Mu3e experiments. The system is comprised of a  $5\ \mu\text{m}$  thin film of CsI(Tl) deposited on a  $3\ \mu\text{m}$  stretched MYLAR substrate via chemical vapor deposition and imaged via an external CCD camera capable of long-term low-light exposures. The system was initially developed using a light-tight box for ease of use and access, and meant for measurements in air, downstream of the beam window. Later, an in situ system was developed and deployed in the vacuum, upstream of the collimator system, and is currently in place in the MEG beamline between the TII quadrupole triplet and BTS. Image analysis software has been built using the OpenCV library and ROOT for perspective transformation, image summation, background subtraction, and profile fitting.

Comparison of the beam profiles of measurements using the pill scintillator to x-y projections of the luminophore foil image shows excellent agreement. The upper estimate on the spatial resolution of the luminophore system of 0.5 mm was determined by using an aluminum grating to partially block the muon beam and represents a combined resolution of the scintillating foil, camera system, and muon beam. Compared to the pill scanner measurements, the luminophore measurement contains the full beam profile information including x-y correlation and avoids the effects of multiple scattering from material between the detector. The light yield versus muon beam intensity was measured using beam line slits and the pill and luminophore measurements are in good agreement over the full range of muon beam intensities. Individual luminophore measurements are completed with exposure times on the order of 10s of seconds, significantly less than the time required for equivalent pill scanner measurements.

The particle rates from range curve measurements in the simulation of the luminophore setup compared with those measured with the pill scanner show excellent agreement. The Bragg peak in simulation differs significantly from the observed Bragg peak by approximately  $70\ \mu\text{m}$ , and requires further investigation, nevertheless the beam momentum determination via the pill range curve and luminophore Bragg curve measurements show consistency at the 2% level. The phase space measurements were conducted sequentially with the pill scanner system and luminophore monitoring system in vacuum and show good agreement. The observed differences in transverse emittance between the pill scanner measurements made in air and the luminophore measurements made in vacuum suggest unaccounted for second order effects.

Further work is needed for the luminophore system to be fully calibrated and integrated with the data collection systems of MEG II and Mu3e. However, the luminophore beam monitoring system provides a fast, in situ, non-invasive method of measuring muon beam intensities necessary for continuous, long-term, and stable beam

delivery for both current and next-generation charged lepton flavor violation experiments.

---

## Summary

---

The Paul Scherrer Institut in Switzerland will host two next-generation charged lepton flavor violation experiments, MEG II and Mu3e. The Mu3e Phase I experiment will search for the rare three body decay  $\mu^+ \rightarrow e^+e^-e^+$  at a sensitivity level  $\mathcal{O}(10^{-15})$ . The MEG II experiment will search for a back-to-back positron and monochromatic photon in the  $\mu^+ \rightarrow e^+\gamma$  decay with an expected sensitivity of  $6 \cdot 10^{-14}$ . Due to the nature of these extremely rare decays, both experiments come with requirement of the highest achievable muon beam rates at  $\mathcal{O}(10^8) \mu^+/s$ , only available at PSI.

An optimization of the current muon production target, Target E, at PSI has been undertaken as part of this thesis in order to fully characterize the production of muons from charged pions, and to aide the design of a new High Intensity Muon Beam (HiMB) for the upgraded charged lepton flavor violation experiments. A new pion production cross section model has been developed as a foundation for these studies, using a parameterization of the available data from meson production facilities around the world. Significant effort has been spent on the geometry of the production target which has been optimized to deliver maximum surface muon rates, while simultaneously preserving the proton intensity characteristics for downstream use in the spallation neutron target SINQ. The resultant rotated slab target geometry has shown, in simulation, rate enhancements between 30-60% depending on beamline and target orientation, equivalent to raising the current proton beam intensity from 2.2 mA to between 2.9-3.5 mA. Material optimization has shown low- $Z$  carbides such as  $B_4C$  or  $Be_2C$  can yield an additional 10-14%.

The muon and positron rates generated in simulation using the new parameterized pion production model have been used to optimize beamline elements, and have been compared with measurements along the beamline. A significant effort has been devoted to the measurement and reduction of beam-correlated positron background and estimating its impact on the sensitivity of the Mu3e experiment. A robust and sensitive method has been developed to differentiate the beam positrons from Michel positrons in beam measurements, and has been used to estimate the absolute beam positron rates reaching the Mu3e experiment. The usefulness of the extensive beam line simulations was demonstrated when an unexpected beam positron background was found and a simulated solution using a lead collimator implemented inside the

quadrupole triplet vacuum chamber, but the elimination of all beam positrons at the Mu3e solenoid injection point has been shown in simulation, by implementing an increased 395 kV symmetric potential to the SEP41 Wien filter. The muon and beam positron rates measured at the Mu3e injection point using the lead positron-stopper are  $\mathcal{R}_{\mu^+} = 1.02 \cdot 10^6 \mu^+/s$  and  $\mathcal{R}_{e_B^+} = 6.53 \cdot 10^6 e^+/s$  @ 2.2 mA  $I_P$  60 mm Target E respectively, and meet the requirements for the Mu3e Phase-I experiment. The expected contribution to backgrounds from beam positrons is twelve orders of magnitude below the dominant background process of Bhabha production from Michel positrons @ 90% CL and will have no impact on the sensitivity of the Mu3e Phase-I experiment.

The searches for rare decays rely on a continuous and uninterrupted beam of muons throughout the data-taking period, therefore unexpected beam rate reductions or loss can have significant consequences. A new beam monitoring system has been developed for use in the MEG II and Mu3e experiments using ultra-thin CsI(Tl) luminophore foils and a high performance CCD camera system. The beam monitor has been tested along the muon beamline and as a permanent in-situ, non-destructive beam detector within the vacuum beam pipe, measuring beam profiles, normalized rates, and the transverse phase space. Furthermore, calibration techniques using a UV LED and raster pattern on the foil frame allow for intensity normalization, pixel-to-millimeter calibrations, and perspective transformation, essentially allowing an online monitoring during the experiment. Comparison of the beam profiles using the pill scintillator scanner to transverse projections of the luminophore foil shows excellent agreement and differences in the transverse emittances between the pill scanner measurements in air and the luminophore measurements in vacuum offer insights into higher order effects, such as momentum dispersion, on the beam. A range-curve and momentum study using both the pill scintillator scanner system and the luminophore system show that range-curve simulations and pill scanner data, both involving counting particles, show reasonable agreement but disagree with the measured luminophore Bragg peak and simulated Bragg peak, based on energy deposition. The difference amounts to  $\sim 70 \mu\text{m}$  of equivalent MYLAR and requires further investigation. A comparison of the beam momentum derived from the pill range curve measurements and the luminophore Bragg curve measurements show consistency at the 2% level. Furthermore, this beam monitor provides a fast, in situ, non-invasive method of measuring muon beam intensities necessary for stable beam delivery for both current and next-generation charged lepton flavor violation experiments running at the intensity frontier.

# Appendices

---

## Pion Cross Section Parameterization

---

The foundation for this cross section parameterization [56] is established by two previous implementations [54, 55] and are repeated here.

The first parametrization [55] is only valid for low pion kinetic energies  $T_{\pi^+} \lesssim 40$  MeV and reactions on carbon at proton energies of 580 MeV. The double-differential cross section is given by

$$\frac{d^2\sigma_{\text{LE}}}{d\Omega dT_{\pi^+}} = S_{01} \sin\left(\frac{\pi T_{\pi^+}}{2T_{01}}\right) - S_{02} \sin\left(\frac{\pi T_{\pi^+}}{2T_{02}}\right) \cos\theta \quad (\text{A.1})$$

with the parameters  $S_{01} = 15.3 \mu\text{b}/(\text{sr MeV})$ ,  $S_{02} = 5.6 \mu\text{b}/(\text{sr MeV})$ ,  $T_{01} = 49.4$  MeV,  $T_{02} = 32.4$  MeV, and the angle  $\theta$  between the momenta of proton and produced  $\pi^+$ .

The second parametrization [54] is valid for all elements, proton energies  $T_p < 800$  MeV, and all pion energies, but will only be used at pion energies above approximately 40 MeV as it performs poorly below that energy. The basic shape is modeled using a Gaussian function with a high-energy cut-off, parameters fitted to data, and amplitude scaled using B-splines.

$$\begin{aligned} \frac{d^2\sigma_{\text{HE}}}{d\Omega dT_{\pi^+}} = & A(\theta, Z, T_p) \exp\left[-\left(\frac{\bar{T}(\theta, Z, T_p) - T_{\pi^+}}{\sqrt{2}\sigma(\theta, Z, T_p)}\right)^2\right] \\ & \times \frac{1}{1 + \exp\left[\frac{T_{\pi^+} - T_F}{B}\right]} \end{aligned} \quad (\text{A.2})$$

The two parameterizations are combined using a smooth sigmoid function in order to transition from the low-energy to the high-energy regime. Additionally, the low-energy parametrization of Equation A.1 is scaled to arbitrary elements and proton energy using the high-energy parametrization. The combined differential cross section is then given by

$$\begin{aligned} \frac{d^2\sigma}{d\Omega dT_{\pi^+}}(T_{\pi^+}, \theta) = & (1 - f_t) f_s \frac{d^2\sigma_{\text{LE}}}{d\Omega dT_{\pi^+}}(T_{\pi^+} - T_{\pi^+}^0, \theta) \\ & + f_t \frac{d^2\sigma_{\text{HE}}}{d\Omega dT_{\pi^+}}(T_{\pi^+}, \theta) \end{aligned} \quad (\text{A.3})$$

with the pion kinetic energy  $T_{\pi^+}$  in MeV. The sigmoidal transition function is given by

$$f_t = \frac{1}{1 + \exp(-(T_{\pi^+} - 40)/10)} \quad (\text{A.4})$$

and the scaling factor by

$$f_s = \frac{\frac{d^2\sigma_{\text{HE}}}{d\Omega dT_{\pi^+}}(T_{\pi^+} = 40, \theta = 90^\circ, Z, T_p)}{\frac{d^2\sigma_{\text{HE}}}{d\Omega dT_{\pi^+}}(T_{\pi^+} = 40, \theta = 90^\circ, Z = 6, T_p = 585)} \quad (\text{A.5})$$

The shift in pion kinetic energy by  $T_{\pi^+}^0$  was observed in [52] and is due to the coulomb repulsion of the nucleus, imparting a minimal kinetic energy on the pion and for nickel was measured to be 5 MeV. This shift is given by scaling the coulomb potential and size of the nucleus for an arbitrary nucleus of atomic number  $Z$  and mass number  $A$  by

$$T_{\pi^+}^0 = 0.696Z/A^{1/3} \quad [\text{MeV}] \quad (\text{A.6})$$

where the simplification  $A \sim 2Z$  is used. Negative cross section values in Equation A.3 are possible for  $T_{\pi^+} < T_{\pi^+}^0$  and are therefore set explicitly to zero.

The original parametrization found in [54] has been modified and the relevant changes and parameters listed here. The high-energy behavior has altered to fall off exponentially, and some parameters were changed to give better agreement between data and parameterization. The special case for hydrogen is not treated separately.

$$\begin{aligned}
& T_{\pi^+} \leq \bar{T}(\theta, Z, T_p) + \sigma(\theta, Z, T_p) : \\
& \frac{d^2\sigma_{\text{HE}}}{d\Omega dT_{\pi^+}} = A(\theta, Z, T_p) \exp \left[ - \left( \frac{\bar{T}(\theta, Z, T_p) - T_{\pi^+}}{\sqrt{2}\sigma(\theta, Z, T_p)} \right)^2 \right] \\
& \quad \times \frac{1}{1 + \exp \left[ \frac{T_{\pi^+} - T_F}{B} \right]} \quad [\mu\text{b}/\text{MeV}/\text{sr}] \\
& T_{\pi^+} > \bar{T}(\theta, Z, T_p) + \sigma(\theta, Z, T_p) : \\
& \frac{d^2\sigma_{\text{HE}}}{d\Omega dT_{\pi^+}} = A(\theta, Z, T_p) e^{-\frac{1}{2}} \\
& \quad \times \exp \left[ - \left( \frac{T_{\pi^+} - (\bar{T}(\theta, Z, T_p) + \sigma(\theta, Z, T_p))}{n(\theta)\sigma(\theta, Z, T_p)} \right) \right] \\
& \quad \times \frac{1}{1 + \exp \left[ \frac{T_{\pi^+} - T_F}{B} \right]} \quad [\mu\text{b}/\text{MeV}/\text{sr}] \quad (\text{A.7})
\end{aligned}$$

The parameters corresponding to Equation A.7 are given by the following equations.

$$\begin{aligned}\bar{T}(\theta, Z, T_p) &= 48 + 330 \exp\left(-\frac{\theta}{T_A(Z, T_p)}\right) \\ \sigma(\theta, Z, T_p) &= \sigma_A(Z, T_p) \exp\left(-\frac{\theta}{85}\right) \\ T_A(Z, T_p) &= \frac{T_A^{730}(Z)(T_p - 585) - T_A^{585}(Z)(T_p - 730)}{730 - 585} \\ T_A^{585}(Z) &= \begin{cases} 28.9 & 1 \leq Z < 9 \\ 26.0 & 9 \leq Z < 92 \end{cases} \\ T_A^{730}(Z) &= \begin{cases} 34.2 & 1 \leq Z < 9 \\ 29.9 & 9 \leq Z < 92 \end{cases}\end{aligned}$$

$$\begin{aligned}
\sigma_A(Z, T_p) &= \frac{\sigma_A^{730}(Z)(T_p - 585) - \sigma_A^{585}(Z)(T_p - 730)}{730 - 585} \\
\sigma_A^{585}(Z) &= \begin{cases} 130 & 1 \leq Z < 9 \\ 135 & 9 \leq Z < 92 \end{cases} \\
\sigma_A^{730}(Z) &= \begin{cases} 150 & 1 \leq Z < 9 \\ 166 & 9 \leq Z < 92 \end{cases} \\
B &= 50 \\
T_F &= T_p - 140 - 2B \\
A(\theta, Z, T_p) &= N(Z) \sum_{n=1}^5 a_n B_n \\
a_1 &= 27 - 4 \left( \frac{730 - T_p}{730 - 585} \right)^2 \\
a_2 &= 18.2 \\
a_3 &= 8 \\
a_4 &= 13 + (Z - 12)/10 \\
a_5 &= 9 + (Z - 12)/10 - (T_p - 685)/20 \\
N(Z) &= c_0 Z^{1/3} + \sum_{m=1}^3 c_m (\ln Z)^m Z^{1/3} \\
c_0 &= 0.8851 \\
c_1 &= -0.1015 \\
c_2 &= 0.1459 \\
c_3 &= -0.0265 \\
n(\theta) &= 0.4 + 0.7\theta/140
\end{aligned} \tag{A.8}$$

The proton and pion kinetic energies  $T_p$  and  $T_{\pi^+}$  are in MeV and the angle  $\theta$  in degrees. The B-splines  $B_i$  are defined over the range 0 to  $180^\circ$  and follow the knot sequence (0, 0, 0,  $30^\circ$ ,  $70^\circ$ ,  $180^\circ$ ,  $180^\circ$ ,  $180^\circ$ ).

While the total cross section can be obtained by integration of the double differential cross section there exists a computationally simpler approximation [54], assuming

a linear behavior between values close to the pion production threshold and the measurements at 585 MeV and 730 MeV.

$$\begin{aligned}
\sigma(Z, T_p) &= \begin{cases} \sigma^{585}(Z) \frac{(T_p - 325)}{(585 - 325)} & 325 \leq T_p < 585 \\ \sigma^{585}(Z) + (\sigma^{730}(Z) - \sigma^{585}(Z)) \frac{(T_p - 585)}{(730 - 585)} & 585 \leq T_p < 800 \end{cases} \\
\sigma^{585}(Z) &= \begin{cases} 9.70 & Z = 1 \\ 28.5(Z/6)^{1/3}(0.77 + 0.039Z) & 2 \leq Z < 12 \\ 19.65Z^{1/3} & 12 \leq Z \end{cases} \\
\sigma^{730}(Z) &= \begin{cases} 13.50 & Z = 1 \\ 35.0(Z/6)^{1/3}(0.77 + 0.039Z) & 2 \leq Z < 12 \\ 24.50Z^{1/3} & 12 \leq Z \end{cases} \quad (\text{A.9})
\end{aligned}$$

with the proton kinetic energy in MeV the total cross section is then given in millibarns.

---

## Image Analysis

---

### B.1 Perspective Transformation

The image perspective transformation procedure follows that outlined in [89] and in the OpenCV library [84]. Pixel coordinates in a 2D image can be described by the coordinate vector,

$$\mathbf{x} = \begin{pmatrix} x \\ y \end{pmatrix} \quad (\text{B.1})$$

or equivalently using homogenous coordinates with the following representation

$$\tilde{\mathbf{x}} = \begin{pmatrix} \tilde{w} x \\ \tilde{w} y \\ \tilde{w} \end{pmatrix} \quad (\text{B.2})$$

where  $\tilde{w}$  is some arbitrary scale factor, and conversion back to the inhomogeneous vector is achieved by dividing each component by the last element  $\tilde{w}$ .

The perspective transformation is a homographic transform and therefore operates on homogenous coordinates through the following

$$\tilde{\mathbf{x}}' = \tilde{\mathbf{H}} \tilde{\mathbf{x}} \quad (\text{B.3})$$

The homogenous perspective transformation matrix is given by

$$\tilde{\mathbf{H}} = \begin{pmatrix} h_{00} & h_{01} & h_{02} \\ h_{10} & h_{11} & h_{12} \\ h_{20} & h_{21} & h_{22} \end{pmatrix} \quad (\text{B.4})$$

The resulting transformed homogeneous coordinates  $\tilde{\mathbf{x}}'$  must be normalized in order to obtain an inhomogeneous result  $\mathbf{x}$ , and is given by the following

$$x'_i = \frac{h_{00}x_i + h_{01}y_i + h_{02}}{h_{20}x_i + h_{21}y_i + h_{22}} \quad (\text{B.5})$$

$$y'_i = \frac{h_{10}x_i + h_{11}y_i + h_{12}}{h_{20}x_i + h_{21}y_i + h_{22}} \quad (\text{B.6})$$

The perspective transformation of an image proceeds in two steps. The transformation matrix  $\tilde{\mathbf{H}}$  is determined based on the input of known co-linear points  $\tilde{\mathbf{x}}'$ , and then solving the following linear system of equations

$$\begin{pmatrix} x'_0 \\ x'_1 \\ x'_2 \\ x'_3 \\ y'_0 \\ y'_1 \\ y'_2 \\ y'_3 \end{pmatrix} = \begin{pmatrix} x_0 & y_0 & 1 & 0 & 0 & 0 & -x_0x'_0 & -y_0x'_0 \\ x_1 & y_1 & 1 & 0 & 0 & 0 & -x_1x'_1 & -y_1x'_1 \\ x_2 & y_2 & 1 & 0 & 0 & 0 & -x_2x'_2 & -y_2x'_2 \\ x_3 & y_3 & 1 & 0 & 0 & 0 & -x_3x'_3 & -y_3x'_3 \\ 0 & 0 & 0 & x_0 & y_0 & 1 & -x_0y'_0 & -y_0y'_0 \\ 0 & 0 & 0 & x_1 & y_1 & 1 & -x_1y'_1 & -y_1y'_1 \\ 0 & 0 & 0 & x_2 & y_2 & 1 & -x_2y'_2 & -y_2y'_2 \\ 0 & 0 & 0 & x_3 & y_3 & 1 & -x_3y'_3 & -y_3y'_3 \end{pmatrix} \begin{pmatrix} h_{00} \\ h_{01} \\ h_{02} \\ h_{10} \\ h_{11} \\ h_{12} \\ h_{20} \\ h_{21} \end{pmatrix} \quad (\text{B.7})$$

where  $h_{22} = 1$ . Once the components of  $\tilde{\mathbf{H}}$  are determined, it can be applied to all pixels in the image to transform the image accordingly using Equations (B.5) and (B.6).

## B.2 Pixel Error Estimate

Due to the small number of measurements in a beam imaging run, the error on an individual pixel is determined using the jackknife resampling technique. The mean for each pixel subsample for  $N$  images is computed excluding the  $ij^{th}$  pixel value ( $i^{th}$  row,  $j^{th}$  column) in the  $k^{th}$  image from the mean via the following

$$\bar{p}_{ijk} = \frac{1}{N-1} \sum_{m \neq k} p_{ijm} \quad (\text{B.8})$$

The mean of this resampled distribution is the average of the  $N$  means and given by the following

$$\bar{p}_{ij} = \frac{1}{N} \sum_k \bar{p}_{ijk} \quad (\text{B.9})$$

The jackknife estimate of the variance of the pixel error is calculated from the variance of the distribution of  $\bar{p}_{ijk}$  by the following

$$\sigma_{\bar{p}_{ij}}^2 = \frac{N-1}{N} \sum_i^N (\bar{p}_{ijk} - \bar{p}_{ij})^2 \quad (\text{B.10})$$

---

## Beam Phase Space

---

The following description for particle transport in static magnetic fields is taken from the first order matrix formalism used in TRANSPORT [90] and repeated here for completeness.

The movement of a charged particle through a system of magnetic beamline elements can be expressed using the multiplication of matrices that represent the action of the field on the particle passing through it. At any position, the particle is represented by the following six dimensional vector

$$\mathbf{x} = \begin{pmatrix} x \\ x' \\ y \\ y' \\ l \\ \delta \end{pmatrix} \quad (\text{C.1})$$

where the components relative to the central trajectory are the following:

$x$  →the horizontal displacement

$x'$  →the angular divergence in the horizontal plane

$y$  →the vertical displacement

$y'$  →the angular divergence in the vertical plane

$l$  →the path length difference

$\delta$  → $\Delta p/p$  the relative momentum deviation

The action of the field on a charged particle is represented to first-order by the unitary matrix  $\mathbf{R}$ , and the relation of the initial ( $\mathbf{x}_i$ ) and final ( $\mathbf{x}_f$ ) positions is the following

$$\mathbf{x}_f = \mathbf{R}\mathbf{x}_i \quad (\text{C.2})$$

When considering beams of particles it is more convenient to work in the collective description of beam ellipsoids, which contain points representing possible particles.

The sum of these points is called the “phase space”, occupied by the beam. The equation for a phase ellipse is given by

$$\mathbf{x}_i^T \sigma_i^{-1} \mathbf{x}_i = 1 \quad (\text{C.3})$$

By using the identity  $\mathbf{R}\mathbf{R}^{-1} = \mathbb{1}$ , one can relate the initial and final phase space ellipsoids by

$$\sigma_f = \mathbf{R}\sigma_i\mathbf{R}^T \quad (\text{C.4})$$

There is no coupling of vertical and horizontal phase space in magnetic beamline elements with mid-plane symmetry (to first order), and therefore the elements of  $\sigma$  can be separated in their horizontal and vertical components. In the two dimensional plane projection of the six dimensional ellipse, the ellipsoid parameters are identical to the Courant-Snyder (Twiss) parameters found in [88] and are given by

$$\sigma = \begin{pmatrix} \sigma_{11} & \sigma_{12} \\ \sigma_{21} & \sigma_{22} \end{pmatrix} = \epsilon \begin{pmatrix} \beta & -\alpha \\ -\alpha & \gamma \end{pmatrix} \quad (\text{C.5})$$

such that the equation for the ellipse is the following

$$\mathbf{x}^T \sigma^{-1} \mathbf{x} = 1 \quad (\text{C.6})$$

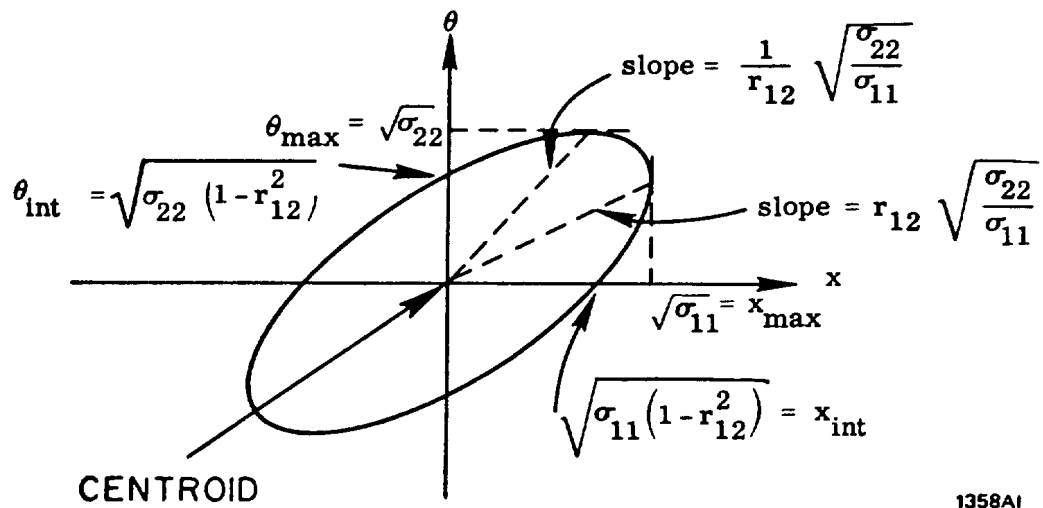
$$\sigma_{11}x'^2 + \sigma_{22}x^2 - 2\sigma_{21}x \cdot x' + \epsilon^2 = \det \sigma \quad (\text{C.7})$$

The area of the ellipse is given by

$$A = \pi \sqrt{\det \sigma} = \pi x_{max} x'_{int} = \pi x_{int} x'_{max} \quad (\text{C.8})$$

as shown in Figure C.1 where  $\theta = x'$  and the phase rotation is given by the off-diagonal term  $\rho = \frac{\sigma_{21}}{\sqrt{\sigma_{11}\sigma_{22}}}$ . The physical correspondence to the elements of the  $\sigma$  matrix is the following

- $\sqrt{\sigma_{11}} = x_{max}$  = the gaussian sigma width of the horizontal beam profile
- $\sqrt{\sigma_{22}} = x'_{max}$  = the gaussian sigma width of the horizontal divergence
- $\sqrt{\sigma_{33}} = y_{max}$  = the gaussian sigma width of the vertical beam profile
- $\sqrt{\sigma_{44}} = y'_{max}$  = the gaussian sigma width of the vertical divergence
- $\sqrt{\sigma_{55}} = l_{max}$  = the longitudinal extent of the particle bunch
- $\sqrt{\sigma_{66}} = \delta$  = the gaussian sigma width of the longitudinal momentum spread



1358A1

Figure C.1: The two dimensional phase space ellipse [88].

---

## References

---

- [1] G. Isidori, “Flavour Physics and Implication for New Phenomena,” *Adv. Ser. Direct. High Energy Phys.* **26**, 339 (2016), arXiv:1507.00867 [hep-ph] .
- [2] G. Isidori, “Lecture notes on flavour physics,” (2016), Universität Zürich.
- [3] Y. Fukuda *et al.* (Super-Kamiokande Collaboration), “Evidence for oscillation of atmospheric neutrinos,” *Phys. Rev. Lett.* **81**, 1562 (1998).
- [4] Q. R. Ahmad *et al.* (SNO Collaboration), “Measurement of the rate of  $\nu_e + d \rightarrow p + p + e^-$  interactions produced by  $^8\text{B}$  solar neutrinos at the sudbury neutrino observatory,” *Phys. Rev. Lett.* **87**, 071301 (2001).
- [5] K. Eguchi *et al.* (KamLAND Collaboration), “First Results from KamLAND: Evidence for Reactor Antineutrino Disappearance,” *Phys. Rev. Lett.* **90**, 021802 (2003).
- [6] Y. Abe *et al.* (Double Chooz Collaboration), “Indication of Reactor  $\bar{\nu}_e$  Disappearance in the Double Chooz Experiment,” *Phys. Rev. Lett.* **108**, 131801 (2012).
- [7] F. P. An *et al.*, “Observation of Electron-Antineutrino Disappearance at Daya Bay,” *Phys. Rev. Lett.* **108**, 171803 (2012).
- [8] S. Ahn *et al.*, “Detection of accelerator-produced neutrinos at a distance of 250 km,” *Physics Letters B* **511**, 178 (2001).
- [9] E. Aliu *et al.* (The K2K Collaboration), “Evidence for Muon Neutrino Oscillation in an Accelerator-Based Experiment,” *Phys. Rev. Lett.* **94**, 081802 (2005).
- [10] D. G. Michael *et al.* (MINOS Collaboration), “Observation of Muon Neutrino Disappearance with the MINOS Detectors in the NuMI Neutrino Beam,” *Phys. Rev. Lett.* **97**, 191801 (2006).
- [11] C. Albright *et al.*, “Physics at a neutrino factory,” (2000), arXiv:hep-ex/0008064 [hep-ex] .
- [12] Z. Maki, M. Nakagawa, and S. Sakata, “Remarks on the unified model of elementary particles,” *Progress of Theoretical Physics* **28**, 870 (1962).
- [13] B. Pontecorvo, “Inverse beta processes and nonconservation of lepton charge,” *Sov. Phys. JETP* **7**, 172 (1958), [*Zh. Eksp. Teor. Fiz.*34,247(1957)].

- [14] A. Rubbia, “Lecture notes on neutrino physics,” (2016), ETH Zürich.
- [15] J. L. Hewett *et al.*, “Fundamental Physics at the Intensity Frontier,” (2012), 10.2172/1042577, arXiv:1205.2671 [hep-ex] .
- [16] P. Minkowski, “ $\mu \rightarrow e\gamma$  at a Rate of One Out of  $10^9$  Muon Decays?” *Phys. Lett.* **67B**, 421 (1977).
- [17] Y. Okada, “Models of lepton flavor violation,” in *Lepton Dipole Moments* (WORLD SCIENTIFIC, 2011) pp. 683–700.
- [18] J. Albrecht *et al.* (Intensity Frontier Charged Lepton Working Group), “Working Group Report: Charged Leptons,” in *Proceedings, 2013 Community Summer Study on the Future of U.S. Particle Physics: Snowmass on the Mississippi (CSS2013): Minneapolis, MN, USA, July 29-August 6, 2013* (2013) arXiv:1311.5278 [hep-ex] .
- [19] Y. Kuno and Y. Okada, “Muon decay and physics beyond the standard model,” *Rev. Mod. Phys.* **73**, 151 (2001), arXiv:hep-ph/9909265 [hep-ph] .
- [20] M. Koike, Y. Kuno, J. Sato, and M. Yamanaka, “New process for charged lepton flavor violation searches:  $\mu^- e^- \rightarrow e^- e^-$  in a muonic atom,” *Phys. Rev. Lett.* **105**, 121601 (2010).
- [21] P.-R. Kettle, “The “Golden” cLFV channels  $\mu \rightarrow e\gamma$  and  $\mu \rightarrow eee$  — the high-intensity frontier,” *Hyperfine Interactions* **214**, 47 (2013).
- [22] G. M. Pruna and A. Signer, “The  $\mu \rightarrow e\gamma$  decay in a systematic effective field theory approach with dimension 6 operators,” *JHEP* **10**, 014 (2014), arXiv:1408.3565 [hep-ph] .
- [23] G. M. Pruna and A. Signer, “Lepton-flavour violating decays in theories with dimension 6 operators,” *Proceedings, Workshop on Flavour changing and conserving processes 2015 (FCCP2015): Anacapri, Capri Island, Italy, September 10-12, 2015*, EPJ Web Conf. **118**, 01031 (2016), arXiv:1511.04421 [hep-ph] .
- [24] A. Signer, “Kappa plot reloaded,” Paul Scherrer Institut, LTP Seminar (2016).
- [25] A. M. Baldini *et al.* (MEG), “Search for the lepton flavour violating decay  $\mu^+ \rightarrow e^+ \gamma$  with the full dataset of the MEG experiment,” *Eur. Phys. J.* **C76**, 434 (2016), arXiv:1605.05081 [hep-ex] .
- [26] A. M. Baldini *et al.* (MEG II), “The design of the MEG II experiment,” (2018), arXiv:1801.04688 [physics.ins-det] .
- [27] A. Blondel *et al.*, “Mu3e Technical Design Report,” In Preparation (2018).

- [28] L. Bartoszek *et al.* (Mu2e), “Mu2e Technical Design Report,” (2014), arXiv:1501.05241 [physics.ins-det] .
- [29] Y. G. Cui *et al.* (COMET), “Conceptual design report for experimental search for lepton flavor violating  $\mu^- \rightarrow e^-$  conversion at sensitivity of  $10^{*-16}$  with a slow-extracted bunched proton beam (COMET),” (2009).
- [30] U. Bellgardt *et al.* (SINDRUM), “Search for the Decay  $\mu^+ \rightarrow e^+e^+e^-$ ,” Nucl. Phys. **B299**, 1 (1988).
- [31] C. Dohmen *et al.* (SINDRUM II), “Test of lepton flavor conservation in  $\mu \rightarrow e$  conversion on titanium,” Phys. Lett. **B317**, 631 (1993).
- [32] W. Honecker, C. Dohmen, H. Haan, D. Junker, G. Otter, M. Starlinger, P. Wintz, J. Hofmann, W. Bertl, J. Egger, B. Krause, S. Egli, R. Engfer, C. Findeisen, E. A. Hermes, T. Kozlowski, C. B. Niebuhr, H. S. Pruyss, and A. van der Schaaf (SINDRUM II Collaboration), “Improved limit on the branching ratio of  $\mu \rightarrow e$  conversion on lead,” Phys. Rev. Lett. **76**, 200 (1996).
- [33] W. H. Bertl *et al.* (SINDRUM II), “A Search for muon to electron conversion in muonic gold,” Eur. Phys. J. **C47**, 337 (2006).
- [34] L. Willmann *et al.*, “New bounds from a search for muonium to antimuonium conversion,” Phys. Rev. Lett. **82**, 49 (1999).
- [35] T. P. Gorringer and D. W. Hertzog, “Precision Muon Physics,” Prog. Part. Nucl. Phys. **84**, 73 (2015), arXiv:1506.01465 [hep-ex] .
- [36] M. Seidel *et al.*, “Production of a 1.3 MW Proton Beam at PSI,” *Proceedings, 1st International Particle Accelerator Conference (IPAC'10): Kyoto, Japan, May 23-28, 2010*, Conf. Proc. **C100523**, TUYRA03 (2010).
- [37] G. Heidenreich, “Carbon and Beryllium Targets at PSI,” AIP Conference Proceedings **642**, 122 (2002).
- [38] “Muon Beams at the Paul Scherrer Institute,” <https://www.psi.ch/lmu/ss-beamlines>, accessed: 2018-03-07.
- [39] P. Bakule and E. Morenzoni, “Generation and applications of slow polarized muons,” Contemp. Phys. **45**, 203 (2004).
- [40] T. Prokscha, E. Morenzoni, K. Deiters, F. Foroughi, D. George, R. Kobler, A. Suter, and V. Vrankovic, “the new  $\mu e4$  beam at psi: A hybrid-type large acceptance channel for the generation of a high intensity surface-muon beam,” Nuclear Instruments and Methods in Physics Research Section A: Accelerators, Spectrometers, Detectors and Associated Equipment **595**, 317 (2008).

- [41] A. M. Baldini *et al.*, “MEG Upgrade Proposal,” (2013), arXiv:1301.7225 [physics.ins-det] .
- [42] A. Blondel *et al.*, “Research Proposal for an Experiment to Search for the Decay  $\mu \rightarrow eee$ ,” arXiv:1301.6113 (2013).
- [43] F. A. Berg, *CMBL - A High-Intensity Muon Beam Line; Scintillation Target with Monitoring System for Next-Generation Charged Lepton Flavour Violation Experiments*, Ph.D. thesis, ETH Zürich (2017”).
- [44] P. R. Kettle *et al.*, “HiMB A Possible Next Generation High-intensity Muon Beam Facility for Particle Physics & Materials Science,” Poster at Physics of fundamental Symmetries and Interactions - PSI2013 (2014).
- [45] C. Patrignani *et al.* (Particle Data Group), “Review of Particle Physics,” *Chin. Phys.* **C40**, 100001 (2016).
- [46] R. M. Djilkibaev and R. V. Konoplich, “Rare muon decay  $\mu^+ \rightarrow e^+e^-e^+\nu_e\bar{\nu}_\mu$ ,” *Phys. Rev. D* **79**, 073004 (2009).
- [47] T. Roberts, “G4Beamline,” <http://g4beamline.muonsinc.com>.
- [48] D. R. F. Cochran *et al.*, “Production of Charged Pions by 730-MeV Protons from Hydrogen and Selected Nuclei,” *Phys. Rev. D* **6**, 3085 (1972).
- [49] F. H. Cverna, P. R. Bevington, M. W. McNaughton, H. B. Willard, N. S. P. King, and D. R. Giebink, “Single and double pion production from 800 mev proton-proton collisions,” *Phys. Rev. C* **23**, 1698 (1981).
- [50] P. Denes, B. D. Dieterle, D. M. Wolfe, T. Bowles, T. Dombeck, J. E. Simmons, T. S. Bhatia, G. Glass, and W. B. Tippens, “Production of positive pions by 800 MeV protons on carbon,” *Phys. Rev. C* **27**, 1339 (1983).
- [51] J. F. Crawford, M. Daum, G. H. Eaton, R. Frosch, H. Hirschmann, R. Horisberger, J. W. McCulloch, E. Steiner, R. Hausammann, R. Hess, and D. Werren, “Measurement of cross sections and asymmetry parameters for the production of charged pions from various nuclei by 585-mev protons,” *Phys. Rev. C* **22**, 1184 (1980).
- [52] J. F. Crawford *et al.*, “Production of low energy pions by 590 MeV protons in nuclei,” *Helv. Phys. Acta* **53**, 497 (1980).
- [53] S. Agostinelli *et al.* (GEANT4), “GEANT4: A Simulation toolkit,” *Nucl. Instrum. Meth.* **A506**, 250 (2003).

- [54] R. L. Burman and E. S. Smith, *Parameterization of Pion Production and Reaction Cross Sections at LAMPF Energies*, Tech. Rep. LA-11502-MS. DE-98-011120. UC-414 (Los Alamos Nat. Lab., Los Alamos, NM, 1989).
- [55] R. Frosch, J. Löffler, and C. Wigger, *Decay of pions trapped in graphite*, Tech. Rep. TM-11-92-01 (Paul Scherrer Institut, 5232 Villigen-PSI, 1992).
- [56] F. Berg, L. Desorgher, A. Fuchs, W. Hajdas, Z. Hodge, P.-R. Kettle, A. Knecht, R. Lüscher, A. Papa, G. Rutar, and M. Wohlmuther, “Target studies for surface muon production,” *Phys. Rev. Accel. Beams* **19**, 024701 (2016).
- [57] A. Pifer, T. Bowen, and K. Kendall, “A high stopping density  $\mu^+$  beam,” *Nuclear Instruments and Methods* **135**, 39 (1976).
- [58] D. Kiselev, “Meson production targets,” Slides at Project X Muon Spin Rotation Forum (2012).
- [59] P. R. Kettle, “HiMB Radial-grooved Target Study Project,” Paul Scherrer Institut (2013).
- [60] A. Savvatimskiy, “Measurements of the melting point of graphite and the properties of liquid carbon (a review for 1963-2003),” *Carbon* **43**, 1115 (2005).
- [61] R. Taylor, K. Gilchrist, and L. Poston, “Thermal conductivity of polycrystalline graphite,” *Carbon* **6**, 537 (1968).
- [62] C. Wood, D. Emin, and P. E. Gray, “Thermal conductivity behavior of boron carbides,” *Phys. Rev. B* **31**, 6811 (1985).
- [63] M. W. Mallet and others, “Preparation and Examination of Beryllium Carbide,” *J. Electrochem. Soc.* **101**, 298 (1954).
- [64] J. J. Neely, C. E. Teeter, and J. B. Trice, “Thermal conductivity and heat capacity of beryllium carbide,” *Journal of the American Ceramic Society* **33**, 363 (1950).
- [65] “The scattering of positrons by electrons with exchange on Dirac’s theory of the positron,” *Proceedings of the Royal Society of London A: Mathematical, Physical and Engineering Sciences* **154**, 195 (1936).
- [66] W. Greiner and J. Reinhardt, *Quantum Electrodynamics* (Springer, 2008).
- [67] G. Folger and J. Wellisch, “The Binary Cascade,” (2005), 10.5170/CERN-2005-002.313.
- [68] C. T. Services, “OPERA-3D User’s Guide, 18th Ed.” (2018).
- [69] “Metal Package Photomultiplier Tube R9880U Series,” [https://www.hamamatsu.com/resources/pdf/etd/R9880U\\_TPMH1321E.pdf](https://www.hamamatsu.com/resources/pdf/etd/R9880U_TPMH1321E.pdf).

- [70] “Premium Plastic Scintillators - Data Sheet,” <https://www.crystals.saint-gobain.com/sites/imdf.crystals.com/files/documents/sgc-bc400-404-408-412-416-data-sheet.pdf>.
- [71] J. B. Birks, *The Theory and Practice of Scintillation Counting: International Series of Monographs in Electronics and Instrumentation* (Pergamon, 2013).
- [72] G. F. Knoll, *Radiation Detection and Measurement* (Wiley, 2000).
- [73] C. Kittel, *Introduction to Solid State Physics* (Wiley, 2004).
- [74] B. K. Cha, J.-H. Shin, J. H. Bae, C. hun Lee, S. Chang, H. K. Kim, C. K. Kim, and G. Cho, “Scintillation characteristics and imaging performance of CsI:Tl thin films for X-ray imaging applications,” *Nuclear Instruments and Methods in Physics Research Section A: Accelerators, Spectrometers, Detectors and Associated Equipment* **604**, 224 (2009), pSD8.
- [75] M. Re, G. A. P. Cirrone, L. Cosentino, G. Cuttone, P. Finocchiaro, P. A. Lojacono, Y. J. Ma, P. Vynck, B. Volckaerts, M. Vervaeke, J. van Erps, A. Hermanne, and H. Thienpont, “Production of inorganic thin scintillating films for ion beam monitoring devices,” in *Proceedings of the 2005 Particle Accelerator Conference* (2005) pp. 808–810.
- [76] A. Pappalardo, L. Cosentino, and P. Finocchiaro, “An imaging technique for detection and absolute calibration of scintillation light,” *Review of Scientific Instruments* **81**, 033308 (2010), <https://doi.org/10.1063/1.3360931> .
- [77] J. S. Lord, “The new muon beam camera,” [nmi3.eu/files/beam\\_camera\\_report.pdf](http://nmi3.eu/files/beam_camera_report.pdf) (2010).
- [78] J. Harasimowicz, C. P. Welsch, L. Cosentino, A. Pappalardo, and P. Finocchiaro, “Beam diagnostics for low energy beams,” *Phys. Rev. ST Accel. Beams* **15**, 122801 (2012).
- [79] V. V. Nagarkar, T. K. Gupta, S. R. Miller, Y. Klugerman, M. R. Squillante, and G. Entine, “Structured CsI(Tl) scintillators for X-ray imaging applications,” *IEEE Transactions on Nuclear Science* **45**, 492 (1998).
- [80] T. Jing, G. Cho, J. Drewery, I. Fujieda, S. N. Kaplan, A. Miresghhi, V. Perez-Mendez, and D. Wildermuth, “Enhanced columnar structure in CsI layer by substrate patterning,” *IEEE Transactions on Nuclear Science* **39**, 1195 (1992).
- [81] E. Kozyrev, K. Kuper, A. Lemzyakov, A. Petrozhitskiy, and A. Popov”, “Performance and Characterization of CsI:Tl thin Films for X-ray Imaging Application”,

- "Physics Procedia" **84**, 245 (2016), "Proceedings of the International Conference "Synchrotron and Free electron laser Radiation: generation and application" (SFR-2016), July 4 - 7, 2016, Novosibirsk, Russia".
- [82] "ICX415AL Device Specifications," [https://www.1stvision.com/cameras/sensor\\_specs/ICX415.pdf](https://www.1stvision.com/cameras/sensor_specs/ICX415.pdf).
- [83] "Digital Camera C11440-22C Instruction manual," [https://www.hamamatsu.com/sp/sys/en/manual/C11440-22C\\_E\\_v.1.4.pdf](https://www.hamamatsu.com/sp/sys/en/manual/C11440-22C_E_v.1.4.pdf).
- [84] G. Bradski, "The OpenCV Library," Dr. Dobb's Journal of Software Tools (2000).
- [85] R. Brun and F. Rademakers, "Root an object oriented data analysis framework," Nuclear Instruments and Methods in Physics Research Section A: Accelerators, Spectrometers, Detectors and Associated Equipment **389**, 81 (1997), new Computing Techniques in Physics Research V.
- [86] A. Badertscher, P. Egan, M. Gladisch, M. Greene, V. Hughes, F. Marian, D. Lu, G. Putlitz, M. Ritter, G. Sanders, P. Souder, and R. Werbeck, "Development of a subsurface positive muon beam at LAMPF," Nuclear Instruments and Methods in Physics Research Section A: Accelerators, Spectrometers, Detectors and Associated Equipment **238**, 200 (1985).
- [87] "DuPont Tedlar Polyvinyl Fluoride (PVF) Films - General Properties," [http://www.dupont.com/content/dam/dupont/products-and-services/membranes-and-films/pvf-films/documents/DEC\\_Tedlar\\_GeneralProperties.pdf](http://www.dupont.com/content/dam/dupont/products-and-services/membranes-and-films/pvf-films/documents/DEC_Tedlar_GeneralProperties.pdf) (2014).
- [88] E. Courant and H. Snyder, "Theory of the alternating-gradient synchrotron," Annals of Physics **3**, 1 (1958).
- [89] R. Szeliski, *Computer Vision: Algorithms and Applications* (Springer, 2011).
- [90] K. L. Brown, F. Rothacker, D. C. Carey, and F. C. Iselin, "Transport: A Computer Program for Designing Charged Particle Beam Transport Systems," (1977).